

ALMA MATER STUDIORUM - UNIVERSITÀ DI BOLOGNA

DOTTORATO DI RICERCA IN
ASTROFISICA

Ciclo XXXV

HYDRODYNAMIC SIMULATIONS OF MULTIPLE STELLAR POPULATIONS IN GLOBULAR CLUSTERS

Settore Concorsuale: 02/C1 - ASTRONOMIA, ASTROFISICA, FISICA DELLA TERRA E DEI PIANETI

Settore scientifico - disciplinare: FIS/05 - ASTRONOMIA E ASTROFISICA

Presentata da:

Elena Lacchin

Coordinatore di Dottorato:

Chiar.mo Prof. Andrea Miglio

Supervisore:

Dr. Francesco Calura

Co-Supervisore:

Chiar.mo Prof. Carlo Nipoti

Esame Finale Anno 2023

*He not busy being born
Is busy dying.*

Bob Dylan

Abstract

The presence of multiple stellar populations in globular clusters is now well accepted, however, very little is known regarding how they formed. Answering this question is one of the major challenges of stellar astrophysics, yet of great interest, given the importance of globular clusters in different fields, from stellar evolution to gravitational waves emission and galaxy assembly.

In this Thesis, I study how multiple stellar populations formed and evolved by means of customized 3D numerical simulations, in light of the most recent data from spectroscopic and photometric observations of both the Local Universe and the high-redshift one, accessible thanks to gravitational lensing. In recent years, the Hubble Space Telescope and the Gaia mission have been crucial to move significant steps toward a more complete and detailed view of globular clusters. Now, with the advent of the brand-new James Webb Space Telescope data, more details on the still-elusive phenomenon of multiple stellar populations will be revealed. This wealth of data will allow us to improve the observational constraints necessary to guide theoretical studies. Numerical simulations are the perfect tool to interpret these data and study the formation and evolution of systems like globular clusters as they represent the best “virtual laboratory” to test the role played by

different physical processes. In particular, hydrodynamic simulations are suited to study the early phases of cluster formation, to follow in great detail the behavior of the gas component, its response to processes such as gas cooling, star formation and stellar feedback. On the other hand, N -body codes permit to study the evolution of stars, coupled with hydrodynamics, to follow the interplay between the gas and stellar components, but also as self-standing tools, to explore the long-term dynamic evolution, up to a Hubble time. For a complete understanding of the multiple stellar population phenomenon, it is necessary to exploit both hydrodynamic and N -body codes to retrieve structural, dynamical and chemical information, at different stages of a cluster life. Such outcomes are then compared with observations, to constrain the origin and reconstruct the evolution of multiple stellar populations in GCs, to which this Thesis is devoted.

Firstly, we study the formation of second-generation stars in a massive globular cluster assuming that the cluster is rotating, given the increasing number of observations of rotating, present-day clusters. Recently, it has been possible also to recover the rotational amplitude for different populations and subgroups of them. We explore, by means of 3D hydrodynamic simulations, different inclinations of the rotational axis and also different velocity profiles, with the assumption that globular clusters have undergone self-enrichment and that second-generation stars are formed out of asymptotic giant branch stars ejecta, diluted by external pristine gas. We focus in more detail on the link between the chemical composition of newborn stars and their dynamic properties. For low pristine gas density, stars mainly formed out of asymptotic giant branch stars ejecta rotate faster than stars formed out of more diluted gas, in qualitative agreement with current observations. The first, newly formed stars are also collected in a disk, which extends for almost 10 pc. When increasing the pristine gas density, new stars, along with being more helium-poor on average, show weak to no rotation due to the stronger dilution. Variations in the inclination angle between the rotation axis, the direction of the infalling gas and the velocity profile slightly alter the extent of the stellar disc and the rotational amplitude.

Then, we study the implications of Type Ia supernovae on the regulation of star formation of second-generation stars and on their chemical composition, traced by iron and helium. Given the large uncertainties of the explosion times of Type Ia supernovae, we tested various scenarios. As before, second-generation stars are assumed to form out of asymptotic giant branch stars ejecta and external gas, for which we tested two density values. In the low-density case, supernovae Ia have a stronger effect on the star formation,

preventing the accretion of pristine gas, which implies that second-generation stars are all extremely helium-enhanced, at variance with observations. On the other hand, in the high-density model, supernovae are less effective in preventing the dilution of the stellar ejecta with pristine gas. Moreover, star formation is mildly affected by supernova explosions, and therefore, the results are similar to the ones obtained without Type Ia supernova feedback. One major difference concerns the iron composition, given that Type Ia supernovae are the main producers of this element, which is significantly enhanced and leads to a spread of ~ 0.14 dex, typical of only a small number of Galactic globular clusters, labelled Type II clusters.

Finally, we focused on the long-term evolution of a globular cluster, composed of two populations and orbiting the disk of the Milky Way. The degree of mass loss suffered by globular clusters, and specifically by the different populations, is, in fact, still poorly understood. In addition, the first population is generally assumed to be more massive at their birth than it is now, in order to match the current mass of second population stars. This assumption implies that, during their long-term evolution, clusters lose around 90% of the first population. We have tested whether such strong mass loss could take place in a massive cluster, performing a series of N -body simulations to explore the parameter space. We have derived that, for an extended first population and a low-mass second one, the cluster loses almost 98% of its initial first population mass and the cluster mass can be as much as 20 times less after a Hubble time. In addition, under these conditions, the derived fraction of second-population stars reproduces the observed value, which is one of the strongest constraints of cluster mass loss.

CONTENTS

1 INTRODUCTION	1
I General background	5
2 GLOBULAR CLUSTERS: AN OBSERVATIONAL PERSPECTIVE	7
2.1 Globular clusters: what are they?	7
2.2 Multiple stellar populations	9
2.2.1 Type I and Type II: a globular cluster classification	12
2.2.2 Chemical variations	14
2.2.2.1 Light element abundance variations	14
2.2.2.2 Helium	16
2.2.2.3 Lithium	18
2.2.2.4 Iron	18
2.2.3 Structural and kinematical properties	19
3 FORMATION OF MULTIPLE STELLAR POPULATIONS IN A GLOBULAR CLUSTER	21
3.1 The formation of multiple populations	23
3.1.1 Asymptotic Giant Branch scenario	24
3.1.1.1 AGB stars	25
3.1.1.2 The scenario	26
3.1.2 Fast rotating massive stars scenario	28

Contents

3.1.3	Super massive stars scenario	29
3.1.4	Massive interacting binaries scenario	31
3.1.5	Single star formation episode vs. Self-enrichment	32
3.1.6	Observational constraints	33
3.1.7	This Thesis	35
II	Methods	37
4	NUMERICAL SIMULATIONS	39
4.1	Hydrodynamics	40
4.1.1	Hydrodynamics in RAMSES	43
4.2	N-body methods	45
4.2.1	Gravity in RAMSES	47
4.3	Subgrid physical ingredients	49
4.3.1	AGB feedback	50
4.3.2	Thermochemistry	51
4.3.3	Star formation	55
4.3.4	Limitations	56
III	Results	59
5	THE ROLE OF INTERNAL ROTATION ON THE SECOND GENERATION FORMATION	61
5.1	Introduction	61
5.2	Simulation setup	64
5.2.1	Initial setup	65
5.2.2	Rotation	68
5.3	Results	68
5.3.1	Rotation perpendicular to the infall	69
5.3.1.1	Low-density model	69
5.3.1.2	High-density model	76
5.3.2	Rotation parallel to the infall	80
5.3.2.1	Low-density model	82

Contents

5.4	Discussion	86
5.4.1	Model with solid body rotation	86
5.4.2	On the chemical composition of SG stars	89
5.4.3	Comparison with literature	89
5.4.4	Dynamical and kinematical features of present-day globular clusters	91
5.5	Conclusions	92
6	THE ROLE OF TYPE IA SUPERNOVA FEEDBACK ON THE SECOND GENERATION FORMATION	97
6.1	Introduction	97
6.2	Type Ia SN feedback	100
6.2.1	The “overcooling” problem	102
6.2.2	The shape of the delay time distribution	105
6.2.3	Numerical issues	105
6.3	Results	106
6.3.1	Low-density model (LD)	107
6.3.1.1	Dynamical evolution of the gas	107
6.3.1.2	Evolution of the stellar component	110
6.3.2	Low-density model with delayed Type Ia SNe (LD_DS)	114
6.3.2.1	Dynamical evolution of the gas	114
6.3.2.2	Evolution of the stellar component	119
6.3.3	High-density model (HD)	122
6.3.3.1	Dynamical evolution of the gas	122
6.3.3.2	Evolution of the stellar component	123
6.3.4	High-density model with delayed cooling (HD_DC)	126
6.4	Discussion	129
6.5	Conclusions	132
7	MULTIPLE STELLAR POPULATION MASS LOSS IN GALACTIC GLOBULAR CLUSTERS	137
7.1	Models and Methods	142
7.1.1	Description of the code	142
7.1.1.1	Galactic potential model	143

Contents

7.1.2	Single stellar population models	143
7.1.2.1	Without long-term stellar evolution	145
7.1.2.2	Adding long-term stellar evolution	145
7.1.3	Two stellar populations models	146
7.2	Results	147
7.2.1	Models with single stellar population	148
7.2.1.1	Models without stellar evolution	148
7.2.1.2	Models with stellar evolution	149
7.2.2	Models with second generation stars	149
7.2.2.1	Model 2N7m1K	154
7.2.2.2	Model 5Y7M3.7K	158
7.3	Discussion	162
7.3.1	Comparison with other theoretical works	162
7.3.2	The fraction of SG lost in the disk	163
7.3.3	High-z proto-clusters	164
7.3.4	Model limitations	165
7.4	Conclusions	166
8	CONCLUSIONS AND FUTURE PERSPECTIVES	169
8.1	Summary and Conclusions	170
8.1.1	The role of internal rotation on the second generation formation . .	170
8.1.2	The role of Type Ia Supernova feedback on the second generation formation	171
8.1.3	Multiple stellar population mass loss in Galactic globular clusters .	172
8.2	Future Perspectives	173
BIBLIOGRAPHY		191
ACKNOWLEDGEMENTS		211

Chapter 1

INTRODUCTION

Why wait any longer for the world to begin?

Lay Lady Lay, Bob Dylan

The discovery of the first globular cluster, now known by the name of M22, is credited to the German amateur astronomer Johann Abraham Ihle, back in 1665. Some of them, such as ω Centauri, were known even before, but easily mistaken for bright stars. Almost a century later, in 1764, Charles Messier was the first who, thanks to telescopes with higher resolution, was able to resolve individual stars in M4. The ability to visually resolve single stars paved the way for the discovery of an increasing number of globular clusters and, therefore, the development of the first cluster surveys. The first collection of these objects was carried out by William Herschel, who is also entitled to have coined, in 1789, the term “globular clusters” to define these new objects, based on their shape ([Herschel, 1789](#)). Later, several astronomers examined these systems to unveil their nature, like Harlow Shapley, who focused on RR Lyrae to determine their distances and use it to determine our distance from the center of the Galaxy, and Henry C. K. Plummer and Ivan King, who derived cluster density distribution laws, which are still widely adopted. After the compilations of Messier and Herschel, other astronomers published continuously updated catalogs, more detailed and with an increasing number of globular clusters, both detected in the Milky Way, but also in nearby galaxies. Nowadays, the most advanced and used catalog is the one compiled by William Harris, in the latest version of 2010 ([Harris, 2010](#)). Our comprehension of globular clusters increased significantly in the last centuries, suggesting they were simple stellar objects, a belief that has been later questioned by an

increasing number of observations. Only in the last decades, it has been revealed that globular clusters host multiple stellar populations and, eventually, multiple generations, a discovery that dramatically changed our view of globular clusters.

Nowadays, the understanding of the origin of multiple stellar populations and, more broadly, of globular clusters, is one of the most intriguing topics of astronomy. Many studies, both from the theoretical and observational points of view, are aimed at explaining the still-elusive phenomenon of multiple populations, which is of great importance for many astrophysical issues. Its understanding would allow to put constraints on stellar evolution and nucleosynthesis, to probe star formation in the early Universe, unveil the role of stellar dynamics in the origin of exotic stellar objects like binary black holes, responsible for the emission of gravitational waves, and to shed light on the role of proto-GCs in the cosmic reionization and in galaxy formation.

This Thesis aims at addressing the following open questions: what are the effects of different physical processes, such as stellar feedback, gravity and rotation on the formation of multiple stellar populations? Which are the required conditions to lead to the survival of globular clusters?

This Thesis is divided into three parts and is organized as follows.

In the first part, I present the framework within which this Thesis is focused, reporting the observational and theoretical results relevant to the development and interpretation of the work.

- In [Chapter 2](#), I describe the main features defining a globular cluster, focusing on the multiple stellar population phenomenon. Significant space is devoted to the chemical anomalies/variations that have been detected in these systems over the last few decades.
- In [Chapter 3](#), I briefly summarize the main observational evidence of star-forming globular clusters candidates. Then, I will review the various scenarios proposed so far to explain the still-eluding phenomenon of multiple stellar populations.

The second part is devoted to the description of the methodology adopted to carry out the work.

- [Chapter 4](#) encloses a brief description of computational fluid dynamics and N -body computational methods. I review the general features of RAMSES, the code I adopt

to carry out the simulations, whose results I will present throughout the Thesis. Moreover, I describe the physical ingredients implemented in the customized version I am exploiting, such as the AGB feedback, cooling and star formation.

The results I have achieved are presented in the third part of the Thesis:

- In [Chapter 5](#), I explored the implications of internal cluster rotation on the formation of stars in a massive, star-forming globular cluster. Particular emphasis is given to the connection between the kinematical and chemical properties of newborn stars and their comparison with observations.
- [Chapter 6](#) is devoted to studying the role of Type Ia supernova feedback in a globular cluster with multiple stellar populations. The focus is twofold: on the star formation, to determine whether this type of supernovae inhibits the formation of new stars, and under which conditions. Secondly, on the chemical composition of the newborn stars, fundamental to compare the results with current observations.
- In [Chapter 7](#), I investigate the long-term evolution of a globular cluster composed of two generations while orbiting the Milky Way in the plane of the disk. Various initial setups, where different parameters have been varied, have been tested to explore whether a significant mass loss could take place during a Hubble time, as requested by many globular cluster formation scenarios.
- In [Chapter 8](#) I draw the final conclusions of the Thesis. Also, I illustrate possible forthcoming paths that could be investigated in the future, as a follow-up of the present work.

Part I

General background

Chapter 2

GLOBULAR CLUSTERS: AN OBSERVATIONAL PERSPECTIVE

*I need somethin' strong to distract my mind
I'm gonna look at you 'til my eyes go blind*

Mississippi, Bob Dylan

While some stars were formed in isolation, most of them were born in star clusters ([Lada & Lada, 2003](#)), collections of stars bound by gravity that move together through space. Historically, stellar clusters are subdivided into two categories: 1) open clusters, composed of dozens to thousands of young, loosely bound stars; 2) globular clusters, which host up to millions of tightly bound stars. They are much denser than open clusters and, given their almost spherical shape, they have been attributed the term “globulars”.

This Thesis is focused on globular clusters from a theoretical perspective, with the aim of studying both their formation and their long-lasting evolution. In this Chapter, I will describe the major features of globular clusters, showing the difficulties still present in stating a clear definition. I will also highlight the peculiarities of these systems, which make them one of the most fascinating and intriguing astrophysical objects.

2.1 Globular clusters: what are they?

Until the beginning of the 21st century, stellar clusters, and therefore also globular clusters (GCs), were thought to be simple systems composed of gravitationally bound stars, sharing

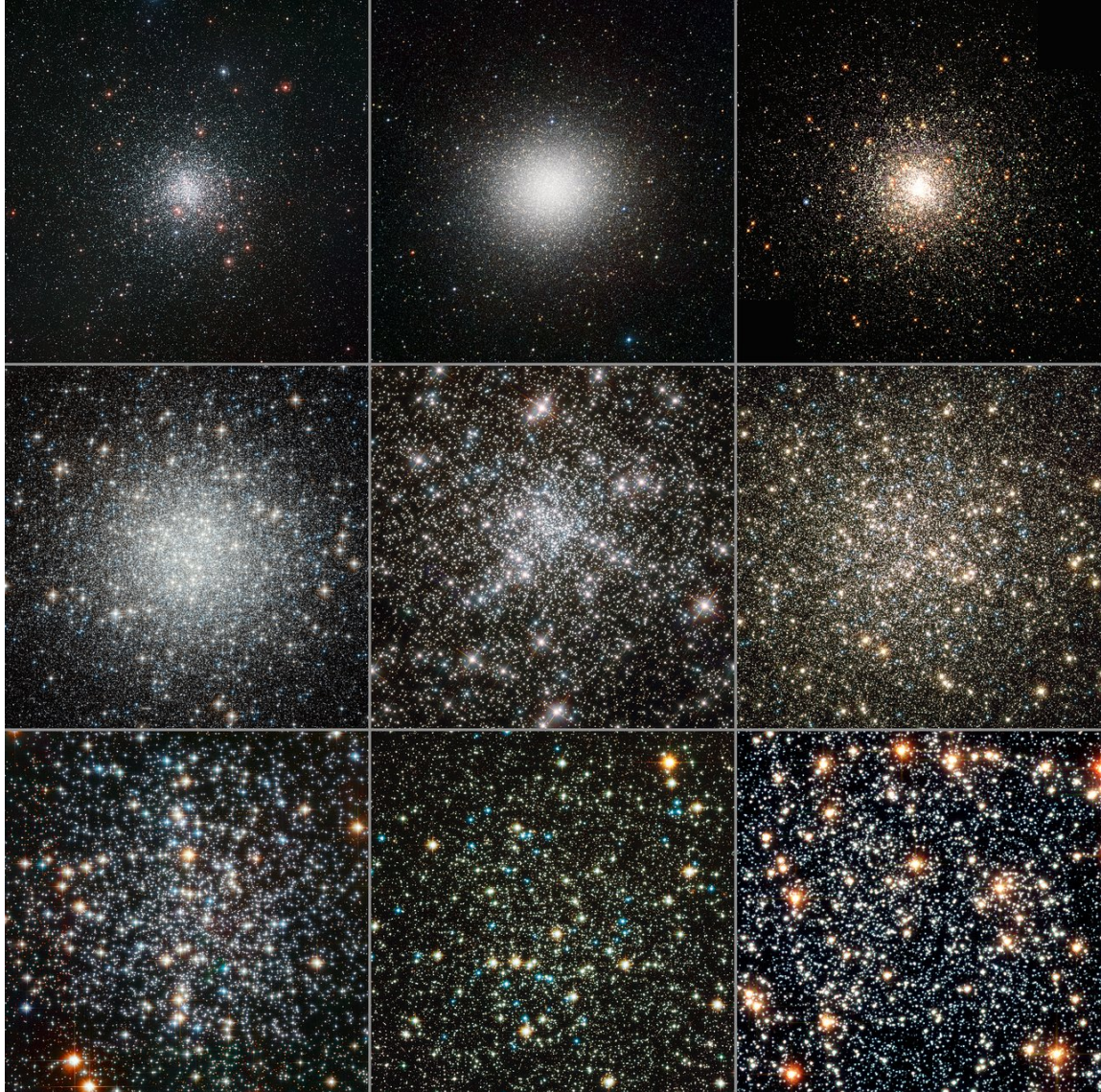


Figure 2.1: A few examples of globular clusters. From left to right, top row: Messier 4 (ESO), Omega Centauri (ESO), Messier 80 (Hubble). Middle row: Messier 53 (Hubble), NGC 6752 (Hubble), Messier 13 (Hubble). Bottom row: Messier 4 (Hubble), NGC 288 (Hubble), 47 Tucanae (Hubble). Credits: ESO.

similar origins and properties. However, with the continuous development of observational facilities and new tools to analyze the incoming data, a different and way more complex picture arose.

[Figure 2.1](#) shows the diversities between several Milky Way (MW) globular clusters, born almost at the same age, but displaying a significantly different morphology.

In general, Galactic GCs have masses between $10^4 - 10^6 M_{\odot}$, with an average mass of $2 \times 10^5 M_{\odot}$, confined in a very narrow region. They are, in fact, very compact, with a half-mass radius of up to few tens of pc. In most cases, as in the MW, they have ages greater than 10 Gyr, even though some younger ones are found in the Magellanic Clouds (MCs) ([Gatto et al., 2020](#)) and in the Andromeda galaxy ([Wang et al., 2021](#)). From the chemical point of view, they generally host metal-poor stars and span, in the MW, a metallicity range of $-2.5 < [\text{Fe}/\text{H}]^1 < -0.5$ dex, with some bulge clusters being slightly more metal-rich.

2.2 Multiple stellar populations

The most peculiar and unique feature regarding the chemical composition of GCs, firstly found through spectroscopic studies already in the 70s ([Osborn, 1971](#)), is that a fraction of their stars shows an “anomalous” chemical composition rarely found in field stars (see e.g. [Carretta et al. 2009a](#), [Carretta et al. 2009b](#), [Carretta et al. 2009c](#), [Gratton et al. 2012](#), [Masseron et al. 2019](#), [Gratton et al. 2019](#) and references therein for more recent studies). These anomalies, mainly seen in light elements (e.g. C, O, Na, Ca, Mg, Si), are not randomly distributed but, on the contrary, are linked by anticorrelations. [Figure 2.2](#) displays several anticorrelations, where it can be seen that they are pointing in a unique direction, departing from the core-collapse supernovae (CC-SNe) yields. Taking as an example the most famous NaO anticorrelation, stars only display Na composition equal or greater than the one produced by massive stars, of about $[\text{Na}/\text{Fe}] = -0.2$ dex, while O is only depleted with respect to the abundance of CC-SNe nucleosynthesis, which is around $[\text{O}/\text{Fe}] = 0.4$ dex (similar values and trends are also observed for Mg). Although all GCs show similar patterns, with stars generally enriched in He, N, Na and depleted in O and C, every GC is different from the other. Moreover, as discussed in [Section 2.2.3](#) their uniqueness is found not only in the chemical composition of their stars, but also in many other

¹The abundance of an element X is expressed as $[\text{X}/\text{H}] = \log(\text{X}/\text{H})_{\star} - \log(\text{X}/\text{H})_{\odot}$. The iron abundance is generally used as an indicator of the metallicity, i.e. the abundance of all elements heavier than He.

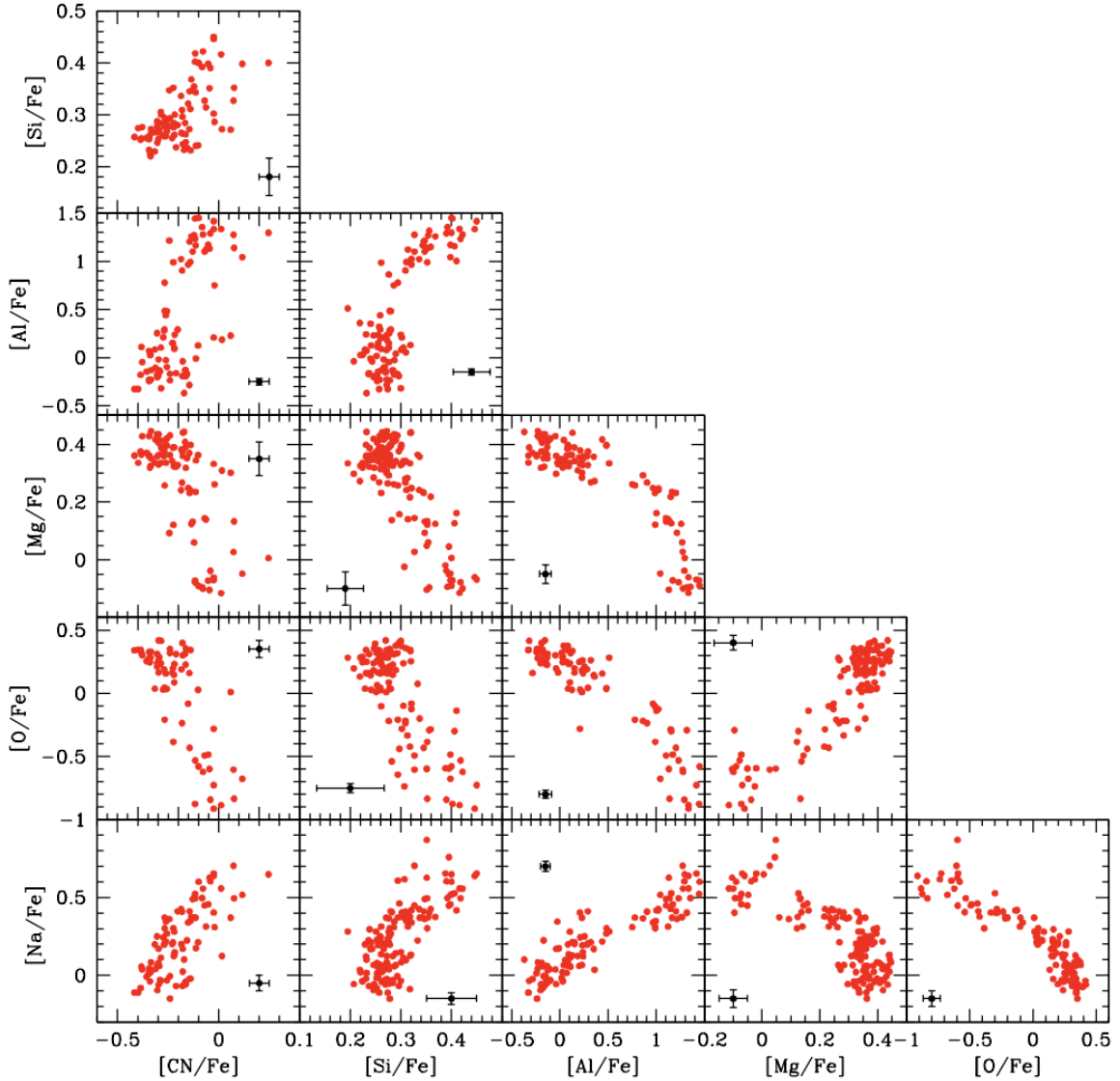


Figure 2.2: (Anti)correlations of light elements in Red Giant Branch stars of the globular cluster NGC 2808. Credits: [Gratton et al. \(2019\)](#). Data from [Carretta \(2015\)](#) and [Carretta et al. \(2018\)](#).

2.2. Multiple stellar populations

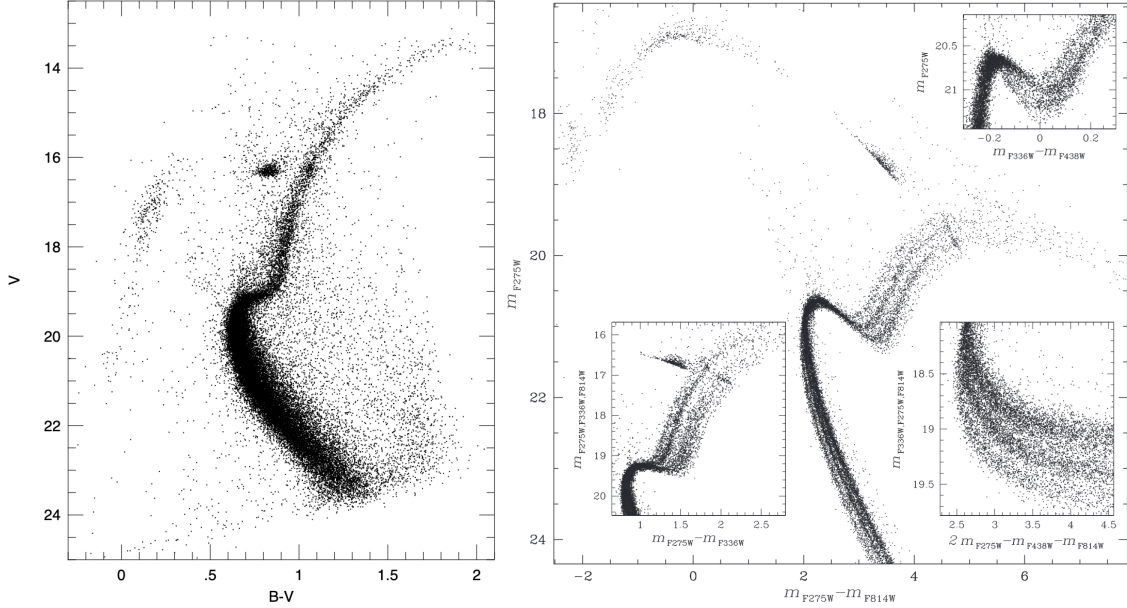


Figure 2.3: Color magnitude diagrams of the globular cluster NGC 2808 from the ground-based 4-m Blanco telescope (left panel, [Walker 1999](#)) and from the Hubble Space Telescope (right panel, [Milone et al. 2015](#)).

structural and kinematical properties.

The presence of stars with different chemical compositions directly implies that GCs are hosting multiple stellar populations (MPs), a staggering discovery, given that for decades globular clusters were considered to be one of the best examples of single stellar populations (SSPs). In particular, stars displaying low Na and high O are labeled as first population, while the ones enhanced in Na and depleted in O are marked as second population.

Later, photometric works mainly based on Hubble images confirmed the presence of various stellar populations within the same GC ([Lee et al., 1999](#); [Pancino et al., 2000](#); [Bedin et al., 2004](#); [Piotto et al., 2005, 2007](#); [Piotto, 2009](#); [Marino et al., 2008](#); [Piotto et al., 2015](#); [Milone et al., 2017](#); [Marino et al., 2019a](#), see [Milone & Marino \(2022\)](#) for a review). In the comparison shown in [Figure 2.3](#), it can be seen the great improvement in the colour-magnitude diagram obtained thanks to the Hubble Space Telescope, where several sequences are clearly visible in different regions, from the main sequence (MS) to the red giant (RGB) and sub-giant branches (SGB).

MPs have been found not only in the MW but also in external galaxies, such as the two MCs ([Mucciarelli et al., 2009](#); [Dalessandro et al., 2016](#); [Niederhofer et al., 2017](#); [Martoc-](#)

chia et al., 2018; Kapse et al., 2022), the Fornax galaxy (Larsen et al., 2014) and M31 (Nardiello et al., 2019). The MP phenomenon is therefore not restricted to our Galaxy, but it is ubiquitous.

After having become aware that globular clusters are not as simple as previously thought, in the last decades, several new tools, mainly based on photometry, have been developed aimed at detecting chemically different populations (see Milone & Marino 2022 for a complete list). We here just mention the chromosome map (ChM), a pseudo-two-color diagram where colors with high sensitivity to light-element and helium abundance variations are chosen in order to maximize the separation of different populations (see Milone et al. 2015, 2017 for ChMs of several clusters). As it will be shown in Section 2.2.1, ChMs are used to distinguish between different types of GCs, depending on how stars populate the plot.

2.2.1 Type I and Type II: a globular cluster classification

While globular clusters are all different from one another, as aforementioned, few attempts have been carried on to classify them. Based on the distribution of stars in the ChM, and their heavy elements abundance, they have been divided into Type I and Type II GCs (Milone et al., 2017).

- **Type I** GCs are mainly composed of two populations sharing similar metallicity but with distinct abundances in some light-elements. In their ChM, two groups of stars are visible, as for NGC 6723 in the left plot of Figure 2.4. Most GCs belong to this group.
- **Type II** GCs comprise almost 20% of the whole GCs and are characterized by a more complex ChM, reflecting their knotty evolution. Clusters belonging to this group possess at least one of the following features (see also the iron complex definition of Johnson et al. 2015):
 1. Together with the two sequences present in the ChM of Type I GCs, additional first and/or second population sequences on the right side of the main ones, e.g. NGC 1851 shown in red in the right plot of Figure 2.4.
 2. Split or broadening of the SGB, not only in color-magnitude diagrams built through UV, but also through optical filters.

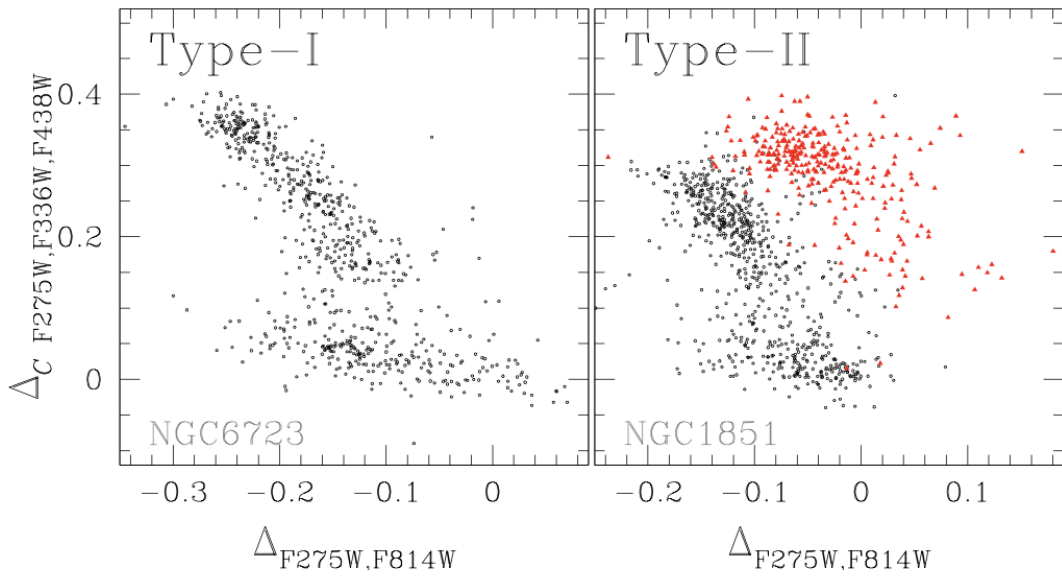


Figure 2.4: Chromosome maps of the Type I GC, NGC 6723 (left), and of the Type II GC, NGC 1851 (right). The first population lies on the bottom of the panel, distributed almost horizontally, and therefore at almost constant in $\Delta_C F275W,F336W,F438W$, while the second one is creating a steep branch above the first population. The red triangles represent the red-RGB stars whose presence characterizes the Type II subgroup. Taken from Milone & Marino (2022) but see Milone et al. (2017) for more examples.

3. Star-to-star variations in metallicity, C+N+O and/or s-process elements abundances (further subclassification based on which of these variations are present and can be found in [Marino et al. 2018](#)).

Type II GCs are usually more massive than Type I clusters; nevertheless, no clear correlation has been found between the current cluster mass and their classification. [Gratton et al. \(2019\)](#) adopted the GC classification provided by [Milone et al. \(2017\)](#) and the derived initial cluster masses from [Baumgardt & Hilker \(2018\)](#) to find possible correlations between several cluster properties. They report that, for a given initial mass, Type II clusters are characterized by a lower interquartile of the distribution of [Na/O] abundance ratios, within the same cluster, meaning that the abundance of polluting material used to form second population stars was lower, maybe diluted by pristine gas of some origin. In addition, several Type II clusters, generally the most massive, show an enrichment of *s*-process elements, which could hint at a longer star formation episode, allowing the possibility for low-mass asymptotic giant branch (AGB) stars to contribute to the enrichment.

Overall, the peculiar nature of Type II GCs seems to reveal a more complex chemical evolution and possibly even more extended star formation than the one of Type I clusters.

2.2.2 Chemical variations

2.2.2.1 Light element abundance variations

Variations in the strength of CN, NH and CH absorption lines were the first evidence of inhomogeneities in the chemical composition of GCs stars, which were initially interpreted as the result of evolutionary mixing happening inside stars. Such hypothesis was later abandoned due to the inconsistency with stellar evolution models predictions (see [Bastian & Lardo 2018](#) for a more detailed description). These chemical anomalies were found not only in evolved RGB stars, but also in unevolved MS ones, and, therefore, could not be explained as a result of stellar evolution.

Carbon, Nitrogen, Oxygen and Sodium are the elements where (anti)correlations are better defined. Second population stars are characterized by enhancement in N and Na and depletion in C and O, resulting in Na-O and C-N anticorrelations ([Carretta et al., 2009a,b](#); [Marino et al., 2008](#)). These patterns are observed in every cluster where multiple populations have been detected.

2.2. Multiple stellar populations

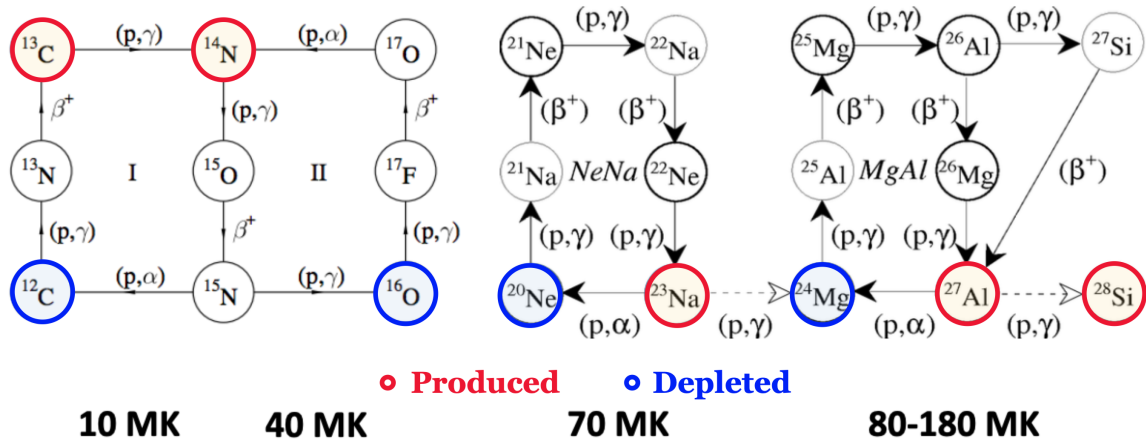


Figure 2.5: The main p -capture cycles with the temperature at which the various cycles become efficient. From left to right the CNO-cycle, the Ne-Na cycle, and the Mg-Al cycle. In red are marked the elements that are produced by these cycles, while in blue are the ones that are depleted. Adapted from [Salaris et al. \(2002\)](#).

Magnesium, Aluminum and Silicon do not vary in all clusters. Second population stars are depleted in Mg and enhanced in Al and Si, therefore, when variations are present, a Mg-Al anticorrelation and a Si-Al correlation are found ([Mészáros et al., 2015](#); [Carretta, 2015](#); [Pancino et al., 2017](#)).

Potassium variations have been found only in three massive clusters, NGC 2419, NGC 2808 and ω Cen ([Cohen & Kirby, 2012](#); [Mucciarelli et al., 2012, 2015](#); [Alvarez Garay et al., 2022](#)). **Scandium** is instead found to anticorrelate with Mg and correlate with Al and Si only in NGC 2808 ([Carretta, 2015](#)). Both these elements are assumed to be formed through the Ar-K chain at temperatures above 150MK ([Ventura et al., 2012](#); [Prantzos et al., 2017](#)).

The nucleosynthetic mechanism responsible for the anticorrelations among light elements is likely to be the proton-capture reactions in the hydrogen-burning at high temperatures. Depending on its core temperature, a star can burn H through different chains, which are involving, as seeds or byproducts, several light-elements, as shown in [Figure 2.5](#).

At inner temperatures greater than 10^7 K, hydrogen is burned through the CN branch of the CNO cycle. The ON branch, instead, requires temperatures $> 4 \times 10^7$ K to be activated, similarly to the NeNa cycle. The famous Na-O anticorrelation, typical of GCs, is expected to originate from these two chains, which are simultaneously converting O

into N, leading to O depletion, and producing Na out of Ne, enhancing the Na abundance. At even higher inner temperatures $> 7 \times 10^7$ K, the MgAl cycle is activated, responsible for the Mg-Al anticorrelation. For temperatures $> 8 \times 10^7$ K, also Si is produced, while K comes from reactions at $T > 1.8 \times 10^8$ K (Prantzos et al., 2017). Currently, most of the stars belonging to GCs are so small that they could not have ignited some of the high-temperature chains, and for very low-mass stars, neither the CNO cycle itself. For this reason, these nuclear reactions must have taken place in other, more massive, stars which are now dead, and not during the evolution of the stars we observe now.

Throughout the Thesis, I will adopt the term “pristine” to indicate gas or stars which have the same chemical composition as the field stars (corresponding to the first population), and “enriched” to label the ones which have been polluted by material coming from the proton-capture reactions described above (e.g. the second population).

It is still unknown which are the types of stars responsible for the production of this enriched material and how this gas was then used to appear now in the atmospheres of low-mass stars. At the moment, several scenarios have been proposed to account for the formation of MPs, such as assuming that the enriched gas is produced by low and intermediate stars while undergoing their AGB phase, by fast-rotating massive stars (FRMS), by very massive stars (VMS) or by massive interacting binaries (MIB). All of these types of stars are sites of the CNO and NeNa cycles whose contribution to the formation of MPs will be extensively described in [Chapter 3](#).

I summarize here the chemical features of different stellar populations in GCs, focusing on those elements that characterize the most the multiple stellar populations’ phenomenon.

2.2.2.2 Helium

Spectroscopic measurements of the abundance of helium are very challenging due to the difficulties in detecting helium lines in the optical for stars cooler than ~ 8000 K. Above this temperature, it is possible to obtain reliable helium abundances only in the horizontal branch (HB) and only until ~ 11500 K. Marino et al. (2014) has estimated the helium content in enriched stars through non-local thermal equilibrium analysis of the photospheric helium lines of HB stars in NCG 2808, recovering a mean value of $Y \sim 0.34$.

A major advance in the study of the helium content of multiple populations in GCs has been carried out through multiband photometry, where colors of the various populations are compared to the ones derived from synthetic spectra with different chemical

2.2. Multiple stellar populations

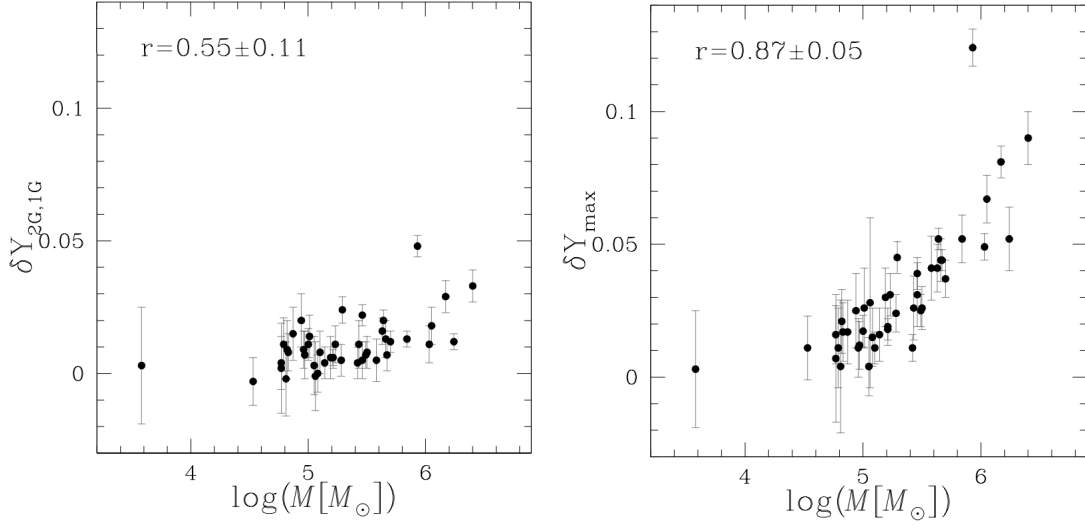


Figure 2.6: Average helium difference between second population (2G) and first population (1G) stars, $\delta Y_{2G,1G}$ (left) and maximum internal helium variation, δY_{max} (right) as a function of the mass of the host cluster. In each panel, it is indicated the Spearman's rank correlation coefficient and the corresponding uncertainty. Taken from [Milone et al. \(2018b\)](#).

composition ([Milone et al., 2012](#)). Thanks to this technique, it is now possible to have homogeneous relative helium estimates between the two populations for more than 70 GCs, both the Milky Way and the Magellanic Clouds ([Marino et al., 2018; Lagioia et al., 2018, 2019; Milone et al., 2020a](#)). The average difference in the helium content between the second and the first population is $\delta Y_{2G,1G} = 0.01$ in the helium mass fraction, while the maximum observed spread ranges from $\delta Y_{max} = 0.01$ to 0.18 in NGC 2419 ([Zennaro et al., 2019](#)). This last quantity is an important constraint for the scenarios of multiple stellar populations. While AGB stars yields predict the most enriched stars to have $Y \sim 0.37$, FRMS are able to eject gas with $Y \sim 0.8$. In addition, δY_{max} is found to correlate with the mass of the cluster, displayed on the right plot of [Figure 2.6](#), as well as with the mass of the single populations, suggesting that more massive clusters form stars out of undiluted material ([Milone et al., 2018b](#)). On the other hand, no correlation has been found between the average relative helium spread of the two populations $\delta Y_{2G,1G}$ and the cluster mass ([Lagioia et al., 2018](#)), as shown on the left plot of [Figure 2.6](#).

2.2.2.3 Lithium

Lithium represents a fundamental chemical element in the investigation of the possible polluters of the enriched material. Its burning temperature of 2.5×10^6 K is much lower than the one of the hot H-burnings and, therefore, the enriched gas used to form new populations of stars should be Li-free. In turn, this would imply a positive correlation between Li and all the elements depleted during the H-burnings, such as O, and an anticorrelation with the ones produced, such as Na. Several studies have exploited high-resolution spectroscopy to derive Li and light-element abundances, finding, for some clusters, the expected significant anticorrelation between Li and Na (and a correlation between Li and O) ([Pasquini et al., 2005](#); [Lind et al., 2009](#); [Shen et al., 2010](#); [D'Antona et al., 2019](#)), while for the rest of them, the Li composition of the two populations were compatible, and therefore no correlation was detected ([D'Orazi et al., 2010, 2014, 2015](#)). Although in some clusters a correlation is found, it characterizes a minority of the enriched population, which is dominated by Li-rich stars ([D'Orazi et al., 2014, 2015](#); [Mucciarelli et al., 2018](#)). Two processes are invoked to explain the lack of depletion in enriched stars: a dilution of the polluters' ejecta with pristine, Li-rich gas, which tends to increase the Li content in mildly enriched stars, and production. Even though Li is mainly destroyed inside stars, such as massive stars, intermediate-mass AGB stars may produce it via the Cameron-Fowler mechanism during the hot H-burning ([Cameron & Fowler, 1971](#)). Scenarios assuming that AGB stars are polluting the gas are therefore favored, relying on the Li content.

2.2.2.4 Iron

A large number of clusters are characterized by an extended first population sequence in the ChM, and, in the most extreme cases, it shows a hint of bimodality as in NGC 2808 ([Milone et al., 2015, 2017](#)). Such behavior is not seen only when creating ChMs with RGB or HB stars ([Dondoglio et al., 2021](#)), but also when considering unevolved MS stars ([Legnardi et al., 2022](#)), which means that these stars were formed out of chemically inhomogeneous gas. While, at the beginning, the extended sequence was thought to be possibly caused by a helium spread ([Milone et al., 2015](#)), recent high-resolution spectroscopic studies have pointed out that first populations stars display a spread in their iron content ([Marino et al., 2019b](#)). Assuming that the observed spread is all in iron, [Legnardi et al. \(2022\)](#) derived that, for the analyzed clusters, the first population could reach iron

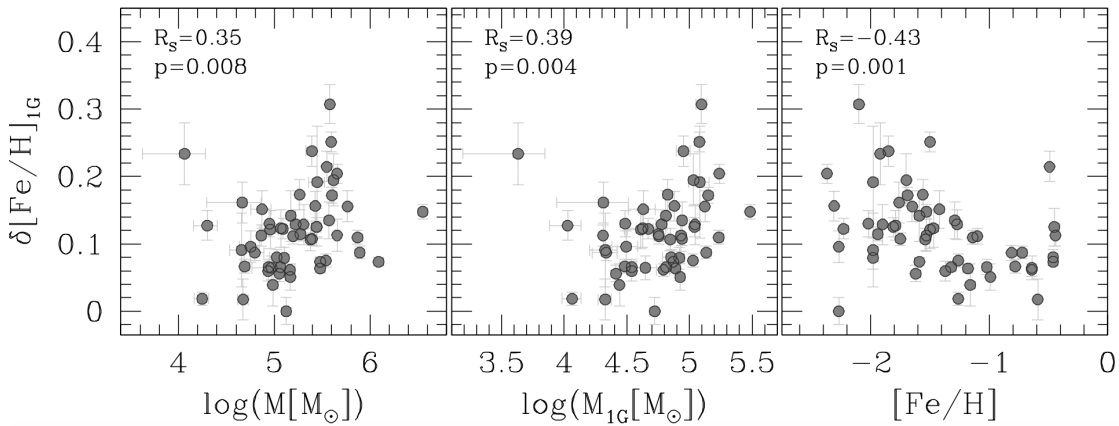


Figure 2.7: The relations between the iron spread $\delta[\text{Fe}/\text{H}]$ of the first population and cluster mass, first population mass, and $[\text{Fe}/\text{H}]$ are plotted. The Spearman's rank correlation coefficient and the associated p -value are quoted in the upper-left corners. Taken from [Legnardi et al. \(2022\)](#).

spreads of 0.30 dex and that it mildly correlates with the mass and the metallicity of clusters, as shown in [Figure 2.7](#). On the other hand, the second population shows a narrower spread, about two times smaller than the first population one, explained by the higher density of the environment out of which they formed, where the crossing time is shorter and, therefore, mixing is much more efficient.

2.2.3 Structural and kinematical properties

Besides the inhomogeneity in their chemical composition, there are several other differences between populations, such as their radial distribution. It has been observed that in most GCs, the second population is much more centrally concentrated than the first one ([Norris & Freeman, 1979](#); [Sollima et al., 2007](#); [Lardo et al., 2011](#); [Milone et al., 2012](#); [Richer et al., 2013](#); [Cordero et al., 2014](#); [Simioni et al., 2016](#); [Dondoglio et al., 2021](#)), with only few clusters showing the opposite ([Larsen et al., 2015](#); [Lim et al., 2016](#)). From the kinematical point of view, second population stars are generally characterized by larger rotational amplitude (e.g. [Lee 2015, 2017](#); [Cordero et al. 2017](#); [Lee 2018](#); [Dalessandro et al. 2019](#); [Kamann et al. 2020](#); [Cordoni et al. 2020a](#); [Szigeti et al. 2021](#) but see also [Chapter 5](#) for a discussion), a lower velocity dispersion ([Bellazzini et al., 2012](#)) but have a higher radial anisotropic velocity distribution ([Richer et al., 2013](#); [Bellini et al., 2015, 2018](#); [Libralato et al., 2019](#)). In addition, the first population hosts an order of magnitude

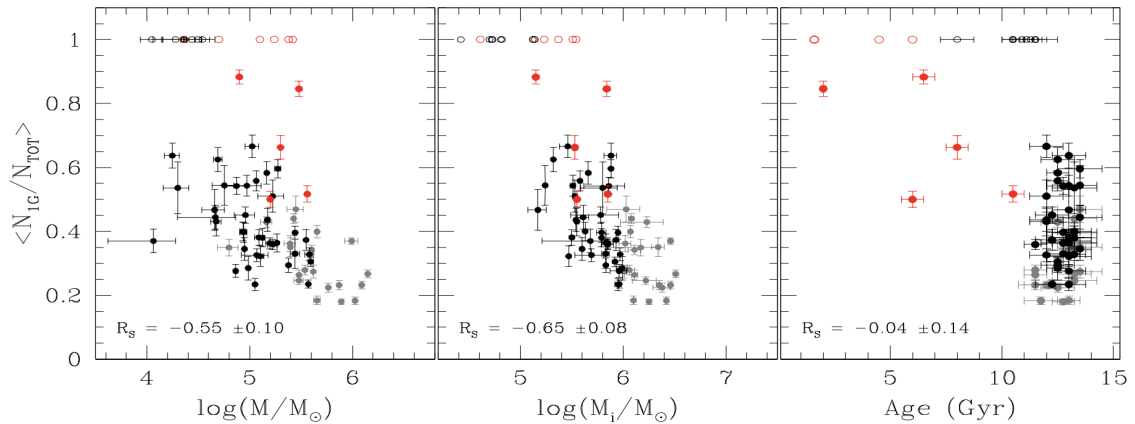


Figure 2.8: Weighted mean of the fraction of FG stars versus the present-day mass (left) initial mass (middle) and the age of the host GC (right). Black and gray dots represent respectively Galactic GCs with $M_{\text{ini}} < 10^6 M_{\odot}$ and $M_{\text{ini}} > 10^6 M_{\odot}$, red dots represent extragalactic GCs. Clusters without MPs are represented with open circles. The Spearman's rank correlation coefficient and the associated uncertainty are quoted in the bottom-left corners. Taken from [Dondoglio et al. \(2021\)](#).

more binaries than the second population ([D'Orazi et al., 2010](#); [Lucatello et al., 2015](#); [Milone et al., 2020b](#)). During the evolution of the cluster, these differences reduce due to the action of two-body relaxation which has been extensively found to lead to a spatial and kinematical mixing of distinct populations. Therefore, the evolutionary state of a cluster is tightly connected with the degree of mixing of the two populations ([Dalessandro et al., 2019](#)).

Another important quantity that needs to be taken into account in the study of MPs, and that will be extensively used in [Chapter 7](#), is the fraction of second population stars hosted in a cluster, at the present day. In massive GCs, $M \sim 10^6 M_{\odot}$, this fraction can reach up to 90%, while low mass ones host around 30% of second population stars ([Milone et al., 2017](#); [Zennaro et al., 2019](#); [Dondoglio et al., 2021](#)). [Figure 2.8](#) shows that this quantity seems also to depend on cluster age, as suggested by clusters in the Large Magellanic Cloud, with older clusters showing a higher fraction of second population stars ([Milone et al., 2020a](#)). Its importance is mainly due to the implications it has on the mass of the two populations and the so-called mass budget problem, which will be discussed in the next Chapter.

Chapter 3

FORMATION OF MULTIPLE STELLAR POPULATIONS IN A GLOBULAR CLUSTER

*The order is rapidly fadin'
and the first one now
will later be last
for the times they are a-changin'*

The Time They Are A-Changin', Bob Dylan

Understanding the origin of GCs and their MPs is a major challenge in modern astronomy. In the local Universe, major recent advances have been made mainly thanks to Hubble Space Telescope and Gaia observations of Galactic GCs. The arrival of the James Webb Space Telescope (JWST) is providing us with fundamental follow-ups, not only allowing us to study with unprecedented detail the populations of local GCs (Marino et al., 2021), but also to probe the high-redshift Universe (Vanzella et al., 2021a, 2022). Hints about how GC looked like at their formation are coming from recent observations of gravitationally lensed fields, an example of which is displayed in Figure 3.1. The presence of several faint systems at redshift $z > 6$, with masses of $\sim 10^6 - 10^7 M_\odot$ and sizes of few tens of parsec have been revealed, compatible with the expectations for GCs precursors (Vanzella et al., 2019).

Characterizing these high-z systems is fundamental to understand how GCs were formed, especially the old clusters, such as the ones in the MW. Our Galaxy, in fact, hosts almost 150 GCs which are populating the bulge, the halo and the thick disk, and all of them are

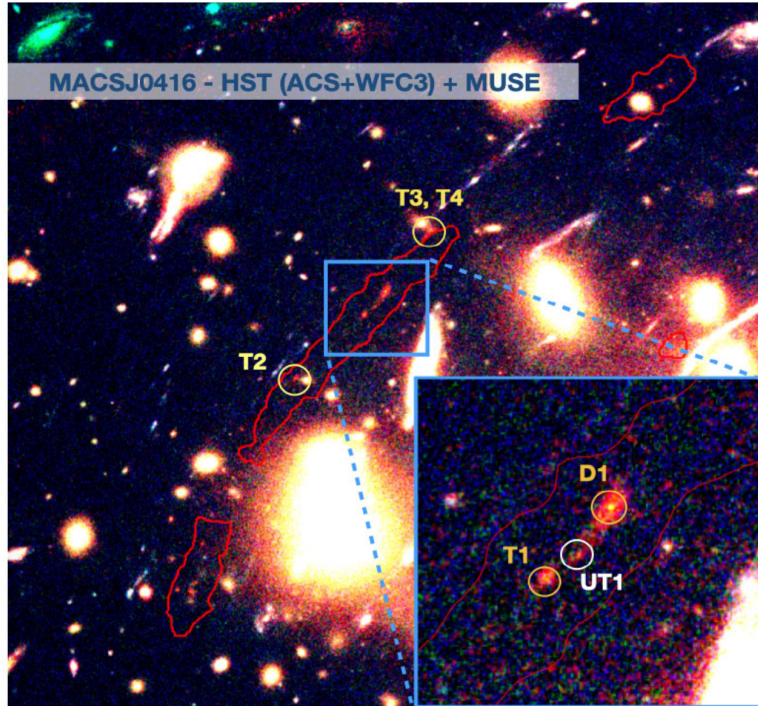


Figure 3.1: Colour-composite image of the field containing the lensed, spectroscopically confirmed star-forming complexes at $z=6.14$, magnified by the galaxy cluster MACS J0416 and that includes proto-GCs ([Vanzella et al., 2019](#)). The extended Lyman- α arcs detected with MUSE at $2-\sigma$ are shown by the red contours. The systems D1 and T1 are shown in the bottom right-hand side inset. A structure is visible between D1 and T1, including a very faint star-forming knot, dubbed UT1, indicated by the white circle. Other detected sources include T2, T3, T4 ([Vanzella et al., 2021b](#)). Taken from [Calura et al. \(2022\)](#).

very old, with an age between 11.5 and 12.5 Gyr. Some of them, the metal-rich ones, are assumed to be formed in-situ, while the metal-poor ones to have been accreted during the growth of our Galaxy. In external galaxies, younger clusters also displaying MPs have been found ([Martocchia et al., 2018](#)), however, exploiting observations of local objects to constrain the formation of MPs and, therefore, of GCs is not so trivial. Firstly, it is unclear whether the mechanism that gave birth to MPs at high-redshift, is the same that produced MPs in younger clusters, due to the expected differences in the environmental conditions at their formation epoch. Assuming that the physical process is the same in principle, younger clusters could be used to put stringent constraints, such as the age spread between different generations, a very important piece of information that is still difficult to derive with enough precision in old GCs. However, even including young clusters, the early phases of MPs formation are still inaccessible both because MPs are detected only in clusters older than 1.5 Gyr ([Kapse et al., 2022](#)) and, perhaps, because of the lack of star-forming regions with the proper conditions to trigger cluster formation in the local Universe.

In this Chapter, I will review the main scenarios that have been proposed through the years to explain the formation of multiple stellar populations in globular clusters. I will also report their strength but especially their weaknesses and their ability to reproduce the observational constraints.

3.1 The formation of multiple populations

As already mentioned in [Section 2.2.2.1](#), the enriched material which we now detect in a fraction of low-mass stars in GCs is produced by proton-capture reactions. The producers of such polluted gas are currently unknown, even though some hypotheses were made. However, for a scenario to work, it is not only mandatory to reproduce the anticorrelations observed among light elements, but many other observational constraints.

In recent years, various works (see [Renzini et al. 2015](#); [Bastian & Lardo 2018](#)) have tested whether the different scenarios are able or not to reproduce all the observational constraints, however, the conclusions they come up with are significantly different.

Among the various proposed scenarios, it is possible to distinguish them into two groups, depending on the star formation episodes the cluster is assumed to undergo:

- **Single star formation episode:** Here, the first and second populations were formed

during the same star formation event. An example is the accretion scenario, firstly proposed by (Bastian et al., 2013a), in which first-population stars eject enriched gas that is later accreted in already-present protostellar cores of low-mass stars. Scenarios assuming an accretion onto pre-existing stars include the Super Massive Stars (SMS) scenario (Gieles et al., 2018), the Massive Interacting Binaries (MIB) scenario (Bastian et al., 2013a).

- **Self-enrichment:** first population stars have polluted the system with gas that was later used to form the second population. Therefore, various star formation events may take place and clusters can experience self-enrichment. In this hypothesis, distinct populations of stars are associated with distinct generations, where the first generation (FG) is composed of coeval stars resembling SSP, and the second generation (SG) is instead formed by stars showing the anomalous chemical composition (enhanced in Na and depleted in O). A few clusters, such as the thoroughly studied NGC 2808 (Milone et al., 2015), where more than two populations are observed, may have undergone multiple episodes of star formation, each of them forming a new generation. Examples of scenarios assuming the formation of more stellar generations are the Asymptotic Giant Branch (AGB) scenario (D’Ercole et al., 2008; Calura et al., 2019), the Fast Rotating Massive Stars (FRMS) scenario (Decressin et al., 2007; Krause et al., 2013), the SMS scenario (Denissenkov & Hartwick, 2014) and the MIB scenario (de Mink et al., 2009).

This distinction is independent of the source of the enriched material, since, as it is shown above, and will be discussed later in this Section, some of the polluters have been adopted in scenarios assuming either one or more star formation episodes. Other scenarios, not described here, involve polluters such as black holes accretion discs (Breen, 2018), stellar mergers (Wang et al., 2020) and massive stars (Elmegreen, 2017).

3.1.1 Asymptotic Giant Branch scenario

It was already claimed back in the 80s that AGB stars could be the source of the enriched material we now detect on the surface of second population stars (Cottrell & Da Costa, 1981). Later, this hypothesis was further developed becoming the most widespread scenario to date. In addition, several aspects introduced to improve the AGB scenario were later included in other scenarios as well. For this reason, and also because it is the one

that I will adopt in most of this Thesis, I will first describe this scenario, starting with a brief summary of the physical processes that are playing a major role in the chemical enrichment process.

3.1.1.1 AGB stars

Before becoming white dwarfs, stars with a mass lower than $8M_{\odot}$ undergo the AGB phase, where various mixing processes are taking place. After the core helium exhaustion, while the star is ascending the AGB, a second-dredge up (SDU) occurs. The surface material is mixed with the interiors, which are partially polluted by the H-burning products, leading to a significant change in the chemical composition of the star. In particular, the SDU is the major driver of the He enrichment, whose intensity varies with the mass of the star, but not with metallicity. In general, it is during the AGB phase that the composition of a star changes the most, and this is driven by the interplay between nucleosynthesis and mixing ([Karakas & Lattanzio, 2014](#)). The He-burning shell is characterized by thermal instabilities, known also as thermal pulses or shell helium flashes, where mainly carbon is produced (s-process elements may also be produced if the temperature is high enough, which could explain Type II cluster with a spread in heavy elements). These flashes cause an expansion of the star and, therefore, a drop in the temperature, which ceases the shell burnings and favors the development of a convective envelope. At this point, the products of the shell burnings are able to reach the stellar surface through convective mixing, named third dredge-up events, that are taking place after each thermal pulse. In addition to the second and third dredge-ups, intermediate-mass stars experience another mixing process during the AGB phase: the hot bottom burning. The convective envelope penetrates in the external regions of the H-burning shell, bringing products of the proton-capture reactions to the stellar surface ([Bloecker & Schoenberner, 1991](#); [Lattanzio, 1992](#); [Boothroyd et al., 1995](#)). The final composition of the star will depend on which mechanisms dominate, which depends on the temperature, mass and metallicity of the star; the third-dredge up brings He-burning products such as C, Ne, O to the surface, while the hot bottom burning mainly carries H-burning products, depleting O and enhancing the Na abundance.

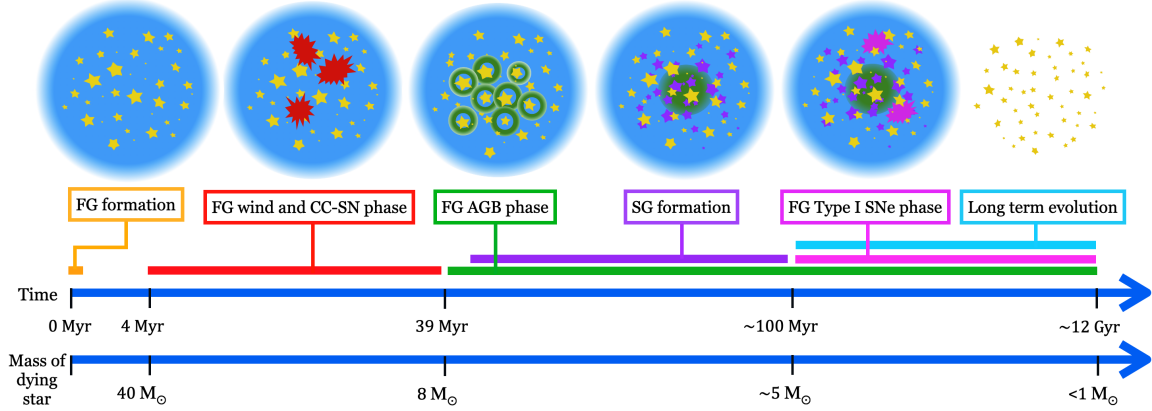


Figure 3.2: Schematic visualization of the different phases of the formation of MPs in a GC in the AGB scenario, highlighting the main feedback sources in action as a function of time and associated mass of dying star.

3.1.1.2 The scenario

The system, firstly composed only of FG stars, is assumed to be located in the disk of a star-forming high-redshift galaxy (a visual representation with a detailed description of the evolution of a star-forming GC within its host galaxy can be found in D’Ercole et al. 2016). Figure 3.2 represents the formation and evolution of MPs in a GC in this scenario. Soon after the formation of the FG, massive FG stars start exploding, creating a bubble that moves outwards until it reaches the height of the disk of the host galaxy. At this point, the superbubble blows out of the disk and the ejecta of massive stars plus the residual gas of the FG formation are left into the space, preferentially in the direction perpendicular to the plane of the disk. At around 40 Myr, after massive stars stopped exploding, the superbubble recollapses towards the cluster center, with a timescale that depends on the density of the interstellar medium (ISM) of the host galaxy. The system is now composed of the compact remnants left behind by SN explosions and low and intermediate-mass stars, the most massive of which are approaching their AGB phase. The winds produced by AGB stars are not fast enough to escape from the system ($v \sim 10 - 30 \text{ km} \cdot \text{s}^{-1}$) and, instead, collapse towards the cluster center creating a cooling flow. This dense, cold and enriched reservoir of gas confined in the center is used to form SG stars. However, the yields of AGB stars produce a correlation between Na and O rather than an anticorrelation (Denissenkov & Herwig, 2003; Herwig, 2004; Karakas & Lattanzio, 2007; Ventura &

3.1. The formation of multiple populations

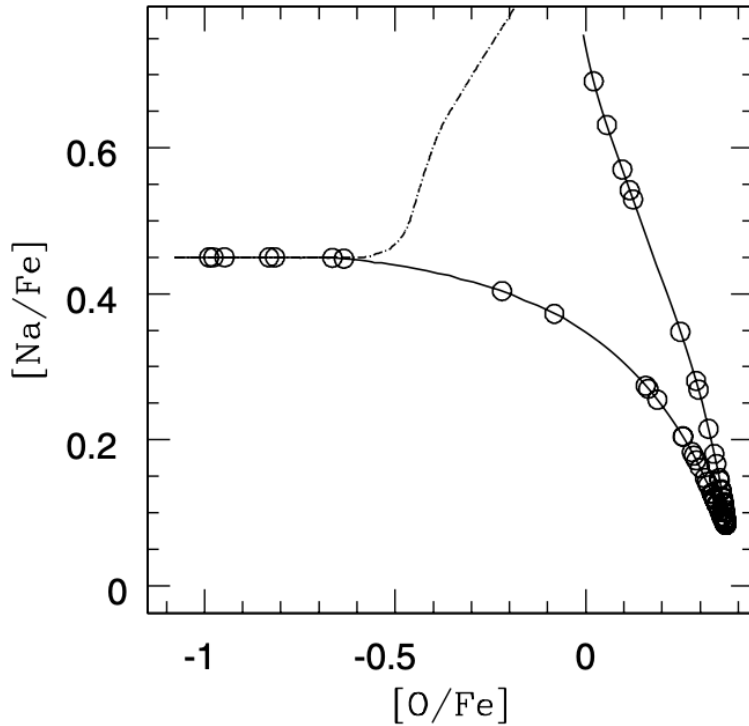


Figure 3.3: Chemical evolution of SG stars in the $[Na/Fe]$ vs. $[O/Fe]$ plane, obtained through a simple one-zone chemical model aimed at studying the composition of SG stars. The dash-dotted line represents the evolution of the gas in the cluster when no accretion of pristine gas is assumed, and, in turn, no dilution is taking place, while the solid line, displays the evolution when the AGB ejecta are diluted with pristine gas. The open circles represent a statistical sampling of SG stars formed along the path. Only few stars are formed along the two branches, while the bulk of them are located near the cusp, that corresponds to the peak of the ISM dilution. Taken from D'Ercole et al. (2010).

D'Antona, 2008). Therefore, to match the observed chemical trends, it is assumed that the AGB ejecta are diluted with ISM gas of the host galaxy (D'Ercole et al., 2010, 2012), which has a pristine composition (same chemistry as the first population). In this way, SG stars composition ranges from pure AGB ejecta yields to the one of the pristine gas. In Figure 3.3, the evolution of the chemical composition of the gas in a cluster is shown both with and without dilution.

3.1.2 Fast rotating massive stars scenario

First proposed by Decressin et al. (2007) and later revised and developed by Krause et al. (2013), it considers, as main source of the enriched materials, massive stars ($m > 20M_{\odot}$) rotating at high velocity ($v = 600 - 1000 \text{ km s}^{-1}$). Figure 3.4 shows an illustration of the scenario. As the AGB one, this scenario assumes the formation of at least two generations of stars, even though the timescales for the enrichment are much shorter ($< 10 - 20 \text{ Myr}$). The SG is formed right after the formation of the first one, before the leftover gas is completely swept up by the FG SNe. Massive stars are able to produce the high-temperature H-burning products along the main sequence (MS) and, at the same time, their winds create hot bubbles around them, which eventually merge but do not lead to the formation of an extended superbubble. However, the enriched material needs to be first transported to the stellar surface rapidly, through internal mixing, which is triggered by rotation. The enriched gas then needs to be lost and, therefore, it is required that stars are fast-rotating, to reach the break-up velocity (velocity at the equator when the centrifugal acceleration equals gravity) at the stellar surface. Fast rotators are supposed to be common in the dense center of clusters (Keller, 2004) and to experience dredge-ups even during the MS (Roy et al., 2020). The enriched material is preferentially lost in the equatorial plane where it forms a disc that is supposed to accrete unprocessed ISM gas in the Krause et al. (2013) formulation. The inner part of the disk is expected to be Toomre unstable, and therefore new stars composed of the products of the H-burnings are formed. Once FG CC-SNe take over, the gas becomes significantly turbulent, and, consequently, the accretion onto the discs is inhibited, quenching the SG formation. This allows to avoid the recycling of SN ejecta and form the cluster in a quite short timescale of few Myr. The composition of the SG will depend not only on the overall amount of pristine gas that is accreted and of enriched gas ejected by FRMS, but also on time, since the equatorial ejecta changes their composition from almost pristine, in the beginning, to progressively H-burning products

rich.

[Charbonnel et al. \(2014\)](#) proposed a variation of this scenario to overcome the mass budget problem, a typical issue in MPs formation scenarios, due to the low mass return fractions of the assumed polluters. As a consequence, the mass available to form SG stars is not enough to reconcile with present-day SG masses (see [Section 3.1.6](#) for further details). They suggest that FG stars were formed with a top-heavy initial mass function (IMF), so all of them have already died by the present time, and that what we call FG is an SG that is formed by material not enriched by the H-burning products.

Observationally, hints of the presence of rotating massive stars have been found in NGC 5253-5 ([Smith et al., 2016](#)). In particular, the nitrogen enrichment detected in the HII region surrounding NGC 5253-5 was not able to be explained considering only the presence of massive stars, but with the combined effects of a high mass and rotation ([Roy et al., 2020](#)).

3.1.3 Super massive stars scenario

[Denissenkov & Hartwick \(2014\)](#) modelled the evolution of a supermassive star (SMS), with masses of the order of $10^4 M_{\odot}$, retrieving good agreement between the light-elements anticorrelations observed in GCs and the yields of SMSs derived through their models. Later, [Gieles et al. \(2018\)](#) further developed the scenario to explain how the second population formed. The existence of SMSs has been motivated by both the increasing evidence of the presence of intermediate-mass black holes in GCs that could be the remnants of SMSs ([Lützgendorf et al., 2013](#)) and the results of numerical simulations, suggesting a runaway massive star collision in the center of young dense clusters which could lead to SMSs formation ([Portegies Zwart et al., 1999, 2004](#)). SMSs are assumed to be formed in the central regions of the system, during the very early phases of a cluster formation, once stars are still accreting gas from the surroundings, causing an increase in the density of the system and, in turn, of the rate of stellar collisions ([Moeckel & Clarke, 2011](#)). This increase in density, however, leads to a decrease in the two-body relaxation time and, when it becomes shorter than the timescale of accretion (a few Myr after the formation of the protostellar cores), the system starts expanding, decreasing the rate of stellar collisions ([Clarke & Bonnell, 2008](#)). Gas accretion is assumed to stop a little bit later, once stellar feedback takes over, and stellar evolution mass-loss fastens the expansion of the system. SMS can therefore grow due to the combination of gas accretion and stellar collision. Once

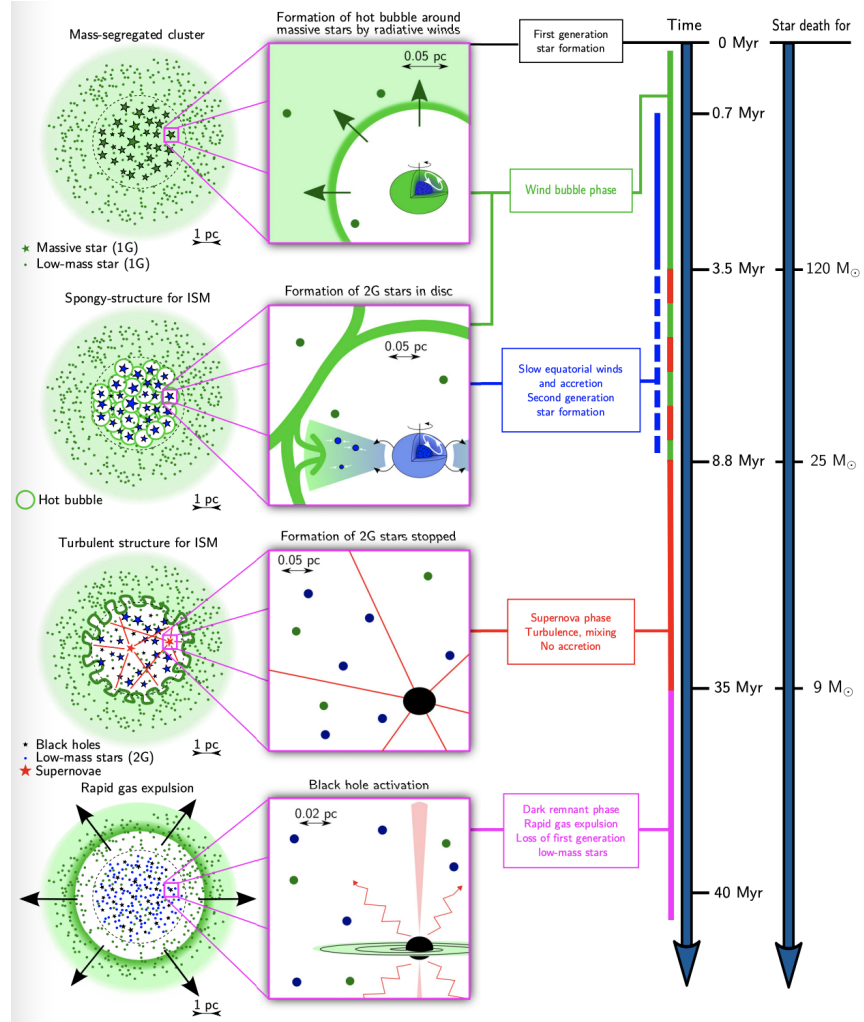


Figure 3.4: Schematic visualization of the various phases of the formation of MPs in the FRMS scenario, with associated time since the formation of the first population and the associated mass of the dying star, on the right. Taken from [Krause et al. \(2013\)](#).

the star reaches the zero-age main-sequence, it will start experiencing wind losses that regulate gas accretion. The amount of mass lost through wind could be significantly larger than the SMS itself, since continuous collisions are providing pristine material that will be then processed in the SMSs, producing H-burning products, mixed due to convection, and then rather easily ejected as winds. The SMS is therefore acting as a “conveyor belt”, fed by gas accretion and stellar collisions, which rejuvenate it and produce enriched material which will be then used to form stars with the typical composition of “anomalous” stars. As for FRMS, the composition of these stars will depend on time, being more pristine at the beginning, and progressively more enriched, but also on the location of formation, with more external stars being less enriched.

Enriched stars could be entirely formed out of the polluted ejecta of SMSs, and therefore constitute another generation, as discussed by [Denissenkov & Hartwick \(2014\)](#), but also be first-population low-mass stars whose composition changed after the accretion of enriched gas, as envisioned by [Gieles et al. \(2018\)](#). In any case, SMSs are not supposed to release He-burning products, for this reason, it is assumed that they should explode as pair-instability SN or implode into a black hole before this happens.

3.1.4 Massive interacting binaries scenario

As in some of the previous scenarios, the polluting stars are belonging to the high mass end of the IMF. In this scenario, firstly proposed by [de Mink et al. \(2009\)](#), the enriched material is assumed to be formed by two massive interacting stars. Observationally, mass transfer has been detected in several short-period binaries, where the lost material shows signatures of the products of the CNO cycle ejected with velocities of $30 - 70 \text{ km s}^{-1}$. The amount of mass loss could be significant, being comparable with the mass of the envelope of the primary star. Defining the primary as the most massive star in the binary system, and the secondary as the least massive one, the interaction between the two stars starts when the primary leaves the main sequence and becomes a giant. Expanding, the primary fills its Roche lobes and transfers mass and angular momentum to the companion through the Lagrangian point. As a consequence, the secondary accretes mass and spins up until it reaches the break-up velocity. From this moment on, the transferred mass is no more accreted, but ejected from the system. After this phase, the primary is deprived of almost all its envelope and ignites helium in the core, becoming a Wolf-Rayet star, while the secondary spins down. A second episode of mass transfer takes place when the primary

expands due to the He-shell burning. As before, a small part of the mass is accreted by the secondary, while most of the primary mass is ejected. As in the previous scenarios, the composition of the ejected material varies with time: at the beginning, the gas has an almost pristine composition, while after almost $2M_{\odot}$ of material is ejected, it starts to be polluted by the products of the H-burning and, therefore, showing He enhancement and the Na-O anticorrelation. The enriched gas can be then used to form a new generation of stars, as suggested by [Renzini et al. \(2022\)](#), or be accreted in a circumstellar disc around low mass pre-main sequence stars and later on the stars themselves, changing their surface chemical composition, as proposed by [Bastian et al. \(2013a\)](#).

3.1.5 Single star formation episode vs. Self-enrichment

Nowadays, several theoretical and observational studies are favouring the formation of multiple stellar populations via self-enrichment, rather than via accretion onto protostellar cores. From observations, the difference in the iron spread between first and second population suggests that they were born in an environment with significantly different densities, a condition that can be fulfilled by the self-enrichment scenarios, challenging, instead the ones assuming one episode of star formation ([Legnardi et al., 2022](#)). In addition, if processed gas was accreted onto protostellar cores, the amount of material would depend on the stellar mass of the accretor, as expected assuming the Bondi-Hoyle-Lyttleton accretion ([Bondi & Hoyle, 1944](#)). As a consequence, the lower the mass of the star the smaller the expected variation in the light element abundances detected on its surface. This trend, however, is not found observationally, suggesting that accretion onto protostellar cores is unlikely the mechanism responsible for the formation of MPs ([Milone et al., 2019; Milone et al., 2023](#)). From the theoretical side, [Sollima \(2021\)](#) has studied, through Monte Carlo simulations, the long-term evolution of clusters composed of two populations and assumed to be formed either via self-enrichment or accretion onto protostellar cores. Assuming the latter scenario, no discreteness between populations was developed and, moreover, the predicted fraction of enriched stars are $\sim 10\%$, significantly smaller than the observed ones.

3.1.6 Observational constraints

The aforementioned scenarios have to reproduce a large number of observational constraints coming from both the old Galactic GCs, but also from younger clusters in the MCs. In this Section, I will list them and focus only on the ones that have stronger implications on the feasibility/practicability of the scenarios (a more detailed description can be found in [Renzini et al. 2015](#) and [Bastian & Lardo 2018](#)).

Mass budget problem: the mass return of the polluters is too small ¹ to form a second population massive enough to reproduce the observed second population fraction ([Milone et al., 2017](#)), in the assumption that the initial mass of the first population is similar to the one we observe now. This is more dramatic in the scenarios assuming a self-enrichment, given that second population stars need to be formed entirely and, therefore, more mass is required. Such a problem is faced by all scenarios but with different degrees, depending on the mass return fraction of the assumed polluter. A general way to solve it is to assume that the first population was initially more massive (around 10 times) and then later, due to the dynamical evolution triggered by both internal and external processes, it loses a significant amount of mass, sometimes even greater than 90%, until the present time.

Na-O anticorrelation: even though the appearance of anticorrelations was the first hint of the presence of MPs, reproducing them is not an easy task. Although several, different polluters have been proposed, the mechanism that is supposed to lead to the formation of MPs and, therefore, of the anticorrelation is the same, as described in [Chapter 2](#). The hydrogen burning at high temperatures leads to a correlation in the Na-O plane, rather than an anticorrelation which could be recovered if the polluters' ejecta are diluted with pristine gas, as reported with more details for the AGB scenario.

Li abundance: the reactions that are supposed to lead to the composition of the “anomalous” stars are ignited at very high temperatures, way too high in comparison with the 2.5×10^6 K, the temperature at which lithium is destroyed. What would be expected is that all second-population stars are lithium-free, which is instead not observed. While in some clusters an anticorrelation between Li and Na has been detected, in some others the Li composition is the same in all populations. Since the reactions producing the enriched material are common to all the proposed polluters, every scenario has to face this problem. As already discussed in [Section 2.2.2.1](#), to explain these trends and especially the pres-

¹For a standard stellar IMF, the mass return fraction by first population stars is 2 – 8%, depending on the stellar type (i.e. AGB, FRMS, SMS, MIB).

ence of Li-rich stars, two mechanisms have been proposed: 1) a dilution of the polluters' ejecta with pristine gas, similar to the one assumed to recover the Na-O anticorrelation; 2) the Cameron-Fowler mechanism, which takes place in intermediate-mass stars during the AGB phase ([Cameron & Fowler, 1971](#)).

Specificity: the presence of second population stars, with their peculiar chemical composition, is common in GCs, but not in other systems. Stars with the same chemistry are rare in the field of the MW and, the few that have been detected, are assumed to be second population stars that have been lost by their parental GC through tidal interaction with the Galaxy ([Vesperini et al., 2010](#); [Martell et al., 2011](#)). Therefore, the specific conditions that lead to the formation of GCs seem to be required to form stars with such anomalies in their chemical composition.

Ubiquity: together with being specific to GCs, the presence of second population stars is found in almost all the clusters that have been analyzed photometrically and/or spectroscopically with reasonable detail. This suggests that the conditions required to form GCs are not only inducing the formation of second population stars, but rather implying it as an unescapable step in the process.

Variety: even though the phenomenon of MPs is ubiquitous, and different classes of GCs can be identified (see [Section 2.2.1](#) for one possible way to distinguish GCs) every GC is unique, with its own specific features. In extreme cases, clusters are composed of up to seven different populations, with their own peculiar chemical pattern, as the well-studied NGC 2808 ([Milone et al., 2015](#)).

Discreteness: the various populations, even the several ones hosted in more complex clusters, appear clearly separated in the color-magnitude diagrams and not like a continuous sequence, as it has been initially found. Such property is very useful to discriminate among different scenarios since some of them struggle to reproduce discrete populations. It mainly concerns scenarios invoking a single star formation episode, where first population stars are accreting material with peculiar chemical composition, becoming then second population stars. To account for discreteness, in fact, it is generally assumed that the cluster has experienced several star formation episodes that create different populations. This is feasible in the AGB scenario, but more complicated to tackle for scenarios involving disks around massive stars, such as the FRMS and the MIB one. In these cases, there is still room for discrete populations, assuming that massive star feedback leads to multiple episodes of star formation.

Supernova avoidance: most of GCs have been found to be almost monometallic, in particular in their second population stars (Legnardi et al., 2022), so supernovae both belonging to the first and second population, whose ejecta are iron enriched, should give little to no contribution to the formation of the second population. To avoid the recycling of supernova ejecta, second population stars must be formed in a very short amount of time (Wirth et al., 2021) or, as an alternative, massive stars should not be formed, be lost before exploding or directly collapse into black holes.

f_{enriched} vs. GC mass: the fraction of enriched stars, namely the second population, correlates with the present-day GC mass, which is the opposite of what is predicted by simulations. However, such simulations generally assume similar initial f_{enriched} at different initial cluster mass (Khalaj & Baumgardt, 2015), which could not be true (Yaghoobi et al. 2022).

3.1.7 This Thesis

Nowadays, it is still uncertain whether globular clusters have undergone self-enrichment or not. However, due to the results of various observational and theoretical investigations, which have highlighted the difficulties of accretion scenarios in reproducing several observational constraints (see Section 3.1.5), I assume that GCs have experienced self-enrichment. Therefore, throughout the Thesis, I will mainly adopt the term stellar generations rather than stellar populations.

Due to its larger spread and more thorough study, most of the work will deal with the AGB scenario, however, some of the outcomes could be applied to other scenarios as well. In particular, the AGB phase is an inescapable step low and intermediate-mass stars have to undergo during their evolution. They will return gas to the system which would be in principle available for star formation. Therefore, scenarios not involving AGBs as polluting sources should be able to explain why AGB ejecta are not recycled to form new stars.

The AGB scenario will be studied thanks to customized numerical simulations, properly taking into account the physical processes in play, to reach a deeper understanding of the properties characterizing these systems. Such explorations are required to interpret the new wealth of data that awaits to be collected through the exploitation of present-day and future instruments, such as JWST and the Extremely Large Telescope, respectively.

Part II

Methods

Chapter 4

NUMERICAL SIMULATIONS

*May you build a ladder to the stars
and climb on every rung*

Forever young, Bob Dylan

Hydrodynamic simulations are unique laboratories to study the formation and evolution of astrophysical systems such as stellar clusters, evolving the collisionless star particles together with the self-gravitating fluid. They allow us to follow the gas and particle dynamics to probe how they evolve and how they affect each other, both in terms of gravitational interactions, but also through star formation and stellar feedback.

One of the main focuses of this Thesis is the implementation of various physical processes within the RAMSES code, a widely adopted code suited for astrophysical hydrodynamic simulations. Such work is fundamental to reaching a deeper knowledge of the role played by different physical processes at the cluster scales, with the final aim of understanding the formation of the still-elusive phenomenon of multiple stellar populations.

Before entering the description of the various processes included in the code, it is worth summarizing the basis of computational fluid dynamics and its customization in astrophysical studies. In this Chapter, I give an overview of how different types of numerical methods deal with gas dynamics and gravity, with a particular focus on the ones specific to RAMSES. In the last part, I present the main physical ingredients already implemented in the code.

4.1 Hydrodynamics

A significant part of astrophysics is based on fluid dynamics, which is fundamental to understanding several topics, which include planet and stellar formation, supernova explosions, AGN feedback, stellar structure, accretion discs and cosmological structures.

Astrophysical fluids typically consist of gas particles, which are not exactly continuous, but they can be approximated as continuous if their mean free path λ is small compared to the scale length L over which the macroscopic quantities, such as density and temperature, expressed as a general quantity q , vary significantly, that is $L \sim q/\nabla q$. If this requirement is fulfilled, one can exploit the hydrodynamic equations to describe the evolution of the gas and introduce the fluid element, a region over which local variables can be defined. The fluid can then be studied by means of its macroscopic properties, significantly simplifying its treatment. The size l of the fluid elements has to be such that $\lambda \ll l \ll L$, but large enough to contain sufficient gas particles to avoid fluctuations due to the finite number of particles.

The gas in the Universe is governed by the hydrodynamic equations, and, at the typical temperatures, densities and pressures generally achieved in galaxy and cluster evolution, it can be treated as an ideal gas. Viscosity is therefore neglected and the gas evolution can be modelled through the Euler equations for a compressible gas, which can be written, in their conservative form, as:

$$\frac{\partial \rho}{\partial t} + \nabla \cdot (\rho \vec{u}) = 0 \quad (4.1)$$

$$\frac{\partial}{\partial t}(\rho \vec{u}) + \nabla \cdot (\rho \vec{u} \otimes \vec{u}) + \nabla p = -\rho \nabla \phi \quad (4.2)$$

$$\frac{\partial}{\partial t}(\rho e) + \nabla \cdot [\rho \vec{u}(e + p/\rho)] = -\rho \vec{u} \cdot \nabla \phi + \frac{\Gamma - \Lambda}{\rho} \quad (4.3)$$

where ρ is the mass density, \vec{u} is the velocity, e is the specific total energy, p is the thermal pressure, ϕ is the gravitational potential, Γ and Λ are the heating and cooling rates, respectively. In most astrophysical hydrodynamic simulations, the gas component is evolved together with a collisionless particle component, coupled via gravitational interactions. Therefore, the potential ϕ must take into account the contribution by both

components.

The specific total energy can be split into kinetic and internal energy (ε) components, like:

$$e = \frac{\vec{u}^2}{2} + \varepsilon \quad (4.4)$$

To close the set of Eulerian equations, it is generally assumed an equation of state that links the thermal pressure to the mass density, specific energy and velocity, through:

$$p = (\gamma - 1)\rho \left(e - \frac{\vec{u}^2}{2} \right) = (\gamma - 1)\rho\varepsilon \quad (4.5)$$

where γ is the adiabatic index, which is equal to 5/3 for a monoatomic gas.

The hydrodynamic equations cannot be solved analytically and, therefore, various codes have been developed over the years to solve numerically the system of equations. They can be distinguished into two main classes, depending on the adopted approach:

- **Eulerian:** the space is discretized using a grid and the fluid properties and their derivatives are computed within each cell of the computational box, i.e. at fixed positions. The first codes, such as ZEUS (Stone & Norman, 1992), divide the computational box into cells of the same size, which is a simple approach, but struggles to reach very high resolution. This is particularly evident when one wants to study in great detail only a small part of the computational box. To solve this issue, new techniques have been proposed, such as the Adaptive Mesh Refinement (AMR) one, where higher resolution is used only where some conditions, decided by the user, are satisfied (Berger & Oliger, 1984; Berger & Colella, 1989). Moreover, AMR is crucial to reduce the computational costs required to perform the simulations, which is always one of the major challenges when dealing with hydrodynamic simulations. Of course, this comes at a price, i.e. dealing with cells of different sizes, that are more difficult to handle. The most used codes exploiting the AMR are ENZO (Bryan et al., 2014), FLASH (Fryxell et al., 2000), ART (Kravtsov et al., 1997), RAMSES (Teyssier, 2002), ATHENA (Stone et al., 2008) with the new version ATHENA++ (Stone et al., 2020), NIRVANA (Ziegler, 2005) and PLUTO (Mignone et al., 2007).
- **Lagrangian:** the fluid elements, which are in this case represented by particles, move within the computational domain. The fluid variables and their derivatives are computed in the reference frame that comoves with them. The most adopted com-

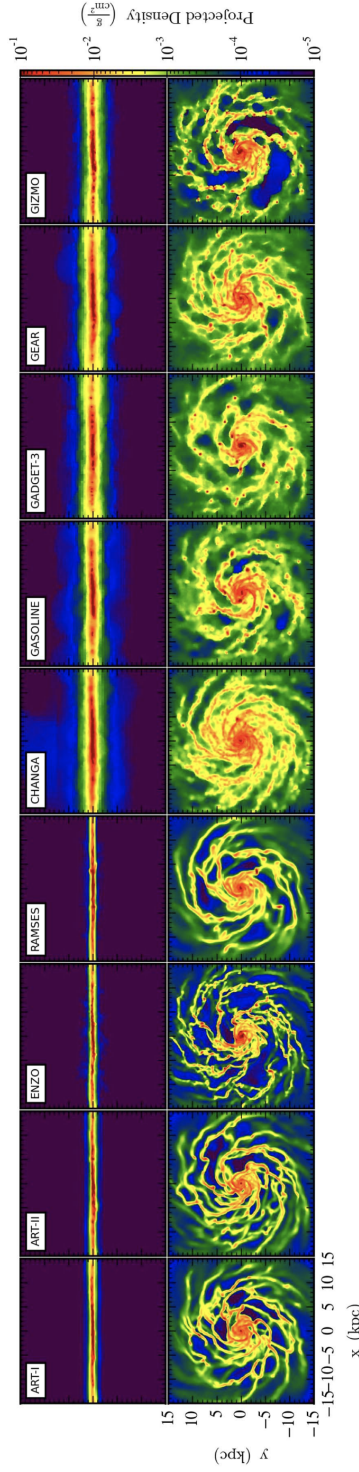


Figure 4.1: Disk surface density of the gas component at 500 Myr in isolated Milky Way-like galaxy simulations for nine of the mentioned hydrodynamic codes both edge on (top panel) and face on (bottom panel). ART-I, ART-II, ENZO and RAMSES use the Eulerian approach and are therefore mesh bases, while CHANGA, GASOLINE, GADGET-3, GEAR and GIZMO adopt the Lagrangian one, being particle-based. All codes aim at modeling similarly star formation, feedback, radiative cooling, UV background, metal enrichment and the pressure floor. Likewise, the resolution is kept constant in all the simulations, although this might be incorrect due to the differences between AMR and SPH. Nevertheless, clear differences can be seen between the results of the various codes, the most evident of which is between mesh and particle-based codes, in particular in the inter-arm regions. The figure is taken from the Agora code comparison project ([Kim et al., 2016](#)).

putational method for this type of approach is the smoothed-particle hydrodynamics ([Lucy, 1977](#); [Gingold & Monaghan, 1977](#)), where a discrete number of particles sample the continuum fluid. The gas properties can be derived at any point of the computational box by smoothing their quantities over a given number of surrounding particles. Largely used Lagrangian codes are GADGET ([Springel et al., 2001](#)), GASOLINE ([Wadsley et al., 2004](#)), GIZMO ([Hopkins et al., 2010](#)), GEAR ([Revaz & Jablonka, 2012](#)), CHANGA ([Menon et al., 2015](#)), PHANTOM ([Price et al., 2018](#)).

It is worth mentioning that, recently, new codes have been developed taking advantage of the strengths of both the grid-based Eulerian approach and the mesh-free Lagrangian one. The most widespread is AREPO ([Springel, 2010](#)), where the hydrodynamic equations are solved on an unstructured moving mesh, using the Voronoi tessellation technique on a discrete number of points. In [Figure 4.1](#), the differences between various aforementioned codes are shown.

4.1.1 Hydrodynamics in RAMSES

All the works presented in this Thesis where hydrodynamics is involved are performed exploiting the RAMSES code, firstly presented by [Teyssier \(2002\)](#). As reported above, it follows the Eulerian approach and it takes advantage of the tree-based AMR technique, shown in [Figure 4.2](#), adopting the Fully Threaded Tree data structure of [Khokhlov \(1998\)](#). For what concerns the particles, RAMSES contains an N -Body solver which is extensively inspired by the ART code ([Kravtsov et al., 1997](#)) and will be described in the next Section. The hydrodynamic equations are solved through a second-order Godunov scheme called Piecewise Linear Method (PLM, [Colella & Glaz 1985](#)).

In general, the Euler equations can be discretized and, when considering a gravitational source S , they take the form of:

$$\frac{U_i^{n+1} - U_i^n}{\Delta t} + \frac{F_{i+1/2}^{n+1/2} - F_{i-1/2}^{n+1/2}}{\Delta x} = S_i^{n+1/2} \quad (4.6)$$

where U_i^n is the numerical approximation to the cell-averaged values of ρ , $\rho\vec{u}$ and ρe at time t^n for the cell i . The time-centered fluxes at cell edges $F_{i+1/2}^{n+1/2}$ are derived by applying the PLM Riemann solver, a second-order Godunov method which does not solve the Riemann problem directly, but exploits the trapezium rule approximation in time. The

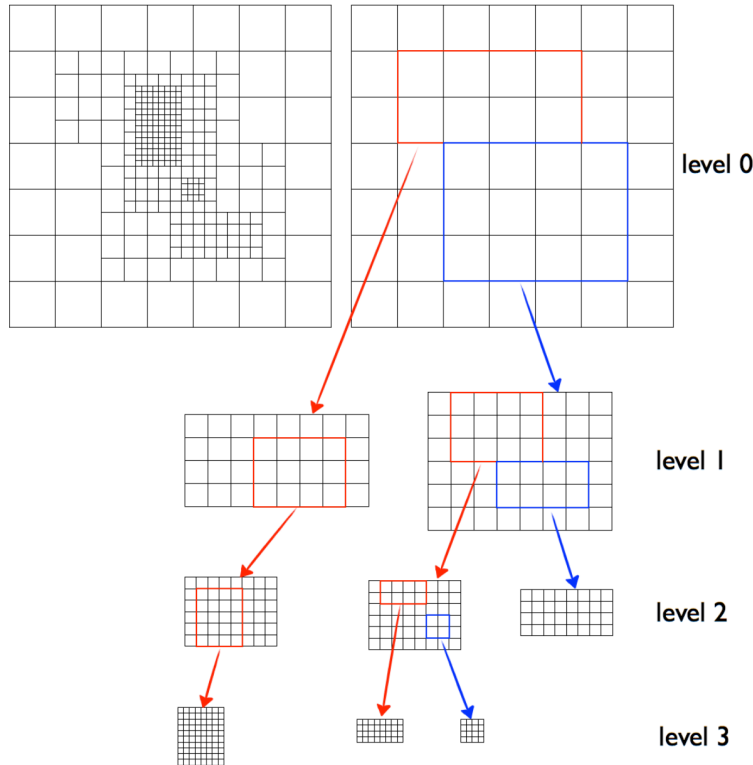


Figure 4.2: The grid hierarchy starts from the coarser grid, level 0, represented by a Cartesian grid, to the subsequent refined levels. As shown on the top left grid, the refinement must be gradual so that neighboring cells can not have refinement levels that differ more than unity. Credits: Fernando Becerra.

user can decide whether directional splitting should be applied, which consists in solving a one-dimensional problem in every direction, instead of the multidimensional problem. As many other methods, the PLM is based on the Monotone Upstream-centred Scheme of Conservation Laws (MUSCL) data reconstruction, first introduced by [van Leer \(1977, 1979\)](#) to reach higher accuracy of the first-order Godunov method by modifying the piecewise constant data (i.e. the cell is assumed to have the same values of U at both interfaces, while, more realistically, information from the neighboring cells are used to derive its values and, therefore, create a gradient in the cell). The easiest change is replacing the constant states U_i^n with piece-wise linear functions $U_i(x)$. In this way, the local piecewise linear reconstruction of U_i^n is:

$$U_i(x) = U_i^n + \frac{(x - x_i)}{\Delta x} \Delta i, \quad x \in [0, \Delta x] \quad (4.7)$$

where $\frac{\Delta i}{\Delta x}$ is the slope of $U_i(x)$ within the cell and can be chosen by the user. However, when going to higher order schemes, spurious oscillations are produced near steep gradients such as shocks, which makes it desirable to implement flux limiters to prevent the development of these oscillations. There are various flux limiters one can adopt, like MinMod, Superbee, MonCen, and Ultrabee (see [Toro 1997](#) for more examples), each one with its own advantages and disadvantages. In addition, different methods can be more or less diffusive, a peculiarity of non-pure Lagrangian codes which stabilizes the solution. Lagrangian codes need, instead, to introduce artificial viscosity to capture discontinuities, limiting spurious oscillations near gradients. In all works presented here, I am adopting the MinMod flux limiter implemented in RAMSES ([Roe, 1986](#)).

The gravitational source terms are computed using a time-centered, fractional-step approach:

$$S_i^{n+1/2} = \left(0, \frac{\rho_i^n \nabla \phi_i^n + \rho_i^{n+1} \nabla \phi_i^{n+1}}{2}, \frac{(\rho u)_i^n \nabla \phi_i^n + (\rho u)_i^{n+1} \nabla \phi_i^{n+1}}{2} \right) \quad (4.8)$$

described in [Saltzman \(1994\)](#) and [Toro \(1997\)](#).

4.2 N-body methods

Stars in globular clusters are tightly bound together thanks to gravity, which is governing their evolution. For this reason, in order to study the formation and evolution of globular clusters, it is necessary to adopt accurate methods to take into account gravitational interactions between stars, and in the early phases, also between the stellar and gas component. The evolution of stars or particles can be computed by adopting N -body methods which allow one to determine the changes of the potential with time. The simplest way is to use the particle-particle (PP) method, where the force acting on a particle is directly computed summing up the contribution from all the other particles in the simulation. The set of equations that need to be solved are:

$$\frac{d\vec{x}}{dt} = \vec{v} \quad (4.9)$$

$$\frac{d\vec{v}}{dt} = -\nabla\phi \quad (4.10)$$

$$\nabla^2\phi = 4\pi G\rho \quad (4.11)$$

which are called Vlasov-Poisson equations. The quantity \vec{x} represents the position vector, \vec{v} the velocity one, ϕ the potential, G the gravitational constant and ρ the density. When particles are point masses, the potential becomes:

$$\phi = - \sum_{i \neq j} \frac{Gm_j}{(|\vec{r}_i - \vec{r}_j|^2 + \epsilon^2)^{1/2}} \quad (4.12)$$

where ϵ is the softening or smoothing length, that prevents to have accelerations approaching infinity when the distance between two particles approaches zero. Although the method is accurate, the computational time scales as $\mathcal{O}(N^2)$, which heavily limits the number of particles one can use in the simulations. Nowadays, 10^6 particles are generally the limit achievable with direct N -body simulations, with some exceptions. For this reason, they are suited and very efficient for low and intermediate-mass stellar clusters, where it is even possible to model single stars rather than star particles, sampling the whole IMF. Moving to massive clusters, whose initial mass could be as high as $10^7 M_\odot$, other, more approximate, methods need to be adopted to solve the gravitational potential. One of the most widespread ones is the particle mesh (PM) method, where the density field is interpolated onto a grid and the Poisson equation is solved in Fourier space through a Fast Fourier Transform (Hockney & Eastwood, 1981; Klypin & Shandarin, 1983). The particle-particle-particle-mesh (P^3M) is, instead a combination of the aforementioned methods, where the PP approach is adopted on small scales, while the PM one on large scales (Hockney et al., 1974; Efstathiou & Eastwood, 1981). An improvement of the P^3M , which suffers a drastic increase of CPU time once particles are clustering, is the Adaptive P^3M (AP^3M), where a higher refinement is applied to grid cells in high-density regions so that they will contain fewer particles (Couchman, 1991). The PP method is then used but, on a smaller number of particles. Another method is the TreePM (Bagla, 2002), based on tree methods (Barnes & Hut, 1986), where the computational box is used to make up a hierarchical tree of cells. For particles belonging to short-range cells, the PP approach will be adopted, while for the long-range ones the PM method.

4.2.1 Gravity in RAMSES

In RAMSES, a customized version of the PM algorithm is implemented to derive the gravitational forces acting on the particles (Teyssier, 2002, see also Kravtsov et al. 1997). The PM approach is however not accurate for capturing forces at short distances, and, therefore, an adaptive grid is adopted, which allows one to refine cells until a user-defined number of particles is reached. In this way, high resolution can be achieved locally, which could significantly affect the performance of the code. As for other grid-based N -Body schemes, the major steps of the method are:

1. compute the mass density ρ on the mesh summing up, in every cell, the gas density with the interpolated particle density, which is calculated adopting the “Cloud-In-Cell” (CIC) approach;
2. use the Poisson equation to derive the potential ϕ on the mesh;
3. compute the acceleration on the mesh using a finite difference approximation for the gradient;
4. derive the acceleration of each particle adopting an inverse CIC interpolation scheme;
5. update the velocities of each particle through the derived accelerations;
6. update particle positions using the new velocities.

The CIC method (Hockney & Eastwood, 1981), used in two steps, is one of the possible algorithms to project the particle mass onto the mesh. While the most straightforward way would be to assign the mass of the particle to the nearest cell, with the CIC method particles are assumed to have a finite size and be tenuous so that they can overlap, being similar to clouds. The mass of a particle is spread all over the nearest cells, even though they are not at the same level of refinement. The algorithm is, in fact, applied to all levels and the mass will be assigned to a cell depending on the volume occupied by the cloud associated with the particle.

Once the density field is derived, the next step consists in solving the Poisson equation over an adaptive grid, which constitutes the most difficult step. RAMSES uses a “one-way interface” scheme, where the solution from a coarser grid is used to derive the boundary conditions and first-guess solution for finer grids (Jessop et al., 1994; Kravtsov

et al., 1997). The coarsest level, which corresponds to the lowest refinement level, is the uniform Cartesian grid, that covers the whole computational box. The Poisson equation can be here solved through a standard Fast Fourier Transform technique (Hockney & Eastwood, 1981), which is much faster than relaxation methods that need to be used on finer grids. When stepping up to the finer first-level mesh, boundary values are obtained interpolating the potential derived for the parental uniform grid and, therefore, the Poisson equation translates into a Dirichlet boundary problem. The relaxation method that is used in RAMSES to solve it is the Gauss-Seidel method with Red-Black Ordering and Successive Over Relaxation (Press et al., 1992). In this method, the Poisson equation becomes a diffusion equation (Kravtsov et al., 1997):

$$\frac{\partial \phi}{\partial \tau} = \nabla^2 \phi - \rho \quad (4.13)$$

where for $\tau \rightarrow \infty$, the initial solution ϕ relaxes to an equilibrium state (i.e. the solution of the Poisson equation). Equation 4.13 can be rewritten in the finite-difference form in three dimensions as:

$$\phi_{i,j,k}^{n+1} = \phi_{i,j,k}^n + \frac{\Delta \tau}{\Delta^2} \left(\sum_{nb=1}^6 \phi_{nb}^n - 6\phi_{i,j,k}^n \right) - \rho_{i,j,k} \Delta \tau \quad (4.14)$$

where nb are the neighboring cells, Δ is spatial resolution of the solution/potential and $\Delta \tau$ a fictitious timestep, which needs to be $\Delta \tau \leq \Delta^2 / 6$ for the stability of the method. With the maximum possible timestep, Equation 4.14 and, in turn, the relaxation interaction, reduces to an average of the potential over the six neighboring cells minus the source term. The solution is then “over-corrected” using the successive over-relaxation technique where the over-relaxation parameter ω is added:

$$\phi_{int}^{n+1} = \omega \phi^n + (1 - \omega) \phi^{n+1} \quad (4.15)$$

where

$$\omega \simeq \frac{2}{1 + \alpha \frac{\pi}{N}} \quad (4.16)$$

for a uniform $N \times N \times N$ Cartesian grid. For an AMR mesh, it is much more complicated to derive, due to the presence of irregular mesh patches. In this case, rather than using N , a much more accurate way to derive ω is to use the average size of these patches \bar{L} .

After the potential is obtained, the acceleration can be computed through a 5-point finite difference algorithm to derive the cell-centered gradient of the potential. Then, to assign every particle its acceleration, an inverse CIC scheme is applied.

When the N -body is coupled with a hydrodynamic code, it is essential that it can handle variable timesteps. The length of the timestep is ruled by the Courant-Friedrichs-Lowy (CFL), condition which states that no information should move more than a cell length in a single timestep. The leapfrog method, generally adopted, does not allow dealing with variable timestep. For this reason, RAMSES uses a second-order midpoint scheme to derive both particle velocities and positions, first making a predictor step knowing the acceleration and the particle positions and velocities at the previous timestep. Then, a corrected step is done, which, however, requires knowing the acceleration at the current time. Its calculation would imply another call to the Poisson solver, but to reduce the computational expenses, it is done at the next time step. Once the new potential is computed, velocities and positions are finally updated.

The second-order midpoint scheme, with adaptive time stepping, is very useful for AMR grids, however, RAMSES allows also to synchronize all levels to work at the finest timestep. Such a possibility is much more computationally expensive but more accurate, reducing the second-order midpoint method to a standard second-order leapfrog scheme ([Hockney & Eastwood, 1981](#)).

4.3 Subgrid physical ingredients

In numerical simulations, reaching the desired resolution is almost always not possible and, therefore, subgrid models must be implemented to take into account many physical processes acting on scales smaller than the resolution. Among them, we can find star formation, supernova feedback, stellar evolution, chemistry, cosmic rays, turbulence, black hole accretion, magnetic field, cooling and heating processes, etc. In this Thesis, I mainly focus on supernova feedback and its impact on the star formation of globular clusters, with a particular emphasis on the stellar chemical composition, fundamental to addressing the enigma of multiple populations. Here, I summarize the main physical ingredients of our simulations. Note that some of them, such as rotation and Type Ia SN feedback, are not included in all the works presented throughout this Thesis, and will be therefore described in the Chapter where they are studied.

4.3.1 AGB feedback

In order to understand the multiple stellar population phenomenon, it is important to test the various scenarios proposed for their formation. In this Thesis, most of the work has been carried out focusing on the AGB scenario, which is both the most widespread one and also the one where the polluters have been studied the most, especially from the chemical point of view. I here summarize how the AGB feedback has been implemented in RAMSES. For further details see [D'Ercole et al. \(2008\)](#) and [Calura et al. \(2019\)](#).

The mass return from AGB stars is taken into account by adding a source term to the mass conservation equation ([Equation 4.1](#)) given by:

$$\dot{\rho}_{\star, \text{AGB}} = \alpha \rho_{\star} \quad (4.17)$$

where α is the specific mass return rate and ρ_{\star} is the density of the FG stars, distributed following a [Plummer \(1911\)](#) profile:

$$\rho_{\star}(r) = \frac{3M_{\text{FG}}}{4\pi a^3} \left(1 + \frac{r^2}{a^2}\right)^{-5/2} \quad (4.18)$$

with mass M_{FG} and Plummer radius a .

The value of α is computed following the formalism of [Ciotti et al. \(1991\)](#) adopting a Kroupa initial mass function ([Kroupa, 2001](#)), and is obtained at every time interpolating the values obtained assuming the ejecta abundances as in [D'Ercole et al. \(2010\)](#). It depends on time, expressed in yr, t_{yr} , as the analytic formula:

$$\alpha(t_{\text{yr}}) = 0.065 \cdot t_{\text{yr}}^{-1.01} \quad (4.19)$$

expressed in yr^{-1} .

In order to trace the helium abundance, important to study MPs, we adopt the yields of [Ventura & D'Antona \(2011\)](#) (for AGBs with a progenitor mass of $8 M_{\odot}$ we have chosen an average value between the model of [Ventura & D'Antona 2011](#) and [Siess 2010](#)) calculated for a metallicity of $Z = 10^{-3}$, which is the adopted value in the simulations. The code follows also the evolution of iron, however, since AGBs are not producing it, their ejecta has the same iron mass fraction of the pristine gas.

The energetic feedback from AGBs is implemented as a source term in [Equation 4.3](#)

of the form:

$$S = 0.5\alpha\rho_*(3\sigma^2 + v^2 + v_{\text{wind}}^2) \quad (4.20)$$

where σ represents the velocity dispersion of the FG stars, computed for a Plummer sphere, following Dejonghe (1987), as $\sigma^2(r) \propto (6\sqrt{1+r^2})^{-1}$, v is the gas velocity, while v_{wind} is the wind velocity of the AGB stars, which is set to 20 km s^{-1} (D'Ercole et al., 2008).

Both $\dot{\rho}_{*,\text{AGB}}$ and S are added at each timestep to the fluid density and energy, respectively.

4.3.2 Thermochemistry

Heating and cooling are fundamental ingredients that need to be taken into account when studying astrophysical objects. The formation of structures in the Universe, even though driven by gravity, is strongly affected by the ability of the gas to cool and condense into potential wells (e.g. dark matter halos, for the formation of galaxies and larger structures). Both cooling and heating processes depend, as will be further explained below, on the abundance of various elements, both in their ionized and neutral form. The major drivers are H and He, which are dominating the gas mass content of the Universe, and, therefore, their contribution is vital, especially when studying the metal-poor early Universe. Cooling is mainly driven by two-body processes that decrease the kinetic energy of the system, such as:

- Collisional excitation: a free electron collides with a bound electron exciting it. The excited electron will then return to the ground state emitting a photon.
- Collisional ionization: a free electron collides with a bound electron ionizing it. The free electron has, therefore, lost part of its energy.
- Recombination: a free electron recombines with an ion, radiating away photons during its cascade towards the ground state.
- Dielectric Recombination: a free electron is captured by an ion and simultaneously excites the ion. Photons are then emitted when the ion deexcites.
- Bremsstrahlung: a free electron is accelerated while passing by a positively charged ion and emits a photon.

- Inverse Compton cooling: an ultrarelativistic electron is scattered by a low-energy photon, transferring part of its energy to the photon.

[Figure 4.3](#) shows the contribution of some of these processes to the total cooling function for a primordial gas ([Katz et al., 1996](#)). For a gas composed of H, He and their ions, the gas can cool down to $\sim 10^4$ K. Further gas cooling is achievable only when molecules, such as H₂ and HD are present, due to rotational and vibrational cooling processes absent in atomic gas, and crucial to trigger gas collapse. Such molecules permit to reach temperatures as low as 10 – 100 K, even though the processes are much less efficient than the ones taking place in atomic gas (see Fig. 4 of [Maio et al. 2007](#)).

The major heating source is photoionisation, where high-energy photons are absorbed by bound electrons increasing their kinetic energy. Other heating mechanisms include cosmic rays, Compton heating by γ -rays or X-rays and photoelectric heating on dust.

In the original version of RAMSES, the equilibrium thermochemistry is implemented in order to derive the internal energy density of a single cell, taking into account radiative processes of heating and cooling which are deeply connected with chemical reactions. Both heating and cooling depend only on features within the cell, and not of neighboring ones, and can be therefore computed in parallel.

RAMSES, rather than dealing with the internal energy density ε , handles the temperature, which is given, in a cell, as:

$$T_\mu \equiv \frac{T}{\mu} = \varepsilon \frac{(\gamma - 1)m_H}{\rho k_B} \quad (4.21)$$

where γ is the adiabatic index, m_H the proton mass, k_B the Boltzmann constant, μ the average mass per particle in the gas, in units of m_H . To determine the value of T_μ at $t + \Delta t$, it is necessary to compute the cooling and heating rates of the gas component. Such quantities are functions of temperature, density, redshift, metallicity and abundances of primordial ion species (n_{HI} , n_{HII} , n_{HeI} , n_{HeII} , n_{HeIII} and n_e). However, the non-RT version of RAMSES assumes photoionization equilibrium (PIE), meaning that primordial ion abundances are functions of temperature, density and redshift. Consequently, when equilibrium thermochemistry is assumed, cooling and heating rates are only functions of temperature, density, redshift and metallicity, simplifying the calculations.

At every coarse timestep, first, the abundance n_i of each of the six primordial species is computed for bins of T_μ and n_H , where $n_H = X\rho/m_H$ is the hydrogen number density

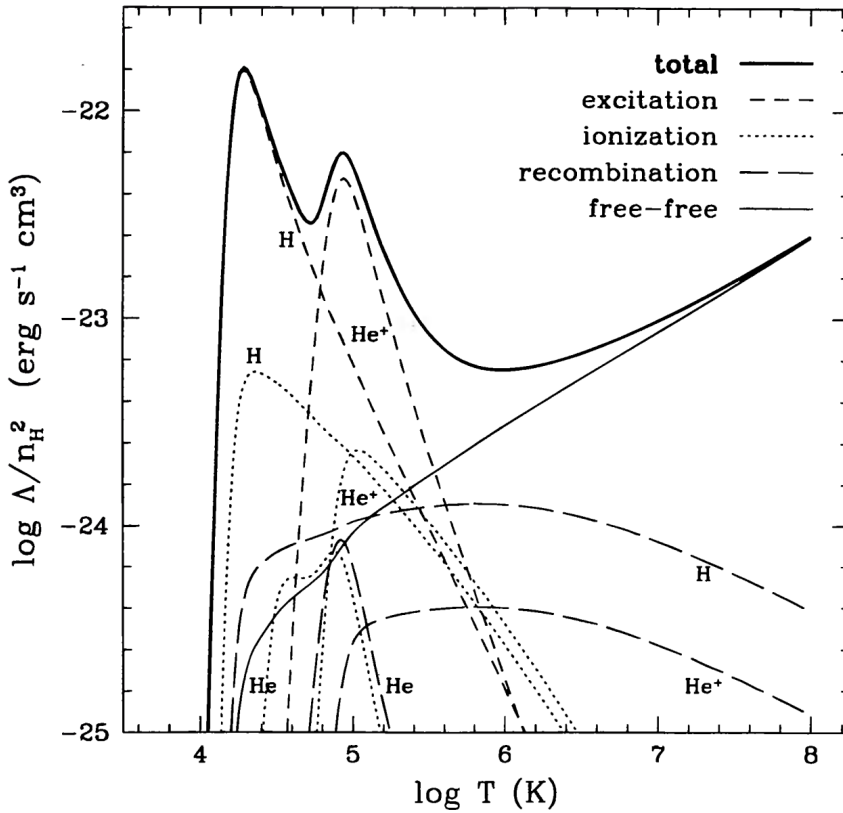


Figure 4.3: Cooling rate as a function of temperature for a primordial gas composed by H and He in collisional ionizing equilibrium. Contributions from some of the channels highlighted in the text are reported. At low temperatures, cooling is dominated by the excitation of H and He, while at high temperatures by bremsstrahlung. Taken from Katz et al. (1996).

and X is the hydrogen mass fraction in the gas component (typically assumed to be 0.76). Such a calculation takes into account all the possible interactions between the different species, which makes up a closed set of equations that are converged iteratively to reach an equilibrium between creation and destruction rates. Starting from the abundances table, the cooling and heating rates are then computed and stored in tables.

In particular:

- Heating rate $\mathcal{H}(T_\mu, n_H)$ is produced by the UV background at a given redshift and is given by the sum of the contributions of the four involved species ($n_{HI}, n_{HeI}, n_{HeII}, e$) of the photoheating rates times the number density of the individual species.

- Primordial cooling $\mathcal{L}(T_\mu, n_H)$, i.e. the cooling rate due to the mixture of H, He and electrons of primordial composition.
- Metal cooling rate $\mathcal{L}_Z(T_\mu, n_H)$, i.e. the per-solar-metallicity cooling rate due to metals in the gas. They are computed assuming collisional ionizing equilibrium ¹ through the photoionization code CLOUDY ([Ferland et al., 1998](#)).

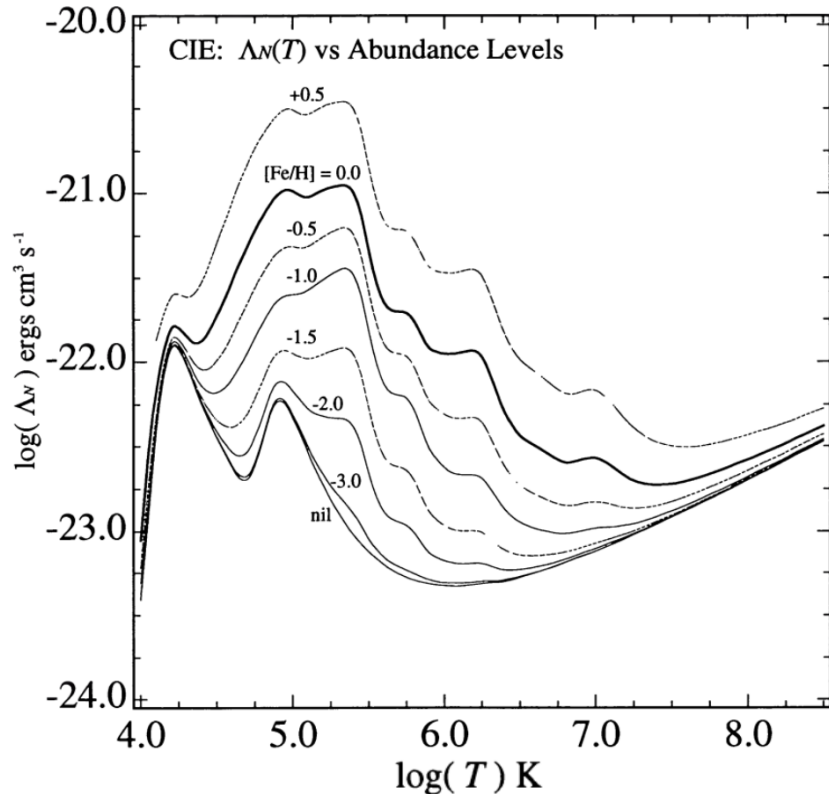


Figure 4.4: Cooling functions variations with temperature and metallicity in collisional ionizing equilibrium. The bottom line represents the case of gas with primordial composition and, therefore, metal-free. The higher the metal content, the stronger the cooling. Taken from [Sutherland & Dopita \(1993\)](#).

These rates, expressed in units of $[{\rm erg\,cm}^3\,{\rm s}^{-1}]$, are collected on-the-fly from the pre-computed tables instead of calculating them for every cell in the computational box, and

¹The gas is assumed to be optically thin to its own radiation and no external radiation field affects the ionisation balance. It is therefore the chemical equilibrium when no ionizing radiation is included.

will be used to update the temperature, solving the following equation:

$$\frac{\partial T_{mu}}{\partial t} = \frac{(\gamma - 1)m_H}{\rho k_B} (\Gamma - \Lambda) \quad (4.22)$$

where $\Gamma - \Lambda \equiv \dot{\varepsilon} = (\mathcal{H} - \mathcal{L} - \mathcal{L}_Z Z/Z_\odot) n_H^2$. Γ is the total radiative heating rate and Λ the total radiative cooling rate, which is shown in [Figure 4.4](#) as a function of temperature and metallicity. Increasing the metal and dust content in the gas leads to an enhancement of the gas cooling rates at all temperatures.

In the simulations presented throughout this Thesis, we use the RAMSES built-in cooling rates which take into account both atomic (i.e. due to H, He) and metal cooling ([Sutherland & Dopita 1993](#), see [Few et al. 2014](#)). For temperatures $T > 10^4$ K, the contribution of metals is derived through a fit of the difference between the cooling rates at zero e and solar metallicity using the photoionization code CLOUDY ([Ferland et al., 1998](#)). For temperatures $T < 10^4$ K, metal-line structure cooling rates are taken from [Rosen & Bregman \(1995\)](#). A temperature floor of $T_{floor} = 10^3$ K is adopted, i.e. the gas is not allowed to cool down below this temperature anywhere in the computational volume. This choice is made in order to avoid artificial fragmentation as a result of a too small Jeans length ([Truelove et al., 1997](#)), which decreases with the minimum temperature, set by the temperature floor. In general, in our simulations numerical convergence is satisfactory and we do not find any artificial fragmentation, which may happen when the Jeans length is not resolved ([Truelove et al., 1997](#)).

4.3.3 Star formation

Understanding how star formation proceeds at different redshifts and in different environments is fundamental to reaching much deeper insights into how the structures in the Universe were formed. However, cluster scale simulations are currently not able to resolve the formation of individual stars. For this reason, this process is modelled in a sub-grid fashion, through the implementation of some prescriptions, which may vary from code to code.

In our work, we use the RAMSES built-in star formation recipe, which is largely described by [Rasera & Teyssier \(2006\)](#). Star formation is allowed only in cells in which the temperature $T < 2 \times 10^4$ K, therefore only where the gas is assumed to be neutral, and where $\nabla \cdot v < 0$, corresponding to the cells in which the net flow is converging. Moreover,

for numerical reasons, not all the gas inside a cell can be used to form stars; in our code, a maximum of 90 percent of the gas in each cell is available for star formation. Then, once the cells eligible for SF are known, gas is converted into stars according to the [Schmidt \(1959\)](#) law, where the star formation rate (SFR) is proportional to the gas density divided by a characteristic timescale:

$$\dot{\rho}_{\star, \text{SG}} = \frac{\rho}{t_{\star}}. \quad (4.23)$$

The quantity t_{\star} represents the star-formation timescale, which is proportional to the local free-fall time, and has been set to be $t_{\star} = 0.1$ Gyr. As demonstrated in [D'Ercole et al. \(2008\)](#), the results of our simulations are independent of the value of t_{\star} , while they depend on the gas replenishing rate. The choice of the Schmidt law is observationally motivated, since, in several local galaxies, the observed SFR surface density correlates with the gas surface density ([Kennicutt, 1998](#)).

Every collisionless stellar particle has a mass $M_p = N m_0$ where $m_0 = 0.1 M_{\odot}$ is the minimum mass, while N is obtained sampling the Poisson distribution with probability:

$$P(N) = \frac{\lambda_P}{N!} \exp(-\lambda_P) \quad (4.24)$$

and a mean value of:

$$\lambda_p = \left(\frac{\rho \Delta x^3}{m_0} \right) \frac{\Delta t}{t_{\star}} \quad (4.25)$$

In this equation, Δt represents the timestep, whereas Δx is the cell size. The chemical composition of each newborn star is the same as the gas of its parental cell. These particles are located at the centre of the cell where they are formed, with a velocity equal to the local fluid one. The mass, momentum and energy associated with the newborn stars are conservatively removed from the parental cell and also from the passive tracers dedicated to following the chemical composition of the gas.

4.3.4 Limitations

The usage of subgrid models to simulate the effects of several physical processes limits significantly the predictive power of numerical simulations. Although they are heavily used, they depend on several free parameters that are generally fine-tuned to reproduce observations, severely limiting our insights into the simulating phenomena. At the moment,

4.3. Subgrid physical ingredients

however, the adoption of subgrid models is inescapable, not only in large cosmological simulations, but also at much smaller scales, such as the ones of stellar clusters. Apart from the ones described above, other subgrid models will be presented throughout the Thesis, and considerations will be made on their implications and their range of validity.

Part III

Results

Chapter 5

THE ROLE OF INTERNAL ROTATION ON THE SECOND GENERATION FORMATION

*Though you might hear laughin', spinnin', swingin' madly across the sun,
It's not aimed at anyone, it's just escapin' on the run
And but for the sky there are no fences facin'.*

Mr. Tambourine Man, Bob Dylan

This chapter is drawn from “The role of rotation on the formation of second generation stars in globular clusters” by [Lacchin et al. \(2022\)](#).

5.1 Introduction

In most studies on GC formation, clusters are modelled as non-rotating systems; however, in the last few years, an increasing number of GCs have been found to show signatures of internal rotation (see e.g. [Pancino et al. 2007](#); [Bellazzini et al. 2012](#); [Fabricius et al. 2014](#); [Lardo et al. 2015](#); [Boberg et al. 2017](#); [Bianchini et al. 2018](#); [Ferraro et al. 2018](#); [Lanzoni et al. 2018a,b](#); [Kamann et al. 2018](#); [Sollima et al. 2019](#); [Vasiliev & Baumgardt 2021](#); [Martens et al. 2023](#)). The observed internal rotation is generally found to be quite moderate with typical ratios between the rotational amplitudes to the central velocity dispersion (V_{rot}/σ_0) ranging from 0.05 to about 0.7 ([Bellazzini et al., 2012](#); [Fabricius et al., 2014](#); [Kamann et al., 2018](#)). Present-day rotation, however, is most likely the remnant of a stronger early rotation ([Hénault-Brunet et al., 2012](#); [Mapelli, 2017](#)) which has been then

lessened under the effects of two-body relaxation (Bianchini et al., 2018; Kamann et al., 2018; Sollima et al., 2019) and tidal forces exerted by the host galaxy. During the long-term evolution of the cluster, the combined effect of angular momentum transport from the cluster centre outwards and of escaping stars, carrying it away, leads to a loss of angular momentum and, therefore, to a decrease of the rotational amplitude (see e.g. Einsel & Spurzem 1999; Tiongco et al. 2017; Livernois et al. 2022).

It has been shown that internal rotation can strongly affect GC long-term evolution, in particular, reducing the relaxation timescale (or shortening the time of core collapse), and, therefore, accelerating its dynamical evolution and the mass-loss rate (Einsel & Spurzem, 1999; Kim et al., 2002, 2004; Ernst et al., 2007; Kim et al., 2008; Hong et al., 2013; Mastrobuono-Battisti & Perets, 2021). Moreover, rotation affects also the present-day morphology (Hong et al., 2013), as well as the dynamics of multiple stellar populations (Mastrobuono-Battisti & Perets, 2013, 2016; Hénault-Brunet et al., 2015; Tiongco et al., 2019; Mastrobuono-Battisti & Perets, 2021).

The observational study of the kinematics of multiple stellar populations is still in its early stages, but a few investigations have already revealed differences in the rotation amplitudes between stellar populations (Lee, 2015, 2017, 2018; Dalessandro et al., 2021; Cordini et al., 2020a; Szigeti et al., 2021), with the SG component rotating faster than the FG, with the exception of ω Cen where Bellini et al. (2018) found the opposite. Recently, Cordero et al. (2017) and Kamann et al. (2020) analyzed the rotational patterns of two GCs subpopulations and found that extreme SG stars (Na-enhanced and extremely O-depleted) are characterized by a larger rotational amplitude than intermediate SG ones (moderately Na-enhanced and O-depleted), as shown in Figure 5.1. In some cases, instead, no difference has been detected in the rotational patterns of distinct populations (Milone et al., 2020a; Cordini et al., 2020a,b; Szigeti et al., 2021). This rotational homogeneity between different populations could indicate that these systems are dynamically evolved, i.e. stars are already well kinematically mixed.

Rotation is, therefore, a fundamental physical process that needs to be included in theoretical models, however, very few studies have investigated its effects on the formation of multiple populations in GCs so far. Bekki (2010), Bekki (2011) and more recently McKenzie & Bekki (2021), studied the effects of rotation on the SG formation in the AGB framework, through 3D hydrodynamic simulations. They found that SG and FG stars display significant differences both in the rotational velocity (V_{rot}) and in the velocity dispersion

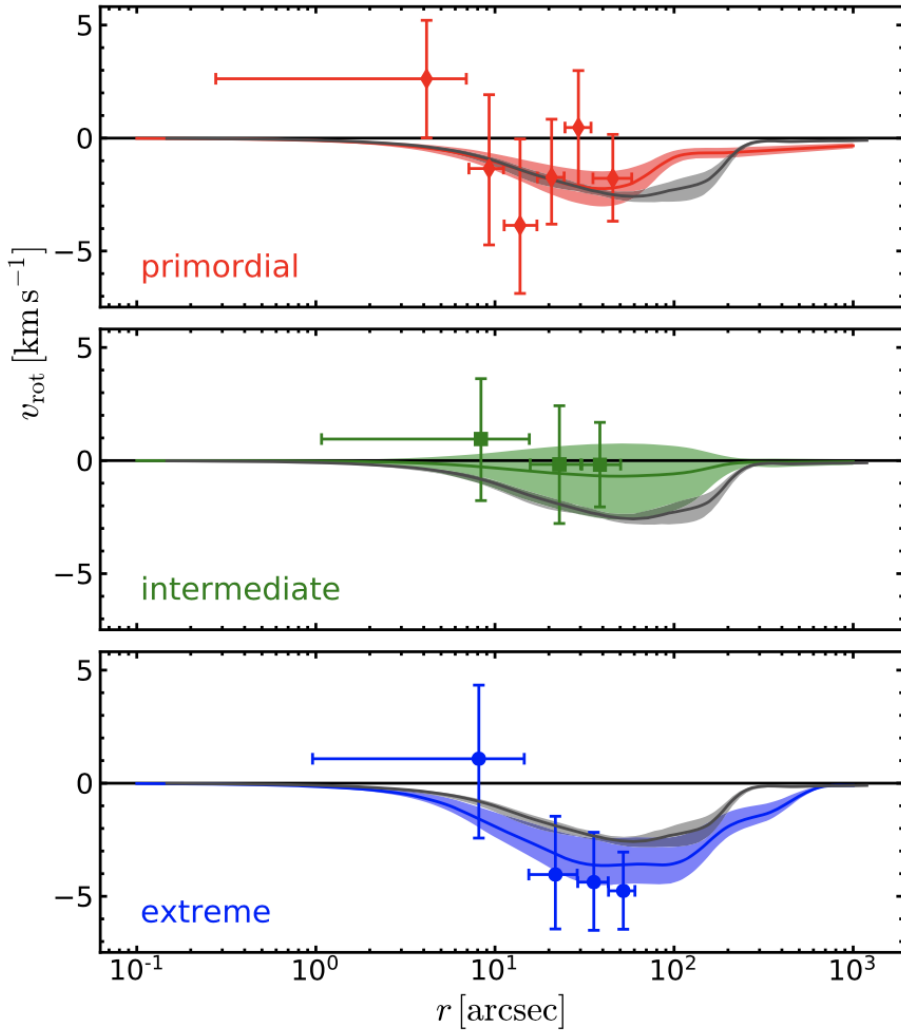


Figure 5.1: The rotation amplitude profiles of NGC 6093 for the primordial (FG) and two sub-groups of the SG, labeled intermediate and extreme populations depending on their degree of enrichment (from top to bottom). Taken from [Kamann et al. \(2020\)](#).

(σ) profiles, with SG stars rotating faster but with a smaller dispersion. Moreover, SG stars show a flattened and compact spatial distribution, which should be smoothed out during the cluster evolution to match the observations. These initial kinematical differences between various stellar populations are found to significantly decrease during the subsequent evolution of the cluster on two-body relaxation time-scales, which points towards a spatial and kinematical mixing of the populations ([Vesperini et al., 2013](#); [Mastrobuono-Battisti & Perets, 2013](#); [Hénault-Brunet et al., 2015](#); [Mastrobuono-Battisti & Perets, 2016](#); [Tiongco et al., 2019](#); [Vesperini et al., 2021](#)).

In this work, we extend the study of [Calura et al. \(2019\)](#) to investigate the effects of FG rotation on the formation of SG stars in a massive proto-GC, through a series of 3D hydrodynamic simulations. In our simulations, we will explore how the interplay between the kinematics of the AGB ejecta released by a rotating FG system and the accreted pristine gas affect the final kinematic properties of SG stars and their dependence on the chemical composition, for different SG subpopulations.

The chapter is organized as follows: in [Section 5.2](#), we present the setup of our simulations, focusing on the implementation of the rotating FG component. [Section 5.3](#) contains the results of our models and describes the dynamics of both the gas and the stellar component. In [Section 5.4](#) we discuss the outcomes of the simulations and compare them with previous results in the literature. Finally, we summarize our conclusion in [Section 5.5](#).

5.2 Simulation setup

The initial setup of this work is similar to the one of [Calura et al. \(2019\)](#) with the difference that we are here assuming a rotational FG. Therefore, all our simulations start $t_{\text{AGB}} = 39 \text{ Myr}$ after the FG formation, once all massive stars have already exploded as core-collapse supernovae (CC-SNe) and the system is completely cleared out of both SN-enriched ejecta and pristine gas ([Calura et al., 2015](#)). At this time, the intermediate-mass stars are undergoing their AGB phase, returning mass and energy in the gas-free system.

We take into account various astrophysical processes such as the mass and energy return from AGB stars, radiative cooling and star formation. For simplicity, the FG system is modelled as a static [Plummer \(1911\)](#) density profile with mass $M_{\text{FG}} = 10^7 M_{\odot}$ and Plummer radius $a = 23 \text{ pc}$. On the other hand, SG stars are instead modelled as collisionless particles; their dynamic evolution is derived by means of a Particle-Mesh solver.

Table 5.1: Simulations parameters.

Parameter	Description	Values
M_{FG}	FG stellar mass	$10^7 M_{\odot}$
a	FG Plummer radius	23 pc
ρ_{pg}	Density of the pristine gas	$10^{-24,-23} \text{ g cm}^{-3}$
v_{pg}	Pristine gas velocity relative to the cluster	20 km s^{-1}
Z_{pg}	Metallicity of the pristine gas	0.001
Y_{pg}	Pristine gas helium mass fraction	0.246
T_{pg}	Temperature of the pristine gas	10^4 K
T_{floor}	Minimum temperature	10^3 K
t_{\star}	Star formation time-scale	0.1 Gyr
v_{pk}	FG velocity at R_{pk} for analytic profile (Eq. 5.3)	2.5 km s^{-1}
v_{SB}	FG velocity at a for solid body profile	2.5 km s^{-1}

This chapter is focused on the formation and early dynamics of multiple populations and an investigation of the origin of the various chemical patterns is beyond the scope of this work. Here we only trace the evolution of the helium abundance of both the gas and the stars and use this abundance to identify the various SG subgroups. In all our simulations, we adopt a size of the computational box of $L^3 = (292 \text{ pc})^3$ uniformly divided into $(512)^3$ cells, which corresponds to a spatial resolution of 0.6 pc and locate the cluster at its centre.

5.2.1 Initial setup

As in [Calura et al. \(2019\)](#), we follow the scenario of [D’Ercole et al. \(2016\)](#) and therefore assume that the cluster is located in the disk of a high- z star-forming galaxy ([Kravtsov & Gnedin, 2005](#); [Bekki, 2012](#); [Kruijssen, 2015](#); [McKenzie & Bekki, 2021](#)). In addition, we assume that the cluster is orbiting in its host galaxy, which leads to an asymmetric accretion of gas from the side towards which the system is moving ([Naiman et al., 2011](#)). In models, this is accomplished by placing the cluster at the centre of the computational box and, at time t_{inf} , gas starts to flow from the yz plane at negative x . Such accretion leads to a dilution of the AGB ejecta with pristine gas which, as discussed in the [Section 3.1.1](#), is required in all the models to match the chemical trends derived by observations. The

Table 5.2: Models description. Columns: (1) name of the model, (2) axis around which the cluster rotates, (3) type of velocity profile, (4) density of the pristine gas, (5) starting time of the infall (the initial time of the simulations is fixed at $t_{\text{AGB}} = 39 \text{ Myr}$), (6) spatial resolution.

Model	Rotational axis	Velocity profile	$\rho_{\text{pg}} (\text{g cm}^{-3})$	$t_{\text{inf}} (\text{Myr})$	Resolution (pc)
HDanax	along x	analytic	10^{-23}	1	0.57
HDanaz	along z	analytic	10^{-23}	1	0.57
LDanax	along x	analytic	10^{-24}	21	0.57
LDanaz	along z	analytic	10^{-24}	21	0.57
LDsbz	along z	solid body	10^{-24}	21	0.57
HD	-	-	10^{-23}	1	0.57
LD	-	-	10^{-24}	21	0.57

beginning of the infall of pristine gas, however, does not correspond to the beginning of the simulation. As in D’Ercole et al. (2016), we assume that FG CC-SNe explosions have carved a large cavity around the cluster, a hypothesis confirmed also by 3D hydrodynamic simulations of the expansion of SN driven bubbles located in galactic disks (Hopkins et al., 2012; Creasey et al., 2013; Walch et al., 2015; Kim et al., 2017).

Once the wind ram pressure of the expanding shell equals the pressure of the surrounding ISM, the bubble stalls, losing its original structure. The maximum radius reached by the cavity, which corresponds to the stalling radius, is:

$$R_{\text{eq},2} = 41.43 \left(\frac{L_{41}}{n_0 V_{w,8} (\sigma_{0,6}^2 + v_{\text{pg},6}^2)} \right)^{1/2} \quad (5.1)$$

where L_{41} is the mechanical luminosity of CC-SNe of FG stars in units of $10^{41} \text{ erg s}^{-1}$ whose value reflects the number of FG CC-SNe and, therefore, on the initial cluster mass. In our case, with a $M_{\text{FG}} = 10^7 M_{\odot}$, its value is around unity, for a standard initial mass function (IMF) like Kroupa (2001). The quantity n_0 represents the ISM number density, while $V_{w,8}$ is the velocity of the wind in units of 10^8 cm s^{-1} (see D’Ercole et al. 2016 for detailed calculations of L_{41} and V_w). The two velocities $\sigma_{0,6} \sim 1$ and $v_{\text{pg},6} \sim 2$, both expressed in units of 10^6 cm s^{-1} , represent the velocity dispersion of the cluster within the galaxy, namely the isothermal sound speed and the velocity of the recollapsing ISM relative to the system, respectively.

5.2. Simulation setup

After the bubble has stalled, the ISM gas starts refilling the cavity with a velocity comparable to the local sound speed. The time at which the ISM gas reaches the system depends on the stalling radius R_{eq} through:

$$t_{\text{inf}} = t_{\text{SNe}} + \frac{R_{\text{eq}}}{\sigma_0 + v_{\text{pg}}} \quad (5.2)$$

where $t_{\text{SN}} = 30$ Myr is the lifetime of the smallest star which explodes as a CC-SN, so after t_{SNe} no more FG massive stars ($m > 8M_{\odot}$) are going off. We have run simulations with the same values of the pristine gas density adopted in [Calura et al. \(2019\)](#): a low-density case with $\rho_{\text{pg}} = 10^{-24} \text{ g cm}^{-3}$ and a high-density one $\rho_{\text{pg}} = 10^{-23} \text{ g cm}^{-3}$, representing, respectively, the typical gas density in a dwarf galaxy and in a high-redshift disc. Since $n_0 \sim \rho_{\text{pg}}/m_p$ we derive that, for a pristine gas density of $\rho_{\text{pg}} = 10^{-24} \text{ g cm}^{-3}$ the infall begins around 60 Myr after the FG was formed, while for a higher ISM density, it starts after 40 Myr. In both cases, the temperature of the pristine infalling gas is fixed to 10^4 K, a typical one for the ISM in a star-forming galaxy which is maintained photoionized by a stable UV radiation field ([Haffner et al., 2009](#)).

At the beginning of the simulation, the boundaries of all six faces of our computational box are set to be outflow. SG stars are formed following the prescriptions described in [Section 4.3.3](#). We here assume that the IMF of the SG is truncated at $8M_{\odot}$ so that no contribution of massive stars is expected (see [D'Ercole et al. 2008](#); [Bekki 2019](#)). [Table 5.1](#) contains a summary of the main parameters assumed for our simulations, whereas [Table 5.2](#) reports a description of the models we have performed with a particular emphasis on the rotational prescriptions we have adopted.

We point out that our model is aimed at exploring the formation of SG stars in a massive cluster with a present-day mass $\approx 10^6 M_{\odot}$. In a future investigation, we will explore the implications of initial rotation for a broader range of initial conditions, including clusters with different masses and structural parameters (see e.g. [Yaghoobi et al. 2022](#) for a study of the formation of multiple populations in non-rotating clusters with different initial masses).

We describe here only the prescriptions adopted for simulating the internal rotation. The description of how the other physical ingredients, such as the AGB feedback, cooling and star formation have been included in the code are reported in [Section 4.3](#).

5.2.2 Rotation

Signatures of internal rotation are found both in simulations of star cluster formation through the collapse of giant molecular clouds (Mapelli, 2017; Ballone et al., 2020; Chen et al., 2021) and from observations of young clusters (see e.g. Fischer et al. 1992, 1993; Hénault-Brunet et al. 2012).

In addition to the setup of Calura et al. (2019), here we assume that the FG system is characterized by the presence of internal rotation. This is implemented by imparting a rotation velocity to the AGB ejecta, following the rotational curve radial profile suggested by Lynden-Bell (1967) and found to provide a good description of the observed rotation profile in several star clusters (Mackey et al. 2013; Kacharov et al. 2014; Bianchini et al. 2018; Kamann et al. 2020; Dalessandro et al. 2021; Leanza et al. 2022) of the form:

$$v_{\text{rot}} = \frac{2v_{\text{pk}}R}{R_{\text{pk}}} \left(1 + \left(\frac{R}{R_{\text{pk}}} \right)^2 \right)^{-1} \quad (5.3)$$

R_{pk} represents the location of the peak of the profile, while v_{pk} is the value of the rotational amplitude at the peak. Here, we have set $R_{\text{pk}} = a$ and $v_{\text{pk}} = 2.5 \text{ km s}^{-1}$; the present-day peak rotational velocity of old clusters is, in most cases, smaller than the value adopted here, a consequence of the effects of long-term dynamical evolution leading to a gradual decrease in the strength of internal rotation (see e.g. Tiongco et al. 2017 and references therein).

In Section 5.4.1 we also report the results of models assuming a solid body rotation. Such a profile has been adopted by some works in literature such as Bekki (2010, 2011) and McKenzie & Bekki (2021). The angular velocity ω has been derived assuming a velocity at the Plummer radius $v_{\text{rot}}(r = a) = 2.5 \text{ km s}^{-1}$.

5.3 Results

In this section, we present the results of the models assuming that the FG internal rotation follows the radial profile in Equation 5.3. We have explored two different orientations for the rotational axis (parallel and perpendicular to the infall, see Tiongco et al. 2018 and Tiongco et al. 2022 for N -body studies of the long-term evolution of clusters with different orientations of the rotation axis) studying their effects for various pristine gas

densities ($10^{-24} - 10^{-23}\text{g} \cdot \text{cm}^{-3}$). All model parameters are reported in [Table 5.2](#).

The results obtained by adopting a solid-body rotation are very similar to those found assuming the profile in [Equation 5.3](#); for this reason, here we present only the results obtained for the models with the analytical profile in [Equation 5.3](#). We discuss the comparison with the models adopting a solid-body rotation in [Section 5.4.1](#).

5.3.1 Rotation perpendicular to the infall

In this section, we present the results obtained assuming that the rotation axis of the FG system is perpendicular to the direction of the external gas infall and therefore lies along the z axis.

5.3.1.1 Low-density model

Gas evolution

In [Figure 5.2](#), we show the 2D density, temperature and helium mass fraction slices for the gas component at 26 and 65 Myr, for the model with a low pristine gas density. To build the slices, we select all cells on the xy plane passing through the centre of the computational box.

We have displayed, on top of the helium mass fraction map, the gas velocity field as white arrows. For a comparison with [Calura et al. \(2019\)](#), we show here the maps at similar evolutionary times.

In the first snapshot, at 26 Myr, the infall has already started. The shock front has just crossed the system creating two “wings” which are both visible in all three maps. Contrary to [Calura et al. \(2019\)](#), the wings are not perfectly symmetric because of the rotation of FG stars and therefore of their ejecta on the xy plane. The presence of the infalling gas is even more clearly visible in the maps of the helium mass fraction where the helium-rich gas ejected by FG stars, marked in red, is located downstream to the cluster and in the central regions, while the blue helium-poor pristine gas of the infall is dominant upstream to the system. In the central part, the system is composed of several cold ($T \sim 10^3\text{K}$) and dense ($\rho = 10^{-19}\text{g cm}^{-3}$) clumps. These structures are the result of the fragmentation of a torus which has been recently described in detail by [Inoue et al. \(2021\)](#) through a linear perturbation analysis. In codes which exploit the AMR technique, the computational box is discretized in multiple grids, which in turn leads to a discretization of the hydrodynamic

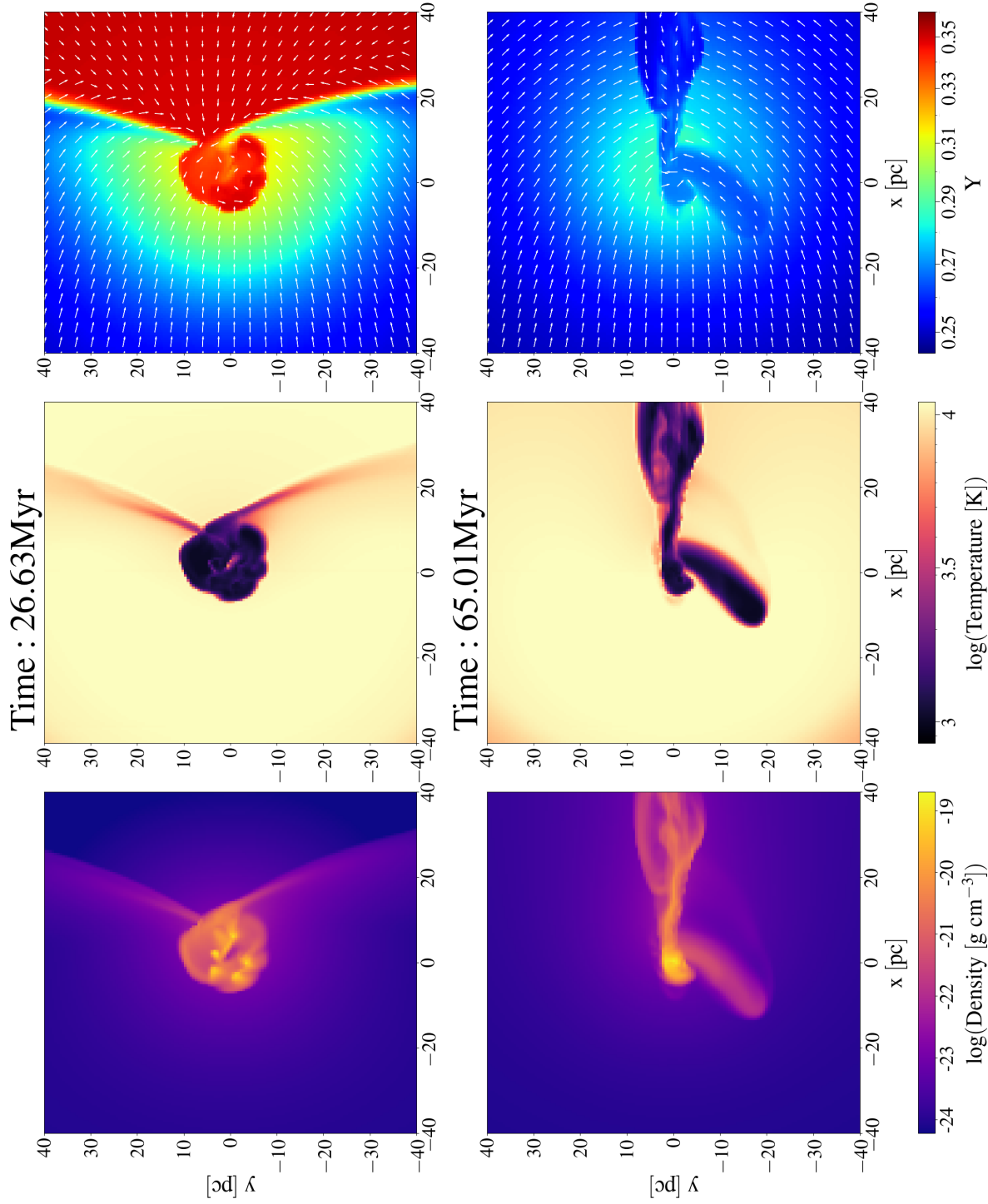


Figure 5.2: Two-dimensional maps of the gas density (left-hand panels), of the temperature (central panels) and the helium mass fraction (right-hand panels) on the x-y plane for the LDanaz simulation. The corresponding evolutionary time of each set of panels is reported at the top. The white arrows in the helium mass fraction maps represent the gas velocity field.

equations. Such modelization can lead to the so-called “artificial fragmentation” which takes place when small perturbations grow to form fragments. [Truelove et al. \(1997\)](#) studied the conditions that give rise to this phenomenon, by means of a 3D hydrodynamic AMR code, finding that, to avoid artificial fragmentation, the Jeans length λ_J ([Jeans, 1902](#)) should be at least four times greater than the resolution element. For the gas properties in our simulation, we end up with a λ_J equal to 2.6 pc, therefore, satisfying the Truelove criterion for avoiding artificial fragmentation. The clumps found in our simulation are thus not numerical artefacts, but rather represent the result of the actual dynamics of the gas out of which SG stars form. A detailed investigation of the formation and evolution of these clumps is beyond the scope of the present work and will be further investigated in a future study.

At the end of the simulation, ~ 65 Myr, a tail of cold and dense gas is pointing towards the cluster centre, the so-called “accretion column”. This helium-poor gas is generated out of the infall event through the Bondi-Hoyle-Litterton accretion mechanism ([Bondi & Hoyle, 1944](#); [Moeckel & Throop, 2009](#)).

Evolution of the stellar component

In [Figure 5.3](#) and [Figure 5.4](#), we plot the 2D surface density, helium mass fraction and line-of-sight velocity maps on the xy and yz planes for the stellar component at the same evolutionary times shown in [Figure 5.2](#).

In the 26 Myr snapshots, stellar particles are preferentially lying on a disk in the xy plane; this is the expected distribution of stars forming out of the gas released from a FG system rotating about the z -axis. The surface density map in the xy plane clearly reveals the presence of five clumps in the very central part of the system. Their average mass is $4 \times 10^4 M_\odot$, and more than 90% of all the particle mass is confined in these clumps. The five clumps are formed and orbit the centre of the system, and eventually merge after a few Myr.

All stars at this stage are strongly helium-enhanced, given that the infall has just started and has not had enough time to dilute the AGB ejecta significantly. These stars are concentrated in the cluster’s innermost regions (their half-mass radius is $r_h = 3.7$ pc) and distributed in a toroidal structure; they are characterized by a significantly more rapid rotation than that of the FG population. Specifically, the SG peak rotational velocity is equal to about $V_{\text{peak}} = 16$ km s $^{-1}$ at a distance from the cluster’s centre of $R_{\text{pk}} = 6.7$ pc.

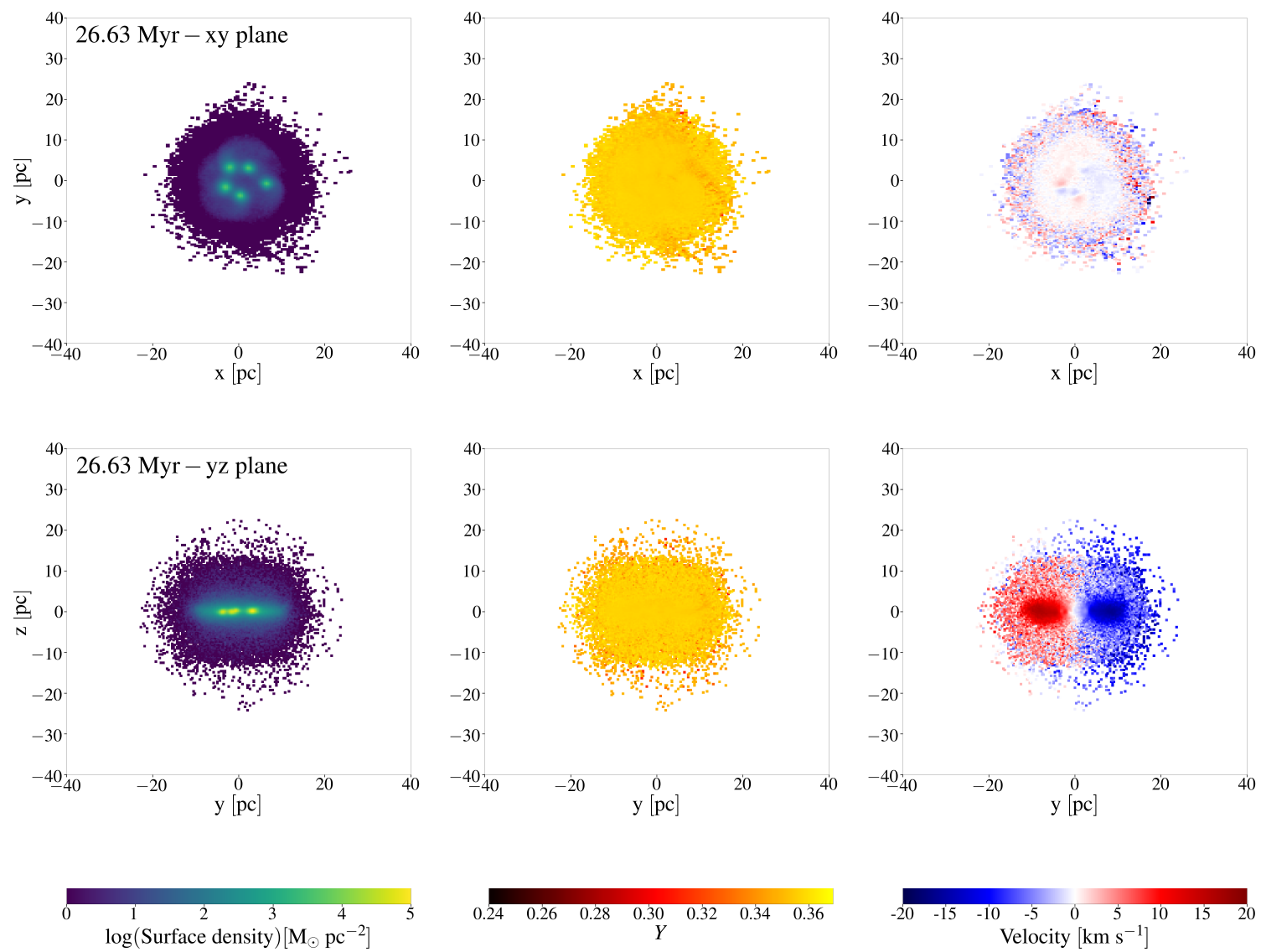


Figure 5.3: Two-dimensional maps of the stellar component at two evolutionary times for the LDana ζ simulation on the *x-y* plane (top panels) and *y-z* plane (bottom panels) at 26 Myr (time reported on the left panels). The first column shows the surface density, the second represents the helium mass fraction Y , and the third the line-of-sight velocity of the stars.

5.3. Results

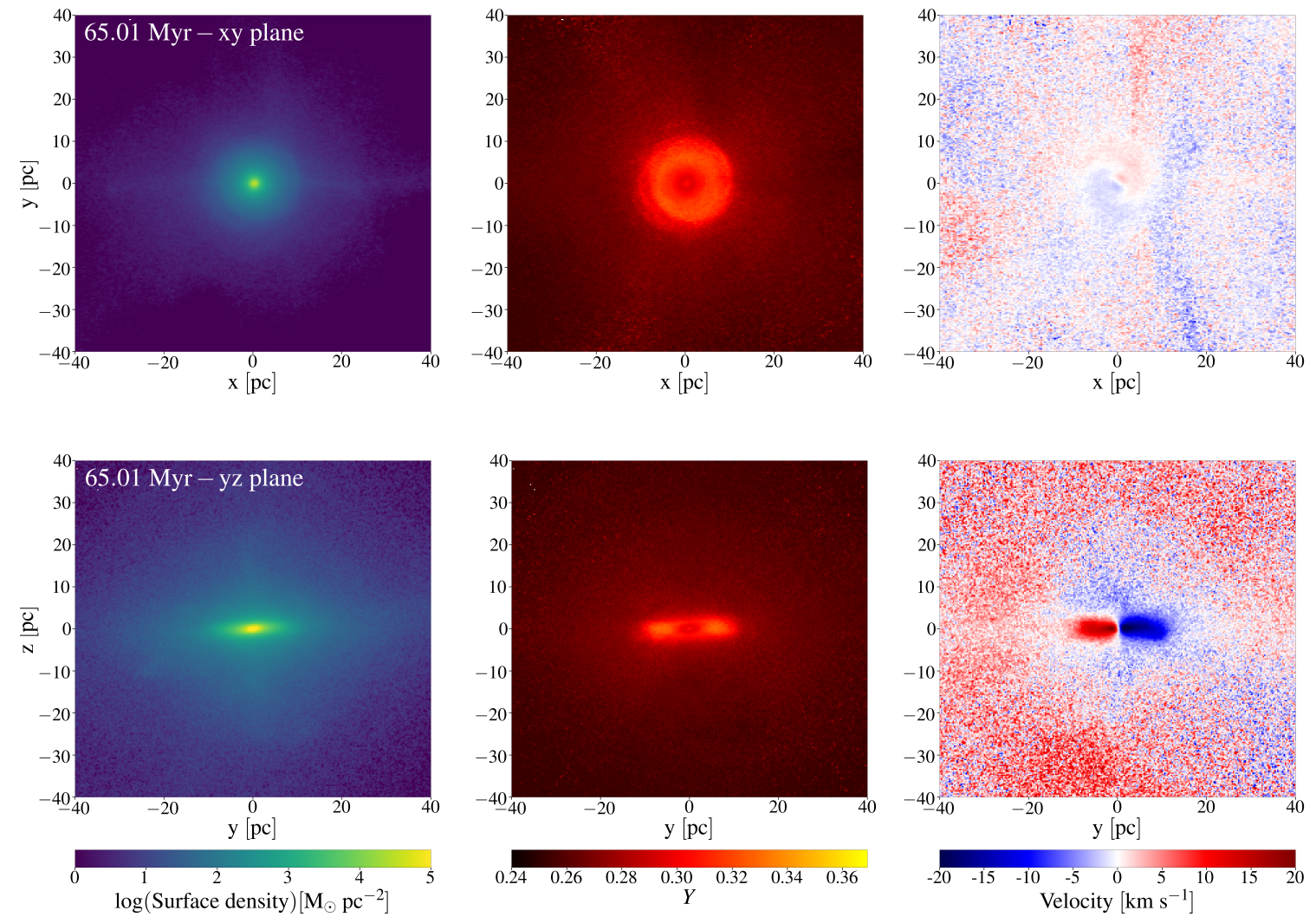


Figure 5.4: Two-dimensional maps of the stellar component for the LDanaz model at 65 Myr. The reported quantities are as in Figure 5.3.

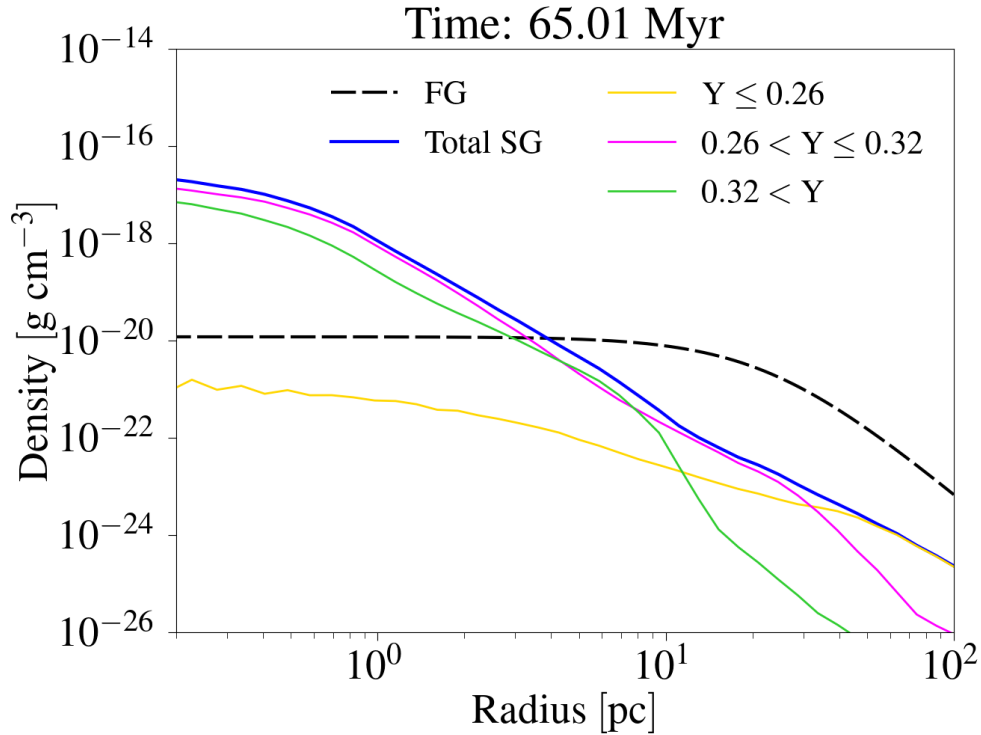


Figure 5.5: Total SG density profile at the end of the simulation and SG density profiles for three intervals of the helium mass fraction Y , for the low-density model LDanaz. The density profile of FG stars is also shown (see the legend for the details).

At 65 Myr the clumps have already merged and collected in the centre. The disk is still clearly visible in all maps and contains 80% of the total mass of the SG. It extends for ~ 8 pc and is composed of helium-enhanced stars that are still significantly rotating. It is interesting to note the presence of a small region in the innermost part of the disk characterized by a helium abundance smaller than in the rest of the disk. This feature is a consequence of the early dynamics of the SG formation: as discussed above, the most He-rich AGB ejecta are first collected in a clumpy toroidal structure, which later forms a stellar disc; the non-rotating pristine gas, on the other hand, flows directly in the centre and creates this small region with slightly lower helium abundance. This is also illustrated by the density profiles presented in Figure 5.5, showing a slightly lower central density of the most He-rich population. In order to link these fine structural and chemo-dynamical features within the SG system with the present-day properties of old GCs, it is necessary to carry out further explorations of the long-term dynamical evolution with initial conditions

5.3. Results

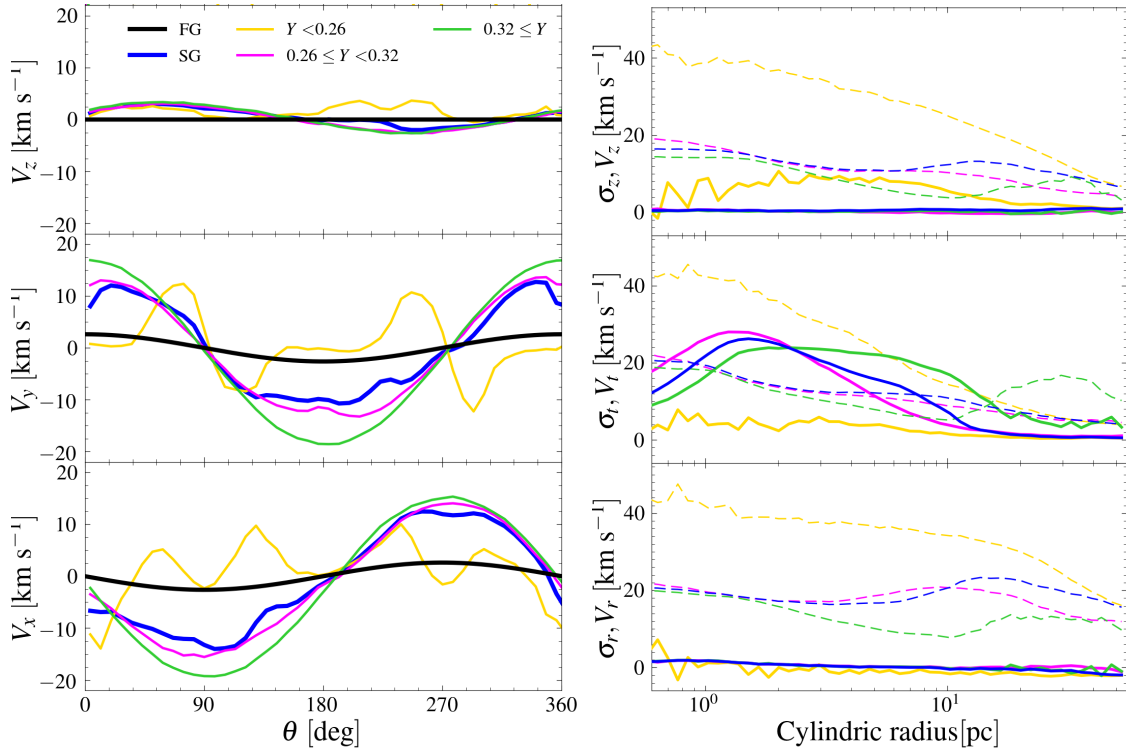


Figure 5.6: Stellar rotation profiles for the model LDanaZ at 65 Myr. On the left: Rotation amplitude of the Cartesian velocity components for SG stars as a function of θ , defined as the angle between the direction of each star projected on the xy plane and the x axis, for three bins of the helium mass fraction Y (see the legend for more details). The FG rotation amplitudes are also shown by the black line. On the right: Radial profiles of the cylindrical velocity components (solid lines) and velocity dispersions σ (dashed lines) for SG stars for three bins of the helium mass fraction Y .

similar to those emerging from our simulations.

In Figure 5.6 we show, for the LDanaZ model, the angular variation of the Cartesian components of the velocity of the SG stars (left panels) and the radial profiles of the mean velocity and velocity dispersions in cylindrical coordinates (right panels) measured at the end of the simulation ($t = 65$ Myr). This figure further illustrates the kinematical properties of the SG population and the various SG subgroups. SG stars rotate more rapidly, with an amplitude of $\sim 12 \text{ km s}^{-1}$, than the FG population, whose amplitude is equal to 2.5 km s^{-1} . Such difference in the rotational intensity between the two populations has been observed in several present-day clusters (Lee, 2017, 2018; Dalessandro et al., 2021;

Szigeti et al., 2021), although the amplitudes are significantly smaller than the ones we obtain, since our simulations do not include the long-term evolution of the system. In addition, more helium-enriched stars are found to rotate faster than weakly enriched ones, qualitatively in agreement with recent observational works on M13 (Cordero et al., 2017) and M80 (Kamann et al., 2020) (with the exception, already discussed above, of the rotation in the very inner regions, where the intermediate SG group rotates slightly faster). The small angular variation in the mean value of V_z results from the fact that the SG disc is slightly tilted (see also Figure 5.4). Moreover, we found that FG and SG stars are rotating in phase, a feature often found in present-day GCs (Milone et al., 2018a; Cordoni et al., 2020b).

Regarding the velocity profiles in Fig. Figure 5.6, it is not surprising that the peak of the SG rotational velocity V_t is located approximately at the SG half-mass radius equal to 1.5 pc, as suggested by observational studies of very young stellar clusters (Hénault-Brunet et al., 2012), but also of older globular clusters (Bianchini et al., 2018).

As for the radial profiles of the velocity dispersion shown in the right panels of Figure 5.6, it is interesting to note the presence of a few bumps indicating that the SG system is still settling into a dynamical quasi-equilibrium. Along the tangential direction, $|V_{rot}/\sigma|$ is greater than unity in the disk region, with a peak of 3.5 at the edge of the stellar disk, confirming that the system is rotationally supported. This ratio is much larger than the observed one, but, as for the rotational amplitudes of the two populations, the long-term evolution has been shown to lead to a significant decrease of this quantity (Tiongco et al., 2017). Finally, we point out that here we have explored a single case for the initial FG rotational profile; an extension of this study to explore different initial FG rotational properties will be carried out in the future. The early study on the formation of SG in rotating clusters by Bekki (2010) suggests that the strength of the SG rotation emerging at the end of the formation phase is correlated with that of the FG system.

5.3.1.2 High-density model

Gas evolution

Figure 5.7 represents the 2D density and temperature slices at 5 and 62 Myr for the HDanaz model. At 5Myr the system encounters the infalling gas, which creates a shock front that is, as in Figure 5.2, not perfectly symmetric because of the rotation of the already

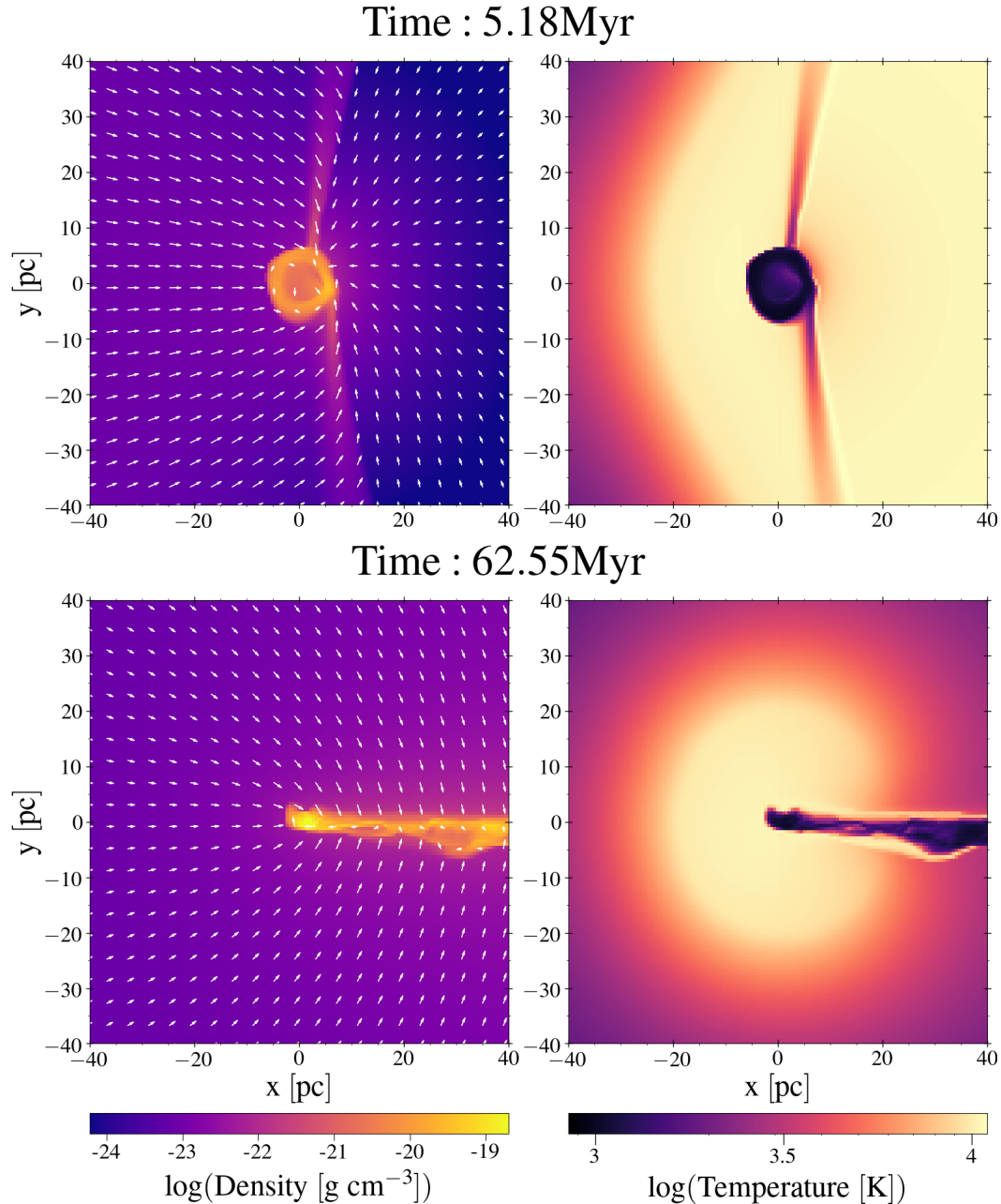


Figure 5.7: Two-dimensional slices of the gas density (left-hand panels) and temperature (right-hand panels) on the x-y plane for the HDanaz simulation. The corresponding evolutionary time is reported on the top of each set of panels. The white arrows in the density maps represent the velocity field of the gas.

present AGB ejecta. The presence of a bow shock is also visible in the temperature map, at a distance comparable to the Plummer radius of the cluster (see also [Naiman et al. 2011](#)). In the central 10 PC, the gas is rotating counter-clockwise due to the imposed rotation of the FG stellar component. In particular, the gas is mainly confined in a torus due to the balancing effects of gravity and rotation.

At 62 Myr the gas is not rotating anymore and, similarly to the results obtained by [Calura et al. \(2019\)](#), the accretion column is carrying pristine gas towards the cluster centre.

We do not report here the maps of the gas helium mass fraction since, at 5 Myr, the map is similar to the one of the `LDanaz` model at 26 Myr and, at the end of the simulation, no feature is visible since the entire computational box is dominated by gas with moderate helium enhancement.

Evolution of the stellar component

Contrary to the `LDanaz` model, here the earlier incoming of the infall prevents the clump formation while the disk is already formed as shown in [Figure 5.8](#) in the snapshot at 5 Myr. Not surprisingly, SG stars are mainly located in a torus resembling the gas distribution.

At 62 Myr the stellar component is much more extended than at the previous snapshot and a significant number of stars form along the accretion column. Small clumps form along the accretion column, move towards the cluster centre and merge with the central component. Instead, a minority of them is kicked away.

In contrast to the `LDanaz` model, in the `HDanaz` one the disk does not survive once the infall starts. The higher density of the accreted gas, and, in turn, its stronger ram pressure, but also its earlier arrival, when the disk is still forming, lead to the disruption of the disk soon after the start of the infall event. The system is dominated by moderate helium-enriched stars which are formed out of the AGB ejecta and a large amount of the infalling pristine gas. Nevertheless, a small fraction of highly enhanced helium stars preserves the rotation acquired at birth.

[Figure 5.9](#) shows the velocity profiles as a function of the θ angle (left, defined as in [Figure 5.6](#)) and radius (right) for the `HDanaz` model. SG stars rotate with an amplitude similar to that of the FG with peaks in the x component. This feature is due to the stars born along the accretion column and consequently possessing a significant velocity towards $-x$. Along z , the velocity is not zero due to the gas motions produced by the infall and the

5.3. Results

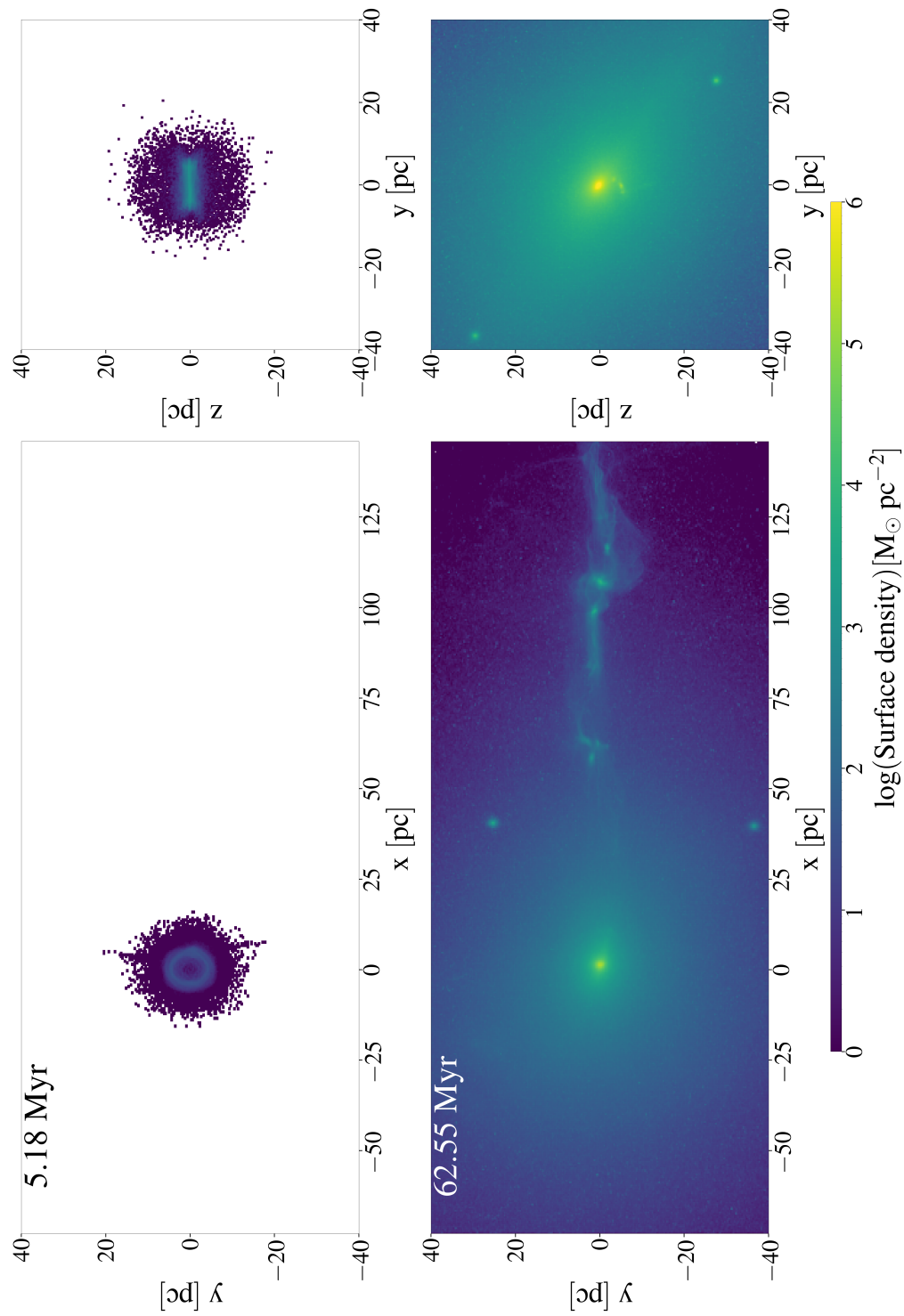


Figure 5.8: Two-dimensional surface density maps of the stellar component at two evolutionary times for the HDanaz simulation on the x-y plane, on the left, and y-z plane, on the right.

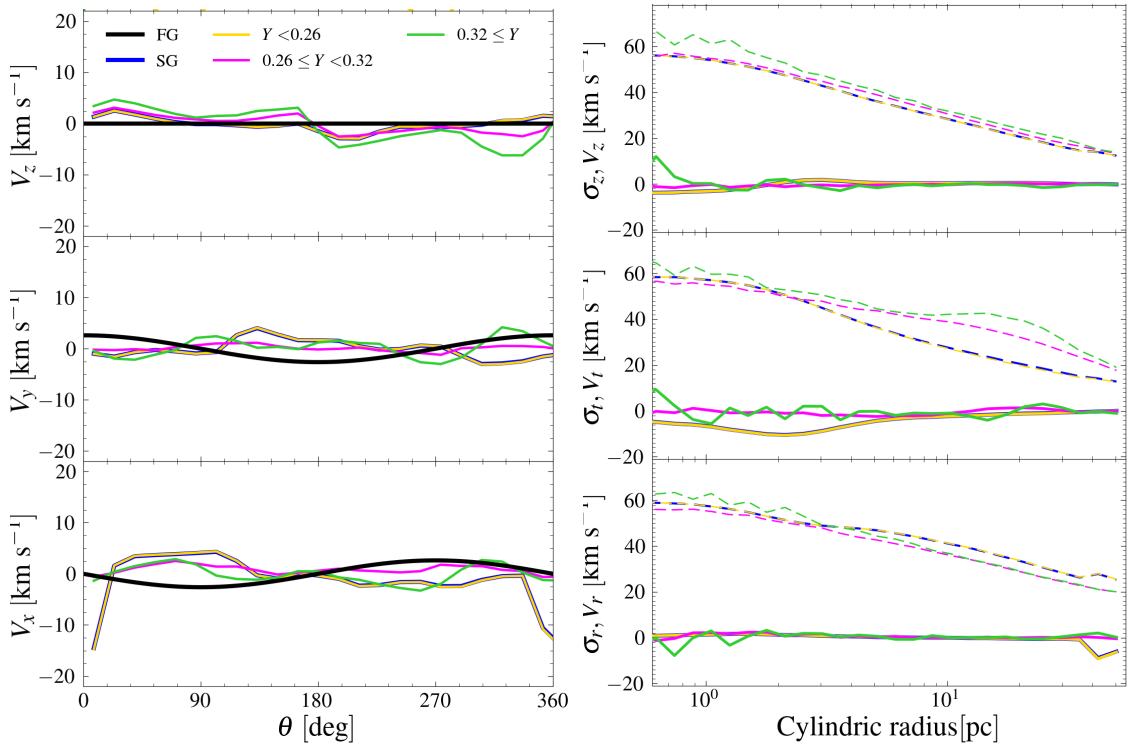


Figure 5.9: Stellar rotation profiles of the model HDanaz at 65 Myr. The reported quantities are as in Figure 5.6.

subsequent formation of the accretion column.

At variance with the low-density model, here the dispersion velocities of all the various SG subgroups are similar. The maximum value of $|V_{rot}/\sigma|$ is 0.2, much smaller than in the low-density models confirming that the system is dispersion-supported.

5.3.2 Rotation parallel to the infall

We present here the results for the model where the FG is assumed to rotate about the x -axis and, therefore, with a rotational axis parallel to the direction of the infall. We describe here only the low-density model (LDanax), given the similar results obtained for the HDanaz and HDanax models. In both cases, a disc is formed both in the gas and stellar components, but, once the infall starts, it is disrupted and no significant rotation is found.

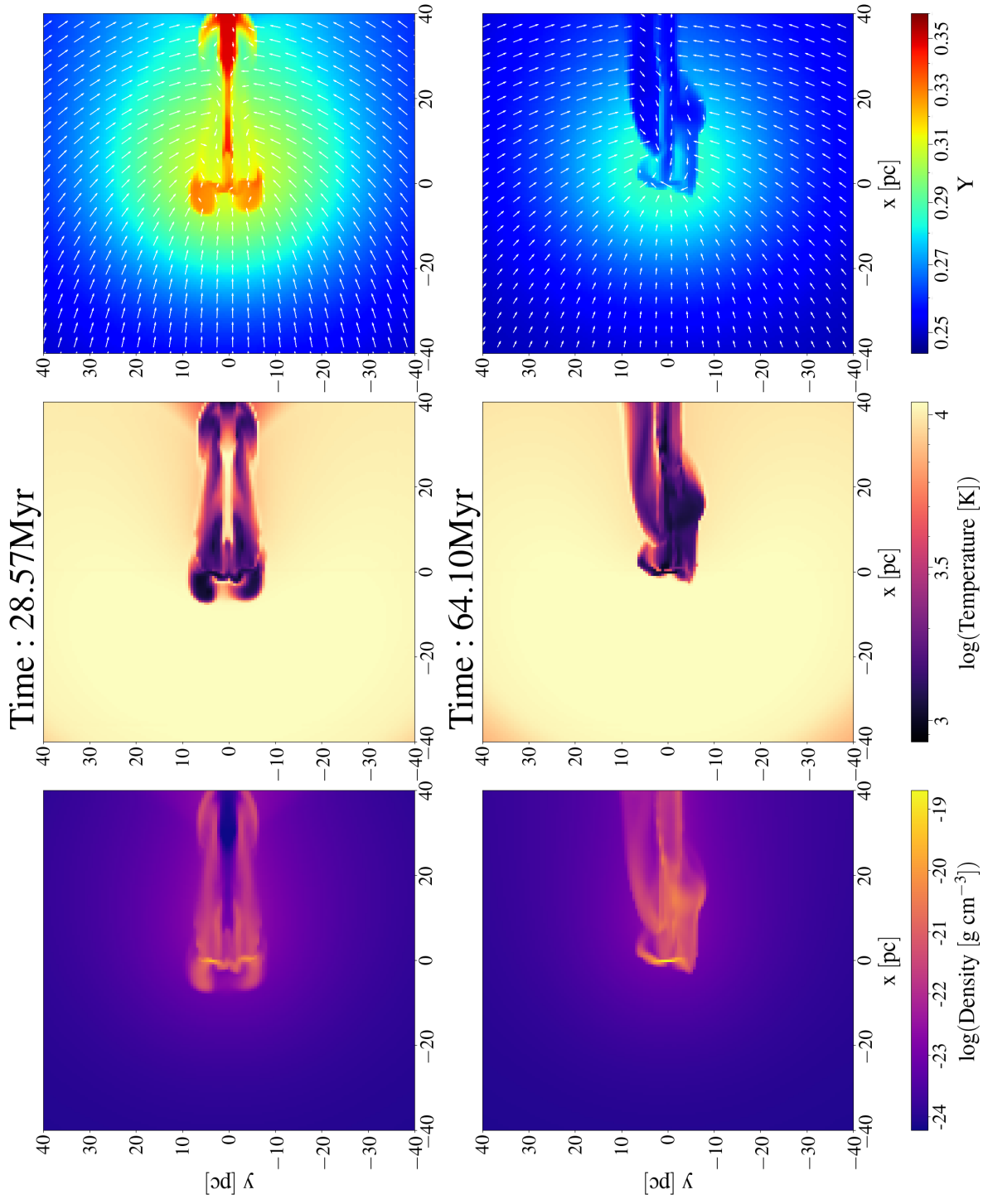


Figure 5.10: Two-dimensional maps of the gas density (left-hand panels), of the temperature (central panels) and helium mass fraction (right-hand panels) on the x-y plane for the LDanex simulation. The time is reported on the top of each set of panels. The white arrows in the helium mass fraction maps show the gas velocity field.

5.3.2.1 Low-density model

Gas evolution

In [Figure 5.10](#) we show the 2D density, temperature and helium mass fraction slices at almost the same times as in [Figure 5.2](#). At 28 Myr, the shock front due to the infalling event has already overcome the cluster and the accretion column has formed. However, the shape of the accretion tail is very different from the one in [Figure 5.2](#) since here the rotation leads to the formation of a disk on the yz plane.

The infalling gas is colliding with the disk face-on and is forced to circulate around the disk giving rise to two accretion columns divided by a very narrow tail, still not polluted by the pristine gas. This feature is even clearer in the helium mass fraction map, where a tight tail of extremely helium-enhanced gas is present downstream of the system. The two helium-enriched blobs near the centre are due to the bounce of the helium-rich gas first pushed by the infalling gas downwards.

At 64 Myr, the tail of extremely helium-enhanced gas has disappeared, while the accretion column has acquired its standard shape. In the central regions, the gas is still enriched in helium, whereas in the outskirts and along the accretion column, the AGB ejecta have been strongly diluted by the infalling gas and have a helium abundance very similar to that of the pristine gas.

Evolution of the stellar component

[Figure 5.11](#) and [Figure 5.12](#) show the 2D maps for the stellar component at the same evolutionary times of [Figure 5.10](#).

At 28 Myr, stars with low helium enhancement start to form both downstream of the system along the two cold and dense tails, as seen in [Figure 5.10](#), and upstream, at around 20 pc from the cluster centre. At this distance, a shock is formed due to the interaction of the infalling gas with the potential well of the cluster, which induces the formation of new stars. Four clumps of extremely helium-enhanced stars are formed in the very centre and located in the disk, similarly to what has been obtained for the `LDanaz` model.

At 64 Myr, the stellar disc is still present and particularly evident in all the maps in Fig. [Figure 5.12](#). Similarly to the `LDanaz` model, we find that the very inner regions host stars slightly less enriched in helium. The disk is slightly thicker than in the `LDanaz` model; this is due to the dynamical effect of the gas infalling along the accretion column

5.3. Results

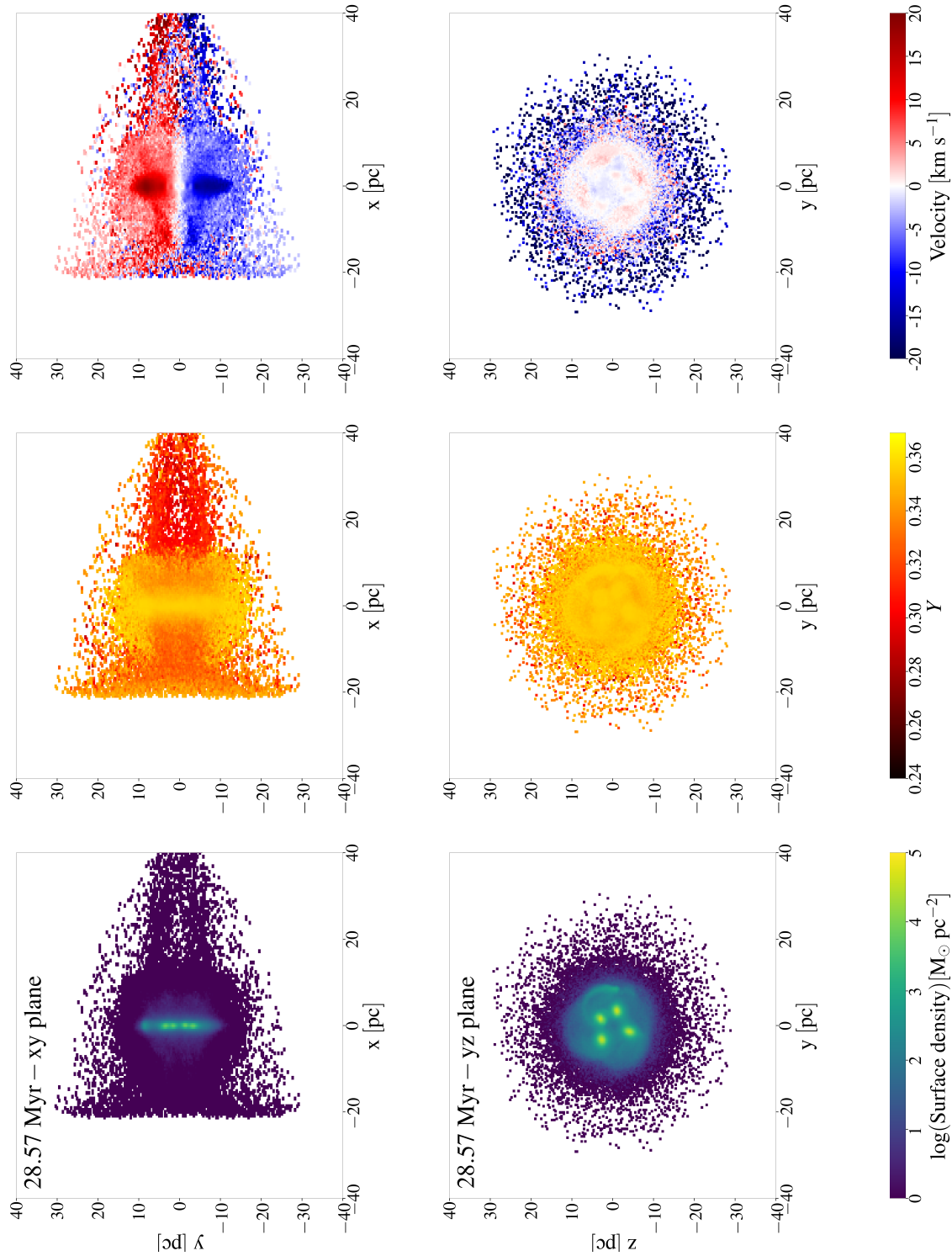


Figure 5.11: Two-dimensional maps of the stellar component for the LDanax model at 28 Myr. The reported quantities are as in Figure 5.3.

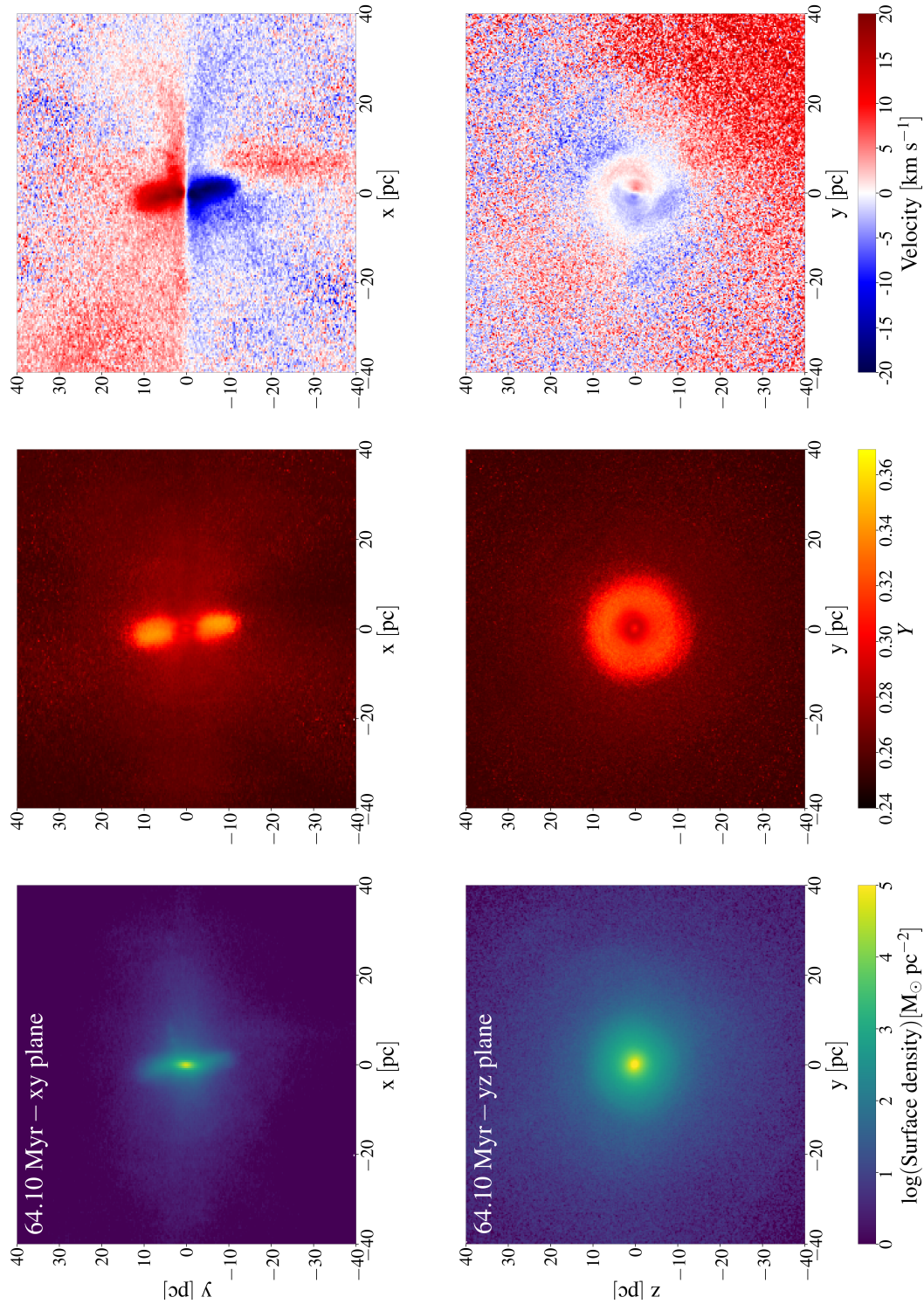


Figure 5.12: Two-dimensional maps of the stellar component for the LDanax model at 64 Myr. The reported quantities are as in Figure 5.3.

5.3. Results

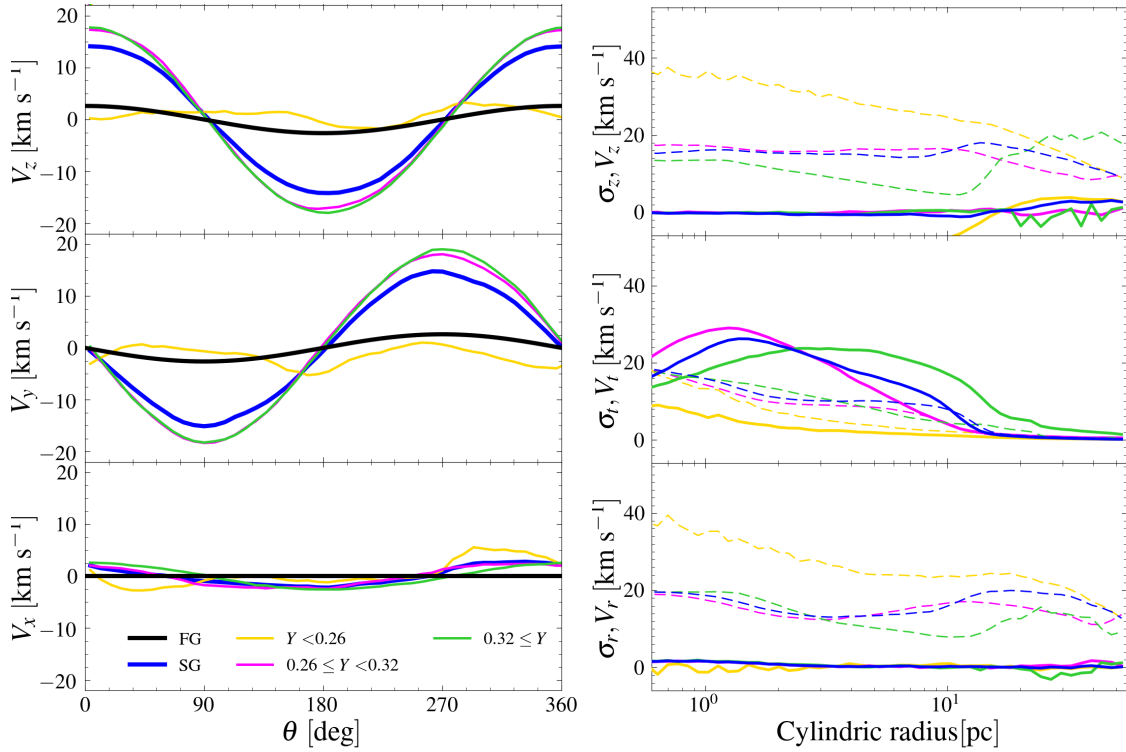


Figure 5.13: Stellar rotation profiles of the model LDanax at 65 Myr. The reported quantities are as in Figure 5.6. Note that the x component is the one parallel to the rotational axis that here is along the x axis.

in the direction perpendicular to the plane of the disk. In addition, the disk appears slightly tilted by about 10 degrees relative to the x - y plane. The left panel of Figure 5.13 shows that the SG component has a higher rotational amplitude than the FG one, with a peak value similar to the one found for the LDanaz model, and, in addition, SG stars with high helium composition are rotating faster than those with moderate helium enrichment. The different orientation of the rotation axis with respect to the direction of the infall implies that the external gas motions do not affect the rotation plane of the disk, leading to a smoother rotation profile, as shown in the left panel of Figure 5.13. Similarly to the LDanaz, $|V_{rot}/\sigma|$ is increasing inside the disk region with a peak of 2, therefore the system is rotationally supported even at large radii.

5.4 Discussion

Our simulations have explored the role of cluster rotation on the formation of SG stars in a massive proto-GC. We have shown how different inclinations and pristine gas densities affect the kinematical and structural evolution not only of the FG and SG, but for the first time, of different subpopulations. We here discuss our results, connecting them with the relevant literature both from the observational and theoretical side.

5.4.1 Model with solid body rotation

Until now, all presented results have been obtained assuming the analytic velocity profile of [Equation 5.3](#) for the FG component. For the low-density model, which is the one where the rotation is much stronger, we have performed, for a comparison, an additional run where we have adopted a solid body rotation profile (LD_{SbZ} , see [Table 5.2](#) for the model description). Such velocity profile was earlier adopted in the 3D hydrodynamic simulations of [Bekki \(2010\)](#), [Bekki \(2011\)](#) and [McKenzie & Bekki \(2021\)](#).

Even in this model, several clumps are formed at around 10 Myr, and clearly visible also at 27 Myr in [Figure 5.14](#), however, their stellar surface density is 3 times lower than in the simulation assuming the analytic velocity profile (LD_{Danaz} model). In addition, stars in the disk possess a stronger line-of-sight velocity in the yz plane, as seen comparing it to [Figure 5.3](#), a consequence of the higher velocity imparted to FG ejecta in the outskirt in the solid body model. At the end of the simulation, the SG velocity is overall larger than the one obtained for the LD_{Danaz} model, due to the slightly larger velocity imposed on the AGB ejecta with the solid body profile. Helium-enhanced stars are, in fact, rotating faster in the outskirts, a consequence of the more extended disk (~ 12 pc), obtained for the model with a solid body profile. In particular, [Figure 5.16](#) shows the rotational amplitudes along the three Cartesian coordinates with an average value of $\sim 15 \text{ km s}^{-1}$ along both the x and y axes. The z component is instead lower than in the LD_{Danaz} model, even though the disk is tilted by about 15° .

It is worth noticing that, even though the FG is set to rotate with a solid body profile, the SG has a pattern much more similar to [Equation 5.3](#), with a peak at around the half-mass radius, which is compatible with the one obtained for the LD_{Danaz} model.

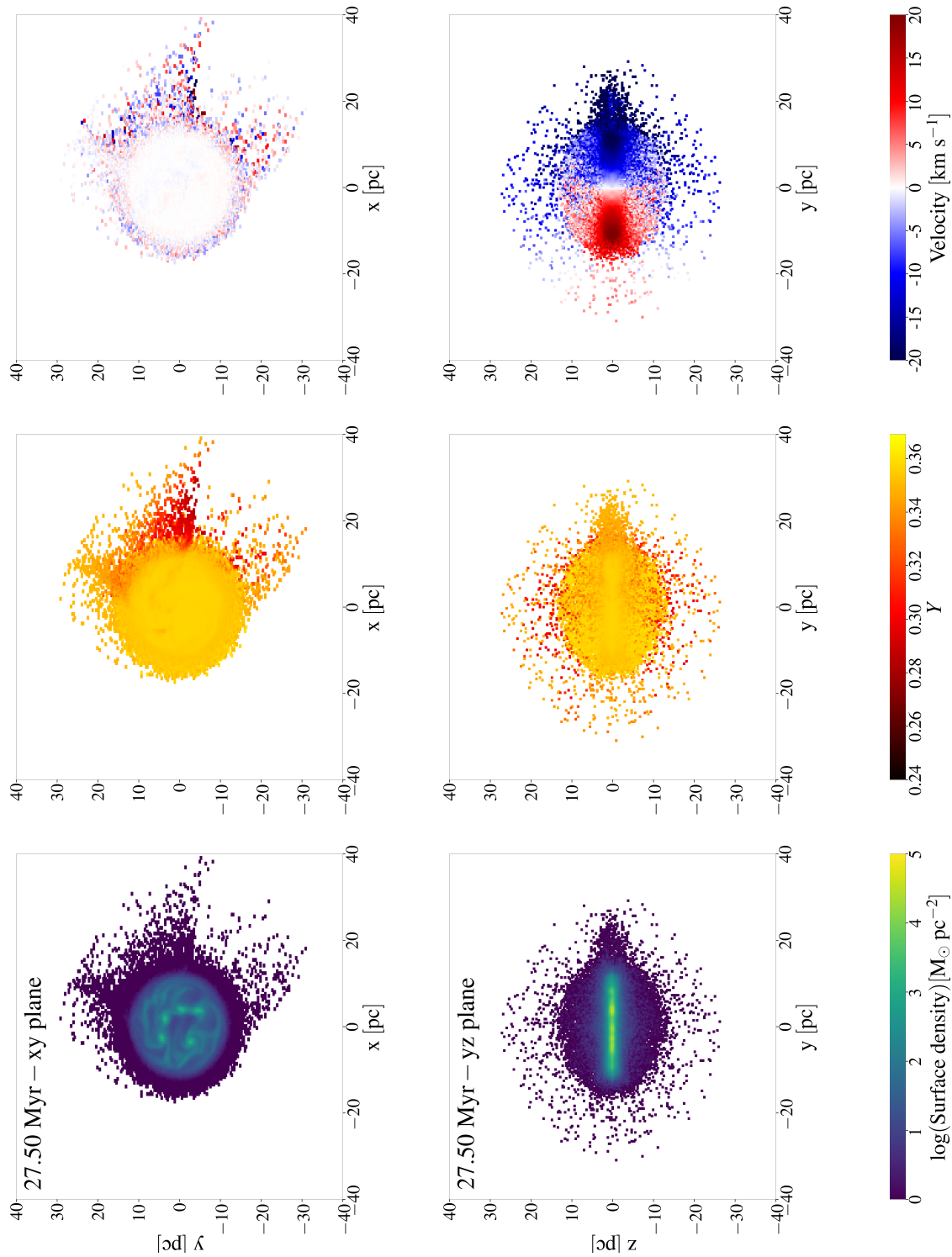


Figure 5.14: Two-dimensional maps of the stellar component for the LDs_{bz} model at 27 Myr. The reported quantities are as in Figure 5.3.

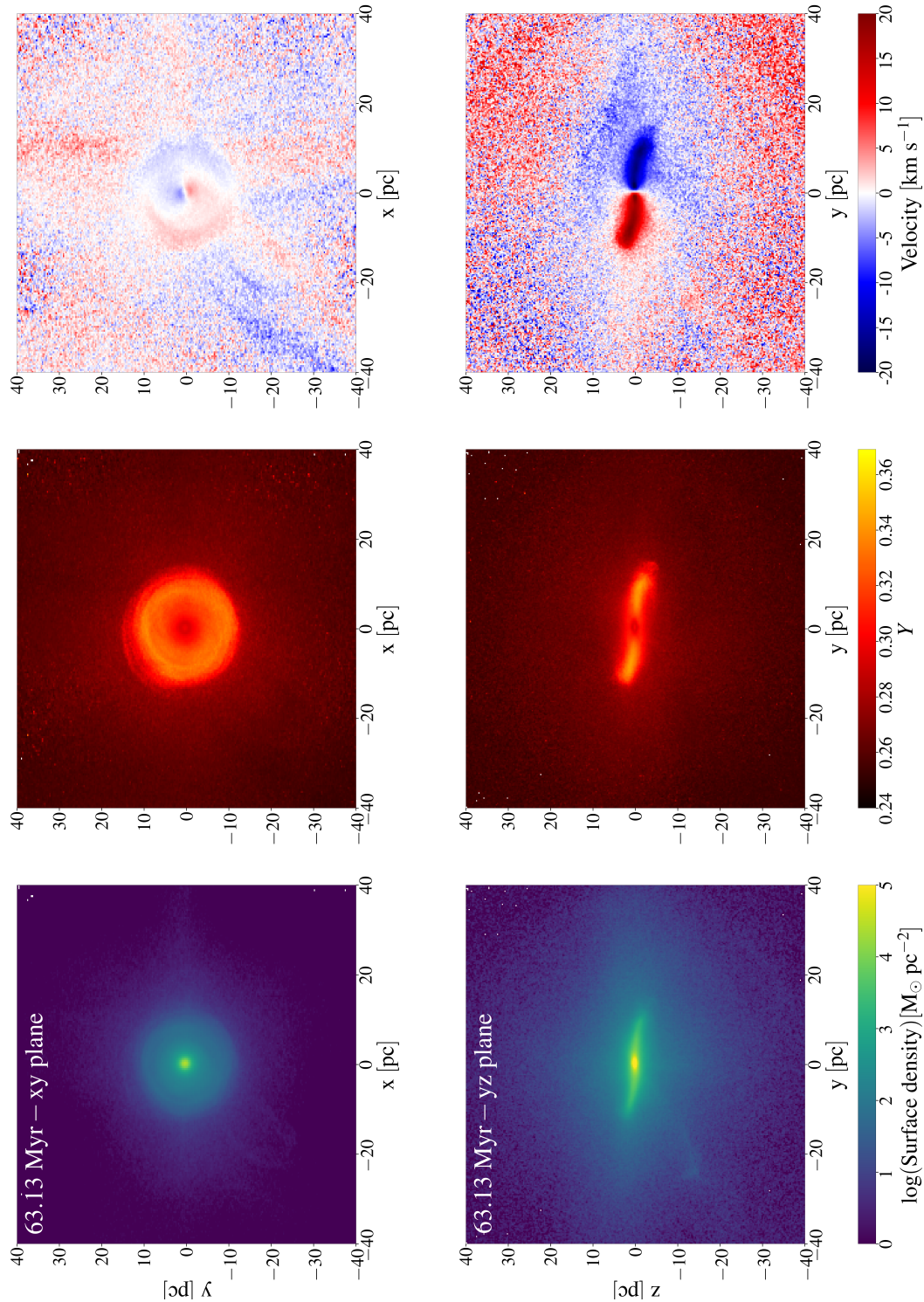


Figure 5.15: Two-dimensional maps of the stellar component for the LDsBZ model at 63 Myr. The reported quantities are as in Figure 5.3.

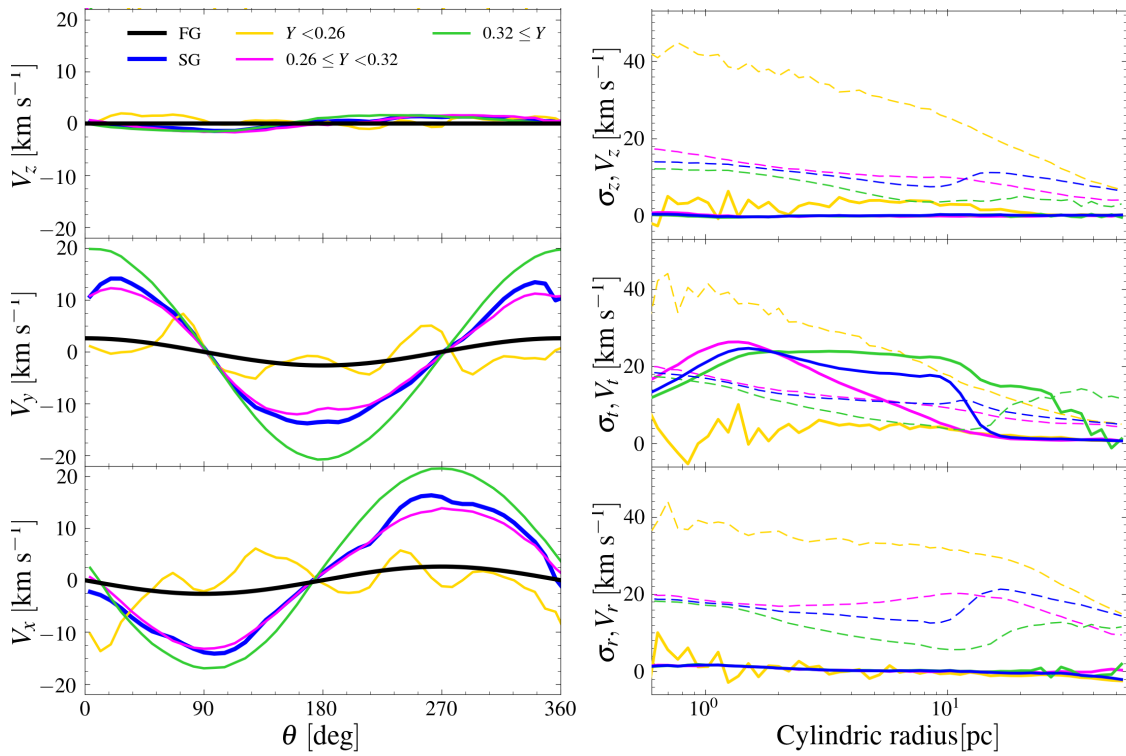


Figure 5.16: Stellar rotation profiles of the model LDsbz at 65 Myr. The reported quantities are as in Figure 5.6.

5.4.2 On the chemical composition of SG stars

While cluster rotation has a significant effect on the morphological and kinematical properties of SG stars, it does not have a strong impact on the overall chemical composition of the system and its final stellar mass. In Figure 5.17, the helium distribution functions of both the low and high-density models are compared. As shown in this figure, for both the low-density and high-density models, the helium distribution is not significantly affected by the orientation of the rotation axis relative to the direction of motion of the cluster in the external gas environment. The two panels are also in general agreement with the helium distribution found in the non-rotating models by Calura et al. (2019).

5.4.3 Comparison with literature

Recently, McKenzie & Bekki (2021) studied the formation of MPs in proto-GCs within the context of their parent galaxy, through 3D hydrodynamic simulations. In all their mod-

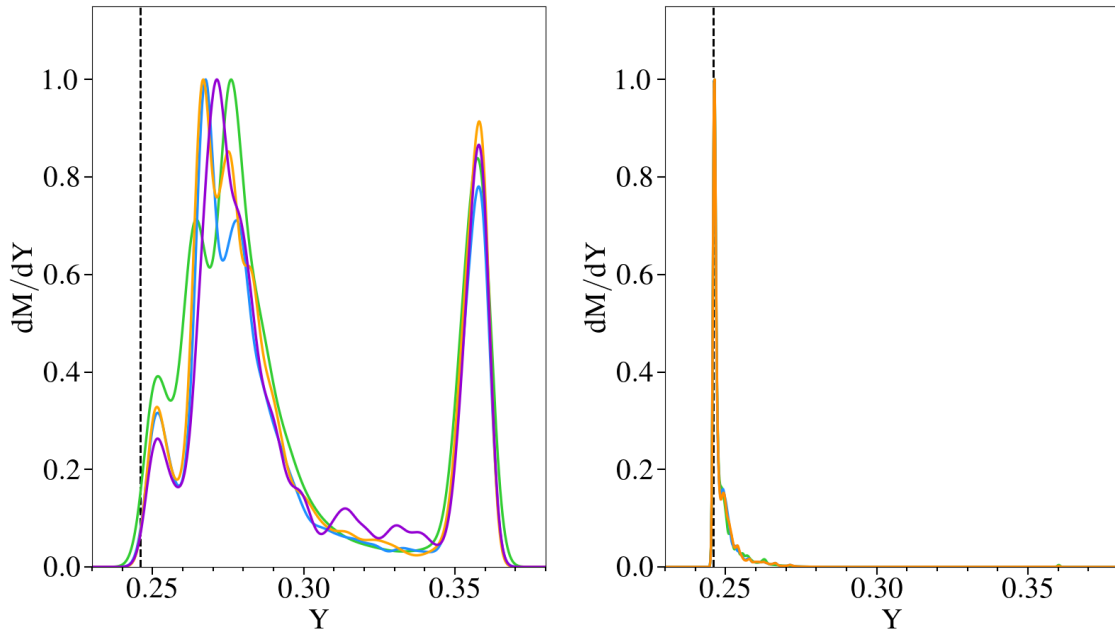


Figure 5.17: The mass distributions of Y in SG stars at the end of the simulations (~ 65 Myr) for different models. On the left: low-density models: LDana z (blue), LDanax (orange), LDsbz (purple) and LD (green). On the right: high-density models: HDanaz (blue), HDanax (orange) and HD (green). Each distribution is normalised to its maximum value. The pristine gas helium mass fraction Y_{pg} is shown by the black dashed line.

els, the cluster is assumed to rotate as a solid body. At variance with our simulations, the infalling gas is modelled as clumpy. For their fiducial model, which assumes a FG of mass $M_{\text{FG}} = 10^6 M_{\odot}$, an order of magnitude lower than in our case, they found a flattened distribution of the SG, similarly to [Bekki \(2010, 2011\)](#) and the present work. Disks, however, are not a common feature in GCs, which are generally described as spheroidal systems, although some degree of ellipticity has been reported by [Frenk & Fall \(1982\)](#) who found an age-ellipticity relation in Galactic and LMC GCs. It is however verified by N -body simulations that SG stars born in a disk mix with FG ones through angular momentum exchange, ending up with a flattened system after 12 Gyr of evolution ([Mastrobuono-Battisti & Perets, 2016](#), see also [Tiongco et al. 2021](#)). At variance with our results, instead, [McKenzie & Bekki \(2021\)](#) found a less concentrated SG compared with the FG, a configuration found only in a few GCs. On the other hand, in both our studies, FG and SG have been derived to rotate in phase, with the SG rotating significantly faster than the

FG. Even though we are exploring here the evolution of a much more massive system, our resulting SG rotational amplitude is in agreement with the mass-amplitude relation found by [McKenzie & Bekki \(2021\)](#).

As in [McKenzie & Bekki \(2021\)](#), we have tested different inclinations of the GC rotational axis with respect to the one of the host galaxy (which is here identified by the direction of the infalling gas). However, in the low-density models, where the disk survives, the inclination of the disk is not significantly affected by the infalling gas and, therefore, it does not align with the host galaxy as it instead happens in their simulations. The models presented here and those of [McKenzie & Bekki \(2021\)](#) differ in various aspects (FG initial mass, external infalling gas, time interval explored). Further investigation is necessary to clarify the origin of the differences between the final SG system orientation found in the two works.

5.4.4 Dynamical and kinematical features of present-day globular clusters

Our simulations follow the formation and very early evolutionary phases of a cluster composed by multiple stellar populations. For a close comparison with the properties of present-day old and intermediate-age GCs, it would be necessary to take into account the effects of the subsequent long-term dynamical evolution. A number of studies have shown that the long-term evolution gradually modifies the properties imprinted by the formation processes. Although, in some dynamically old clusters, the differences between the dynamical properties of SG and FG stars may be completely erased during the clusters' long-term evolution, in dynamically younger ones some memory of these differences may still be preserved (see e.g. [Mastrobuono-Battisti & Perets 2013, 2016](#); [Vesperini et al. 2013](#); [Hénault-Brunet et al. 2015](#); [Vesperini et al. 2021](#); [Tiongco et al. 2019](#); [Sollima 2021](#); [Hypki et al. 2022](#)). Indeed, many of the observational studies cited in the [Section 5.1](#) have found that SG stars are more centrally concentrated than the FG population, in general agreement with what found in this work and in previous theoretical studies (e.g. [D’Ercole et al. 2008](#); [Bekki 2010](#); [Calura et al. 2019](#)).

As for the kinematical properties on which this chapter is focused, a number of observational studies (see the discussion in the [Section 5.1](#)) revealed that, in some clusters, the SG system rotates more rapidly than the FG, in agreement with what found in our work. The observational study of the kinematics of multiple populations is still in its early stages and much work remains to be done to build a comprehensive observational picture

of the kinematical differences between FG and SG stars and, for clusters with multiple SG groups, between the various SG groups. Concerning the possible difference between various SG subgroups, our study predicts that the more extreme SG population is initially rotating more rapidly than the intermediate (moderately enriched) SG groups; this result is consistent with the trend found by [Cordero et al. \(2017\)](#) and [Kamann et al. \(2020\)](#) in M13 and M80, respectively. As for the morphology of different stellar populations, a few early studies have found that in some clusters the SG subsystem is more flattened than the FG one (see [Lee 2017](#); [Cordoni et al. 2020a,b](#); see also [Lee 2018](#) for a cluster showing instead an opposite trend) providing possible examples of clusters retaining some memory of the initial differences emerging from our simulations. Additional observational studies and numerical simulations exploring the long-term evolution of clusters with initial conditions informed by our study will be necessary to further explore these aspects of the structure and kinematics of multiple stellar populations.

Finally, we conclude this section with a brief remark on the mass of SG stars forming in our simulations. The total mass of SG stars formed by the end of our simulation is about 0.1 the mass of the FG system, in the low-density models, and about equal to the mass of FG stars, in the high-density models. As shown in a number of previous studies (see e.g. [D'Ercole et al. 2008](#); [Vesperini et al. 2021](#); [Sollima 2021](#)), the fraction of the total cluster mass in SG stars may significantly increase as a result of the preferential loss of FG stars during the cluster's early and long-term evolution but, as already pointed out in [Calura et al. \(2019\)](#), the extent of mass loss required to reach the values of the SG mass fraction observed in present-day globular clusters (see e.g. [Milone et al. 2017](#)) is much less extreme than sometimes reported in the literature. More extended surveys of simulations exploring the formation of multiple populations are necessary to test the role of various physical ingredients (e.g. FG structural properties and initial stellar mass function, stellar feedback, external environment) and shed further light on the initial mass of the SG population and its dependence on the initial FG properties (see e.g. [McKenzie & Bekki 2021](#); [Yaghoobi et al. 2022](#) for two recent studies addressing these issues).

5.5 Conclusions

An increasing number of observational studies of the kinematics of star clusters are revealing that internal rotation is a common kinematic feature of these stellar systems. It is

therefore important to include rotation in theoretical studies of star clusters and explore its role in their formation and dynamical evolution.

In this Chapter, by means of 3D hydrodynamic simulations, we have studied the role of rotation in the formation and early dynamics of multiple stellar populations in GCs.

Our models follow the formation of SG stars out of the ejecta released by AGB stars in a rotating FG system and the external pristine gas accreted by the cluster. We have explored the resulting structural and kinematical properties of the SG subsystem and studied the differences between the dynamical properties of FG stars and those of the various SG subgroups.

In our simulations, we have modelled a massive proto-GC with a FG mass of $10^7 M_\odot$, moving through a uniform gas distribution for which we have assumed two different density values: a low-density one characterized by $\rho_{pg} = 10^{-24} g \text{ cm}^{-3}$ and a high-density one with $\rho_{pg} = 10^{-23} g \text{ cm}^{-3}$. In order to explore the interplay between the internal rotational dynamics of the AGB ejecta and that of the external infalling gas, we have considered two different configurations: one in which the FG rotational axis is perpendicular to the motion of the cluster through the external medium and one in which it is parallel to it.

The main results of this work are the following:

- i) Our simulations have revealed the complex hydrodynamics/stellar dynamics of the SG formation phase in the presence of a rotational FG system. As derived in previous investigations, we find that the SG forms concentrated in the innermost regions of the FG cluster. Both the SG morphology and kinematics are significantly affected by rotation and the interaction between rotating AGB ejecta and non-rotating infalling external gas. The AGB ejecta initially collect in a disk of gas in the inner regions of the FG cluster and form a rotating disk of helium-enhanced SG stars. The disk survives in the model of a cluster moving in a low-density external medium where the infalling, non-rotating gas has a minor effect on the overall evolution of the system. An inner SG disk also forms in the high-density model but, as a consequence of the earlier arrival of the infalling gas and its higher density, it is disrupted before the end of the simulation. Although the long-term dynamical processes may gradually alter the SG disk and drive it towards an increasingly spherical spatial distribution, massive clusters forming a helium-enhanced population in a low-density external environment are those where some memory of an initial flattened SG subsystem might be found.

- ii) The SG populations forming in a rotating FG cluster embedded in low-density pristine gas are characterized by a rotational amplitude larger than that of the FG population. The differences between the SG and the FG rotational kinematics we find in our simulations are generally consistent with the findings of previous theoretical (Bekki, 2010, 2011; McKenzie & Bekki, 2021) and observational investigations (Cordero et al., 2017; Cordini et al., 2020a; Dalessandro et al., 2021; Szigeti et al., 2021).
- iii) The more He-rich SG subgroups forming earlier, mainly out of AGB ejecta, rotate around the cluster's centre more rapidly than SG stars forming later, out of a mix of rotating AGB ejecta and non-rotating infalling pristine gas. However, for a comparison with the present-day properties of old GCs, it is necessary to take into account the effects of the cluster long-term dynamical evolution (Mastrobuono-Battisti & Perets, 2013, 2016; Hénault-Brunet et al., 2015; Tiogco et al., 2019; Mastrobuono-Battisti & Perets, 2021; Sollima et al., 2022; Vesperini et al., 2021). The findings of our simulations are generally consistent with those of the first observational studies that have explored the kinematics of different SG subgroups and found that the more helium-enhanced SG stars rotate faster than the helium-poor ones (Cordero et al., 2017; Kamann et al., 2020). When SG stars are formed from a rotating FG component embedded in high-density pristine gas, no significant differences are found both between the SG subgroups and the FG and SG systems.
- iv) Very minor differences have been found between models assuming a FG solid-body rotational profile and those assuming the analytic profile of Equation 5.3 or changing the orientation of the rotational axis with respect to the direction of the infalling external gas.
- v) The more complex hydrodynamics of SG formation in a rotating FG cluster does not significantly affect the final distribution of the helium abundances of the SG populations.

In future studies, we will further expand the investigation presented here to fully explore the dependence of our results on the initial properties of the FG clusters (e.g. initial mass, structure, strength of initial rotation) and those of the external environment (e.g. a clumpy ISM). In addition, the results obtained for the low-density model could be used to set the initial conditions for N -body simulations, with the aim of following the long-term

5.5. Conclusions

evolution of the cluster. In this way, it would be possible to quantitatively compare the simulation results with the observed rotational velocities detected in globular clusters.

Chapter 6

THE ROLE OF TYPE IA SUPERNOVA FEEDBACK ON THE SECOND GENERATION FORMATION

*You don't need a weatherman
To know which way the wind blows.*

Subterranean Homesick Blues, Bob Dylan

This chapter is drawn from “On the role of Type Ia supernovae in the second-generation star formation in globular clusters”, [Lacchin et al. \(2021\)](#).

6.1 Introduction

One of the still open questions regarding the Asymptotic Giant Branch (AGB) scenario, proposed for GC multiple populations, deals with how the SG formation was quenched. However, this issue concerns more in general all the scenarios for the formation of multiple stellar populations since, even though most of them are not assuming any pollution from AGB stars, low and intermediate-mass stars will release enriched gas. To prevent AGB pollution, this gas must not be recycled to form new stars and therefore star formation has to be already quenched by some process. In the AGB framework, [D’Ercole et al. \(2008\)](#) ran simulations including Type Ia SNe feedback to test whether these stars could halt the SF in a GC. They performed 1D hydrodynamic simulations comparing the results with and without SNe Ia feedback. They found that, assuming a constant SN rate, the AGB ejecta are rapidly wiped out from the system almost immediately after the first SN

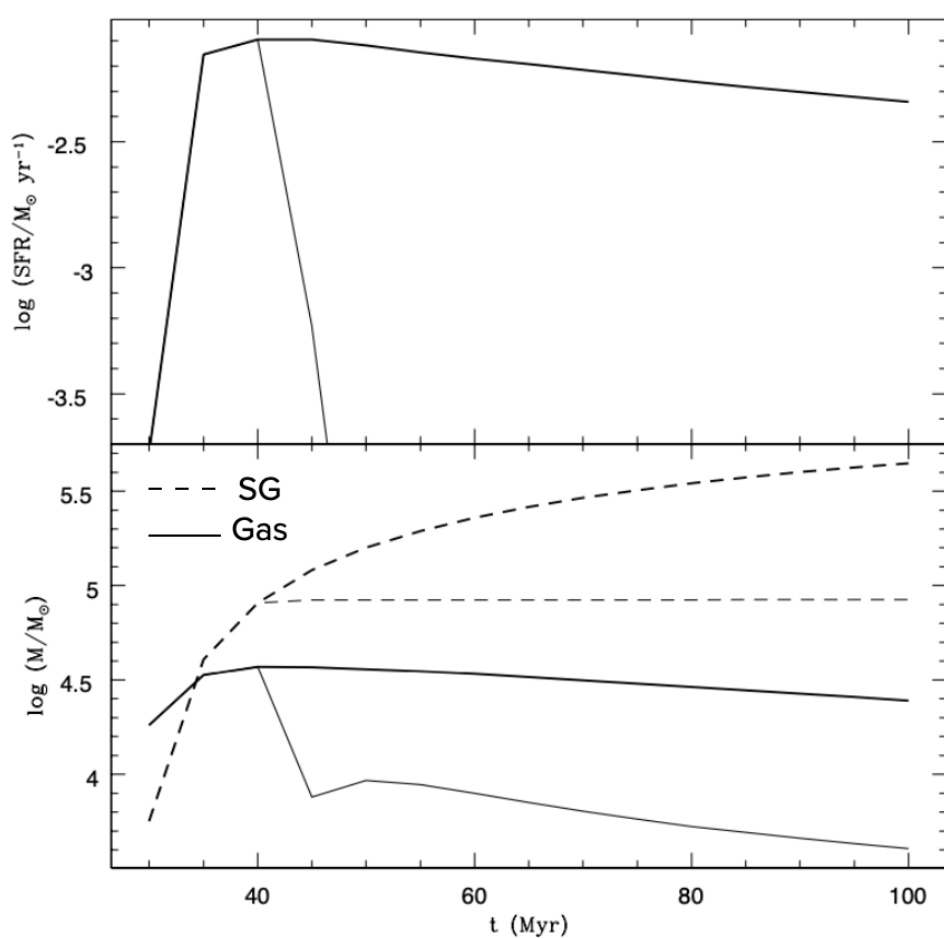


Figure 6.1: Evolution of a massive cluster $10^7 M_\odot$ by means of 1D hydrodynamic simulations. Upper panel: star formation rate evolution. Lower panel: evolution of the amount of mass in gas (solid line) and of SG stars (dashed line). In both panels, the thick lines refer to the model without SNe Ia, while the thin lines represent the model where SNe Ia are exploding every 5×10^4 yr starting at 40 Myr. Taken from D'Ercole et al. (2008).

6.1. Introduction

Ia explosions, which results in a sudden halt of the SF. Figure 6.1 shows the evolution of the star formation in their simulations with and without Type Ia SNe which are assumed to start exploding at 40 Myr. However, they located all SNe Ia at the centre of the cluster, a very strong assumption that could lead to significant overestimations of the effects of feedback, in particular in 1D simulations.

On the other hand, from the chemical point of view, the bulk of GCs are characterized by a narrow internal iron dispersion of $\sigma_{[\text{Fe}/\text{H}]} < 0.1 \text{dex}$ (Carretta et al., 2009c), in particular among SG stars (Legnardi et al., 2022), suggesting that Type Ia SNe belonging to the FG, which are significant Fe producers, should not provide a significant contribution to the gas out of which SG stars are formed. This would be consistent with the results of D’Ercole et al. (2008) where SNe Ia are halting the SG formation very quickly. There are however about 20 percent of the Galactic GC (referred to as Type II clusters in Milone et al. 2017; see also Johnson et al. 2015 and Section 2.2.1) that are instead characterized by a significant dispersion in Fe; the origin of this spread and its link with the SG formation is still unknown.

In this Chapter, we present a series of 3D hydrodynamic simulations to explore the effects of the feedback of SN Ia explosions on the duration of the SG star formation phase and on the chemical properties of the SG stars. The aim is to test whether in 3D and with a different and more realistic distribution, SNe Ia are still efficient in clearing out the system and quenching star formation. In addition, we study the effects of SNe Ia on the iron composition, which has never been accounted for in previous investigations.

The initial configuration of the simulations is the same presented in Calura et al. (2019) which has been described in Section 5.2 where instead of rotation we model the feedback from Type Ia SNe. This is one of the first “wind tunnel” experiments on cluster scale (Priestley et al. 2011, Calura et al. 2019), in which the effects of feedback are investigated in 3D (together with Chantereau et al. 2020, who included photoionization). As in Chapter 5, the system is located at the centre of a cubic computation box which has now a volume $L^3 = (160 \text{ pc})^3$. In all our simulations we adopt a uniform grid reaching a resolution of $\sim 0.3 \text{ pc}$ for the run performed at the highest level of refinement.

The Chapter is organized as follows: in Section 6.2 we describe Type Ia SNe and how their feedback is implemented in the code. In Section 6.3 we present the results we have obtained which are then discussed in Section 6.4. Finally, in Section 6.5, we draw our conclusions.

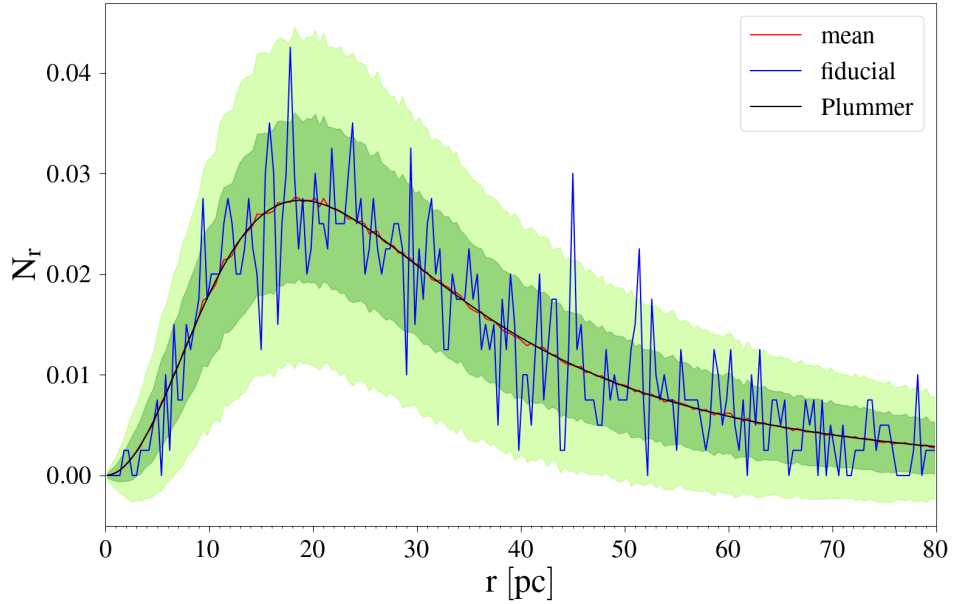


Figure 6.2: Spatial distribution of Type Ia SNe as a function of the radius. In black, we show the analytical result for the Plummer profile assuming $M_{\text{FG}} = 10^7 M_{\odot}$ and a Plummer radius $a = 23 \text{ pc}$. The red line indicates the mean of 1000 realizations with the associated regions within 1 and 2σ in green and light green, respectively. The chosen realization is shown in blue, corresponding to the one that deviates less from the mean among the 1000 realizations. All the plotted lines are normalized imposing $\int_0^{r_{\text{max}}} N_r dr = 1$ with maximum radius $r_{\text{max}} = 80 \text{ pc}$, which corresponds to half the size of the computational box.

6.2 Type Ia SN feedback

The novelty of this work is the introduction of Type Ia SN feedback on the study of a star-forming cluster by means of 3D hydrodynamic simulations. Type I SNe are originated from the thermonuclear explosion of white dwarfs in binary systems. When a Type Ia explodes, we assume that one Chandrasekar mass ($1.44 M_{\odot}$) is released into the ISM with an amount of iron of $0.5 M_{\odot}$ (Scalzo et al., 2014) and a metallicity equal to 1. Each SN will also release 10^{51} erg of thermal energy in the ISM. To every Type Ia SN progenitor, we have associated an explosion time assuming the delay time distribution (DTD) of Greggio (2005, their Equation 16) for the single degenerate scenario, due to its higher rate at short times. Therefore, the SNe are assumed to start exploding 40 Myr after the FG formation.

Given that the number of Type Ia SNe per unit mass for the Kroupa IMF (Kroupa, 2001) is 10^{-3} , assuming a FG mass of $10^7 M_{\odot}$ we end up with 10^4 Type Ia SN explosions

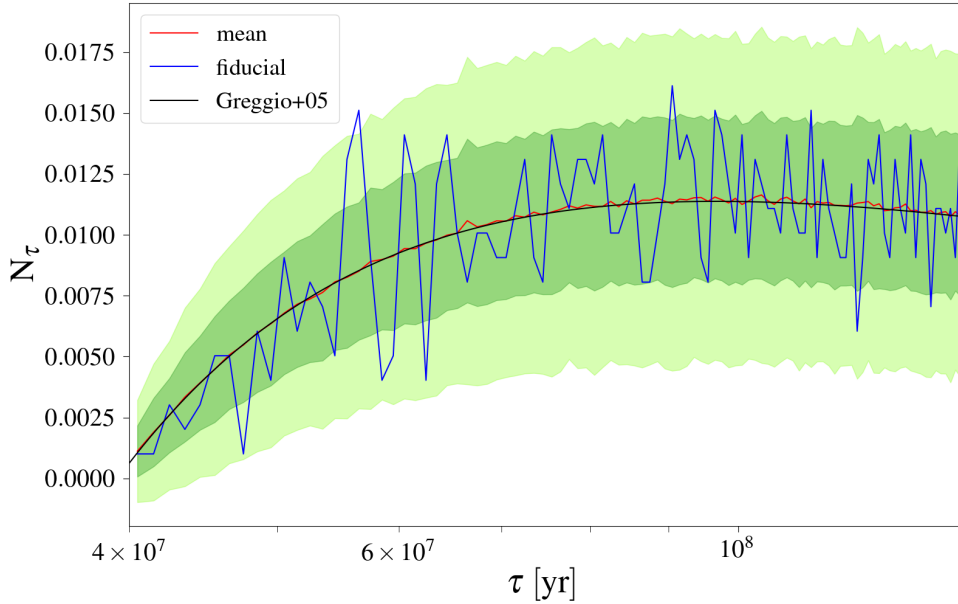


Figure 6.3: Delay time distribution function. In black, we show the theoretical one from Eq.16 of Greggio (2005) assuming $\alpha = 2.35$ and $\gamma = 2$. The red line indicates the mean of 1000 realizations with the associated regions within 1 and 2 σ in green and light green, respectively. The chosen configuration among the 1000 realizations is shown in blue, namely, the one that deviates less from the mean. The plotted lines are all normalized imposing $\int_{\tau_i}^{\tau_x} N_\tau d\tau = 1$ where $\tau_i = 40$ Myr is the lifetime of a $8M_\odot$ star and $\tau_x = 140$ Myr in order to cover all the timespan we are focusing on, with the normalization factor in units of Gyr $^{-1}$.

in 10 Gyr. In the first 0.1 Gyr, the timespan we are interested in, ~ 1000 SNe explosions would take place. Spatially, SNe have been distributed following the Plummer profile ([Plummer, 1911](#)) computed for a cluster mass of $10^7 M_\odot$ and a Plummer radius of $a = 23$ pc. The maximum radius of the distribution has been set to 80 pc, the radius of the sphere inscribed in the computational box; this means that all the SNe are located inside our region of interest.

In order to have a good sampling both of the DTD and of the Plummer profile, we have created 1000 random realizations for each function and then selected the realization that deviates less from the mean. This configuration has been then used to derive the positions and the explosion times of the 1000 SNe. In [Figure 6.2](#) and [Figure 6.3](#) we show the mean over all the realizations in red with the uncertainties at 1 and 2σ and the chosen realization in blue. In black, we have reported the two functions that have been sampled.

6.2.1 The “overcooling” problem

The dynamical evolution of a SN remnant (SNR) can be split into various phases, each of them characterized by a different expansion rate. Immediately after the explosion, the material ejected by the SN expands freely into the ISM. Once the SN ejecta interacts with the circumstellar medium, a forward and a reverse shock are formed; in particular, the reverse shock moves inward heating up the expanding ejecta which results in high temperatures and pressures. This phase lasts until the mass of the swept-up gas becomes comparable to the ejected mass. From then on, the system evolves almost adiabatically during the so-called Sedov Taylor (ST) phase, as long as radiative losses become important. However, when, as in our case, SN feedback is modelled through thermal energy injection, if the SNR is not well resolved the injected energy can be artificially radiated away very quickly, reducing the duration of the ST phase ([Katz, 1992](#)). As a consequence, the impact of SN explosions on the ISM heavily decreases, leading to the “overcooling problem”. [Kim & Ostriker \(2015\)](#) studied the evolution of a SNR varying the numerical grid resolution in order to find the maximum cell size one has to assume to model the SN feedback without falling into the overcooling regime. They found that the numerical resolution Δ has to be at least 3 times smaller than r_{sf} , the radius at the shell formation which is given by:

$$r_{sf} = 22.1 n_0^{-0.43} \text{ pc} \quad (6.1)$$

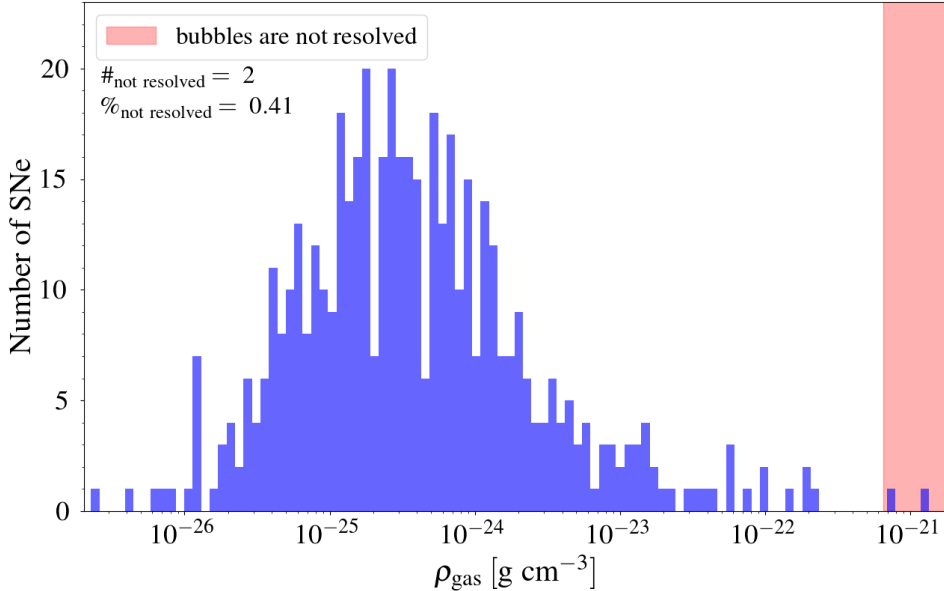


Figure 6.4: The distribution of the gas density in the cells where the SNe are exploding for the low-density simulation. The red shaded area represents the region of densities for which the [Kim & Ostriker \(2015\)](#) criterion is not satisfied.

for a uniform medium.

We have therefore applied the criterion to our simulations to determine whether our SNe are resolved or not.

In [Figure 6.4](#) and [Figure 6.5](#), we report the results obtained for the LD and HD models, respectively. It has to be said that, given that we have truncated our simulations at different times, in the LD model, more SNe have exploded than in the HD one. What emerges is that the number of SNe that do not satisfy the criterion is greater in the HD model than in the LD one. This is a direct consequence of [Equation 6.1](#): the higher the density of the gas the lower the radius at shell formation and, therefore, the required numerical resolution increases. However, for computational limitations, we have assumed the same Δ for both two models.

Focusing on the LD case, the fraction of exploded SNe that does not meet the [Kim & Ostriker \(2015\)](#) criterion is very low, i.e.. 0.41%. In the HD model, this fraction is still very low, although it is nearly a factor ~ 10 larger (3.5%) than in the LD model.

To better investigate this issue, we have decided to perform, for the HD model, a second simulation in which cooling is artificially switched off in the cells surrounding the SNe

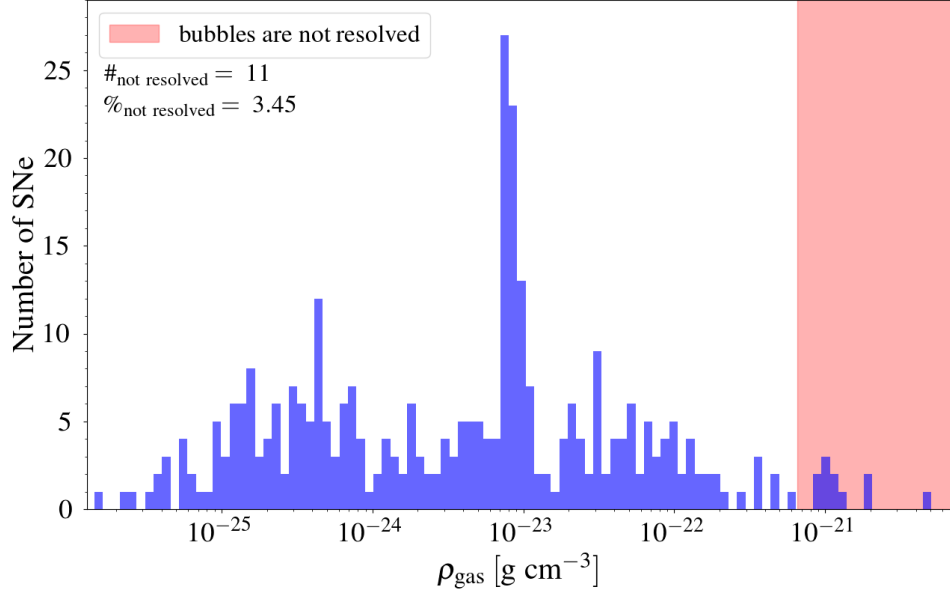


Figure 6.5: The distribution of the gas density in the cells where the SNe are exploding for the high-density simulation. The red shaded area represents the region of densities for which the [Kim & Ostriker \(2015\)](#) criterion is not satisfied.

at the time of their explosion. This method is widely used in literature to prevent the occurrence of the overcooling problem. However, in the literature, there is no unique way to switch off cooling manually, nor a definition of the extent of the region of interest in which cooling has to be switched off, nor of the duration of this phase ([Rosdahl et al., 2017](#)). In this work, we turn off cooling using the RAMSES built-in prescription described in [Teyssier et al. \(2013\)](#). Each Type Ia SN is supposed to inject an equal amount of thermal and non-thermal energy into the ISM; the energy density of the non-thermal component is stored in a new variable, e_{turb} , which acts as a passive tracer. In each cell, the velocity dispersion associated with the non-thermal component is calculated through:

$$\sigma_{\text{turb}} = \sqrt{2 \frac{e_{\text{turb}}}{\rho}} \quad (6.2)$$

where ρ is the density of the gas inside the cell. The cooling is switched off, according to [Teyssier et al. \(2013\)](#), in all the cells where $\sigma_{\text{turb}} > 10 \text{ km s}^{-1}$. This method allows overcoming the still poorly understood causes leading to the problem of “overcooling”, being them related either to resolution or lack of physics (such as turbulence and radiative

feedback).

6.2.2 The shape of the delay time distribution

Many studies have been done so far aimed at constraining the shape of the DTD, the Type Ia SN rate resulting from a brief burst of star formation. The uncertainties concern both its slope and the time interval, with a particular focus on its starting point. While most of the observations agree with $\propto t^{-1}$ dependence at $t > 2$ Gyr, theoretical works find different shapes, especially at short times as shown in Maoz et al. (2014, their Figure 8). Some models predict the first explosions after $\sim 30 - 40$ Myr like the one proposed by Greggio (2005), while others after some hundreds of Myr. However, the duration of SG formation is assumed to end before stars with $m < 3M_{\odot}$ undergo their AGB phase (Renzini et al., 2015; D'Antona et al., 2016), corresponding to an age of $\sim 200 - 300$ Myr, in agreement with the upper limits found by Nardiello et al. (2015) and Lucertini et al. (2020), therefore we have focused our attention on the DTD with short delay times. Nevertheless, given the uncertainties of the starting point of the DTD, we have decided to test a further case in which Type Ia SN explosions are shifted of 25 Myr with respect to the Greggio (2005) formulation, in order to study its effect on the SF of the SG stars. We have chosen this time because we want to study the case in which SNe start exploding when the infall of pristine gas has already started. We have performed one run with delayed Type Ia SN explosions for the low-density case since the effects of SNe for this model are stronger than for the high-density one.

6.2.3 Numerical issues

Together with the “overcooling” problem, the introduction of Type Ia SNe feedback leads to other numerical difficulties. SNe explosions inject fast fluid into the ISM with velocities as high as 10^3 km s^{-1} which have strong effects on the timestep of the simulation. To satisfy the Courant-Friedrichs-Lowy condition, in fact, the timestep is heavily reduced, reaching the order of 10 yr in the highest resolution model (see also Romano et al. 2019). Emerick et al. (2019) overcome this difficulty by lowering artificially the velocity of the fluid to be able to follow the evolution of the system for various hundreds of Myr. In all our simulations we do not apply such artifact, therefore we are able to study only a limited timespan. In addition, the high-density models are slower than the low-density

Table 6.1: Models description. Columns: (1) name of the model, (2) description of the model, (3) pristine gas density, (4) time of pristine gas reaccretion, (5) starting time of Type Ia SN explosions, (6) resolution. Times listed in (4) and (5) are expressed assuming $t_{\text{AGB}} = 39 \text{ Myr}$ as the time zero.

Model	Description	ρ_{pg} (g cm $^{-3}$)	t_{inf} (Myr)	t_{Ia} (Myr)	Resolution (pc)
LD	Low density	10^{-24}	21	0	0.6
LD_HR ^a	Low density at high resolution	10^{-24}	21	0	0.3
LD_DS	Low density with delayed Type Ia SNe	10^{-24}	21	25	0.6
LD_DSI ^b	Low density with delayed Type Ia SNe	10^{-24}	21	25	0.6
HD	High density	10^{-23}	1	0	0.6
HD_DC	High density with delayed cooling	10^{-23}	1	0	0.6

^a truncated after 17 Myr

^b infall stopped once the first SN bubble reaches the boundary from which the infalling gas is entering the box (~ 28 Myr).

ones because of the higher cooling efficiency (e.g. [Romano et al. 2019](#)). Therefore, we have truncated all our low-density models after 48 Myr while the high-density ones after 39 Myr.

6.3 Results

In this chapter, we present the results for four models, all of them including the feedback from Type Ia SNe.

We have performed two runs, the LD and the HD, varying only the density of the pristine gas (see [Table 6.1](#) for the details of all the models). In addition to these models, we have performed, for the low-density one, a run shifting the Type Ia SNe explosions of 25 Myr given the large uncertainties on the shape of the DTD highlighted in [Section 6.2.2](#). We have chosen to perform such a test for the low-density case since, as we will show, the major effects of Type Ia SN feedback are observed in this model.

In addition, we have run a simulation in which cooling is temporarily switched off in

6.3. Results

regions surrounding the SN explosions, for the high-density scenario. This choice was motivated by the non-negligible number of Type Ia SNe not meeting the [Kim & Ostriker \(2015\)](#) criterion.

Lastly, we performed a simulation similar to the LD_DS one but assuming that infall is stopped once the first SN bubble reaches the negative x boundary, namely the face out of which the gas is entering the box. We tested this case since in all our models we are imposing, for simplicity, that gas continues to enter the box even when SN bubbles are pushing it back, far from the cluster. We will not focus in detail on this model, referring to it only for comparison in [Section 6.4](#).

Here we show the results obtained at various times during the evolution of the system. It has to be clarified that all the times are expressed assuming $t_{\text{AGB}} = 39 \text{ Myr}$ as the time zero.

6.3.1 Low-density model (LD)

6.3.1.1 Dynamical evolution of the gas

In [Figure 6.6](#), we show four snapshots of the two-dimensional density and temperature maps at different evolutionary times, for the low-density model. The maps have been obtained by selecting all the cells laying on the plane centered in the middle of the computational box and perpendicular to the z -axis.

In the gas density map, the velocity field has been overplotted as black arrows. In addition, we have highlighted in green the regions where the velocity of the gas is pointing towards the cluster centre (the pristine gas infall is not included). It has to be clarified that, to compute such regions, we have used all the cells laying in the selected plane, while the black arrows are drawn only for some, equispaced cells. Finally, the white dots in the temperature maps represent the newborn stars (with a lifetime of $< 0.05 \text{ Myr}$), while the red contour describes the region enclosing 50% of the SG mass.

We have decided to show the maps at the same evolutionary times as [Calura et al. \(2019\)](#) for a comparison. However, for computational reasons, we have truncated our run at 48 Myr, therefore the last map represents the system at this time, at variance with [Calura et al. \(2019\)](#). The other three maps are taken at $t = 10 \text{ Myr}$, $t = 26 \text{ Myr}$ and $t = 39 \text{ Myr}$.

At ~ 10 Myr most of the gas in the system is composed of AGBs ejecta. The remaining gas is coming from Type Ia SNe which creates several cavities filled with hot, low-density

Chapter 6. The role of Type Ia Supernova feedback on the second generation formation

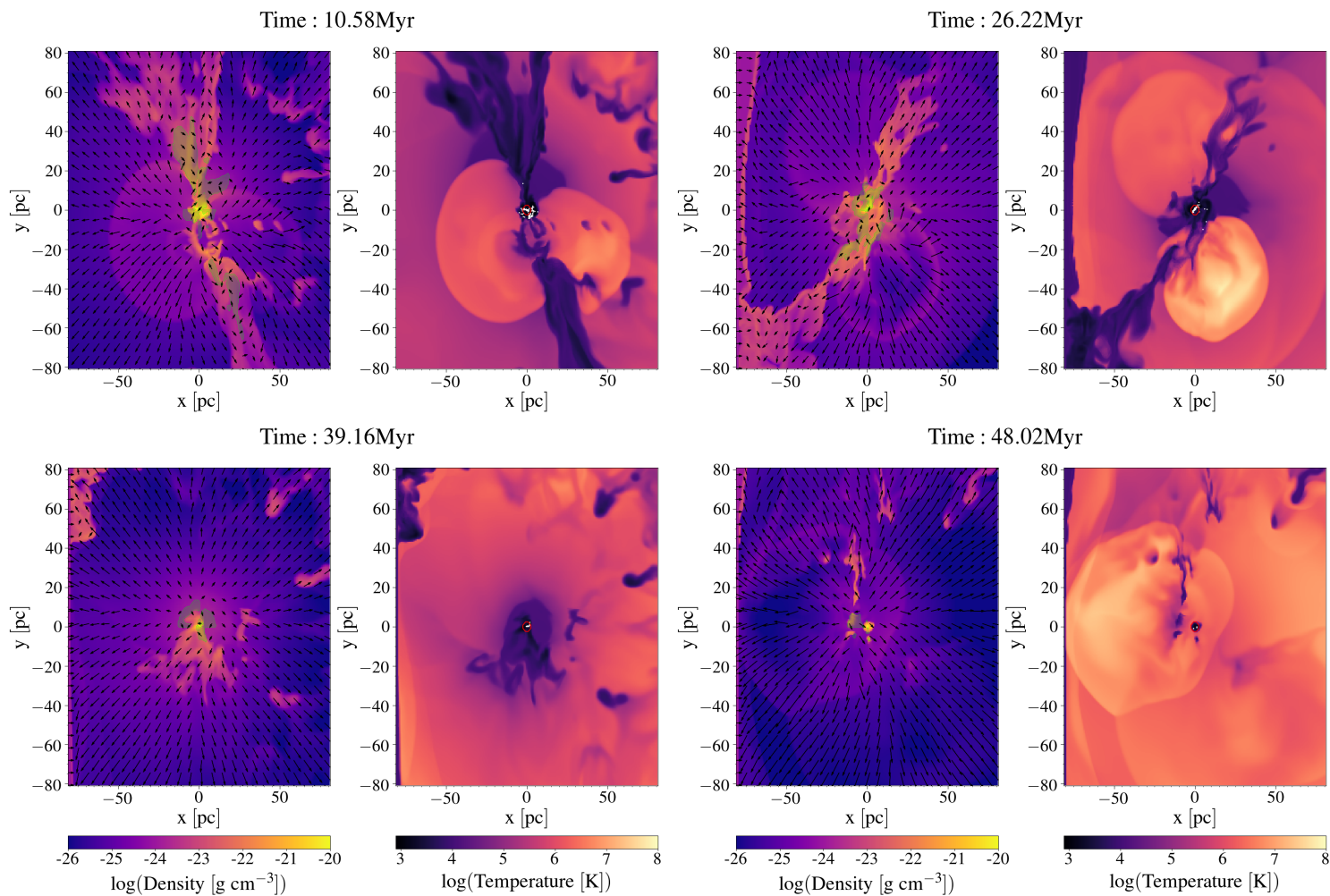


Figure 6.6: Two-dimensional maps of the gas density (left-hand panels) and of the temperature (right-hand panels) in the x - y plane at different evolutionary times (reported on top of each pair of panels) for the low-density simulation (LD). From the top left to the bottom right: $t = 10, 26, 39, 48$ Myr. The black arrows in the density maps represent the velocity field, while the green shaded areas represent the regions of the plane where the gas is moving toward the cluster centre (see the text for details). The white dots in the temperature maps represent the newborn stars (with a lifetime of < 0.05 Myr). The red contour in the temperature maps describes the region enclosing 50% of the SG mass

6.3. Results

gas expanding at high velocity, of the order of 10^7 cm s^{-1} . Two of these bubbles can be clearly seen in both maps. The effect of such explosions influences almost all the computational box, as shown by the velocity field which is pointing towards the boundaries. In the case without Type Ia SNe (taken from [Calura et al. \(2019\)](#), renamed LD_C19), instead, a cooling flow composed by AGB ejecta is formed. The fast ejecta released by SN explosions push the gas out of the system. However, this outward motion does not happen isotropically, because SNe are distributed in space. In this map, two cold and dense filaments are departing from the centre of the cluster, one pointing upward and the other downward. The gas within them has a lower velocity than their surroundings, and cooling flows pointing toward the cluster core are formed, as it is highlighted by the green shaded areas. Very few stars are formed in these dense regions, while most of the stars are born in the very central part of the system.

In the second panel, at 26 Myr, a clear separation between the pristine gas and the hot material carried by the SN bubbles appear both in the gas density and temperature maps; as shown in these maps, the pristine gas and the hot material are pointing in opposite directions. However, due to the large pressure of the material ejected by the SNe, the pristine gas cannot penetrate deeply into the system as in the case without Type Ia SNe (LD_C19). Two SN bubbles can be seen with the one located at negative y -coordinates reaching a temperature of $T \sim 10^8 \text{ K}$ and high velocities ($\sim 5 \times 10^7 \text{ cm s}^{-1}$), meaning that the explosion is very recent. Even in this case, most of the gas in the computational box is moving outwards at high velocity, imprinted by the SN explosions. Two filaments of cold and dense gas are present, and, also, in this case, part of the gas within them is moving towards the centre in a cooling flow. The very central part of the cluster remains dense and stars are still formed, but to a lower extent compared with the previous evolutionary time. Very few stars are instead formed along the filaments.

At 39 Myr, the pristine gas is still confined at the border of the box by the SN explosions. The velocity field is pointing outwards, even in the central part of the cluster, and the gas is generally hot and rarefied due to the SN explosions. Here very few filaments of cold and dense gas can be seen at variance with the previous maps. No cooling flow is generated since almost all the gas is highly perturbed by SN explosions whose filling factor is grown with time as a result of the increased SN rate (see [Figure 6.3](#)).

In the last maps, taken at 48 Myr, almost all the box is filled with hot, rarefied and high-speed gas moving away from the system. The pristine gas remains confined at the

boundaries due to the SN expanding bubbles. No cooling flow is formed, and the regions of cold and dense gas are strongly reduced in comparison with the previous times, and, as a consequence, also the regions where stars can be formed. Only in the core of the system, the gas is dense and cold enough to allow star formation.

6.3.1.2 Evolution of the stellar component

In the first column of [Figure 6.7](#), we plot the density profiles of the FG (magenta dashed lines) and of the SG, the total with black solid lines, and the profiles computed for different ranges of the helium mass fraction Y , as indicated in the legend. The same has been plotted in the third column but for the [Fe/H] ratio. The density profiles have been computed placing the origin in the centre of mass of the system. In the third and fourth columns, the Y and the [Fe/H] mass distributions are plotted, respectively. The vertical black dashed line represents the pristine gas abundance, which is the same as the FG stars while the solid black line in the fourth column represents the normalized cumulative mass as a function of the [Fe/H] ratio.

At ~ 10 Myr all the stars are highly enriched in He, meaning that the effects of Type Ia SNe on the helium enrichment is almost negligible. However, the density of SG stars in the centre of the system is around an order of magnitude lower than in LD_C19 (see [Calura et al. 2019](#), their Figure 3). As for iron, the most metal-poor stars, at this stage, have a $[Fe/H] \sim -1.48$ dex, which reflects the chemical composition of the ejecta of the most massive AGBs. The vast majority of the stars are however more enhanced in iron, due to the pollution of the AGB ejecta with the material expelled by Type Ia SNe, as can be seen from the [Fe/H] mass distribution function. We can therefore define enriched stars as the ones with a $[Fe/H] > -1.48$ dex, while the ones with $[Fe/H] < -1.48$ dex are produced by a mix of AGB ejecta and pristine gas, whose $[Fe/H] \sim -1.55$ dex. It has to be said that the AGB yield of He decreases as a function of stellar mass, which means that, without iron polluters, also the [Fe/H] of the ejecta would decrease during the evolution of the system. However, the variation is almost negligible during the time interval we are looking at.

At 26 Myr, the bulk of the stars are still highly enriched in helium and are therefore formed mostly from AGB ejecta, while only a negligible number of stars are poorly enriched in He. Such stars, formed out of diluted gas, are mainly located far from the centre since, as seen in the maps, the external gas hardly penetrates into the system. A large spread is visible in the [Fe/H] ratio of [Figure 6.7](#), where three peaks can be clearly seen.

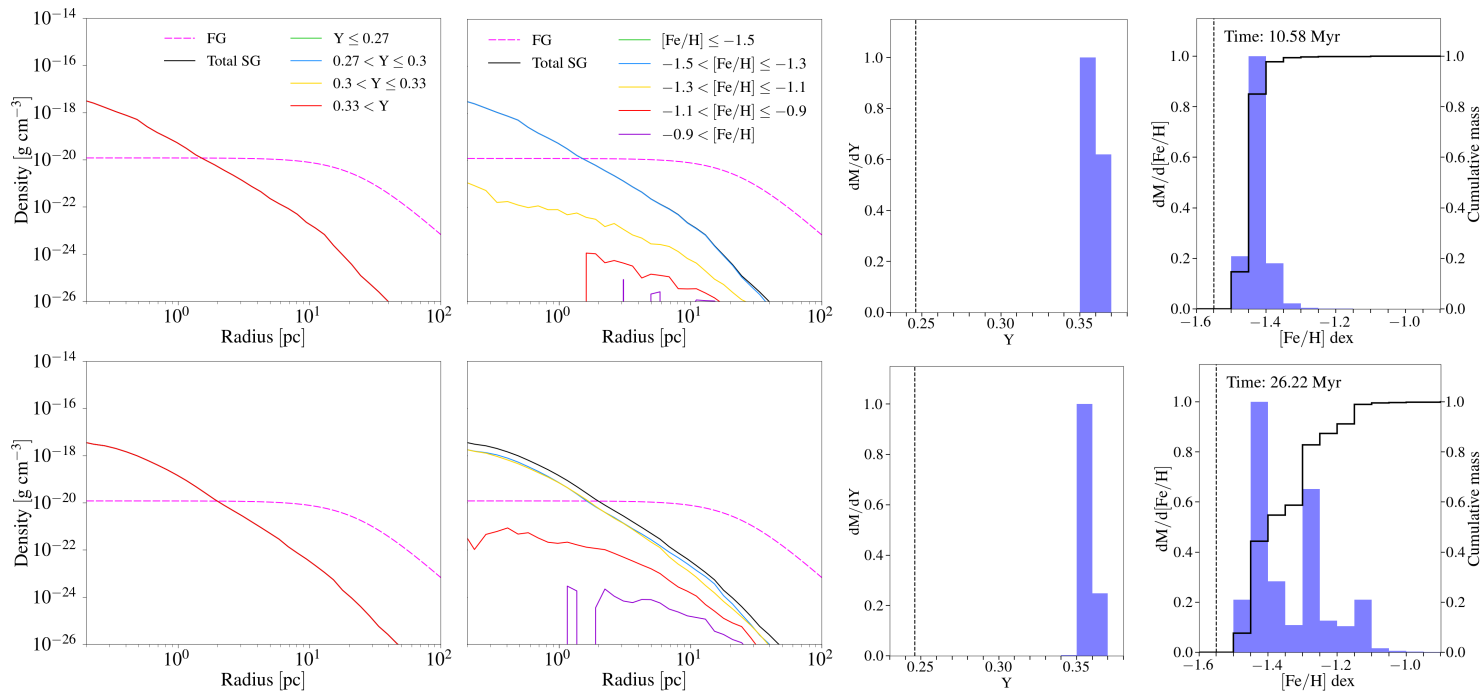


Figure 6.7: First and second columns: total density profile of SG stars at $t = 10, 26, 39, 48$ Myr and density profiles of SG stars for several ranges of the helium mass fraction Y and the $[\text{Fe}/\text{H}]$ ratio, respectively, for the low-density model (LD). The FG density profile is also plotted (see the legend for the details). Third and fourth columns: the mass distribution of Y and $[\text{Fe}/\text{H}]$ ratio, respectively, in the SG stars at the aforementioned evolutionary times (reported in each panel). The distributions have been obtained by summing, in each bin, the masses of the stars belonging to it, and then normalizing every distribution to its maximum value. The black dashed lines represent the pristine gas composition both for Y and $[\text{Fe}/\text{H}]$ ratio, while the solid black line represents the normalized cumulative mass as a function of the $[\text{Fe}/\text{H}]$ ratio.

Chapter 6. The role of Type Ia Supernova feedback on the second generation formation

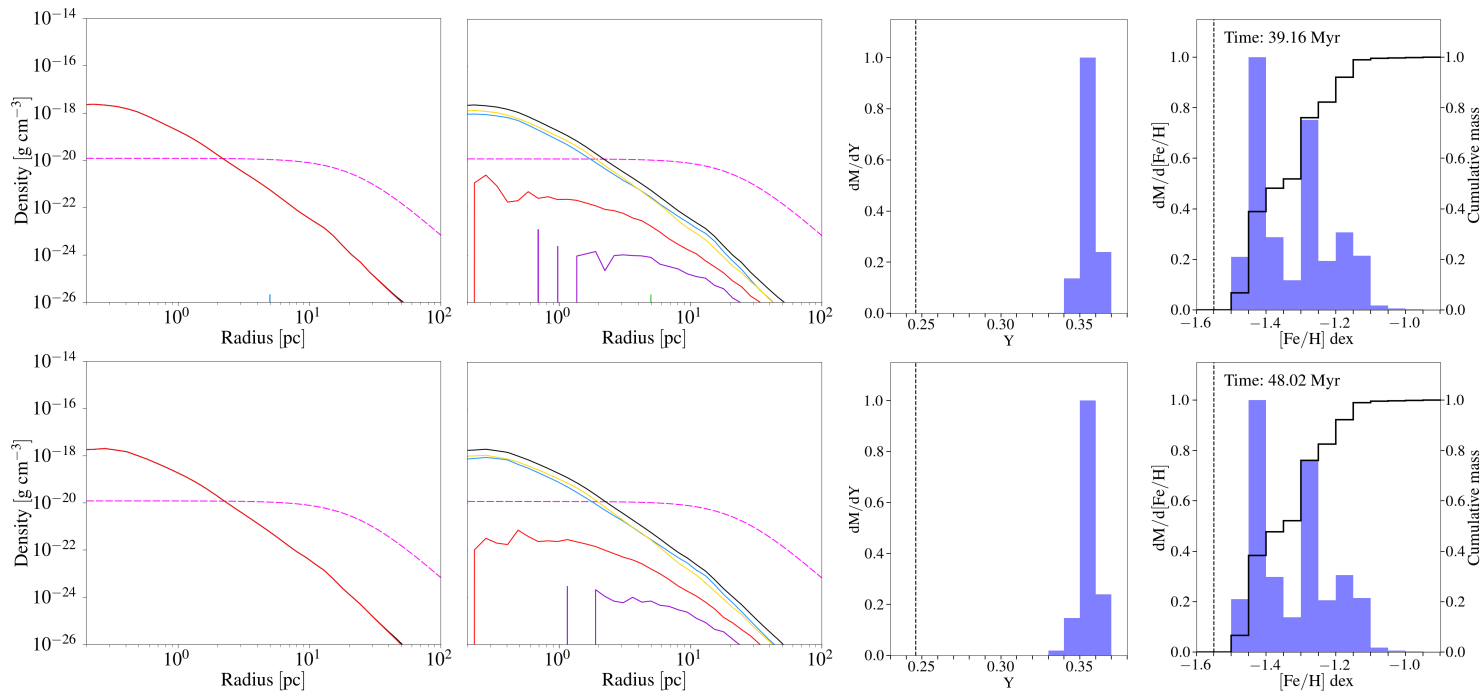


Figure 6.7: Continued

6.3. Results

As we will discuss further on, the star formation in this model is not constant during the evolution of the system as it happened in LD_C19, namely the case without Type Ia SNe. Some small, but still relevant, bursts of star formation are present which lead to peaks in the [Fe/H] mass distribution where, in general, the higher the [Fe/H] ratio of the peak, the younger the stars. The density profile in the third column of Figure 6.7 shows that the bulk of the stars have a [Fe/H] ratio between -1.5 and -1.1 dex, with an increased number of enriched stars in comparison with the previous snapshot.

At 39 Myr, most of the stars still have an extreme He enrichment, at variance with LD_C19, where a peak at intermediate helium enrichment is formed in the Y distribution. This results from the inability of the pristine gas to mix with the AGB ejecta, since the SNe are confining it to the border. Stars not showing an extreme He enrichment give a negligible contribution to the mass of the system and, therefore, also to the density. Focusing instead on the [Fe/H] ratio of the Figure, the contribution from the two more metal-rich peaks is increased in comparison with the previous snapshot, meaning that newborn stars are formed from gas significantly polluted by Type Ia SNe.

In the last evolutionary time, at 48 Myr, not many differences can be seen in the graphs if compared with the previous ones. The intermediate helium-enriched stars give a negligible contribution to the mass, at variance with what is obtained without Type Ia SNe (LD_C19), therefore the bulk of the stars still show an extremely He enrichment. Also, the [Fe/H] mass distribution is almost unchanged, since the SF is lowered and stars produced at this time give a negligible contribution.

At all the evolutionary times we have selected, SG stars are dominant in the central 2-3 pc, while, at larger radii, most of the stars belong to the FG, in agreement with observations (Lardo et al., 2011; Dalessandro et al., 2019). This result is similar to the one obtained by Calura et al. (2019), however, the total stellar density of the SG in the central region is almost two orders of magnitude lower than in their case. The other major difference regards the helium enrichment in the SG stars; we find that SG stars with an extreme He composition are dominant at all radii, at variance with Calura et al. (2019) where this population is concentrated in the central part of the system but it is not prevailing in the outskirts.

At the end of the simulation, the average [Fe/H] of SG stars is -1.32 dex with a dispersion of $\sigma_{[\text{Fe}/\text{H}]}^{\text{SG}} = 0.11$ dex. To obtain this, we have converted the $dM/d[\text{Fe}/\text{H}]$ of each bin into a number of stars assuming a Kroupa IMF truncated at $8M_{\odot}$, following the results

of [Bekki \(2019\)](#). In order to compare our results with observations, we have estimated the internal iron dispersion of the whole cluster assuming that most FG stars are lost during the subsequent evolution, ending up with a fraction of SG stars of ~ 0.7 , as observed in massive GCs ([Milone et al., 2017](#)). In this way, we derive $\sigma_{[\text{Fe}/\text{H}]} = 0.14$ dex, which is larger than the observed value in the bulk of GCs ([Carretta et al. 2009c, Bailin 2019](#)) but in agreement with the typical spread found in Type II GCs. However, in this model, the infalling gas dilutes negligibly the AGB ejecta, and SG stars mostly display an extreme helium abundance, at variance with observations. Moreover, as shown by [D’Ercole et al. \(2011\)](#), dilution is required by the AGB scenario in order to reproduce the Na-O anticorrelation. Here, instead, Type Ia SNe prevent the accretion of pristine gas and, therefore, the dilution of AGB ejecta. For these reasons, the LD scenario is not viable and has to be discarded.

6.3.2 Low-density model with delayed Type Ia SNe (LD_DS)

6.3.2.1 Dynamical evolution of the gas

In [Figure 6.8](#) we show the two-dimensional maps for the case in which Type Ia SN are delayed, with respect to the standard [Greggio \(2005\)](#) formulation, of 25 Myr. In this scenario, the infall of pristine gas starts before the first SN explosion, at variance with the LD scenario. The maps are taken at the same evolutionary times as for the low-density model, with the exception of the second snapshot for which we have decided to show the maps at 27 Myr.

At 10 Myr the system is isolated and the gas, composed only by AGB ejecta, creates a cooling flow towards the cluster core, as seen looking at the velocity field. The gas concentrated near the cluster centre has a high density and is cold ($\sim T_{\text{floor}} = 10^3$ K) with an almost spherical shape. Stars belonging to the SG have already formed in the centre of the cluster, as shown both by the contours and by the white dots. This stellar component is more compact than the SG in the LD model.

At 27 Myr, the infall of pristine gas is already started, the front shock has crossed the centre of the system and the first Type Ia SN has just exploded in the central regions. In most of the computational volume, the gas velocity field reflects the motion of the pristine gas. Far from the system, the arrows are parallel to the x -axis, meaning that the gas is not affected by the presence of the cluster. As we approach the cluster core, the velocities are

6.3. Results

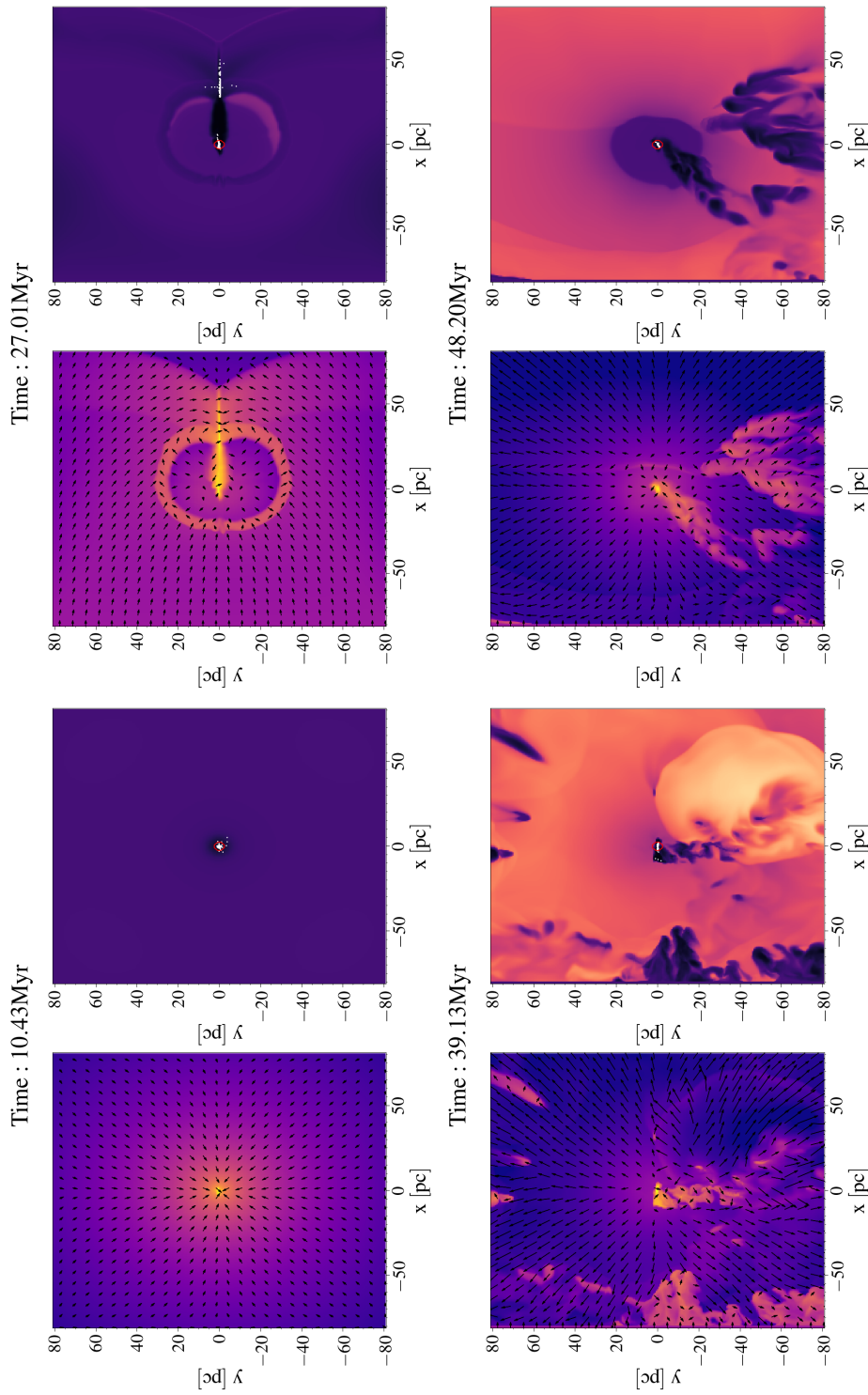


Figure 6.8: Two-dimensional maps of the gas density on the left-hand panels of each plot and of the temperature on the right-hand panels in the x - y plane at different evolutionary times for the low-density simulation with delayed Type Ia SNe (LD_DS). From the top left to the bottom right: $t = 10, 27, 39, 48$ Myr. Other symbols and lines as in Figure 6.6.

increasingly distorted in the y -direction, as a result of the gravitational force exerted by the cluster. Even the front shock is distorted, displaying two symmetric “wings” downstream of the system. These wings delimit the gas already shocked from the unperturbed one; the latter, besides being less dense, is still collapsing towards the cluster centre. The only other part of the box in which the velocity field is not driven by the infall is the central region, where a SN explosion has created a bubble. Near the shell, the density is high, while, inside the bubble, it is almost equal to the pristine gas one except for the very central region where the density remains high and stars continue to be formed. It is worth noting that the temperature distribution inside the bubble is asymmetric, being hotter next to the shell downstream of the shock, while cold upstream of it. Such an inhomogeneity, which also appears in the density maps, even though it is less evident, is due to the infall of pristine gas. Upstream the density is higher, given the direct effect of the infall which leads to stronger cooling and, consequently, a lower temperature.

Despite the SN explosion, a clear tail of dense and cold gas moving toward the cluster centre is formed. Through this accretion column ([Bondi & Hoyle, 1944](#); [Shima et al., 1985](#); [Moeckel & Throop, 2009](#)), the gas can flow and reach the central part of the system, mixing with the AGB ejecta to form new stars. Newborn stars are present also along the tail, but only in the portion still not perturbed by the SN shock front. In the part of the tail already crossed by the SN expanding shell almost no stars are formed due to the perturbation produced by the shock wave.

At 39 Myr, pristine gas is no more falling deep inside the system, as it happens in the previous snapshots. SNe explosions are confining it to the border of the computational box, as in the LD model. Gas is still falling towards the centre in limited areas of the system, next to the cluster centre. However, the bulk of the gas velocity is pointing outwards, driven by the continuous SN explosions. Even the tail and the related accretion column formed by the infall and visible at 27 Myr have already disappeared. Stars are formed almost only in the very central region, where cold and dense gas is still present.

At 48 Myr, the pristine gas is still confined far from the system by the gas moving outwards, perturbed by shock waves generated by SNe. Only in the central region, cold gas is falling towards the cluster centre, where stars are still forming.

6.3. Results

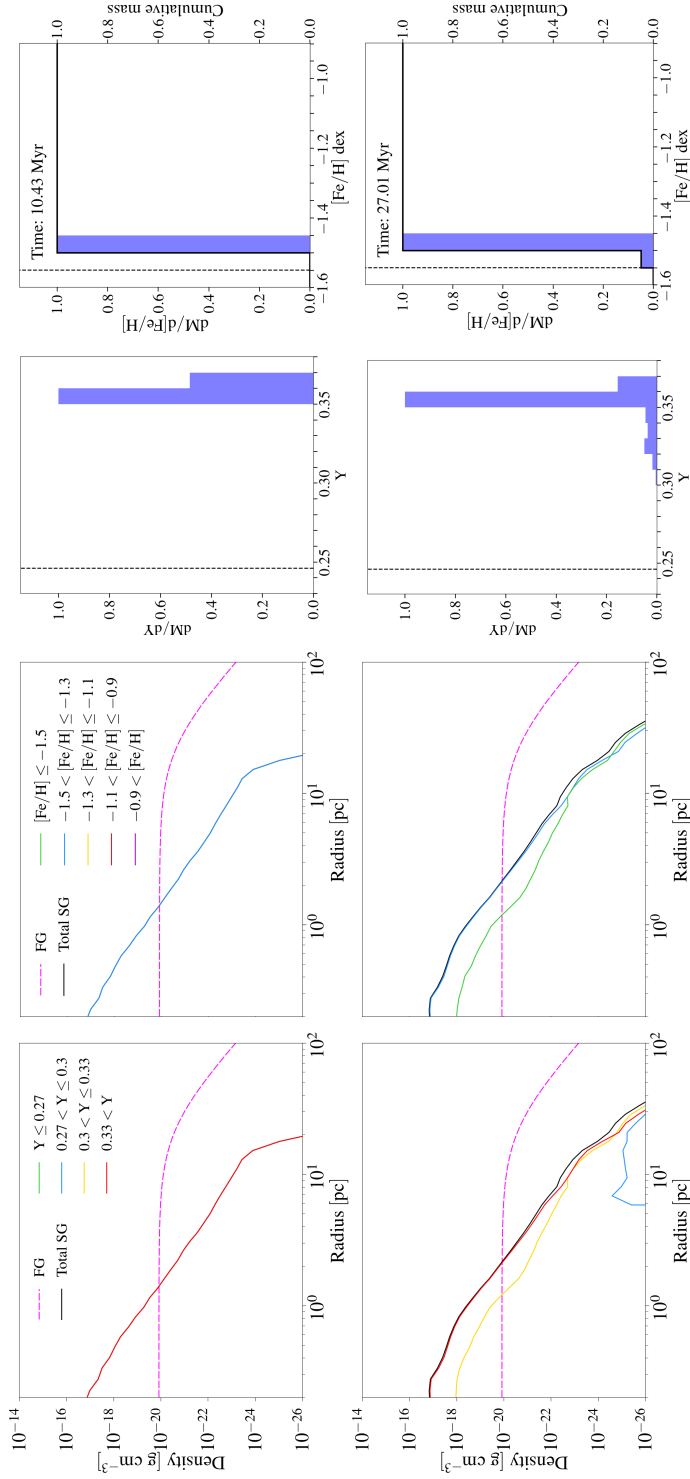


Figure 6.9: First and second columns: total density profile of SG stars for several ranges of the helium mass fraction Y and the $[Fe/H]$ ratio, respectively, for the low-density model with delayed Type Ia SNe (LD_DS). The FG density profile is also plotted (see the legend for the details). Third and fourth columns: the mass distribution of Y and $[Fe/H]$ ratio, respectively, in the SG stars at the aforementioned evolutionary times (reported in each panel). Other symbols and lines as in Figure 6.7.

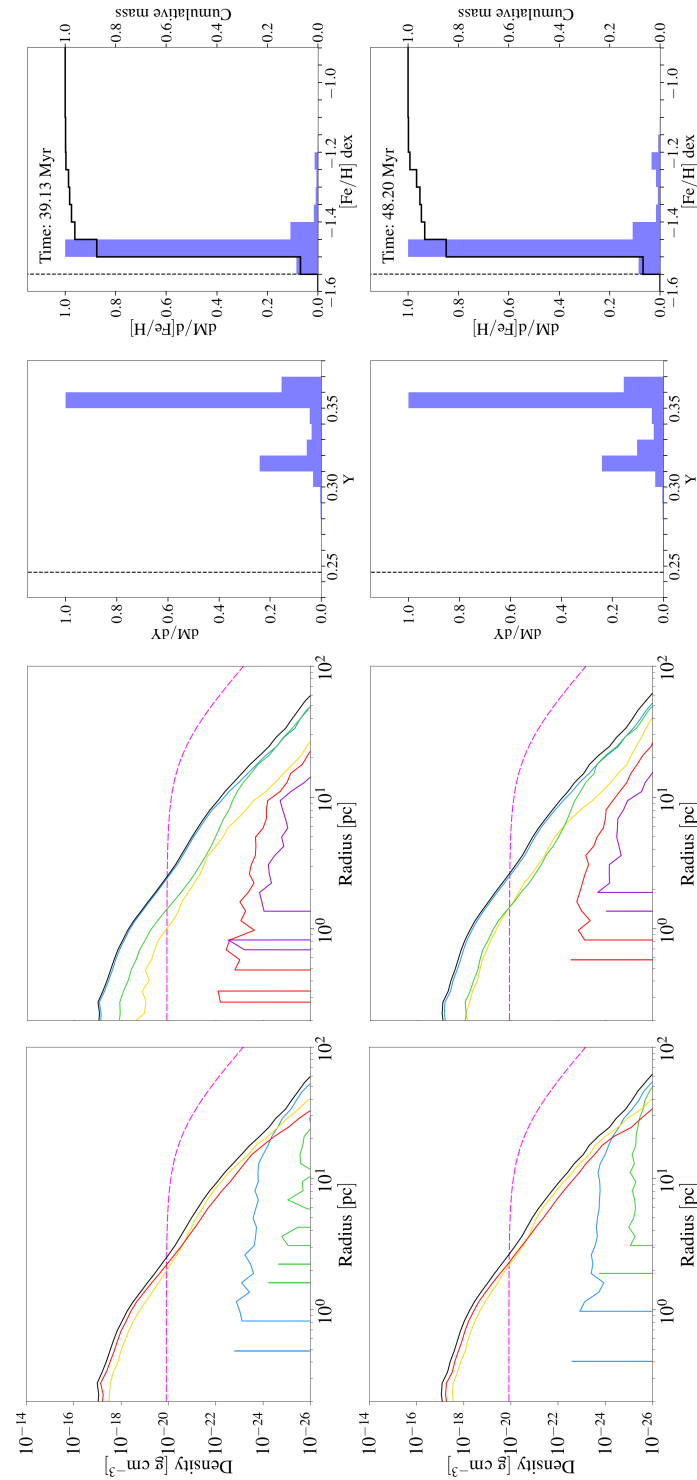


Figure 6.9: Continued

6.3.2.2 Evolution of the stellar component

In [Figure 6.9](#), we plot the density profiles of SG (both total and for various helium composition and [Fe/H] ratio), together with the Y and [Fe/H] mass distributions for the low-density model with Type Ia delayed of ~ 25 Myr, at different evolutionary times.

At 10 Myr, all the stars are extremely helium-enriched, since the only gas present at this stage comes from the AGB ejecta. Also, the iron composition is peaked at the AGB value because no Type Ia SN has exploded yet. The density in the central region is higher than in the LD model, since, at this time, star formation is not hindered by SN explosions. In addition, a sharp cut-off is present at ~ 10 pc because the gas eligible for star formation is concentrated at the centre and is distributed almost isotropically.

Later, at 27 Myr, the pristine gas is diluting the AGB ejecta, especially in the outer regions, where stars with lower helium enrichment and [Fe/H] ratio are formed, being, in the outermost regions, even the dominant component. The pristine gas has, in fact, the same iron mass fraction of the AGB ejecta, but a higher hydrogen one¹. Very few stars with an enhanced iron composition are already formed, since only one SN is exploded and the iron it has ejected has not been used to create new stars yet.

At 39 Myr, instead, an increasing number of stars is formed out of mixed gas with intermediate helium composition, which gives rise to a second smaller peak in the Y distribution. These stars are less centrally concentrated than those with extreme helium enrichment. The presence of a small fraction of stars with a higher [Fe/H] ratio indicates that the iron produced by Type Ia SNe has been recycled. Most of these stars are located in the central regions, where, however, the dominant component remains the one composed of stars formed mainly from AGB ejecta, followed by stars born out of AGB ejecta plus pristine gas ($[\text{Fe}/\text{H}] < -1.5$ dex).

At 48 Myr, few differences are visible compared to the previous timestep. The reason lies in the decreased star formation rate (SFR) and, as a consequence, in the almost negligible increase of the total SG stellar mass between the two evolutionary times.

Many are the differences between the model we are describing here and the LD one. Firstly, while in the LD scenario almost all stars are characterized by extreme helium

¹Before and during the AGB phase stars experience various dredge-ups, deepenings of the convective envelope which lead to mixing of the outer envelope with products of the H and He burnings. The consequence, from the chemical point of view, is that the hydrogen mass fraction in the external parts of the envelope, and therefore also on the ejecta, is reduced.

enrichment, here stars with intermediate helium composition contribute significantly, in particular at large radii where they become the dominant component. This result resembles what has been obtained by [Calura et al. \(2019\)](#), although in our model the contribution from mildly enriched stars is lower. Unlike the LD model, in the LD_DS one the pristine gas is able to reach the central part of the system and stars with a mixed composition are formed. As for iron, with delayed SNe, stars with [Fe/H] ratios similar to the pristine gas one are formed even in the central part of the cluster, while in the LD model this component is absent. On the contrary, very few stars in the scenario with delayed SNe are strongly enriched with respect to the AGB yield value, whereas three peaks at higher [Fe/H] ratios are present in the LD model ([Figure 6.7](#)). In the LD_DS scenario, in fact, no burst of SF is present, at variance with the LD one, as shown in [Figure 6.13](#).

The mean [Fe/H] ratio of SG stars at the end of the LD_DS simulation is -1.45 dex with a dispersion of $\sigma_{[\text{Fe}/\text{H}]}^{\text{SG}} = 0.06$ dex. As for the LD model, we have calculated the iron dispersion of the whole cluster assuming that the SG account for the 70% of the stars, obtaining $\sigma_{[\text{Fe}/\text{H}]} = 0.07$ dex, which is within the range of values found in Type II clusters. However, similar to the LD model, most of the SG stars show extreme helium abundance. Even though a second peak at intermediate Y is formed (see [Figure 6.9](#)), the spread in helium is still too large compared to observations, meaning that dilution is still too low. The extent of dilution depends on the delay of Type Ia SN explosions with respect to the onset of the infall, becoming more significant with larger delays and approaching the results of [Calura et al. \(2019\)](#). To better constrain the timescales at play, more chemical elements need to be traced and more delay times to be tested in future works.

Overall, our results and those of [Calura et al. \(2019\)](#) suggest that in the context of low-density models, longer delay times, possibly leading to the first SN Ia explosions around 80 – 100 Myr after the FG formation, are required to produce multiple-population properties consistent with those observed in Galactic GCs. Concerning the central SG density, the LD model predicts a lower value than the case with delayed SNe due to the larger number of explosions.

6.3. Results

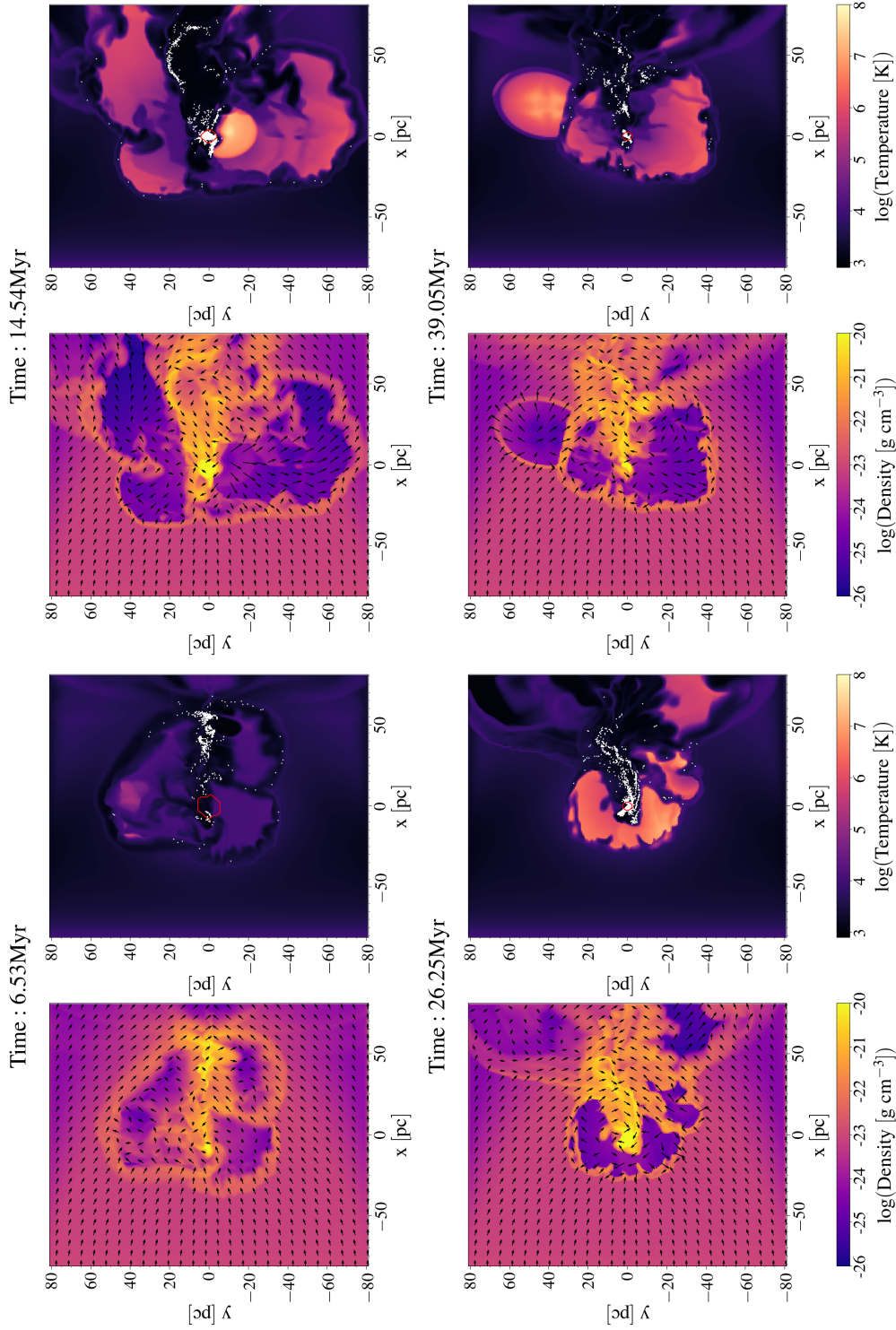


Figure 6.10: Two-dimensional maps of the gas density on the left-hand panels of each plot and of the temperature on the right-hand panels in the x-y plane at different evolutionary times for the high density (HD) simulation. From the top left to the bottom right: $t = 6, 14, 26, 48$ Myr. Other symbols and lines as in Figure 6.6.

6.3.3 High-density model (HD)

6.3.3.1 Dynamical evolution of the gas

In our high-density simulations, we have assumed that the density of the pristine gas is $\rho_{\text{pg}} = 10^{-23} \text{ g cm}^{-3}$, a value 10 times greater than that adopted in the lower density model. Through [Equation 5.2](#), we have derived that, for this value of the pristine gas density, the infall starts around 40 Myr after the FG formation, which corresponds to ~ 1 Myr after the starting point of our simulations. In [Figure 6.10](#), we show the density and temperature maps on the x-y plane computed at the same evolutionary times as [Calura et al. \(2019\)](#), except for the last map. The times associated with the four snapshots are $t = 6$ Myr, $t = 14$ Myr, $t = 26$ Myr and $t = 39$ Myr.

A comparison of these maps with the ones obtained for the LD case, shown in [Figure 6.6](#), shows that, in the HD model, the infalling pristine gas is able to penetrate deeper into the cluster, limiting the expansion of the SN bubbles. The pristine gas surrounds the system, at variance with the low-density case, in which it remains confined at the border of the computational box. In addition, a significantly larger number of stars are formed, not only in the very central part of the cluster, but also along the accretion column, absent in the LD model, downstream of the system.

At 6 Myr, the pristine gas has already crossed the system, however, the cold, dense and narrow tail formed in [Calura et al. \(2019\)](#) simulation is not clearly seen here because it is constantly disrupted by the continuous Type Ia SN explosions. Dense regions can be found also around the shell of the SN bubbles, where the swept-up gas collides with the pristine gas. Here, stars can be formed far from the cluster centre, however, most of the stars are forming in the central region and along the perturbed tail.

At later times, at 14 Myr, the overlap of various bubbles has created an extended region of hot and rarefied gas surrounding the dense, cold stream visible along the x-axis. A large number of stars are formed in the central part of the system, but also in the dense region corresponding to the tail location, where a flow of dense material is pointing towards the centre of the cluster. The infalling pristine gas is acting against the expansion of the bubbles, in particular pushing them rightwards. The stellar component has expanded with respect to the previous snapshot, especially downstream of the system.

At 26 Myr, hot bubbles are present as a result of recent SN explosions near the centre of the system. Nevertheless, the bubbles are not expanding through the entire computational

6.3. Results

box as in the low-density case ([Figure 6.6](#), top right panel). The bubbles are more confined and their shape is far from being spherical. This is the result of the ram pressure of the pristine gas, which is stronger in the HD model. The velocity field reveals, also in this case, the presence of a flow of gas extending in a tail. A large number of stars are formed in this region of cold and dense gas, even though the bulk of young stars are in the proximity of the centre of the system.

At 39 Myr, the system has not changed much; cold and dense gas is forming new stars both in the central regions and along the accretion column, which is still present at this time. The gas heated up by SNe explosions is still confined by the pristine gas.

6.3.3.2 Evolution of the stellar component

In [Figure 6.11](#) we plot the density profiles of the SG for various ranges of Y and [Fe/H] ratio at different evolutionary times for the high-density model, together with the helium and [Fe/H] ratio mass distribution functions.

At 6 Myr, the shock caused by the infall of pristine gas has already crossed the system and stars are formed from a mixed gas. In the external region, stars with no helium enrichment, and therefore formed mainly out of pristine gas, are dominant, while in the central region the AGB ejecta have been less diluted, and stars display extreme helium abundances. However, the component not enriched in helium is dominant in mass, as visible from the Y mass distribution, where three peaks at low, intermediate and extreme helium enrichment can be clearly seen. On the other hand, the iron mass distribution is peaked around $[Fe/H] \sim -1.45$ with a long tail towards higher values, which however contributes almost negligibly to the total stellar mass. The density of the SG is higher than the FG one in the central region, but it is lower than the case without Type Ia SNe studied by [Calura et al. \(2019\)](#) (HD_C19).

At 14 Myr, stars with almost no helium enhancement (with respect to FG stars) have become dominant at all radii, while those with high helium abundances give the lowest contribution, as illustrated by both the density profiles and the Y distribution. Therefore, the pristine gas comprises a large fraction of the gas out of which SG form, at variance with the LD case, but similar to HD_C19. Conversely, the [Fe/H] ratio of the bulk of the stars is increased: this means that, even though the pristine gas is significantly diluting the AGB ejecta, iron from Type Ia SNe is retained by the system and recycled to form new stars. Most of the stars show a significant iron enrichment, in particular in the central

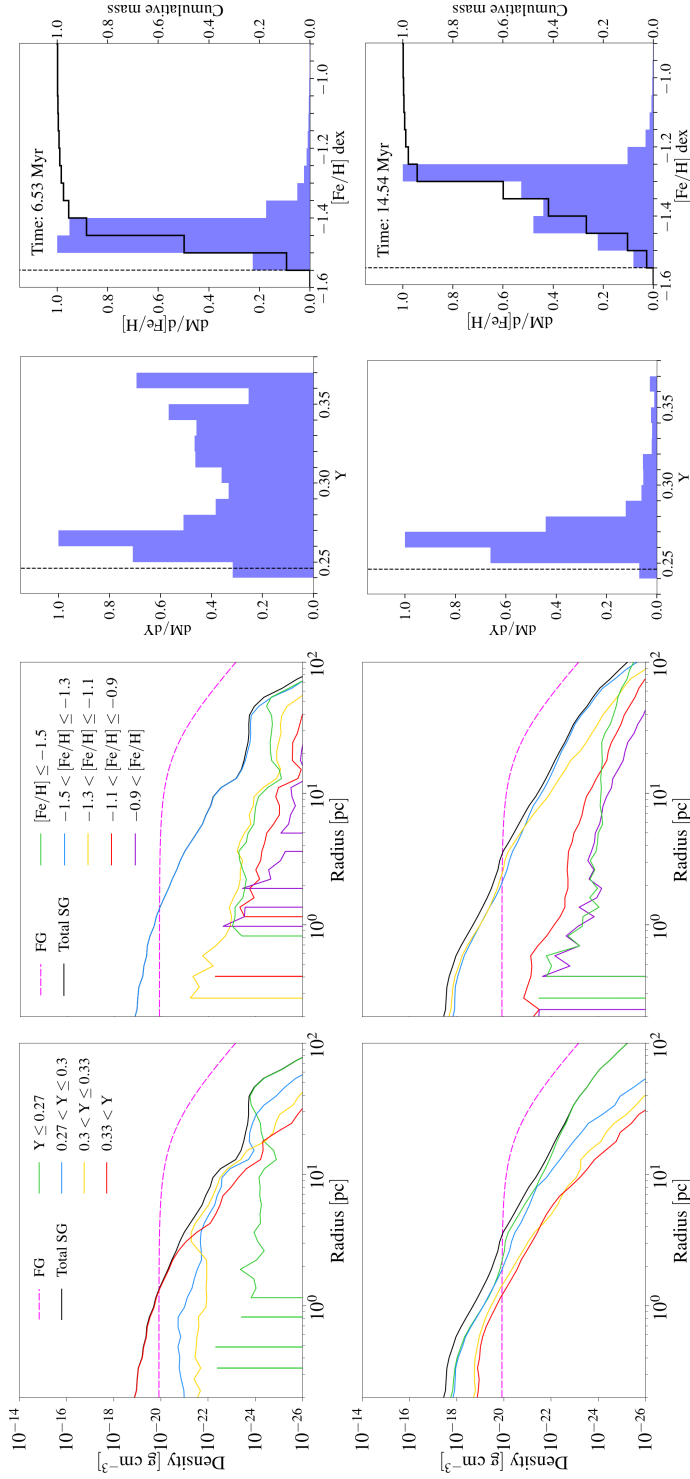


Figure 6.11: First and second columns: total density profile of SG stars at $t = 6, 14, 26, 39$ Myr and density profiles of SG stars for several ranges of the helium mass fraction Y and the $[\text{Fe}/\text{H}]$ ratio, respectively, for the high-density model (HD). The FG density profile is also plotted (see the legend for the details). Third and fourth columns: the mass distribution of Y and $[\text{Fe}/\text{H}]$ ratio, respectively, in the SG stars at the aforementioned evolutionary times (reported in each panel). Other symbols and lines as in Figure 6.7.

6.3. Results

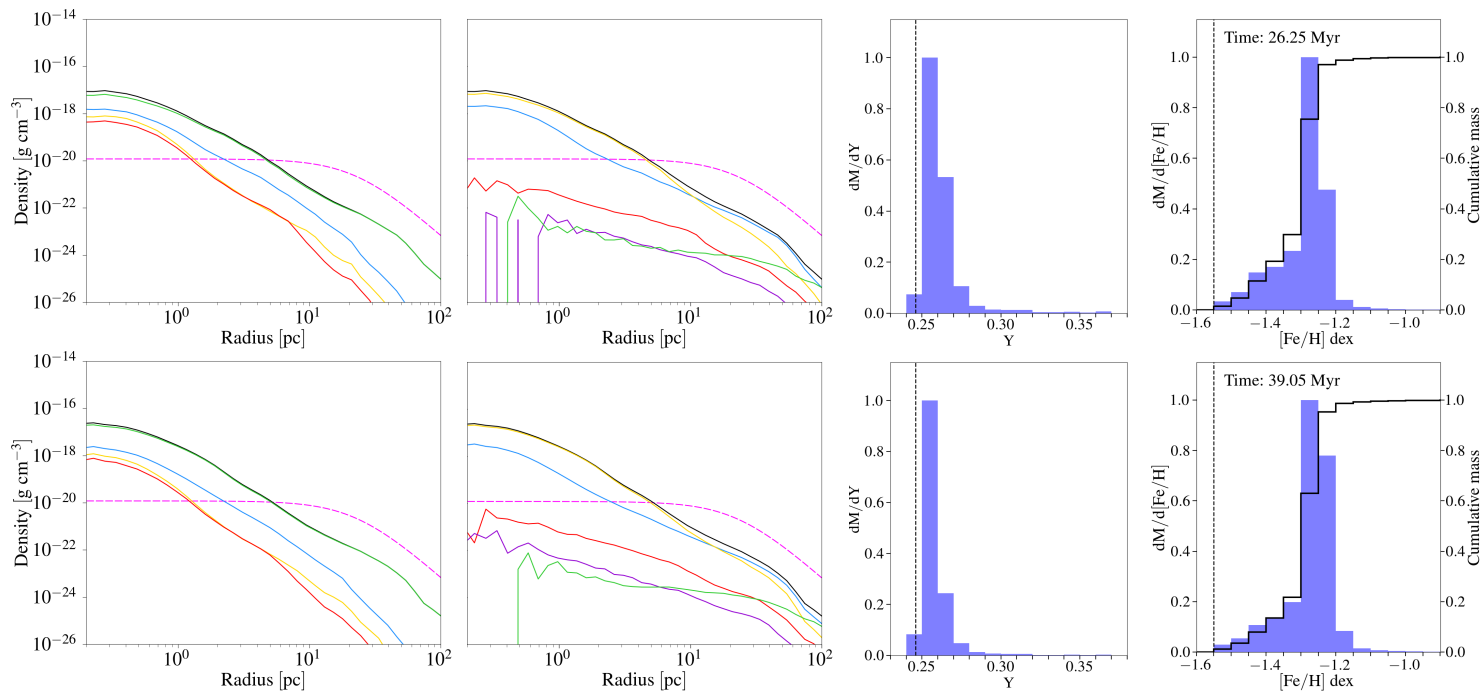


Figure 6.11: Continued

region, while poorly iron-enriched stars represent a small fraction of the total stellar mass.

Later, at 26 Myr, the SG is dominated at all radii by stars with modest helium enrichment. In this scenario, Type Ia SNe are not able to confine the infalling gas like in the low-density models, as visible from the two-dimensional maps. The [Fe/H] mass distribution becomes narrower and peaks around -1.25 dex, whose stars are the dominant component in the central part of the system. The density in such a region is similar to what has been obtained by [Calura et al. \(2019\)](#). With the exception of a large number of Fe-enriched stars formed in our simulation, our results are similar to HD_C19, meaning that SN effects in a dense medium are significantly reduced with respect to the low-density case.

At 39 Myr, the density in the centre of the cluster is slightly increased and the peaks both in the Y and [Fe/H] distributions are sharper than at 26 Myr. The bulk of the stars are mildly enriched in helium but remarkably enriched in iron, in particular in the central region.

The average stellar [Fe/H] ratio of SG stars at the end of the simulation is -1.28 dex, slightly larger than the LD value, with a dispersion of $\sigma_{[\text{Fe}/\text{H}]}^{\text{SG}} = 0.08$ dex. As for the previous two models, we have estimated the internal iron dispersion of the whole cluster assuming that 70% of stars belong to the SG. We derive $\sigma_{[\text{Fe}/\text{H}]} = 0.14$ dex, which agrees with the typical spread in Type II clusters ([Milone et al., 2017](#); [Johnson et al., 2015](#)). As for the helium abundance, its spectroscopic determination is much more challenging than the iron one, therefore, most of the studies rely on photometric determination of the relative helium abundance between multiple populations ([Milone et al. 2015, 2018b; Martins et al. 2021](#) and references therein). We derive the average mass fraction $\bar{Y}_{\text{SG}} = 0.258$ for the SG stars, which leads to a spread between second and first generation of $\Delta Y_{\text{SG-FG}} = 0.012$, in very good agreement with observations. Some of the Type II GCs analyzed by [Milone et al. \(2018b\)](#), in fact, display small helium spreads between the two generations, in some cases even smaller than what we have derived for the HD model.

6.3.4 High-density model with delayed cooling (HD_DC)

As shown in [Figure 6.5](#), in the HD model, 3.5% of all the SNe do not meet the [Kim & Ostriker \(2015\)](#) criterion, hence they are basically not resolved. One potential risk of this result is that, in the HD simulation, the global effects of SN feedback might be underestimated. In order to better assess the impact of this issue on our simulation and to

6.3. Results

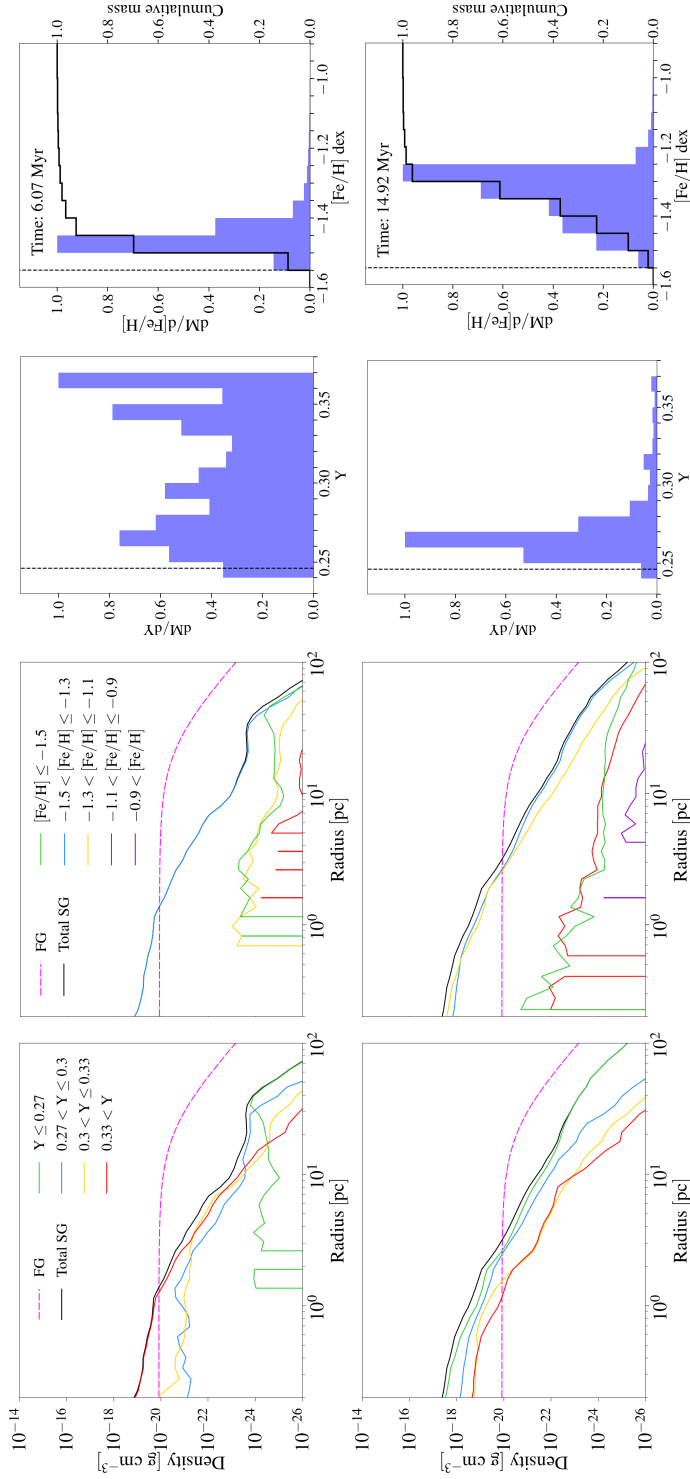


Figure 6.12: First and second columns: total density profile of SG stars at $t = 6, 14, 26, 39$ Myr and density profiles of SG stars for several ranges of the helium mass fraction Y and the $[Fe/H]$ ratio, respectively, for the high-density model with delayed cooling (HD-DC). The FG density profile is also plotted (see the legend for the details). Third and fourth columns: the mass distribution of Y and $[Fe/H]$ ratio, respectively, in the SG stars at the aforementioned evolutionary times (reported in each panel). Other symbols and lines as in Figure 6.7.

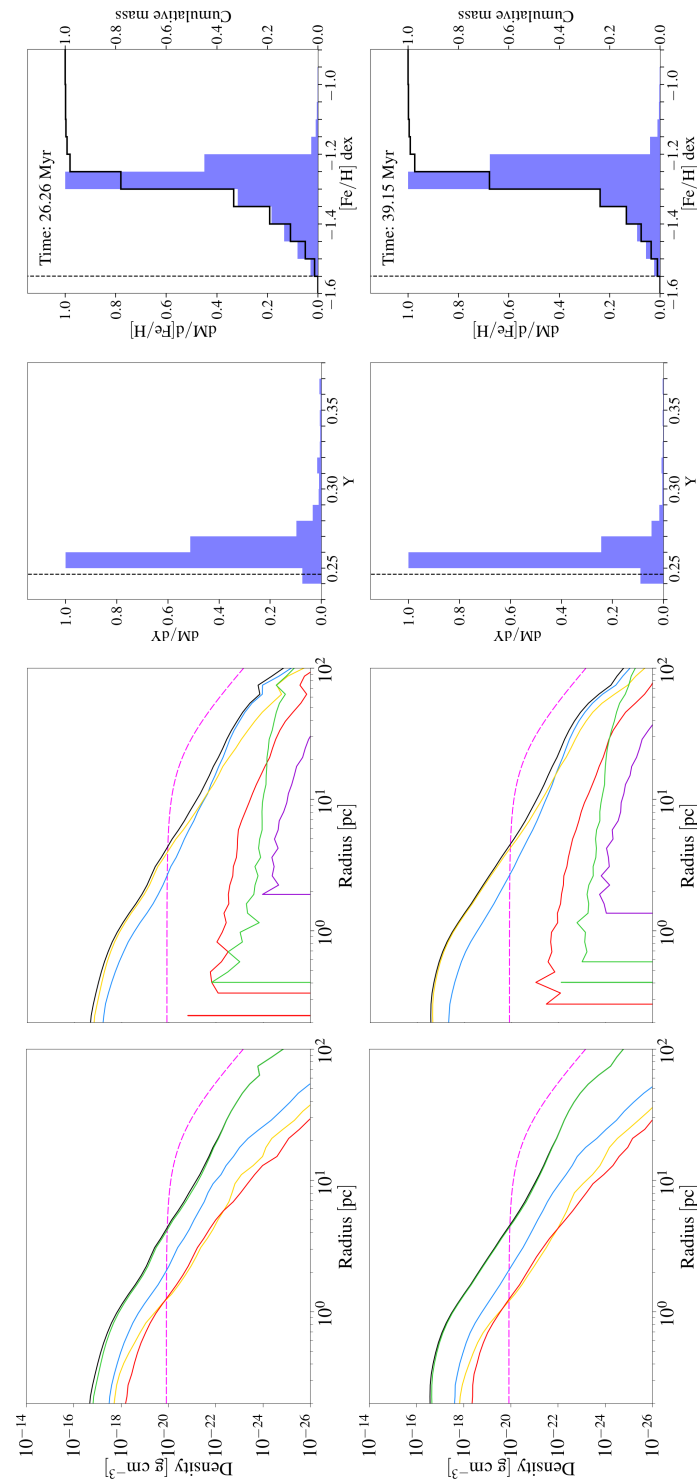


Figure 6.12: Continued

be sure that this does not lead to a severe underestimation of SN feedback, we performed another simulation where radiative cooling has been delayed, i.e. temporarily switched off, in all the locations where SNe explode. We have followed the prescriptions described in [Teyssier et al. \(2013\)](#) to artificially turn off cooling. Here we focus on the density profiles of the SG and on its abundance patterns, as shown in [Figure 6.12](#), which are quantities not particularly sensitive to the stochasticity of processes such as star formation or the local effects of a small number of SN explosions.

As for such quantities, no substantial differences can be seen with respect to the HD model, which denotes that even though some SNe did not satisfy the condition of [Kim & Ostriker \(2015\)](#), the cluster capability to accrete gas and form new stars is not affected. We have also verified that the SNe not meeting the criterion are located far from the centre of the system, and therefore, in the HD_DC scenario, they are not significantly perturbing the gas in the inner regions.

6.4 Discussion

With the exception of [D'Ercole et al. \(2008\)](#) who, by means of 1D simulations, found that a few SN Ia are able to halt the SF immediately after their explosion, our study is the first that addresses the effects of Type Ia SNe on the star formation in GCs through hydrodynamic simulations. It is, however, important to stress that Type Ia SNe do not play any role in regulating the star formation history of FG stars, which is expected to have lasted only a few Myr.

In [Figure 6.13](#), we show the evolution of the cumulative mass in the upper panel and of the SFR in the lower one and compare our results with the ones of [Calura et al. \(2019\)](#).

As discussed in [Section 6.3.1](#), with the short delay time adopted in this work the LD models are strongly affected by SN Ia feedback, which prevents the reaccretion of pristine gas. In the LD model, SN Ia feedback halts the SG star formation at early times, limiting the total mass of the SG population. The infall of pristine gas, which starts at 21 Myr, does not have a significant effect on the evolution of the system, as shown in [Figure 6.6](#) and [Figure 6.7](#).

Focusing on the SFR, it can be seen that its evolution is characterized by three major peaks in the first 15 Myr which are responsible for the peaks in the [Fe/H] mass distribution. Only during these peaks, the SFR is comparable with the one of the model without

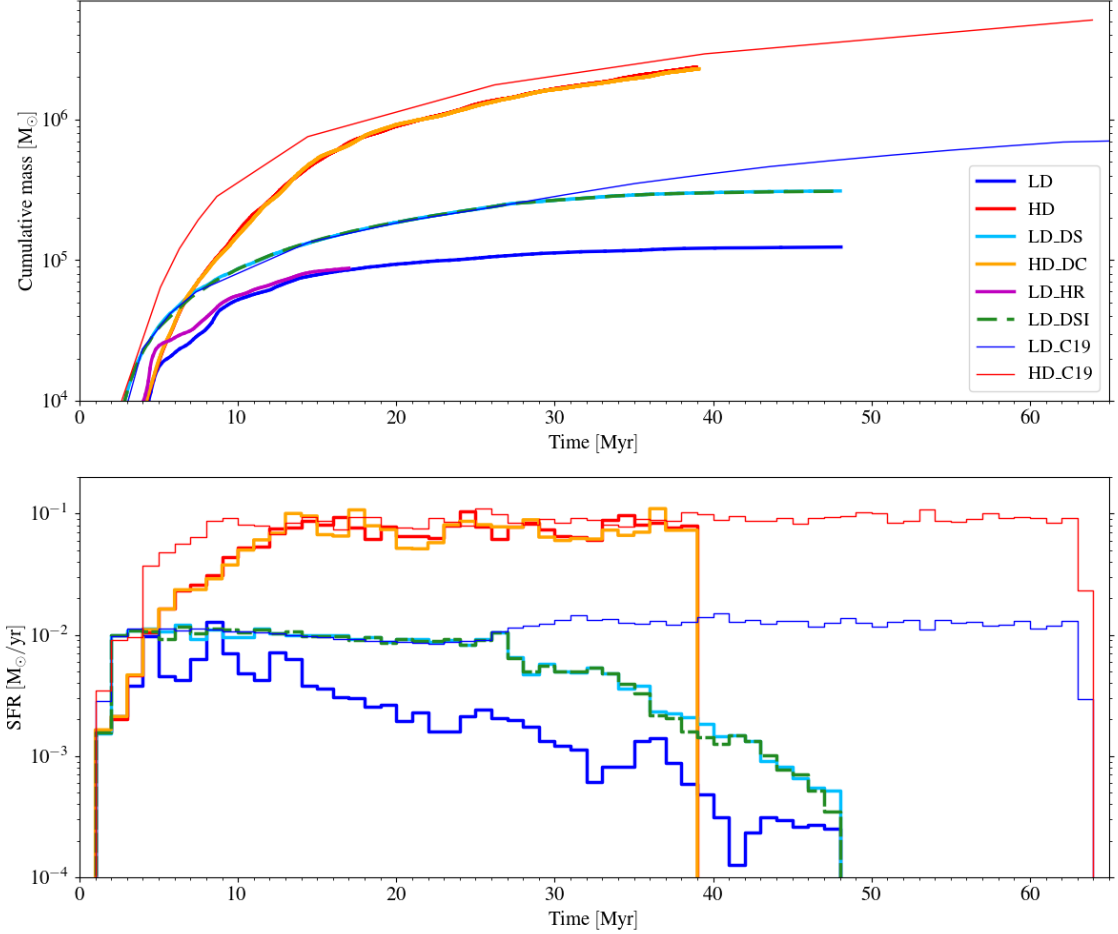


Figure 6.13: Upper panel: evolution of the SG stellar mass for all our simulations. Lower panel: evolution of the SFR for all our models. The blue lines represent the standard low-density models while the red lines the high-density ones. The thin lines show the results obtained by Calura et al. (2019) for their high-resolution simulations. The purple line in the upper panel represents the result of the low-density model at high resolution (LD_HR). The orange lines represent the high-density model with delayed cooling while the light-blue lines represent the low-density model with delayed Type Ia SNe. The green dashed lines represent the low-density model where the infall is switched off once the first SN bubble has reached the negative x boundary.

6.4. Discussion

SNe (LD_C19), while between the peaks it is almost halved. After 15 Myr, the SFR decreases with several peaks at later times which, however, do not affect significantly the total stellar mass.

To test the convergence of our simulations, we have also plotted the time evolution of the cumulative mass for the LD_HR model, namely the low-density LD model at higher resolution (0.3 pc). In the beginning, it deviates from the result obtained at a lower resolution, but this discrepancy has to be ascribed to the stochasticity of the SF process. At later times, in fact, the gap between the two models decreases. This means that, in our simulations, the numerical convergence is satisfactory.

Moving to the LD_DS model, in the beginning, both the cumulative mass and SFR evolution have the same trends of LD_C19, with small differences due to the stochastic method used to associate a mass to each newborn star, as we have described in [Section 4.3.3](#). At around 27 Myr, when the first supernovae start exploding, the SFR starts decreasing significantly, whereas it remains almost constant in the case without SNe.

Once Type Ia start exploding, a comparison of the SFR evolution in the two low-density models shows that an overall smoother SFR decline characterizes the one with delayed SNe. This difference is due to the lower gas density achieved in the LD case, which leads to a more inhomogeneous distribution of gas.

In all our simulations, we have assumed that pristine gas continuously enters the box, even when SNe are reaching the border, as in the low-density models. We have, therefore, tested whether preventing new gas infall after SNe has reached the edge of the box may affect the result. In [Figure 6.13](#), we also report the results obtained for LD_DSI, a model similar to LD_DS, but where we stopped the infall at around ~ 28 Myr. The two models show a similar evolution of the SFR and cumulative mass. We can therefore conclude that our simplistic assumption regarding the infall implementation does not affect the evolution of the system. This is true even as far as the particle density profiles and the mass distribution of Y and [Fe/H] are concerned.

On the other hand, our HD run predicts a lower SFR in the first 10 Myr than HD_C19, namely the case without SNe, which translates into a lower cumulative mass. However, after this first phase, both the SFR and the cumulative mass are similar to the values obtained without SNe. The total stellar mass at the end of our simulation is, in fact, $2.3 \times 10^6 M_{\odot}$ slightly smaller than the one obtained by [Calura et al. \(2019\)](#) at the same evolutionary time. It results that the fraction of the initial FG over the total SG mass is equal to 4,

which is in agreement with previous studies within the AGB scenario ([D'Antona et al., 2013](#); [Ventura et al., 2014](#)). However, it has to be noted that in this model the cumulative mass is still increasing at 39 Myr, therefore this ratio has to be taken as an upper limit.

Finally, the HD_DC model shows a similar evolution of the cumulative stellar mass with the HD model, reaching the same final SG stellar mass. Small variations can be seen instead in the SFR evolution. The reason for such small differences lies in the stochasticity of the star formation whose effects are more evident in the SFR than in the cumulative mass evolution.

To compare our results with observations, we should refer to clusters of the same age, namely young massive clusters (YMCs), which are sometimes regarded as proto-GCs. [Bastian et al. \(2013b\)](#) did not find any evidence of ongoing star-formation in almost 130 YMCs with an age range between 10 Myr and 1Gyr. Similar results have been found by [Cabrera-Ziri et al. \(2014, 2016\)](#), however, YMC younger than 2 Gyr do not show any sign of multiple populations ([Martocchia et al., 2018](#)). A comparison with YMCs of the same age is therefore not feasible. As for the recently discovered high-redshift progenitors of GC, precise measures of their star formation rates and ages are still challenging to derive. To shed important light on the SF history of young GCs, a still star-forming system that already contains multiple populations should be found at high redshift. It is however not achievable with present instruments but perhaps possible in the future, in particular with the ELT with the aid of specific techniques, such as adaptive optics ([Fiorentino et al., 2017](#); [Vanzella et al., 2019](#)).

6.5 Conclusions

In this chapter, we have modelled, by means of grid-based, three-dimensional hydrodynamic simulations, the formation of SG stars in a massive cluster moving through a uniform gas distribution, including the feedback from FG Type Ia SNe, which represents the novelty of our work. Our aim is, specifically, to explore the role of Type Ia SN feedback in determining the duration of SG formation epoch and study the effect of SN Ia ejecta on the chemical properties of the SG population. Our simulations start at the end of the FG Type II SN epoch, when the ejecta of the most massive AGB stars are released in the cluster and the SG formation starts. During this stage, Type Ia SNe belonging to the FG start exploding and external gas with pristine (i.e. same as FG stars) composition is accreted from

6.5. Conclusions

the surroundings. SG stars are, therefore, formed out of a mixed gas, whose composition depends on which of these three sources is dominant. In all our simulations, the cluster is already in place composed only of FG low- and intermediate-mass stars and surrounded by an extended cavity created by the explosions of FG Type II SNe, which is later replenished by the collapse of interstellar gas. We have studied models with two different values for the external pristine gas density: a low-density one $\rho_{\text{pg}} = 10^{-24} \text{ g cm}^{-3}$ and a high-density one $\rho_{\text{pg}} = 10^{-23} \text{ g cm}^{-3}$. Different values of the pristine gas density lead to different infall times, which, in turn, have a significant impact on the chemical composition and the stellar mass of the SG stars. Moreover, in this chapter, we have focused our attention on models with short SN Ia delay times. Given the large uncertainties still present on the timing of Type Ia SN explosions, we have considered two delay time distributions: firstly, we have assumed that SNe Ia start exploding and releasing gas at the beginning of the SG formation epoch together with the most massive AGBs; then, we have performed a simulation, in the low-density scenario, where we have delayed the beginning of the SN Ia by 25 Myr.

Finally, we have run a simulation in which cooling is switched off locally, to assess the possible effects of unresolved SN explosions in high-density regions, a typical artificial phenomenon in numerical simulations.

We summarize here our main results:

- i) In the low-density model (LD) with SN Ia explosions starting at the beginning of the SG star formation epoch, the continuous explosions of Type Ia SNe do not halt the SG formation abruptly, as in 1D simulations by D'Ercole et al. (2008), but they significantly lower the SFR. In the beginning, cooling flows are still formed but Type Ia SNe increasingly diminish their formation. Most of the SG stellar mass is formed, in fact, in the first 20 Myr, before the beginning of pristine gas accretion. SNe explosions confine the infalling gas far from the system and, therefore, no accretion column is formed, at variance with the case without Type Ia SNe. This implies that the AGB ejecta are poorly diluted with pristine gas, a necessary requirement for the AGB scenario in order to reproduce the observed anticorrelations. Moreover, the negligible dilution leads to the formation of a SG dominated by stars with extreme helium enrichment, at variance with observation, making this model not viable.
- ii) In the low-density model with Type Ia SNe starting 25 Myr after the beginning of the SG formation (LD_DS), the SFR decreases after the first Type Ia SN explosions,

but it is always higher than the case without delay. The infall of pristine gas starts before the SN explosions, so some of it is accreted by the system and dilutes the AGB ejecta. At variance with the previous model, not all the stars show an extreme helium enrichment; a small fraction of stars display an intermediate helium enrichment as a result of a dilution and are spatially less concentrated than the extreme population. The accretion of pristine gas continues for about 5 Myr but, eventually, Type Ia SNe confine the gas far from the cluster centre, as it happened in the model without delay. However, dilution is still too low and the spread in helium between the two generations is still much larger than the observed values. Therefore, longer delay times for the onset of Type Ia SNe are needed by the low-density models in order to increase the contribution of the pristine gas and therefore the extent of dilution.

- iii) In the high-density model (HD), Type Ia SNe have only mild effects both on the SFR evolution and on the helium enrichment. The final SG mass is only 1.2 times smaller than without Type Ia SNe. The higher density assumed for the pristine gas prevents Type Ia from confining it in the cluster outer regions, as found in the low-density models. In this model, the pristine gas slows the SN bubble expansion decreasing the growth of their filling factor. In this case, an accretion column is present, even though it is continuously perturbed by SN explosions. The overall continuous accretion of gas leads to a SG dominated by stars with very modest helium enrichment ($\bar{Y}_{\text{SG}} = 0.258$), similar to what is obtained without Type Ia SNe. On the contrary, the SG iron distribution is significantly affected by the presence of Type Ia SNe. Since their bubbles are confined by the infalling gas, most of the iron released during their explosions is retained by the system and then recycled to form new stars, which show a significant iron enrichment. The mean [Fe/H] ratio of SG stars is, in fact, equal to $[\text{Fe}/\text{H}] = -1.28$ dex. Assuming that, after the subsequent evolution, SG stars account for 70% of the whole cluster, we derive an internal iron dispersion of $\sigma_{[\text{Fe}/\text{H}]} = 0.14$ dex, in good agreement with the typical spread observed in Type II GCs.
- iv) No substantial difference has been found between the standard high-density model and the one with delayed cooling, meaning that, overall, the impact of Type Ia SNe is not artificially suppressed by cooling.

It has to be noted that in all our simulations we do not include ionizing feedback from SG stars which could lead to a steeper decrease of the SFR ([Chantereau et al., 2020](#)).

6.5. Conclusions

Massive stars belonging to the SG, if any, should contribute to heating up the ISM further, reducing the amount of gas eligible for star formation. However, the SG formation is supposed to take place in an environment already crowded by the FG stars, a scenario in which the SF process is still unexplored (Renzini et al., 2015). The shape of the IMF characterizing the SG is not known so far, even though some studies have suggested that it could be truncated at around $m \sim 8 - 10 M_{\odot}$ (D'Ercole et al., 2010; Bekki, 2019).

Our simulations have shown that the SG formation can continue during the Type Ia SNe epoch, and the ejecta of these supernovae can contribute to the mix of gas out of which SG stars form. The formation of SG stars from mixed gas of SN Ia ejecta and AGB gas revealed by our study indicates a possible avenue for the formation of Galactic GC with multiple populations characterized by a spread in Fe; these clusters represent about 20 percent of the Galactic globular cluster system (see Marino et al. 2015; Johnson et al. 2015; Milone et al. 2017; Marino et al. 2019a) and have been shown to host stellar populations enriched also in s-process elements which could be produced by low-mass AGBs (see e.g. D'Antona et al. 2016). Moreover, as shown by Gratton et al. (2019), Type II GCs are relatively massive, which might suggest a correlation between iron enrichment and cluster mass. We intend to further extend the initial set of simulations presented in this chapter to study a broader range of initial conditions and explore the possible dynamics and formation history of these complex clusters.

Chapter 7

MULTIPLE STELLAR POPULATION MASS LOSS IN GALACTIC GLOBULAR CLUSTERS

When you ain't got nothing, you got nothing to lose

Like A Rolling Stone, Bob Dylan

Different populations do not differ only in their chemical abundances but also in their structural and kinematical properties, suggesting a deep connection between the origin of the chemical imprints in MPs and the formation and the subsequent dynamical evolution of the whole cluster.

Although the long-term dynamical evolution these systems have undergone is gradually erasing the structural and kinematical differences that MPs had at birth, dynamically young clusters may retain the memory of the original differences between MPs until the present day, in particular in their outskirts (Vesperini et al., 2013). By means of observational data analysis, supported by N -body models, Dalessandro et al. (2019) have shown the tight connection between the relative degree of concentration of different populations and the evolutionary stage of the cluster. In particular, larger differences in the spatial radial distributions between distinct populations are found in clusters that are dynamically young and have experienced lower mass loss, as depicted in Figure 7.1. The difference between the two populations is not restricted to the spatial distribution. Observational studies have revealed that second population stars are generally characterized by a more radially anisotropic velocity distribution (Richer et al., 2013; Bellini et al., 2015, 2018; Libralato et al., 2019), a more rapid rotation (Lee, 2015, 2017; Cordero et al., 2017; Lee,

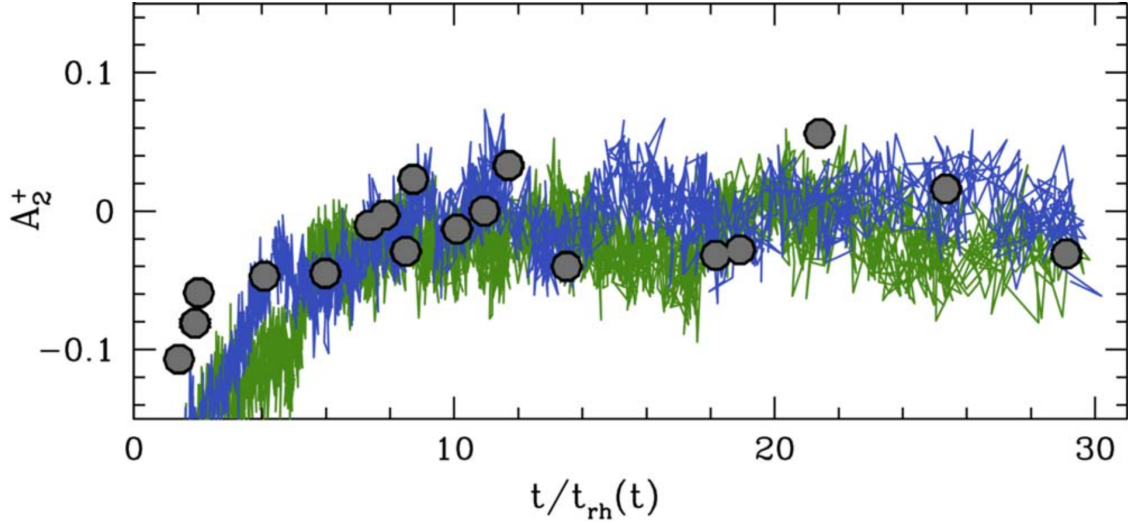


Figure 7.1: Distribution of the A_2^+ parameter as a function of t/t_{rh} . The A_2^+ parameter is calculated as the area enclosed between the cumulative radial distributions of the two populations, and therefore reveals the degree of mixing. The quantity t_{rh} is the half-mass relaxation time, which determines the dynamical age of the system. The grey dots represent the observed clusters, out of which one belongs to the Small Magellanic Cloud, one to the Large Magellanic Cloud, and the rest to the Milky Way. The blue and green lines are the results of N -body simulations for a second population 5 ad 10 times more centrally concentrated than the first population, respectively. Taken from [Dalessandro et al. \(2019\)](#).

2018; [Dalessandro et al., 2019](#); [Kamann et al., 2020](#); [Cordoni et al., 2020a](#); [Szigeti et al., 2021](#)), a lower fraction of binaries ([D’Orazi et al., 2010](#); [Lucatello et al., 2015](#); [Milone et al., 2020b](#)) and are much more concentrated ([Norris & Freeman, 1979](#); [Sollima et al., 2007](#); [Lardo et al., 2011](#); [Milone et al., 2012](#); [Richer et al., 2013](#); [Cordero et al., 2014](#); [Simioni et al., 2016](#); [Dondoglio et al., 2021](#)) than the first population.

In addition to the different degrees of variations in the structural and kinematical properties between MPs, more massive clusters are generally found to host a higher fraction of second-population stars (up to 90%) than lower mass ones (down to 30-40%) ([Milone et al., 2017](#); [Zennaro et al., 2019](#); [Dondoglio et al., 2021](#)). This quantity is the result of a complex combination of formation history and evolutionary effects since, due to the differences between the two populations at birth, they will experience distinct dynamical evolution and, therefore, distinct mass loss rates, which will imply a change of the fraction of SG with time.

The physical processes modulating the mass loss in stellar clusters are manifold. Firstly,

two-body relaxation was found to gradually set up a Maxwellian velocity distribution, which leads loosely bound stars to overcome the cluster escape velocity (Ambartsumian, 1938; Spitzer, 1940). Later, Chernoff & Weinberg (1990) followed the evolution of multi-mass clusters with a tidal cut-off, driven by two-body relaxation and stellar evolution mass loss. They found that the combination of these two processes leads to a stronger mass loss than the sum of the two independent contributions. The dynamical evolution of a stellar cluster is, however, affected by many other factors, such as binarity (Tanikawa & Fukushige, 2009; Fujii & Portegies Zwart, 2011), tidal fields (Baumgardt & Makino, 2003), gravitational and tidal shocks (Gnedin & Ostriker, 1997; Vesperini & Heggie, 1997), mass segregation (Baumgardt et al., 2008; Haghi et al., 2014) and the presence of dark remnants (Contenta et al., 2015; Banerjee & Kroupa, 2011; Giersz et al., 2019). All these quantities are, however, known for several present-day clusters, but not for star-forming clusters, posing challenges in setting the initial conditions for simulated clusters. Such uncertainty on the initial values affects also many other parameters, such as the initial mass of the cluster (and also its radial distribution), which would be vital to understand how clusters form and dynamically evolve. Indirect derivations can be obtained starting from clusters' present-day mass and the fraction of enriched stars. If the mass of the FG is assumed to be comparable to the present-day mass of GCs, one ends up with a mass released by the FG polluters that is much lower than the mass of SG stars observed today, which leads to the so-called "mass budget problem". To overcome this problem, it is generally assumed that the cluster, and therefore the FG, was much more massive, between 5 and 20 times (Decressin et al., 2007; D'Ercole et al., 2008; Schaefer & Charbonnel, 2011; Cabrera-Ziri et al., 2015), at its birth but then, during the evolution, most of the FG stars (up to $\sim 95\%$) were lost, so the observed relative number of SG and FG is still reproduced.

Few attempts have been carried out in order to determine whether, during the long-term evolution, clusters are able to lose a significant fraction of FG stars and then reproduce, after a Hubble time, the observed clusters' features. The pioneering work on the topic was done by D'Ercole et al. (2008), who performed a series of N -body simulations in the AGB framework, concluding that a cluster with a more concentrated SG generation loses a substantial number of FG stars, at variance with the SG ones, deriving fractions of main sequence stars (MS) $f_{MS} = N_{SG,MS}/N_{FG,MS}$ in agreement with observations.

Later, Bastian & Lardo (2015) found no correlation between the present-day fraction

of SG, which lies between 50 to 90%, and various cluster parameters such as the Galactocentric distance, the metallicity, and the cluster mass. They also showed that, combining the observational data with the results of the N -body studies of [Baumgardt & Makino \(2003\)](#) and [Khalaj & Baumgardt \(2015\)](#), no match was found, concluding that neither gas expulsion nor the effect of tidal fields could lead to the present-day fraction of SG.

By means of Monte Carlo simulations, [Vesperini et al. \(2021\)](#) and [Sollima \(2021\)](#) have studied the dynamical evolution of a cluster composed of two populations and a mass of $\sim 10^6 M_\odot$. Similarly to [D'Ercole et al. \(2008\)](#), they find that the cluster loses more FG stars and reaches, after 13 Gyr, the typical values of SG fraction observed in present-day GCs. Similar results were obtained by [Sollima et al. \(2022\)](#), who focused on the binary fractions of the populations. They concluded that the present-day SG binary fraction can be used to constrain the initial concentration of SG stars, providing a relation between the initial size of the SG and total cluster mass.

From E-MOSAICS cosmological simulations, [Reina-Campos et al. \(2018\)](#) explored the impact of dynamical cluster disruption of multiple stellar populations deriving the degree of mass loss and the fraction of enriched stars as a function of cluster mass, Galactocentric distance, and metallicity. They found discrepancies with observations and therefore concluded that mass loss is unlikely to have a strong impact on shaping the present-day GCs. They also derived that, to reconcile the observations, a significantly larger half-mass radius has to be assumed at birth, and a higher initial SG fraction than the currently adopted ones would be necessary.

Although the fraction of enriched stars is a very strong constraint widely used to compare simulated clusters with observed ones, other fundamental pieces of information can be extracted from the unbound stars ([Arunima et al., 2023](#)). [Larsen et al. \(2012\)](#) found that around 1/5 of the metal-poor stars in the Fornax dwarf spheroidal galaxy belongs to the four GCs, meaning that these GCs could have been, at most, 5 times more massive at their birth, posing a strong upper limit on the fraction of stars that could have been lost by GCs. Fornax GCs have been found to resemble the Galactic ones ([Larsen et al., 2014](#)), and therefore they could have shared a common origin and evolution. Based on the stellar chemical composition, several studies have been carried out aimed at determining the contribution that GCs could have given to the formation of the Galactic halo ([Carretta et al., 2010](#); [Martell & Grebel, 2010](#); [Martell et al., 2011](#); [Ramírez et al., 2012](#); [Martell et al., 2016](#)). Recently, [Koch et al. \(2019\)](#) have analyzed the spectra of halo field giant stars. They found

that 2% of the stars in the sample show the “anomalous” chemical composition typical of SG stars, in agreement with the previous investigations. In addition, they derived that 11% of the stars in the Galactic halo were formed in GCs. This quantity is however strongly affected by the adopted mass loss rate in the early phases and the number of completely dissolved clusters, reaching up to 40 – 50% when assuming a mass loss factor, i.e. the ratio between initial and final cluster mass, greater than 10 ([Vesperini et al., 2010](#)). Both the fraction of field SG stars and field GC stars are extremely precious, providing further constraints to the models, not only on cluster scales, but also at larger ones, to understand how the Galaxy assembly proceeded.

In this Chapter, we intend to study the long-term evolution of a globular cluster with a mass $M \sim 10^7 M_{\odot}$, extending the work of [Calura et al. \(2019\)](#) which is focused on the early phases, when SG stars have been formed, by means of a series of direct N -body simulations. The cluster is composed of two stellar populations, and it is assumed to orbit the Milky Way. From the results derived by [Calura et al. \(2019\)](#), confirmed also by [Lacchin et al. \(2022\)](#), the fraction between FG and SG is larger than the present-day ones, but the mass loss that these clusters should undergo to match observations is not as dramatic as often suggested in the literature. Here we aim at quantifying the mass loss factors that are needed to reproduce the observed SG fraction for such a massive GC. The cluster is located in the disk of the Milky Way and, therefore, likely belongs to the in-situ population. There are various reasons why studying disk GCs is important. First, the distribution of metal-rich MW GCs are more concentrated and flatter than the metal-poor component, and generally, they are associated with the thick disc and bulge populations ([Armandroff & Zinn, 1988](#); [Armandroff, 1989](#); [Zinn, 1985](#); [Minniti, 1995](#); [Côté, 1999](#); [Van Den Bergh, 2003](#); [Bica et al., 2006, 2016](#)). In addition, disc GCs, which now constitute almost one-third of the total MW GCs ([Harris, 2010](#)), could have been much more in the past. Field stars showing GC-like features have been discovered in the inner Galaxy ([Schiavon et al., 2017](#); [Fernández-Trincado et al., 2022](#)), a detection supported by simulations showing that tidal effects in the inner regions of MW-like galaxies could have gradually destroyed disc GCs, decreasing their population ([Renaud et al., 2017](#)). Lastly, kinematical heating due to several accretion events could have also deprived the disc of GCs, which would now be part of the inner halo ([Kruijssen, 2015](#)).

We aim at determining the degree of mass loss in the two different stellar components, to verify whether a significant mass loss, as the one required to solve the mass budget

problem, is feasible and whether the final cluster is compatible with the observed GCs. We take into account both the stellar evolution, the tidal effects of the Galactic potential, and primordial segregation.

The Chapter is organized as follows: in Section [Section 7.1](#), we describe the model we are adopting and the novelty introduced in the present work. [Section 7.2](#) deals with the results we have obtained for our sets of simulations. In [Section 7.3](#), we discuss the outcomes of the simulations and compare them with the literature and observations. Finally, we draw our conclusions in [Section 7.4](#).

7.1 Models and Methods

We study the internal evolution of a series of cluster models, including either one or two stellar populations, and neglecting or taking into consideration the effects of star formation and stellar evolution. In the next subsections, we provide details on the initial set-ups adopted for our simulations, illustrating the assumptions we adopted depending on the characteristics of the model and the phenomena that we explored.

7.1.1 Description of the code

We ran our simulations using an updated version of NBSymple ([Capuzzo-Dolcetta et al., 2011](#)), a direct and symplectic N -body code parallelized on GPUs. Several versions of this code are available and have been used to study various aspects of GCs evolution in the Galactic potential (see e.g. [Mastrobuono-Battisti et al. 2012](#); [Sollima et al. 2012](#); [Leigh et al. 2014](#); [Mastrobuono-Battisti et al. 2019](#)). This new version includes a star formation and stellar evolution routine for the first and second generations separately. The softening length adopted to avoid close encounters is equal to the mean interparticle distance within the half-mass radius and it is calculated separately for the first and second generations. Our choices for the softening length and the number of particles used to represent the clusters are motivated by the computational limitations, as we aimed at 12 Gyr long simulations. The mass loss due to stellar evolution is instantaneously removed and, therefore, energy and angular momentum are not conserved.

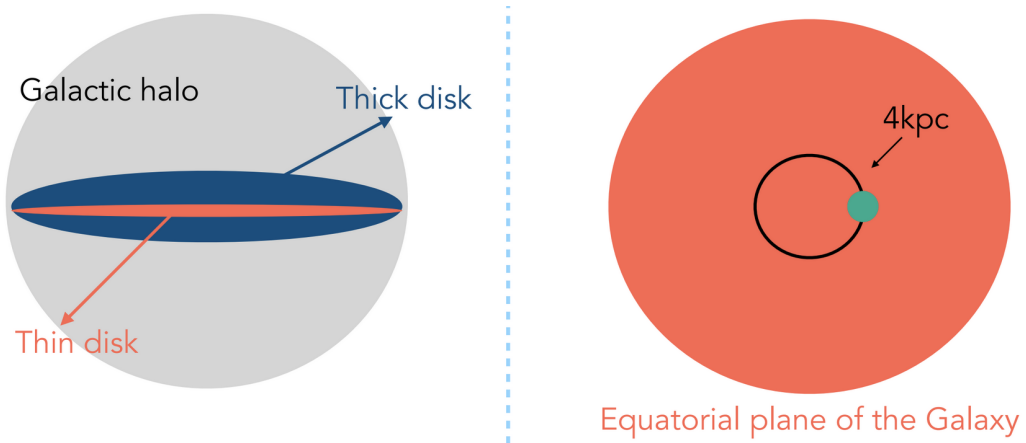


Figure 7.2: Schematic representation of the Galaxy model adopted for the simulations, on the left, includes the presence of both the thick and thin disk plus the halo, while the effects of the bulge are here not considered. On the right, it is shown the GC model, where the simulated cluster is located at 4 kpc from the Galactic centre and is assumed to orbit on the plane of the disk. Credits: Alessandra Mastrobuono-Battisti.

7.1.1.1 Galactic potential model

Our Galactic model consists of a dark matter halo with both a thin and thick disk, as shown in the left panel of Figure 7.2 (see also Mastrobuono-Battisti et al. 2019). The functional forms of these components are taken from Allen & Santillan (1991) with the parameters from Model II of Pouliasis et al. (2017), which aims at reproducing the actual MW. Such a model is able to reproduce various observables, such as the rotational curve, thin and thick disk scale lengths and heights, and stellar density in the solar neighborhood. The bulge is considered part of the Galactic disk, so it is not represented as an independent component (Di Matteo, 2016). The mass assumed for the halo is $2.07 \times 10^{11} M_{\odot}$ with a scale height of 14 kpc. The thick disk has a mass of $3.91 \times 10^{10} M_{\odot}$ with radial and vertical scale length of 2 kpc and 800 pc, while the thin disk has a mass of $3.68 \times 10^{10} M_{\odot}$, a radial scale length of 4.8 kpc and a scale height of 250 pc.

7.1.2 Single stellar population models

Our single population clusters are modelled using the King (1966) profile, adopting different values for the half-mass radius, r_h , and for the dimensionless central potential W_0 (Binney & Tremaine, 2008), which varies between 2 and 7. In this way, we explore the

behaviour of both loose and dense clusters. The cluster initial mass is, for all models, $10^7 M_{\odot}$, since we aim at modelling very massive clusters, like the ones in [Calura et al. \(2019\)](#) and [Lacchin et al. \(2021, 2022\)](#). The initial positions and velocities of the particles, in the absence of the external gravitational galactic potential, are derived using the software NEMO, through the *mkking* routine ([Teuben, 1995](#)). Our clusters are single-mass models (i.e. all stellar particles have the same mass) and are represented either with $N = 102400$ or $N = 25600$ particles, meaning that each particle is significantly more massive than a star. This choice is due to current computational limitations in running direct N -body simulations of systems with 10^6 or more particles for a timespan of 12 Gyr. Each cluster in our simulation starts with an actual mass that is slightly lower than $10^7 M_{\odot}$. Since the simulation starting point is set after the explosion of FG core-collapse supernovae (i.e. at a time equal to $t_0 = 30$ Myr), we remove 16% of the initial cluster mass reaching $M_0 = 8.4 \times 10^6 M_{\odot}$, to mimic the effect of the death of massive stars. This value is the mass return fraction due to the evolution of stars with a mass larger than $8 M_{\odot}$ for the [Kroupa \(2001\)](#) initial mass function (IMF) with a final-to-initial mass relation from ([Agrawal et al., 2020](#)).

We explore both clusters with and without primordial mass segregation. Primordial mass segregation has been found to have a significative effect on the cluster mass loss due to the cluster expansion in response to the massive star mass loss, happening preferentially at the cluster centre ([Vesperini et al., 2009; Haghi et al., 2014](#)). In case the clusters are mass segregated, we use the software McLuster ([Küpper et al., 2011](#)) to calculate the radius comprising all the massive stars in a primordially segregated model. We then remove the mass that is lost due to the explosion of stars more massive than $8 M_{\odot}$ within this radius, keeping a King profile for the density. All the models orbit the Galaxy in the plane of the disk at a galactocentric distance of 4 kpc, as shown in the right panel of [Figure 7.2](#). This is the same distance assumed by [D'Ercole et al. \(2008\)](#), albeit using a simpler model, including a point-like mass located at the galaxy centre. It is worth mentioning that in our model, the mass enclosed within a radius of 4 kpc, derived integrating the density distribution, is $4.0 \times 10^{10} M_{\odot}$. This is in very good agreement with the mass assumed for the point- mass galaxy potential assumed by [D'Ercole et al. \(2008\)](#). The clusters are tidally filling, i.e. their tidal radius, r_t , is equal to the distance at which the cluster potential and the Galactic potential have the same value ([von Hoerner, 1957; Baumgardt & Makino, 2003; Webb et al., 2013](#)). As the tidal radius is fixed to 200pc, the core radius and half-

7.1. Models and Methods

Table 7.1: Models with neither stellar evolution nor SG stars run in this work. The initial mass of each simulated cluster is $M_0 = 8.4 \times 10^6 M_\odot$, after the removal of 16% of its mass.

Model ^(a)	W_0 (M_\odot)	r_h (pc)	Segregation	Number of particles	Softening (pc)	$f_{mass\ loss}$
n7N	7	23	N	25600	1.65	0.44
n7Y	7	23	Y	25600	1.65	0.58
n5N	5	37	N	25600	2.57	0.50
n5Y	5	37	N	25600	2.57	0.57
n2N	2	60	N	25600	4.20	0.72
n2Y	2	60	Y	25600	4.20	0.79
N2N	2	60	N	102 400	2.65	0.57

(a) Model name: n/N = small/large number of particles + W_0 + N/Y = non-segregated/segregated.

Columns: 1) Name of the model; 2) the adimensional central potential parameter W_0 of the FG; 3) half-mass radius of the FG; 4) primordial segregation of the FG (N = not segregated, Y = segregated), 5) number of particles N_{tot} , 6) softening, 7) mass loss fraction defined as $f_{mass\ loss} = (M_{ini} - M_{fin})/M_{ini}$.

mass radius of each of the models vary depending on the value of the W_0 parameter.

7.1.2.1 Without long-term stellar evolution

We initially modelled clusters hosting a single stellar population, that are only affected by dynamical effects (i.e. not considering any long-term stellar evolution effect). To start with the same cluster mass, we here remove the 16% of the initial mass, as we will do in all the other models. The details on the models are reported in Table 7.1.

7.1.2.2 Adding long-term stellar evolution

In our second set of models, we still have only one stellar population, but we considered the effects of long-term stellar evolution. This is done through a mass return fraction given by:

$$m_{loss}(t) = m_p(t) - m_p(t)[b_0 + b_1 \log(t+t_0) + b_2 \log^2(t+t_0)] + m_p(t)[b_0 + b_1 \log(t_0) + b_2 \log^2(t_0)] \quad (7.1)$$

where $t_0 = 0.03$ Gyr to take into account that we simulate our system starting from 30 Myr. This represents an analytical fit to the stellar mass return of the low and intermediate-mass stars models of [van den Hoek & Groenewegen \(1997\)](#).

Table 7.2: Models with simplified stellar evolution and without SG stars run in this work. The initial mass of each simulated cluster is $M_0 = 8.4 \times 10^6 M_\odot$, after the removal of 16% of its mass.

Model ^(a)	W_0 (M_\odot)	r_h (pc)	Segregation	Number of particles	Softening (pc)	$f_{mass\ loss}$
n7Ne	7	23	N	25600	1.65	0.63
n7Ye	7	23	Y	25600	1.65	0.74
n5Ne	5	37	N	25600	2.57	0.70
n5Ye	5	37	Y	25600	2.57	0.79
n2Ne	2	60	N	25600	4.20	1.00
n2Ye	2	60	Y	25600	4.20	1.00
N2Ne	2	60	N	102400	2.65	1.00

^(a) Model name: Model name: n/N = small/large number of particles + W_0 + N/Y = non-segregated/segregated + e = with stellar evolution.

Columns: 1) Name of the model; 2) W_0 of the FG; 3) half-mass radius of the FG; 4) primordial segregation of the FG (N = not segregated, Y = segregated), 5) number of particles N_{tot} , 6) softening, 7) mass loss fraction defined as $f_{mass\ loss} = (M_{ini} - M_{fin})/M_{ini}$.

The details for these models can be found in Table 7.2.

7.1.3 Two stellar populations models

In our third set of simulations, we finally added the SG, embedded inside the FG component. All the particles in the system have the same mass, for a total number of particles $N_{tot} = 102400$. Both components are spherical and represented by King (1966) models. The FG component, modelled with N_{FG} particles, is a King model with $W_{0,FG}$ ranging between 2 and 7, a total initial mass of $M_{FG}^{ini} = 10^7 M_\odot$ and a tidal radius of 200 pc, to mimic a tidally filling system. As before, we build the initial positions and velocities using the software NEMO, through the *mkking* routine (Teuben, 1995).

The SG component is a King model where we vary $W_{0,SG}$ from 5 to 7, its mass from $M_{SG}^{ini} = 7 \times 10^5 M_\odot$ to $3 \times 10^6 M_\odot$ (as a consequence, also the number of SG particles $N_{SG} = N_{tot} - N_{FG}$ will change from 7877 to 26947, respectively) and a half-mass radius from 1 to 6 pc. We vary the SG mass to test different initial SG fractions. We vary the velocity dispersion of the SG as well, to explore the effect of this parameter on the cluster's mass loss rate. We run models with different central velocity dispersion equal to 0 km s^{-1} , 10 km s^{-1} and to the velocity dispersion of the generated King model where, for the first

7.2. Results

two values, we rescaled the velocities derived for the King. In the third case, the SG is in equilibrium as an isolated system, while, in the other cases, it is radially out of equilibrium and it tends to collapse and readjust after a phase of violent relaxation.

As before, the mass of the FG at the beginning of the simulation is slightly lower than its initial mass, since 16% of the mass is removed due to the explosions of core-collapse supernovae. After that, the FG starts to evolve dynamically as FG stars lose their mass due to stellar evolution, with a cumulative mass return fraction given by [Equation 7.2](#).

The SG appears after 10 Myr from the beginning of the simulation (i.e. at a time of $t_1 = 40$ Myr) and grows its mass at a constant star formation rate of $0.05 M_{\odot} \text{ yr}^{-1}$ (for $M_{\text{SG}}^{\text{ini}} = 3 \times 10^6 M_{\odot}$; $0.01 M_{\odot} \text{ yr}^{-1}$ for $M_{\text{SG}}^{\text{ini}} = 7 \times 10^5 M_{\odot}$) for a total of 60 Myr. To avoid the contribution of SG massive stars, which would chemically pollute the AGB ejecta with e.g. iron, we assume, as it is generally done in the AGB scenario, a truncated SG IMF composed only of stars with masses smaller than $8 M_{\odot}$ (see [D'Ercole et al. 2010](#); [Bekki 2019](#)). SG stars are kept fixed with respect to the cluster centre of density while they are forming. Once the total initial mass of the SG is reached, they start to evolve dynamically. After an additional 30 Myr, the SG has accumulated enough mass and its stars start evolving following a cumulative mass return fraction law:

$$m_{\text{loss}}(t) = m_p(t) - 1.27133m_p(t)[b_1 \log(t - t_1 + t_0) + b_2 \log^2(t - t_1 + t_0)] + 1.27133m_p(t)[b_1 \log(t_0) + b_2 \log^2(t_0)] \quad (7.2)$$

where t_1 is expressed in Gyr.

The mass is added or removed in equal measure from each star in the relevant component of the cluster.

7.2 Results

In this section, we present the results obtained from our simulations. First, we describe the outcomes of models where the FG only is modelled and stellar evolution is not taken into account. Secondly, we report the results of the runs assuming stellar evolution but still with the FG component only. Lastly, the outcomes of the simulations with both stellar evolution, FG, and SG components are described.

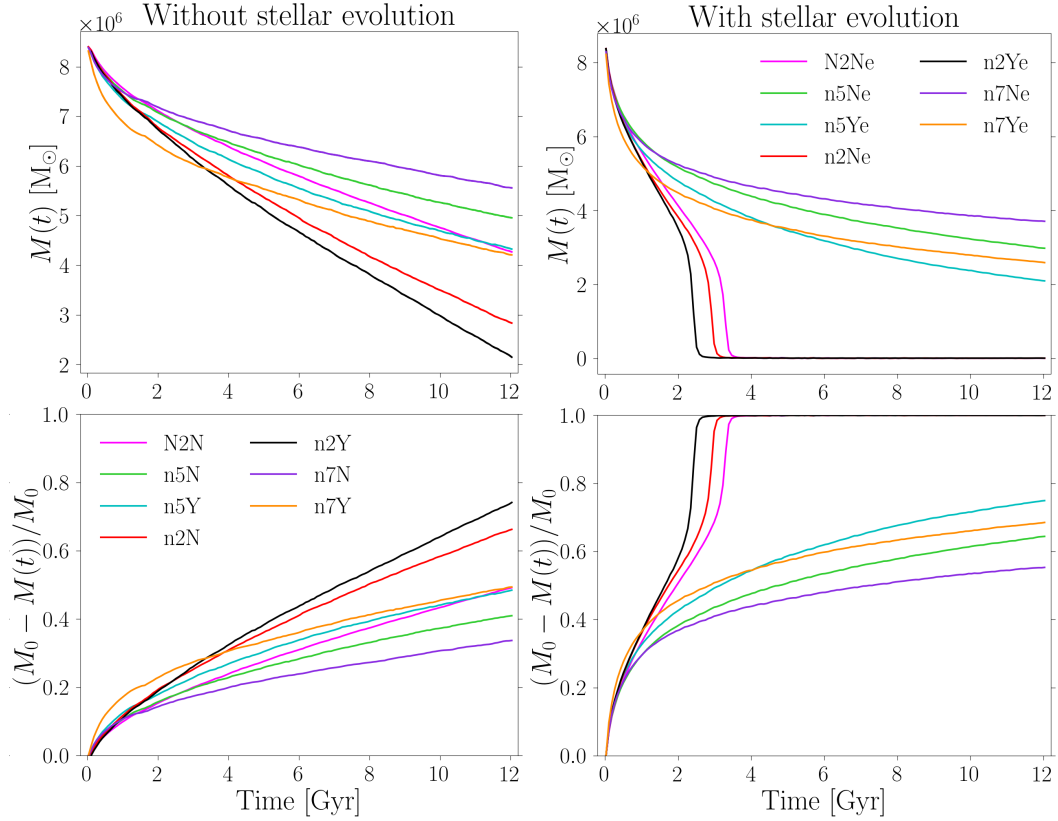


Figure 7.3: Mass (top) and mass loss (bottom) as a function of time. The models with the FG only and without stellar evolution, listed in Table 7.1, are shown on the left, while the models with only FG but where stellar evolution is taken into account, listed in Table 7.2, are shown on the right.

7.2.1 Models with single stellar population

7.2.1.1 Models without stellar evolution

We have first studied the long-term evolution of a massive cluster, $M_{ini} = 10^7 M_{\odot}$, composed only by the FG. At the beginning of the simulation, the stellar mass is equal to $M_0 = 8.4 \times 10^6 M_{\odot}$, which represents the mass of low and intermediate-mass stars plus the remnants of the massive ones left in the system after massive stars have gone off.

In Table 7.1, we summarize the main parameters of our models together with the resulting mass loss fraction $f_{mass\ loss} = (M_{ini} - M_{fin})/M_{ini}$, with M_{fin} the final mass of the whole cluster, at the end of each simulation. Stellar evolution is not taken into account

for the moment. [Figure 7.3](#) shows the evolution of the cluster mass, on the top left, and of the normalized mass loss, at the bottom left. As one can expect, the shallower the potential well, and therefore the lower the values of W_0 , the greater the mass loss at the end of the simulation. However, model $n7Y$, which is characterized by $W_0 = 7$, is losing more mass than models with lower W_0 values, in the first few Myr. The higher concentration coupled with initial segregation is responsible for this behavior, which affects also other models described throughout the Chapter. Initial segregation is, in general, leading to a stronger mass loss since segregated systems will have, after the death of massive stars, a larger r_h , making the system less bound. Apart from varying physical parameters, we have also changed the number of particles from 25600 to 102400 retrieving that, when more particles are used, as in $N2N$, the cluster loses less mass as a result of both the deepening of the potential well due to the smaller softening and the longer relaxation time, which scales as $N/\log(N)$, with N the number of particles.

7.2.1.2 Models with stellar evolution

[Figure 7.3](#) shows, on the right, the mass (top) and normalized mass loss (bottom) evolution for the models listed in [Table 7.2](#), where stellar evolution is taken into account. For comparison, the initial conditions we have here adopted are the same as for the models without stellar evolution described above.

As expected, mass removal due to stellar evolution leads to a shallower cluster potential well and, therefore, spurs subsequent mass loss, in the form of lost stars. For models with $W_0 = 2$, the addition of stellar evolution leads to the dissolution of the cluster after ~ 3 Gyr, due to the already shallow potential at the beginning of the simulation. In all other cases, stellar evolution is not so catastrophic, even though the final mass of the cluster is significantly smaller, from one-third to half, with respect to the case without stellar evolution. As before, initially segregated clusters suffer a stronger mass loss than not segregated ones.

7.2.2 Models with second generation stars

In [Table 7.3](#), we report the initial conditions of the thirteen simulations we have performed, taking into account the stellar evolution and with the SG, together with the final values of masses, half mass radii, the fraction of enriched stars within the cluster (e.g. considering

Table 7.3: Models with both simplified stellar evolution and SG stars. The initial FG mass of each simulated cluster is $M_0 = 8.4 \times 10^6 M_\odot$, after the removal of 16% of its mass. Masses are all in terms of 10^5 .

Model ^(a)	Initial						Final							
	$W_{0,FG}$	$r_{h,FG}$	Segr	M_{SG}	$V_{0,SG}$	$r_{h,SG}$	M_{FG}	M_{SG}	$f_{SG}^{r_{h,tot}}$	f_{SG}^{lost}	$r_{h,FG}$	$r_{h,SG}$	$r_{h,tot}$	$\log(\rho_c)$
				M_\odot		pc		M_\odot	pc	pc	pc	pc	pc	M_\odot/pc^3
5N7M3.70	5	37	N	30	7	3.7	35.4	18.0	0.44 (0.34)	0.16	25.0	12.5	19.9	3.61
5N7M3.710	5	37	N	30	7	3.7	33.6	18.5	0.49 (0.35)	0.15	25.5	10.1	18.9	4.08
5N7M3.7K	5	37	N	30	7	3.7	36.3	19.8	0.49 (0.35)	0.14	24.1	9.34	17.3	4.11
5Y7M3.7K	5	37	Y	30	7	3.7	26.3	19.3	0.58 (0.42)	0.13	27.4	9.22	18.2	4.41
5Y7M1K	5	37	Y	30	7	1	22.9	15.7	0.46 (0.40)	0.16	27.8	22.4	25.4	2.36
5Y5M1K	5	37	Y	30	5	1	21.0	15.5	0.48 (0.42)	0.15	27.7	22.4	25.2	2.36
5Y7m1K	5	37	Y	7	7	1	21.9	4.42	0.23 (0.16)	0.03	32.1	20.2	29.9	2.15
2N7M1K	2	60	N	30	7	1	12.6	14.1	0.58 (0.52)	0.15	24.4	19.9	21.8	2.34
4N7M4.5K	4	45	N	30	7	4.5	27.8	18.8	0.58 (0.40)	0.13	29.3	7.84	19.4	4.90
2N7m6K	2	60	N	7	7	6	3.02	3.33	0.56 (0.52)	0.04	13.2	10.8	11.8	2.55
2N5m6K	2	60	N	7	5	6	2.93	3.50	0.59 (0.54)	0.03	12.9	10.2	11.3	2.45
2N7m1K	2	60	N	7	7	1	1.89	2.00	0.59 (0.52)	0.05	10.9	6.19	8.32	4.98
2N5m1K	2	60	N	7	5	1	2.15	2.09	0.57 (0.49)	0.05	10.7	6.11	8.25	4.47

(a) Model name: $W_{0,FG} + Y/N = \text{with/without segregation} + W_{0,SG} + m/M = \text{low/high initial } M_{SG} + \text{initial } r_{h,SG} + \sigma_{0,SG}$
(K=King velocity dispersion)

Columns: 1) Name of the model; 2) W_0 of the FG; 3) half-mass radius of the FG; 4) Primordial segregation of the FG ($N = \text{not segregated}$, $Y = \text{segregated}$), 5) mass of the SG; 6) W_0 of the SG; 7) half-mass radius of the SG; 8) the total mass of FG bound stars; 9) the total mass of SG bound stars; 10) fraction of SG stars within the half-mass radius of the whole cluster (fraction of SG stars of the whole cluster); 11) fraction of SG stars among unbound stars; 12) half-mass radius of the unbound stars, respectively; 13) half-mass radius of the bound SG; 14) half-mass radius of the whole cluster (i.e. only bound stars); 15) central density.

7.2. Results

only bound stars), the fraction of unbound SG stars and central density. It has to be stressed that, as for the previous models, the reported value for $r_{h,FG}$ is not the half-mass radius at the time of FG formation, but after the gas expulsion and violent relaxation phases, when the system is considerably more extended than at its formation. During these phases, the half-mass radius of a cluster can increase of 3 or 4 times (Lada et al., 1984; Baumgardt & Kroupa, 2007). Its exact value depends on many parameters, e.g. the IMF, the star formation efficiency, the gas and stellar density and the gas expulsion timescale. Further discussion regarding the scale radius of star-forming stellar clusters is reported in Section 7.3.3.

In all models, we have assumed that the SG is initially more centrally concentrated than the FG and, at the end of the simulations, all clusters still show, at different degrees, this configuration.

We have varied several parameters in order to determine their effects on the evolution of the system focusing on the fraction of SG stars, which has been determined for several GCs, both in the Milky Way and external galaxies (Milone et al., 2020b; Dondoglio et al., 2021). We here calculate it as the mass of bound SG particles over the mass of all the bound particles, $f_{\text{enriched}}(< r) = M_{SG}(< r)/M_{\text{tot}}(< r)$, both within the half-mass radius and for the whole cluster. In Section 7.2.2.1, we discuss the caveats that need to be considered when comparing the theoretical value to the observed one.

First, we studied models with different values of the central velocity dispersion, equal to 0 km s^{-1} , 10 km s^{-1} and the velocity dispersion of the generated King model. We find that such a quantity poorly affects the evolution, and the resulting clusters possess very similar fractions of SG stars. For this reason, all the subsequent models have been performed assuming the same velocity dispersion distribution, corresponding to the King one.

As found for the previous models, with and without stellar evolution and without the second generation, a segregated cluster loses a larger amount of mass than not segregated ones. Comparing models 5N7M3.7K and 5Y7M3.7K, we derive that the FG loses significantly more mass in the segregated system, while the SG mass is weakly affected, since we have imposed the segregation only to the FG. As a consequence, the f_{enriched} is higher for the segregated system, especially within the half-mass radius.

We have then varied the $W_{0,SG}$ parameter, but we found very weak effects on the evolution of the system, both in terms of mass loss by the two populations, f_{enriched} , half-

mass radii and central density (see the pairs 5Y7M1K – 5Y5M1K, 2N7m1K – 2N5m1K, 2N7m6K – 2N5m6K).

The parameters whose variation has a stronger and more complex impact of the mass loss and f_{enriched} are, instead, the $W_{0,FG}$, the M_{SG}^{ini} and the initial $r_{h,SG}$. In general, analogously to what has been derived for the simulations without SG, the greater the concentration of the FG, and therefore the larger the $W_{0,FG}$ value, the less the mass lost by the whole cluster, as well as by the two populations separately, at the end of the simulation. While for $W_{0,FG} = 5$, a low mass of the SG equal to $7 \times 10^5 M_{\odot}$ (model 5Y7m1K) leads to a mild FG mass loss and a small final f_{enriched} (0.16), for $W_{0,FG} = 2$, the same initial SG mass (e.g. model 2N7m1K) allows losing more than 95% of the FG mass. Consequently, when $W_{0,FG} = 2$, the final FG mass is one order of magnitude lower than in the model with $W_{0,FG} = 5$, and the cluster reaches a final f_{enriched} in agreement with the typical value observed in GCs of 0.59. Similarly, model 2N7M1K loses more FG mass than 5Y7M1K, reaching a final SG fraction of 0.58.

Interestingly, however, for fixed $W_{0,FG} = 2$, variations of M_{SG}^{ini} lead to significantly different final masses and $r_{h,tot}$, but f_{enriched} slightly changes (models 2N7M1K – 2N7m1K). In model 2N7M1K, a higher SG mass implies a larger initial SG fraction, so even though the cluster has lost almost an order of magnitude less mass, and consequently has a cluster radius more than double, the final SG fraction is very similar to the one of model 2N7m1K. On the other hand, for fixed $W_{0,FG} = 5$, variations of M_{SG}^{ini} lead to similar FG masses but significantly different SG ones (see 5Y7M1K – 5Y5m1K). Therefore, the f_{enriched} values differ by almost a factor of 2. These differences in the evolution suggest that there is not a positive correlation between the initial and final values of f_{enriched} . This is also visible in [Figure 7.4](#), where models assuming the same $W_{0,FG}$ do not always follow the same evolution. Therefore, clusters with an initially higher SG fraction do not straightforwardly have a higher final one.

A similar behavior can be found when changing the initial $r_{h,SG}$. While for clusters with a massive initial SG, a smaller $r_{h,SG}$ leads to a stronger SG expansion and lower f_{enriched} (see models 5Y7M3.7K–5Y7M1K), for initial low mass SG, clusters with smaller initial $r_{h,SG}$ are more compact at the end of the simulations, with final SG fractions similar to the ones of models starting with larger $r_{h,SG}$ (see models 2N7m6K – 2N7m1K and 2N5m6K – 2N5m1K). Therefore, an initially more compact SG does not imply a lower SG mass loss.

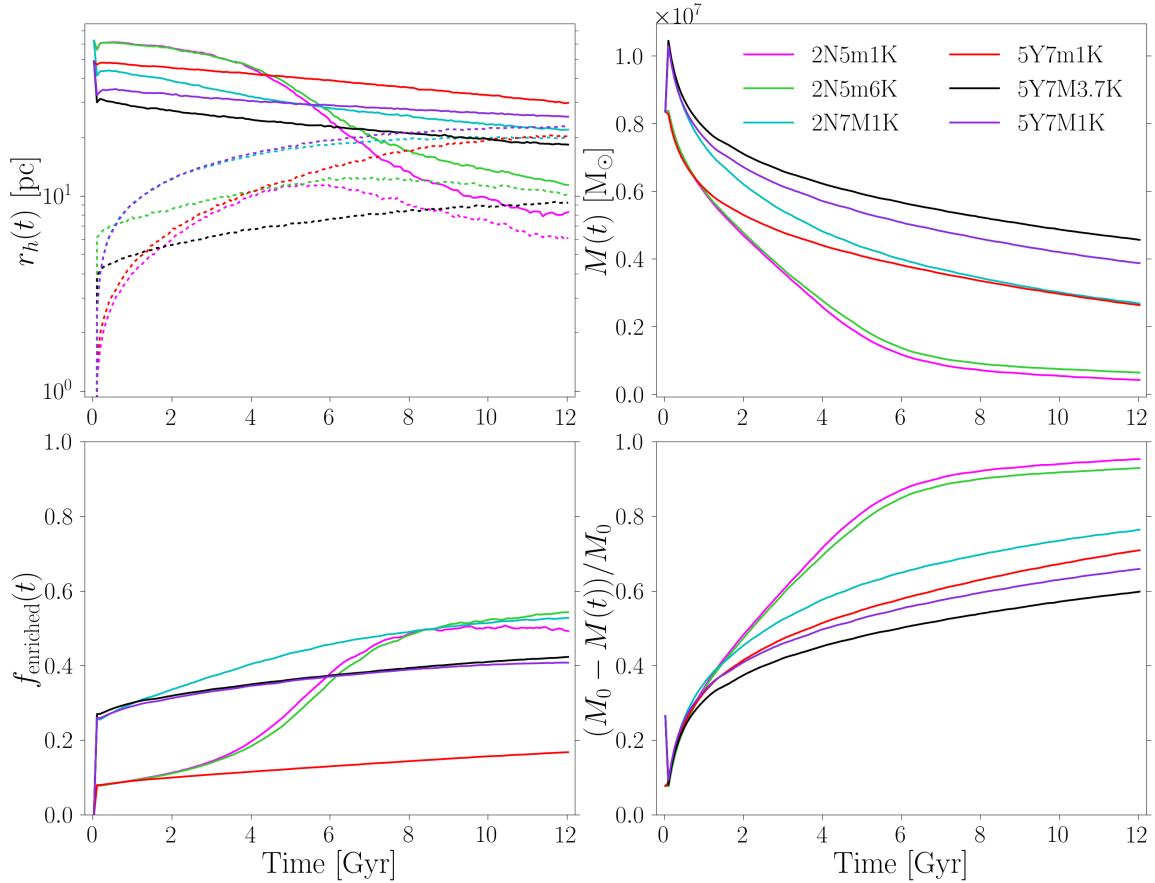


Figure 7.4: Evolution of the half mass radius (top left), mass (top right), SG mass fraction (bottom left), mass loss (bottom right) for some of the models in Table 7.2 reported in the legend. The solid lines in the top panels represent the whole cluster, and the dotted the SG.

Comparing more quantitatively all the models with observed GCs, with a particular focus on the final masses and half mass radii, it is clearly visible that models assuming $M_{SG}^{ini} = 3 \times 10^6 M_\odot$ and $W_{0,FG} = 5$ produce a cluster with a mass almost two times greater than ω Centauri, the most massive globular cluster known to date (Baumgardt & Hilker, 2018). The very massive SG prevents a significant mass loss in these systems, and therefore, also the SG fraction is too small (0.45-0.50) in comparison with the observations. The only exception, in terms of SG fraction, is model 5Y7M3.7K, where the combination between FG segregation and large initial $r_{h,SG}$ implies a greater loss of FG while poorly affecting the SG. Similar results are obtained decreasing $W_{0,FG}$, like in models 2N7M1K and 4N7M4.5K, where a stronger FG mass loss is taking place leading to a higher final $f_{enriched}$. Moreover, all models with a massive SG are characterized by a fraction of SG stars lost among the total unbound stars f_{SG}^{lost} of ~ 0.15 . This is between 3 to 5 times larger than what is found for a low-mass SG.

On the other hand, clusters with $M_{SG}^{ini} = 7 \times 10^5 M_\odot$ lose much more mass, whose intensity is related to the $W_{0,FG}$. As highlighted above, for low $W_{0,FG}$, clusters undergo a strong mass loss, especially in the FG, resulting in final clusters with $M \sim 4 - 6 \times 10^5 M_\odot$, in agreement with present-day ones.

In Figure 7.4 we show the evolution of the models 2N5m1K, 2N5m6K, 2N7M1K, 5Y7m1K, 5Y7M3.7K and 5Y7M1K to highlight the effects of changing $W_{0,FG}$, the M_{SG}^{ini} and the $r_{h,SG}$. Models 2N5m1K and 2N5m6K are the ones undergoing the strongest mass loss and consequently also their r_h and $f_{enriched}$ suffer deep changes during the evolution in the opposite direction; while $r_{h,tot}$ decreases of about 6 times after 12 Gyr, $f_{enriched}$ increases of almost the same amount.

Interestingly, comparing the results obtained with SG and $W_{0,FG} = 2$ with the ones with the same $W_{0,FG}$ but without SG, we clearly see that the formation of a concentrated SG within a shallow FG prevents the disruption of the clusters. An SG, even not very massive, located at the centre of the system, is enough to strengthen the potential well of the cluster, decreasing the potential energy of the particles which will become more bound.

7.2.2.1 Model 2N7m1K

We here focus on the analysis of the model 2N7m1K, which is the one whose final fraction of SG, defined as $f_{enriched}(< r) = M_{SG}(< r)/M_{tot}(< r)$, is more in agreement with current observations, which find fractions between 50% and 80% (Milone et al., 2017).

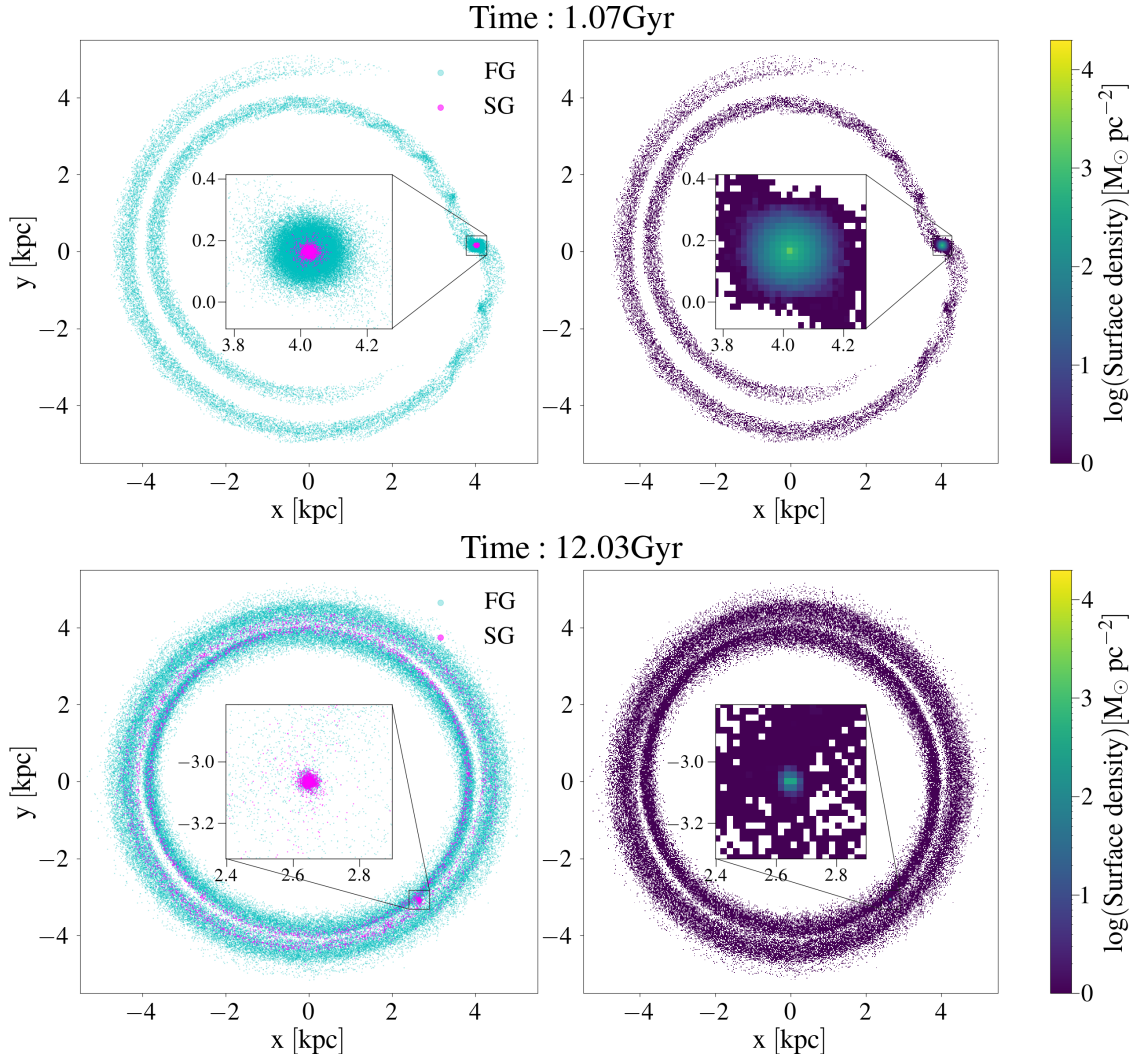


Figure 7.5: Two-dimensional maps at 1 ad 12 Gyr for the model 2N7m1K. Left panel: Distribution of the FG (cyan) and SG (magenta) Right panel: Mass surface density of the whole cluster. At the centre of both panels, we show a zoom-in focused on the centre of mass of the cluster.

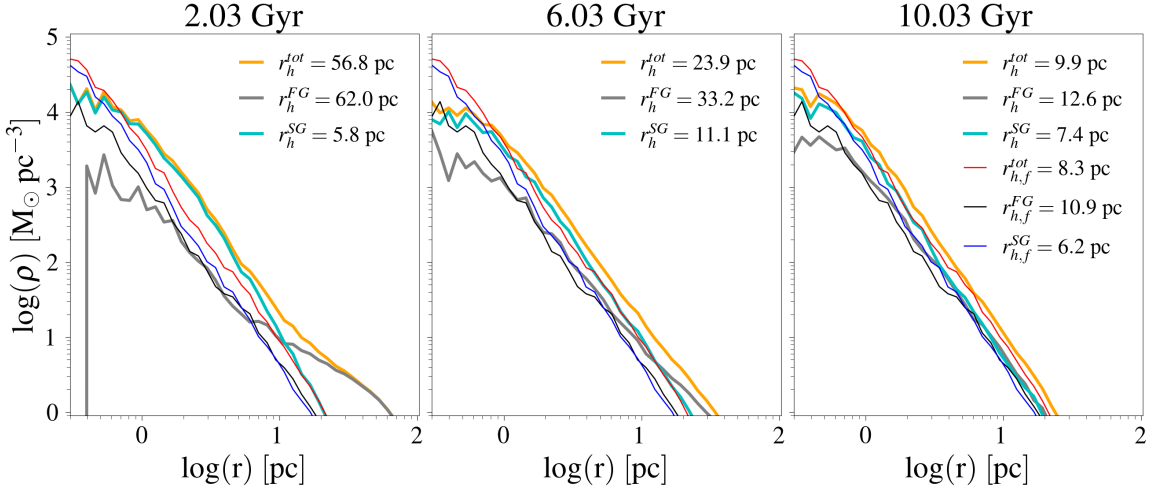


Figure 7.6: Density profiles of the FG (grey), SG (cyan) and the whole cluster (orange) for the model 2N7m1K at three different times, indicated on top of each panel. The half-mass radii of the three components are reported in the legend. In black, blue and red are reported the density profiles at 12 Gyr of the FG, SG and the whole cluster, respectively, for comparison, with the corresponding half-mass radius in the right panel.

In Figure 7.5, we show the distribution of the two populations, on the left, and the projected surface density, on the right, at 1 and 12 Gyr, with a zoom-in centred in the centre of mass of the system in the small inset in the middle of each panel. Already at 1 Gyr, the interaction of the initially spherical cluster with the Milky Way tidal field causes a distortion of the system which develops two significant tidal tails, one leading (internal) and one trailing (external), departing from the centre of the disrupting cluster. Most of the stars in the tails belong to the FG, which is still more extended than the SG, as it was at the beginning of the simulation. Later, the tails lengthen reaching the main body and two concentric circles appear on the maps. At 12 Gyr, the tails are dominated by the FG, while only 5% of the particles belong to the SG. Due to the intensive mass loss suffered by the FG, the cluster is significantly more compact, as clearly shown in the surface density maps, and dominated by SG stars. Even though the system has been highly distorted, its central region preserves a spherical shape after 12 Gyr.

As expected, the two populations, which were spatially and kinematically different at the beginning, move towards a mixing, which is spatially highlighted by the change in the density profiles and, in turn, in the half-mass radii. Such behaviour can be clearly seen in Figure 7.6, where we display the density profiles for the two populations together with the

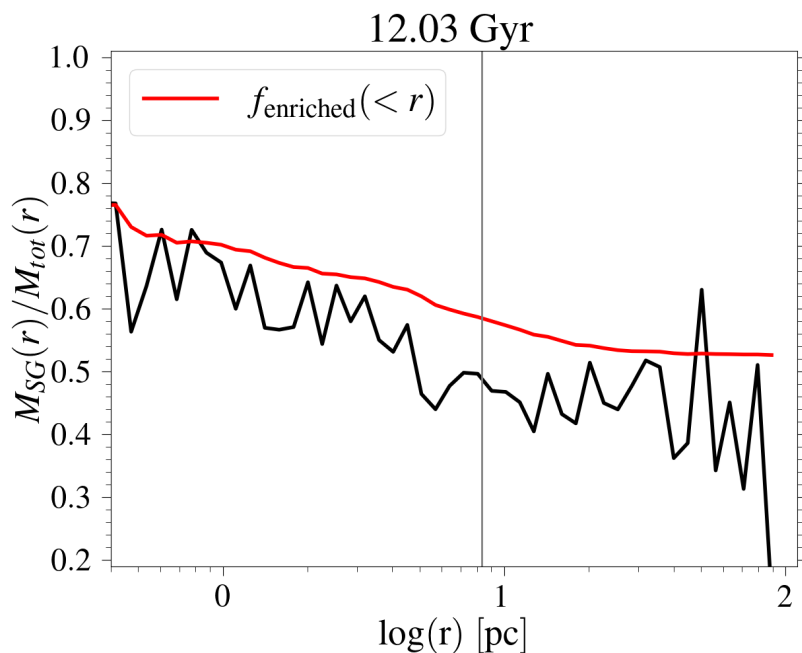


Figure 7.7: The profile of M_{SG}/M_{tot} in black and the fraction of enriched stars within r , $f_{\text{enriched}}(< r)$, in red for the model 2N7m1K at 12 Gyr. The vertical grey line represents the half-mass radius of the whole cluster, $r_{h,tot}$.

one of the whole cluster, compared with the profiles at the end of the simulation. While the SG is always dominant in the centre and its central density does not vary significantly over time, the FG undergoes a notable change in its profile. The FG increases its central density and decreases its half mass radius, resulting from the loss of stars in the outskirts due to the interaction with the Galactic tidal field. Overall, the central density of the cluster is in good agreement with the ones derived in present-day GCs (Baumgardt & Hilker, 2018), while its half-mass radius of 8.3 pc is slightly larger than the ones of GCs with mass $\sim 4 \times 10^5 M_\odot$ (McLaughlin & van der Marel, 2005; Krumholz et al., 2019). It loses almost 98% of FG stars, as generally predicted to match the observed SG fraction, with a final mass loss factor of about 20, which is significantly smaller than the one reported in various other studies.

Although the two populations become more and more mixed with time, at the end of the simulation they are still well distinguished one from the other, with the SG being much more concentrated than the FG. Such difference in the shape of the profiles of the two populations affects the radial fraction of SG stars M_{SG}/M_{tot} , which decreases with the distance from the Galactic Centre, as highlighted in Figure 7.7. This means that also the fraction of SG stars within r , $f_{\text{enriched}}(< r)$, is not flat all over the cluster, but decreases as well from around 0.7 in the centre, down to 0.54 when considering the whole cluster. Such a decrease has been observed in Milky Way GCs such as 47 Tucanane and NGC 5927 (Milone et al., 2012; Cordero et al., 2014; Dondoglio et al., 2021; Jang et al., 2022) and in simulations (D’Ercole et al., 2008). Regarding f_{enriched} , it is important here to stress that the observational values of this quantity are rarely calculated for the whole cluster, but, due to the limited field of view (e.g. Milone et al. 2017), they often refer to the fraction of enriched stars within the inner regions of a cluster (typically between the center and $r \sim 0.5 - 1.5r_h$). It is, therefore, important to compute f_{enriched} within regions similar to those observed to account for its possible radial variations.

7.2.2.2 Model 5Y7M3.7K

For comparison, we report the description of model 5Y7M3.7K, whose initial conditions are significantly different from the ones of 2N7m1K, but leading to similar f_{enriched} . In Figure 7.8, we show the face-on view of the distribution of the two populations, on the left, and of the surface density of the whole cluster, on the right, at two evolutionary times for model 5Y7M3.7K. Comparing it with Figure 7.5 of the model 2N7m1K, the

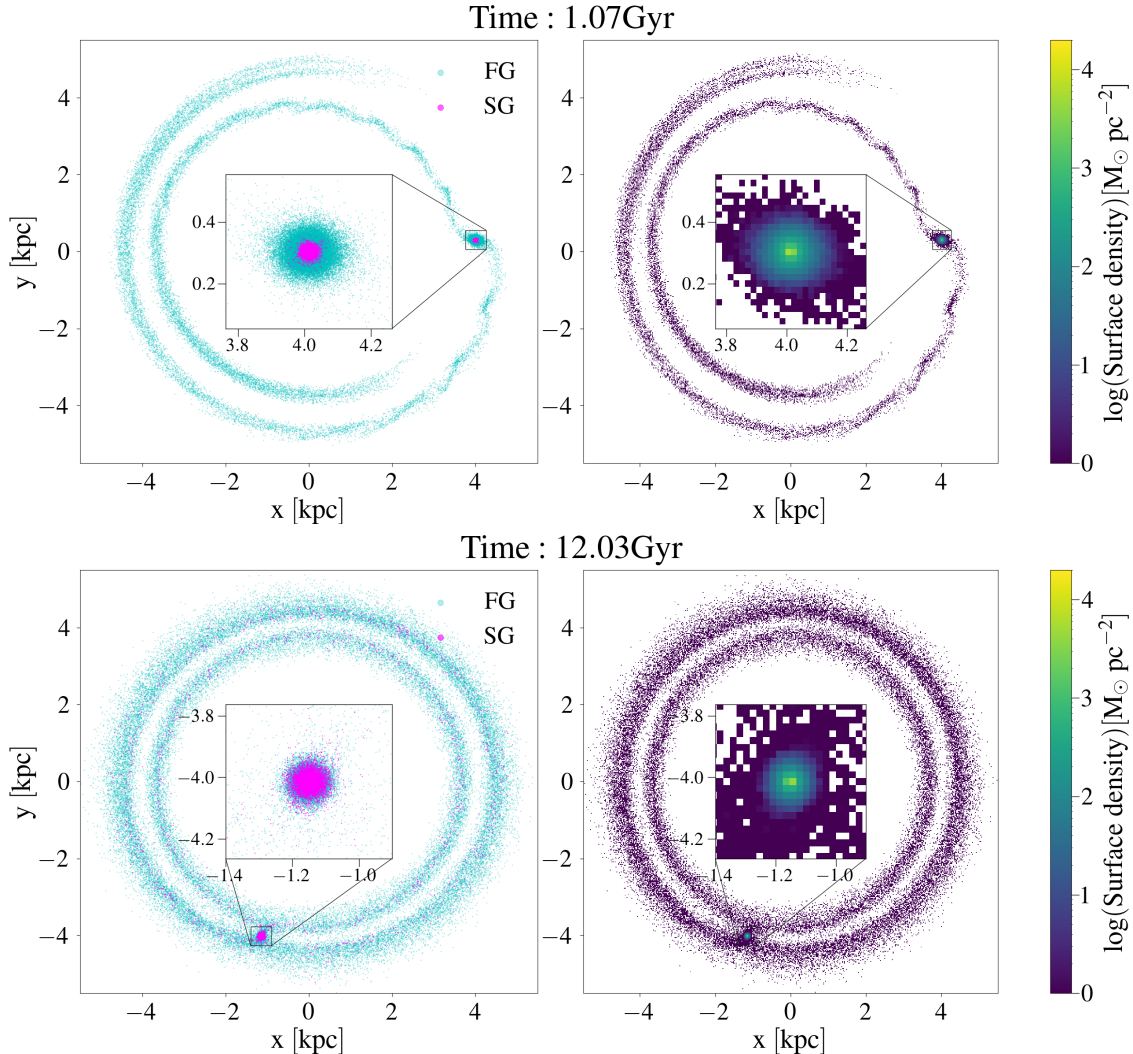


Figure 7.8: Two-dimensional maps at 2 ad 12 Gyr for the model 5Y7M3.7K. Left panel: Distribution of the FG (cyan) and SG (magenta) Right panel: Mass surface density of the whole cluster. At the centre of both panels, we show a zoom-in focused on the centre of mass of the cluster.

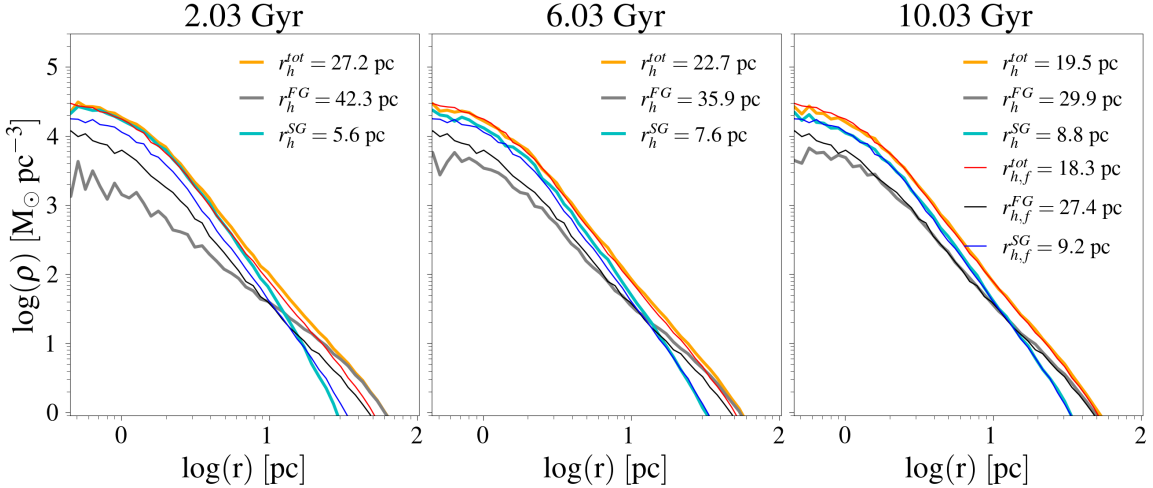


Figure 7.9: Density profiles of the FG (grey), SG (cyan) and the whole cluster (orange) for the model 5Y7M3.7K at three different times, indicated on top of each panel. The half-mass radii of the three components are reported in the legend. In black, blue and red are reported the density profiles at 12 Gyr of the FG, SG and the whole cluster, respectively, for comparison, with the corresponding half-mass radius in the right panel.

central surface density is here slightly higher and, in general, the cluster appears more concentrated at 1 Gyr. At 12 Gyr, the cluster of model 5Y7M3.7K is less concentrated, which is reflected on the larger r_h reported in Table 7.3. The cluster has, in fact, lost fewer stars due to both the higher SG initial mass and the larger $W_{0,FG}$. The milder loss of stars can also be seen looking at the less populated tidal tails.

The profiles of the two models are also quite different; while model 2N7m1K has a very steep profile at the centre after 12 Gyr (see Figure 7.6, model 5Y7M3.7K shows a shallower density profile in the inner regions, as shown in Figure 7.9. The density profile of the whole cluster is only slightly changed over time and therefore the final r_h is still very large, not matching the observed values of Galactic GCs. Also, the total mass of the system is significantly greater than the ones of the bulk of Galactic GCs, meaning that with the initial conditions adopted for this model, the cluster is not losing significant mass but still, it ends up with an f_{enriched} in the observed range, as shown in Figure 7.10. f_{enriched} is well above 0.6 inside 10 pc while it drops to 0.4 when considering $r > r_{h,tot}$. Here, the difference between the f_{enriched} calculated at the half-mass radius and for the whole cluster has the largest difference among all models, stressing again the mismatch between the two values.

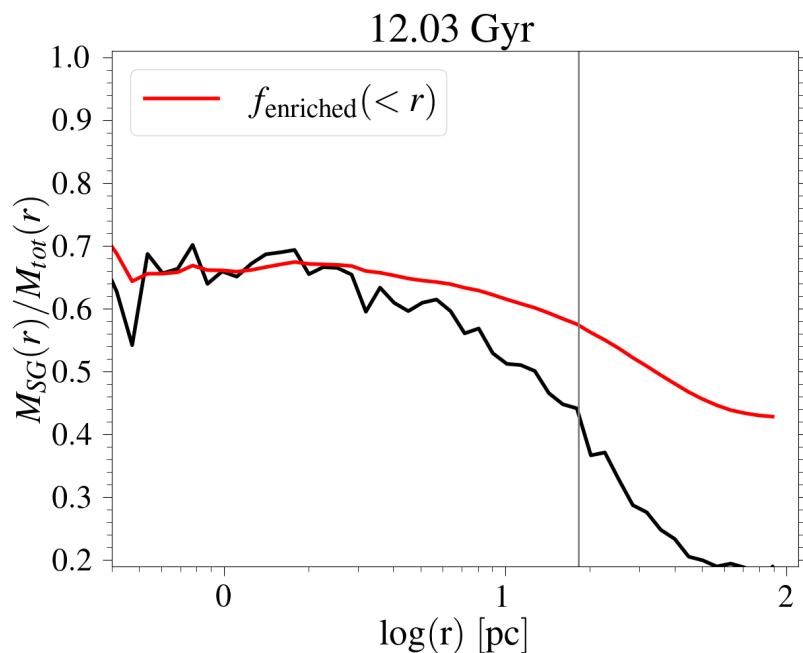


Figure 7.10: The profile of M_{SG}/M_{tot} in black and the fraction of enriched stars within r , $f_{\text{enriched}}(< r)$ in red for the model 5Y7M3.7K at 12 Gyr. The vertical grey line represents the half mass radius of the whole cluster, $r_{h,tot}$.

7.3 Discussion

Through N -body simulations, we have explored the effects of various structural and kinematic properties on the mass loss of a massive GC. We here compare our results with the relevant literature and discuss the strengths and limits of our approach.

7.3.1 Comparison with other theoretical works

Understanding whether a cluster can lose a significant number of FG stars, and therefore reproduce the observational constraints discussed at the beginning of this Chapter, has been the goal of several studies in the past.

Firstly, [D'Ercole et al. \(2008\)](#) addressed the issue proving the feasibility of such a strong mass loss. It is however worth noticing that their simulated cluster has an initial mass of $10^4 M_\odot$, significantly smaller than the one we have adopted here, but also of the typical Galactic GC. Clusters with these masses are more prone to lose mass given their shallower potential, therefore it is not surprising that they are able to reach higher values of f_{enriched} .

Later, [Reina-Campos et al. \(2018\)](#) derived that, once assuming an initial $f_{\text{enriched}} = 0.05$, their clusters lose a very small number of stars, ending up with fractions of 5-10% for massive systems. Their result resembles the one we have obtained for the model 5Y7m1K which starts with a similar f_{enriched} value. In addition, they stated that extrapolating from their results, a present-day massive cluster $M_{cl} = 10^6 M_\odot$ should be initially composed by a remarkably high fraction of SG stars (~ 0.8) to reproduce the present-day f_{enriched} values, at variance with what it is generally assumed, and that, even in this case, the cluster would be too extended, with a $r_h \sim 10^2$ pc, more than one order of magnitude greater than the observed ones. Although in our simulations an extended cluster has to be assumed to match the observed f_{enriched} , the final r_h of the whole cluster reduces significantly during the evolution (in the most extreme case of 2N5m1K the final cluster r_h is more than 7 times smaller than the FG initial one), which is instead maintained fixed in the [Reina-Campos et al. \(2018\)](#) study. On the other hand, we noted that a high initial f_{enriched} not always leads to a higher final SG fraction and, therefore, we do not need to assume a massive SG to reproduce the observed fraction. Such a mismatch between our results and the ones of [Reina-Campos et al. \(2018\)](#) may be ascribed to the positive correlation between the initial and final SG fraction assumed in their work, which we have shown is not always

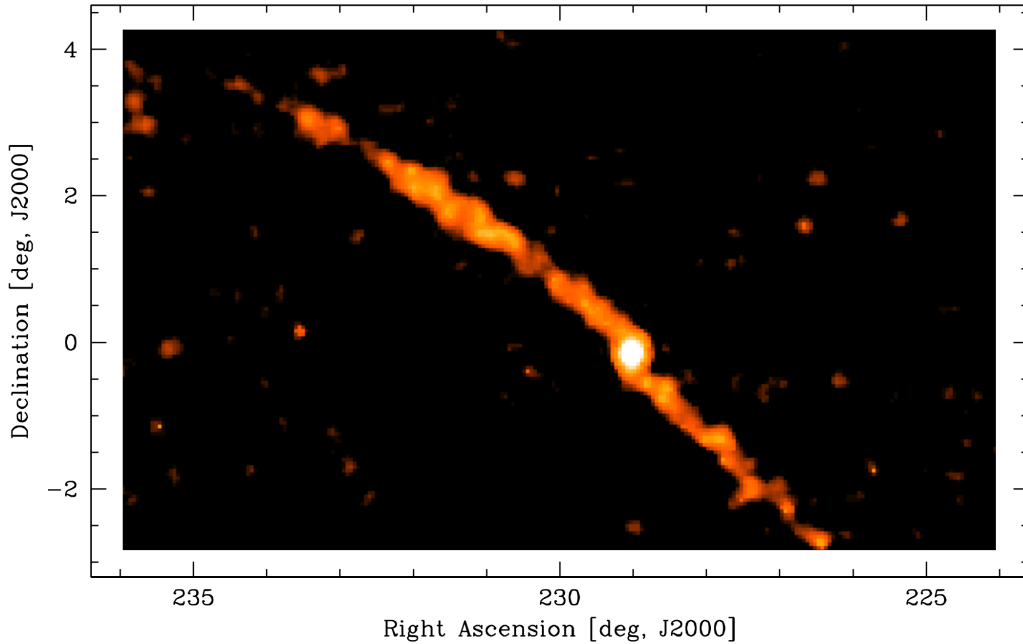


Figure 7.11: The distribution of stars of the Palomar 5 Galactic globular cluster. The white blob represents the stellar cluster, while the two orange tidal tails are its leading (right) and trailing arms (left), which are extending for almost 10 kpc ([Odenkirchen et al., 2003](#)) and are even more massive than the cluster itself. Credits: Sloan Digital Sky Service.

true.

Recently, [Sollima et al. \(2022\)](#) studied the evolution of multiple stellar populations using the binary fraction as a tool to recover the initial concentration required for the SG. Although we do not include the treatment of binaries, model 2N7m1K nicely satisfies the relation required to reproduce the present-day SG binary fraction found by [Sollima et al. \(2022, their eq. 3\)](#). Similarly, [Vesperini et al. \(2021\)](#) and [Sollima \(2021\)](#) modeled clusters with masses of the order of $10^6 M_\odot$, reproducing the observed SG fractions, much higher than the ones retrieved in this work ([Hypki et al., 2022](#)). For a thorough comparison, other tests should be performed at lower cluster masses.

7.3.2 The fraction of SG lost in the disk

In [Table 7.3](#) we have listed also the fraction of unbound SG over the total mass of unbound stars, f_{SG}^{lost} . The models can be distinguished into two subgroups: when assuming a massive SG, the unbound stars are composed of $\sim 15\%$ of SG, while low mass SG leads to

fractions of $\sim 5\%$. This quantity is important to study GC evolution in terms of mass loss and their contribution to the Galaxy. Ongoing loss of SG stars has been recently identified both in the tails of the disrupting GC Palomar 5 (Phillips et al., 2022), shown in Figure 7.11, and in the bulge cluster NGC 6723 (Fernández-Trincado et al., 2021). Due to the limited sample, a robust fraction of SG in the tails of these two objects cannot be derived, but would be useful to add further constraints on the cluster mass loss.

On the other hand, in the Galactic halo field, several observational studies have searched for SG-like stars identified by their peculiar chemical composition. In particular, recent investigations have determined fractions of $\sim 2 - 5\%$ (Carretta et al., 2010; Martell & Grebel, 2010; Martell et al., 2011; Ramírez et al., 2012; Martell et al., 2016; Koch et al., 2019). However, this is just a lower limit to the fraction of SG stars that are lost by GCs, due to the high uncertainties regarding the fraction of halo stars that were formerly belonging to GCs. Further difficulties arise when focusing on the Galactic disk, where measurements of SG fraction are now not available. With the upcoming arrival of 4MOST and WEAVE coupled with Gaia, new insights into the contribution of GCs to the Galactic disk will be provided.

7.3.3 High-z proto-clusters

The mass and half-mass radius of present-day clusters are much smaller than the initial values we have assumed for our simulated clusters; however, our assumptions may not be too distant from the real conditions at birth. Accessing the properties of star-forming young GCs is now possible by exploiting gravitational lensing, which permits to reveal faint stellar objects at high redshift, in the epoch of their formation (Vanzella et al., 2017). Recently, some proto-GC candidates have been identified, like the ones in the extended star-forming region strongly magnified by the galaxy cluster MACS J0416.1-2403 (Vanzella et al., 2019; Calura et al., 2021). The region is dominated by two star-forming systems: D1, which has a stellar mass of $2.2 \times 10^7 M_{\odot}$ and a size of 44 pc, and T1, which is less massive, with its $2 \times 10^6 M_{\odot}$ and a size of < 30 pc. Interestingly, D1 also shows a nucleated star-forming region surrounded by a diffused component. More extended samples of lensed clumps have been presented (Meštrić et al., 2022; Vanzella et al., 2022; Claeysens et al., 2023), detected in various lensed fields and across a wide redshift range (from $z \sim 1$ to $z \sim 8$). These samples are composed of clumps of 10 – 100 pc size and mass between $10^5 M_{\odot}$ and $10^9 M_{\odot}$, therefore including systems with size and mass in the range of our

models.

An open problem is to determine if the observed systems represent single star clusters, extended star-forming complexes, super star clusters (SSCs) or dwarf galaxies. In the MPs framework, the idea that GCs may form in hierarchical complexes or SSCs is not new (Bekki et al., 2017). Young GCs might be embedded into a larger structure with similar properties, and a portion of the parent galaxy or SSCs may provide processed materials for the creation of MPs generations (Renzini et al., 2022).

The James Webb Space Telescope is opening a new window on the high redshift observations of GCs. In addition to compact clumps and young proto-GCs at high redshift, a recent, exciting discovery has revealed the presence of quiescent, evolved and massive GCs associated with their host galaxy in the Sparkler system (Mowla et al., 2022). Considering that now we are only in the earliest stages of calibration of in-flight data from JWST, we have exciting times ahead of us as it is presumable that the current samples may grow rapidly and provide new, fundamental insights on the formation of GCs.

7.3.4 Model limitations

We have studied the evolution of a massive cluster orbiting the Milky Way to explore whether it can lose mass, as a result of tidal effects of the Galactic potential. We have derived that, in order to reproduce present-day clusters, an initially very extended FG has to be assumed. However, we have not included ingredients that are known to increase the rate of mass loss, such as gravitational and tidal shocks and the presence of binaries, and dark remnants. The addition of these processes would likely increase the mass loss in our simulations and possibly increase the final f_{enriched} . On the other hand, the assumed static Galactic potential overestimates the tidal field acting on the GC, which has been shown to be much weaker at early times (Renaud et al., 2017). To overcome these limitations, a study of the dynamical evolution of a GC with MPs is to be performed in a fully cosmological context. Attempts to study the early formation of GCs in cosmological simulations are being performed (Kimm et al., 2016; Ma et al., 2020; Li & Gnedin, 2019), sometimes with resolution high enough to study the feedback of individual stars (Calura et al., 2022). Although still challenging, it is foreseeable that in the forthcoming future, such tools will allow us also to model MPs and their long-term dynamical evolution.

7.4 Conclusions

Most of the scenarios proposed so far for the formation of multiple stellar populations, have to deal with the “mass budget” problem. To overcome it, what it is generally assumed is that clusters were initially more massive, between 5 to 10 times but in some cases even 100 times, than they are now. As a consequence, during their evolution they must lose a significant amount of mass, to reconcile with the observational values. We have here explored, through a series of N -body simulations, whether a massive cluster with an initial mass of $M \sim 10^7 M_{\odot}$, and composed by two different populations, can undergo a significant mass loss during its evolution and end up, after 12 Gyr, with structural properties in agreement with the present-day GC ones. Our cluster is located in the disk of the Galaxy, and it orbits around the centre at 4 kpc. It is therefore evolving under the effect of the tidal field of the Milky Way. We have tested the effects of various parameters on the mass loss and the fraction of SG stars, f_{enriched} , one of the strongest observational constraints.

Before performing the simulations with two populations, we investigated the evolution of single-population clusters. These results are useful to determine the effects of various parameters and for a comparison with the ones obtained with two populations.

We here summarize the main results of the work:

- Our best model 2N7m1K, which starts with $W_{0,FG} = 2$ and a low mass SG of $M_{SG}^{ini} = 7 \times 10^5 M_{\odot}$, suffers a strong mass loss, particularly in the FG. It predicts a final total mass of $\sim 4 \times 10^5 M_{\odot}$ with f_{enriched} at $r_{h,tot} = 8\text{pc}$ of 0.59, in agreement with observations. The FG is reduced by almost 98% of its initial mass and the final mass loss factor is around 20, milder than what is often reported in the literature.
- The parameters that affect the most the mass loss rate and, in general, the evolution of the clusters are the degree of primordial segregation, the FG initial concentration as determined by the initial value of the King dimensionless central potential $W_{0,FG}$, the initial mass of the SG, M_{SG}^{ini} , and the initial half-mass radius of the SG, $r_{h,SG}$. In order to lose enough mass to reconcile with the observed masses and f_{enriched} , a $W_{0,FG} = 2$ and a low mass SG of $M_{SG}^{ini} = 7 \times 10^5 M_{\odot}$ have to be assumed. Clusters with these initial conditions are able to lose more than 90% of their FG mass, as required to solve the mass budget problem. Such a large $W_{0,FG}$ implies an extended

7.4. Conclusions

FG, which is however not too large compared with the ones observed in high redshift star-forming systems.

- From a comparison between the single population models and the two population ones with $W_{0,FG} = 2$, it has been derived that the presence of an SG, even not very massive, prevents the disruption of the system, as it happens when no SG is included.
- Clusters with an initially higher SG mass, and therefore with a higher SG fraction, f_{enriched} , are not always showing a higher final SG fraction with respect to clusters starting with a low mass SG. This is particularly true when small values of $W_{0,FG}$ are assumed. Such behavior suggests that a positive correlation between the initial and final f_{enriched} may not be always verified.
- Our clusters are all initially composed of a centrally concentrated SG. This difference between the spatial distribution of the two populations is also found at the end of the simulations for all models. Consequently, f_{enriched} is not flat as a function of radius, and, in particular, it is higher at the centre and decreases moving outwards. Since observations are hardly ever able to derive f_{enriched} for the whole cluster, but rather for some fraction of r_h only, caution has to be made when comparing the simulation results with observed values. In our cases, differences up to 20% have been found between f_{enriched} of the whole cluster and f_{enriched} at $r_{h,\text{tot}}$.
- Clusters with low mass SG lose a small fraction of SG stars, generally between 4 to 5% of all unbound stars in the tails. On the other hand, clusters with initially massive SG lose 15% of SG stars. These values may be used for comparison with GCs where tidal tails have been detected, such as Palomar 5 and NGC 6723.

Possible follow-ups of the current work could be to expand it, fully exploring how the intensity of mass loss depends on the initial properties of both the FG and the SG components (e.g. initial masses, Galactocentric distance, galaxy potential). A promising tool to perform large series of simulations would be to run a single one-component model, and then interpret it a posteriori as a multi-component system, a technique recently applied by [Nipoti et al. \(2021\)](#) to a two-component dwarf-galaxy orbiting the Milky Way (see also [Bullock & Johnston 2005](#); [Errani et al. 2015](#)).

Moreover, to achieve a more realistic modelization of the phenomenon, the implementation of other physical processes (e.g. binaries, natal kicks, shocks), not taken into

account here, would be crucial, given that could potentially trigger more mass loss.

The models could also be adapted to study external galaxies, such as the Magellanic Clouds, where dynamically younger and FG-dominated globular clusters have been found. Such studies would contribute to refining our knowledge of stellar cluster evolution and the assembly history of the Galaxy.

Chapter 8

CONCLUSIONS AND FUTURE PERSPECTIVES

*Yesterday's just a memory,
Tomorrow is never what it's supposed to be*

Don't Fall Apart On Me Tonight, Bob Dylan

This Thesis has been devoted to the study of the formation and evolution of multiple stellar populations in globular clusters (GC), a phenomenon widely explored but still poorly understood. This work has been carried out by means of hydrodynamic and N -body simulations to bring new insights into the physical processes at play, comparing our results with current observational data, and providing estimates that will be useful for future investigations. First, I explored the role played by internal cluster rotation of the formation of the second, chemically “anomalous”, population. Secondly, I explored how the second population formation is shaped by Type Ia supernova explosions. Finally, I investigated whether an initially massive cluster can undergo the significant mass loss required to solve the “mass budget” problem, a common issue faced by multiple population formation scenarios, and reconcile, after a Hubble time, with the present-day GC features. In general, in all the works we have assumed that GCs have undergone self-enrichment and that second-population stars were formed out of ejecta of asymptotic giant branch (AGB) stars plus interstellar medium (ISM) gas with pristine composition. In the following Sections, I sum up the main results of this Thesis and outline the possible future perspectives of this work.

8.1 Summary and Conclusions

8.1.1 The role of internal rotation on the second generation formation

Signatures of internal rotation in GCs have been detected only in the last decade or so (Bianchini et al. 2018; Kamann et al. 2018; Sollima et al. 2019; Vasiliev & Baumgardt 2021 and references therein) and, for this reason, cluster rotation has rarely been taken into account in simulations. Even though the observed rotation is generally weak, it is likely the remnant of a stronger initial one, later lessened due to two-body relaxation. Recently, first Cordero et al. (2017) and later Kamann et al. (2020), measured the rotational amplitudes of different populations, retrieving that the first is rotating slower than the second, as found in other investigations as well. In addition, they were also able to distinguish the second generation (SG) into two subgroups, where the chemically extreme group was found to rotate faster than the mildly enriched one.

To explore the conditions necessary to form a rotating SG and the connection between rotation and degree of enrichment, we have performed a series of hydrodynamic simulations exploiting a customized version of the RAMSES code. We have modelled the formation of the SG starting from a massive, rotating first generation (FG) and tested various cluster inclinations, rotational profiles and ISM densities. We have focused on the structural and dynamical properties of SG stars, which have been subdivided thanks to their helium composition.

We find that the evolution of the system strongly depends on the density of the infalling ISM gas: while for a low density of 10^{-24}g cm^{-3} the rotating ejecta give birth to a stellar disk, mainly composed of extremely helium-enhanced stars, for an ISM density one order of magnitude higher, the AGB ejecta are significantly more diluted with non-rotating pristine gas and, therefore, new stars are born with small to no memory of the FG rotational pattern. Focusing on the low-density model, we retrieve that overall, the SG is rotating faster than the FG and it is also much more centrally concentrated. In addition, the He-rich SG subgroup, which has formed earlier and is poorly diluted, rotates more rapidly than the He-poor subgroup, formed out of more diluted ejecta. These findings are qualitatively in agreement with observations; for a more quantitative comparison, the long-term evolution of the cluster has to be considered, during which the SG disk would tend to a more spherical distribution and, in turn, rotation amplitude would decrease. Assuming the same ISM density, similar results have been found either adopting a solid body rotational

8.1. Summary and Conclusions

profile, rather than the analytic profile proposed by Lynden-Bell (1967) or changing the orientation of the rotational axis with respect to the direction of the infalling gas.

8.1.2 The role of Type Ia Supernova feedback on the second generation formation

Age difference measurements between populations suggest that star formation in GCs has lasted for a maximum of a few hundred Myr. In principle, AGB ejecta are released for several Gyr, therefore, some mechanism should act on a much shorter timescale to quench the SG formation. In the past, D’Ercole et al. (2008) found, by means of 1D hydrodynamic simulations, that Type Ia supernovae (SNe) are effective in removing gas from the system, which, in turn, halts the star formation of SG stars. In their work, SNe Ia are all located at the centre of the system, and the explosion time distribution is constant.

Through a series of hydrodynamic simulations in 3D, we explore whether Type Ia SNe affect the formation of SG stars, assuming a more realistic spatial and temporal distribution of the explosions. As before, we have tested various ISM densities, which leads also to different times for the arrival of the diluting material, and explored different starting points for the SNe Ia explosions, given the high uncertainties still present regarding the timescales of this process. In addition, we also follow the iron composition of SG newborn stars, given that Type Ia SNe are the major producers of this element. In GCs, and especially among the SG, narrow iron spreads have been detected (Carretta et al., 2010; Legnardi et al., 2022). Only about 20% of Galactic GCs show a spread in iron, which are labelled Type II clusters (Milone et al., 2017).

We find significant differences in both the chemistry and the star formation history as a function of the adopted ISM density. At densities of $10^{-23} \text{ g cm}^{-3}$, Type Ia SNe mildly affect the intensity of star formation, with a final mass slightly reduced compared to the case without SNe. Also, the helium distribution is poorly influenced, with the bulk of the stars being poorly He-enhanced. On the other hand, the iron composition changes, leading to an estimated present-day spread of $\sigma_{[\text{Fe}/\text{H}]} = 0.14 \text{ dex}$, in agreement with observations of Type II clusters. On the other hand, for a density ten times lower, independently from the time at which SNe Ia start exploding, once it begins, the infalling gas (if present) is confined far from the centre and the star formation rate drops, but not sharply as in D’Ercole et al. (2008). Both the final mass of the SG and its chemical composition depends, instead, on the starting time of SNe Ia. When the explosions start together with the AGB phase, the bulk of the SG system is already formed before the infall begins, meaning that the SG

is dominated by extremely helium-enriched stars, at variance with observations. The AGB scenario requires, in fact, that the AGB ejecta should be diluted with pristine gas, which is almost not happening in this case. The negligible dilution, together with the continuous explosions of Type Ia SNe, significantly reduces the final mass of the SG, which is about 80% less than what has been derived without SNe Ia. Slightly milder changes are found when delaying SNe Ia explosion, however, dilution is still too low to reproduce the measured helium mass fraction distributions.

In conclusion, we found that star formation is not halted immediately after the first Type Ia explosions, and rather continue for several Myr. In particular, in the case where SNe Ia have a stronger effect on the star formation, they also prevent the dilution of pristine gas, leading to unobserved helium compositions. This suggests that Type Ia SN alone are not able to quench the SG formation and other mechanisms might need to be invoked. Besides the effects on the star formation, SNe ejecta has been found to mix and be recycled to form new SG stars which will show an iron spread, around $\sigma = 0.14$ dex, indicating a possible venue for the formation of Type II clusters.

8.1.3 Multiple stellar population mass loss in Galactic globular clusters

During their evolution, globular clusters lose stars belonging both to the first and second population. The mass loss rate depends on several factors (e.g. binarity, dark remnants, tidal fields and shocks, mass segregation) and is shaped by various processes (e.g. two-body relaxation, stellar evolution), which have been thoroughly studied in the past ([Chernoff & Weinberg, 1990](#); [Spitzer, 1940](#); [Vesperini & Heggie, 1997](#); [Baumgardt et al., 2008](#); [Tanikawa & Fukushige, 2009](#); [Contenta et al., 2015](#)). Nevertheless, a clear understanding of the dynamical evolution of FG and SG stars is still missing. Part of this is due to the large uncertainties on the initial cluster masses. While a reasonable assumption would be that the initial mass is similar to the observed one, the high fraction of SG stars detected in the bulk of GCs challenges it. A FG with a mass comparable to the present-day cluster mass would process and release an amount of mass significantly lower than the actual SG mass. This is known as the “mass budget” problem, and mainly affects self-enrichment scenarios, such as the AGB one. To solve it, the FG is assumed to be much more massive at birth, and then, during its evolution, a large number of stars ($\sim 90\%$) are lost, to reconcile with the present-day FG mass. So far, some works have tested the feasibility of such a strong mass loss, but controversial results have been found ([D’Ercole et al., 2008](#);

[Reina-Campos et al., 2018](#)).

To address this issue, we have followed, by means of the direct N -body code NB-Symply, the evolution of a massive cluster of $10^7 M_\odot$, similar to the ones modelled before, while orbiting the Milky Way at 4 kpc for a Hubble time. We have explored the variation of mass loss as a function of several structural and kinematic parameters. Firstly, we have performed runs with a single population, with and without taking into account stellar evolution. Secondly, we have evolved a system composed of two populations, to mimic a typical GC.

We find that a low mass SG with $M_{SG}^{ini} = 7 \times 10^5 M_\odot$ located at the centre of a shallow FG with $W_{0,FG} = 2$ results in a present-day cluster with total mass $4 \times 10^5 M_\odot$ and a final SG fraction f_{enriched} of 0.59. Such a large initial extension of the FG (with a half-mass radius of 60 pc after the gas expulsion and violent relaxation phases), which we remind it is not the one at birth but after the gas expulsion and violent relaxation phases, reduces of a factor more than 7 after a Hubble time, reconciling with the spatial scales of present-day GCs. Moreover, while when only a stellar population is modelled, $W_{0,FG} = 2$ combined with stellar evolution leads to the dissolution of the system, the presence of the SG saves the cluster from its fatal fate.

Regarding f_{enriched} , we have noticed that to derive high final values, it is not always necessary to start with high fractions, as for our best model. In addition, due to the different spatial distributions of the two populations, depending within which radius we compute it, the value of f_{enriched} may vary significantly, as found in some clusters ([Milone et al., 2012](#); [Cordero et al., 2014](#)).

Another quantity we have looked at is the fraction of SG stars lost in the field. These stars, due to their peculiar composition are detected much more easily than FG stars. Therefore, in the last decade, various estimates of SG fractions have been carried out in the Galactic halo. Our low-mass SG models predict a fraction three times lower than the massive SG ones. Therefore, an observational estimate of this quantity would be useful to set further constraints on the mass loss experienced by GCs.

8.2 Future Perspectives

In the last decades, observations of local globular clusters have provided fundamental data that has allowed us to reveal the complex nature of these systems. One of the major

Chapter 8. Conclusions and future perspectives

discoveries, and probably the most enigmatic one, is the presence of multiple stellar populations. This still unexplained phenomenon will be further investigated with the use of new facilities, such as the James Webb Space Telescope (JWST) (Marino et al., 2021), the China Survey Space Telescope (Li et al., 2022), Euclid (Lançon et al., 2021), and new surveys, like 4MOST and WEAVE. Besides observations of local clusters, the high redshift Universe is now accessible thanks to gravitational lensing, and will be the focus of future studies with the arrival of a new wealth of data from JWST first (Vanzella et al., 2022; Mowla et al., 2022; Faisst et al., 2022; Lee et al., 2022; Claeysens et al., 2023), and later from the Extremely Large Telescope. Such investigations are and will be crucial to unveil the conditions that led to the formation of GCs. From the theoretical point of view, the portion of the parameter space probed so far is very small. Simulations, such as the ones described here, are unique tools to study both the formation and evolution of stellar clusters, interpret the observational data and provide estimates to guide future studies.

Despite the work done in this Thesis and the results we have obtained, several questions on the multiple population phenomenon and, in general, on globular clusters are still unaddressed.

In the remainder of the Chapter, I will list some possible follow-ups to the works reported in this Thesis.

- In Chapter 5, it has been derived a variation of the rotational amplitude with He-enrichment, similar to what has been observed in some clusters. In addition, a stellar disk of helium-rich stars is formed. To compare quantitatively the results of our simulations with present-day measurements, and determine the fate of the stellar disk, a series of N -Body simulations would be required. It will also be important, as for the clusters we have modelled in the last Chapter, to derive the impact of internal rotation on the mass loss, with the novelty of having more than one population rotating at different velocities.
- In the works devoted to studying the early phases of GC formation, we have followed the evolution of two chemical elements: iron and helium. These elements are important to understand the physical processes at play in the formation of MPs. While the iron composition could reveal an inhomogeneous ISM or a SN contribution, helium is heavily produced during the H-burning at high temperatures and, therefore, traces the enrichment in light elements. A proper comparison between the observed

8.2. Future Perspectives

anticorrelations and theoretical ones is however required and could provide further information on the enrichment process. Therefore, yields of AGB stars for light elements and, in case, also the *s*-process ones, could be implemented in the code and their composition could be followed during the early phases.

- All the work described in this Thesis is focused on massive GCs. Nevertheless, to achieve a clearer view of the role played by processes like Type Ia SNe explosions, cluster rotation in the early phases, and Galactic tidal field and two-body relaxation on longer time scales, a wider exploration of the cluster initial mass would be beneficial. In addition, theoretical scaling relations could be compared with observed ones to verify the feasibility of the scenario, as done by [Yaghoobi et al. \(2022\)](#).
- The code we have developed can be customized to explore other proposed scenarios, in particular the ones invoking self-enrichment. Previous works, such as [Renzini et al. \(2015\)](#) and [Bastian & Lardo \(2018\)](#), have determined, for some scenarios, their ability in reproducing various observational constraints. The results they came out with are quite different, and generally, they are based on a qualitative analysis. This reflects the lack of studies carrying out a detailed modellization of MP formation assuming a scenario different from the AGB one. Although they are less popular, other scenarios need to be accurately tested to derive their strengths and weaknesses and, ultimately, determine their feasibility.
- Together with the addition of rotation and the extension to lower masses, the *N*-body simulations that we have performed and described in [Chapter 7](#) could be extended to Magellanic Cloud (MCs) GCs. Various works have studied the stellar content in both MCs, finding that the fraction of first-generation stars is much higher than in Galactic GCs, becoming in some cases even the dominant component ([Dalessandro et al., 2016](#); [Milone et al., 2020a](#); [Dondoglio et al., 2021](#)). This could be the result of a milder mass loss, as a consequence of the lower mass of the two Clouds, or different conditions for the birth of the MPs. In addition, MCs GCs are spanning a wider range of ages, which would allow one to constrain the evolution not only at the present time, but also at earlier epochs.
- The results presented in [Chapter 5](#) and [Chapter 6](#) will be a benchmark for future studies aimed at studying the interplay between different physical processes, in a

Chapter 8. Conclusions and future perspectives

more realistic framework, as the SIEGE project ([Calura et al., 2022](#)). However, cosmological simulations, despite being more realistic in taking into account the effects of the surrounding environment, are significantly more computationally expensive, which severely limits the possibility to explore the parameter space. For this reason, simulating isolated clusters is still essential to test different prescriptions, which can then be implemented in cosmological simulations.

LIST OF FIGURES

2.1 A few examples of globular clusters. From left to right, top row: Messier 4 (ESO), Omega Centauri (ESO), Messier 80 (Hubble). Middle row: Messier 53 (Hubble), NGC 6752 (Hubble), Messier 13 (Hubble). Bottom row: Messier 4 (Hubble), NGC 288 (Hubble), 47 Tucanae (Hubble). Credits: ESO.	8
2.2 (Anti)correlations of light elements in Red Giant Branch stars of the globular cluster NGC 2808. Credits: Gratton et al. (2019) . Data from Carretta (2015) and Carretta et al. (2018)	10
2.3 Color magnitude diagrams of the globular cluster NGC 2808 from the ground-based 4-m Blanco telescope (left panel, Walker 1999) and from the Hubble Space Telescope (right panel, Milone et al. 2015).	11
2.4 Chromosome maps of the Type I GC, NGC 6723 (left), and of the Type II GC, NGC 1851 (right). The first population lies on the bottom of the panel, distributed almost horizontally, and therefore at almost constant in $\Delta_C F_{275W,F336W,F438W}$, while the second one is creating a steep branch above the first population. The red triangles represent the red-RGB stars whose presence characterizes the Type II subgroup. Taken from Milone & Marino (2022) but see Milone et al. (2017) for more examples.	13

List of Figures

2.5 The main p-capture cycles with the temperature at which the various cycles become efficient. From left to right the CNO-cycle, the Ne-Na cycle, and the Mg-Al cycle. In red are marked the elements that are produced by these cycles, while in blue are the ones that are depleted. Adapted from Salaris et al. (2002)	15
2.6 Average helium difference between second population (2G) and first population (1G) stars, $\delta Y_{2G,1G}$ (left) and maximum internal helium variation, δY_{max} (right) as a function of the mass of the host cluster. In each panel, it is indicated the Spearman's rank correlation coefficient and the corresponding uncertainty. Taken from Milone et al. (2018b)	17
2.7 The relations between the iron spread $\delta[\text{Fe}/\text{H}]$ of the first population and cluster mass, first population mass, and $[\text{Fe}/\text{H}]$ are plotted. The Spearman's rank correlation coefficient and the associated p-value are quoted in the upper-left corners. Taken from Legnardi et al. (2022)	19
2.8 Weighted mean of the fraction of FG stars versus the present-day mass (left) initial mass (middle) and the age of the host GC (right). Black and gray dots represent respectively Galactic GCs with $M_{ini} < 10^6 M_\odot$ and $M_{ini} > 10^6 M_\odot$, red dots represent extragalactic GCs. Clusters without MPs are represented with open circles. The Spearman's rank correlation coefficient and the associated uncertainty are quoted in the bottom-left corners. Taken from Dondoglio et al. (2021)	20
3.1 Colour-composite image of the field containing the lensed, spectroscopically confirmed star-forming complexes at $z=6.14$, magnified by the galaxy cluster MACS J0416 and that includes proto-GCs(Vanzella et al., 2019). The extended Lyman- α arcs detected with MUSE at $2-\sigma$ are shown by the red contours. The systems D1 and T1 are shown in the bottom right-hand side inset. A structure is visible between D1 and T1, including a very faint star-forming knot, dubbed UT1, indicated by the white circle. Other detected sources include T2, T3, T4 (Vanzella et al., 2021b). Taken from Calura et al. (2022)	22

List of Figures

- 3.2 Schematic visualization of the different phases of the formation of MPs in a GC in the AGB scenario, highlighting the main feedback sources in action as a function of time and associated mass of dying star. 26
- 3.3 Chemical evolution of SG stars in the [Na/Fe] vs. [O/Fe] plane, obtained through a simple one-zone chemical model aimed at studying the composition of SG stars. The dash-dotted line represents the evolution of the gas in the cluster when no accretion of pristine gas is assumed, and, in turn, no dilution is taking place, while the solid line, displays the evolution when the AGB ejecta are diluted with pristine gas. The open circles represent a statistical sampling of SG stars formed along the path. Only few stars are formed along the two branches, while the bulk of them are located near the cusp, that corresponds to the peak of the ISM dilution. Taken from [D'Ercole et al. \(2010\)](#). 27
- 3.4 Schematic visualization of the various phases of the formation of MPs in the FRMS scenario, with associated time since the formation of the first population and the associated mass of the dying star, on the right. Taken from [Krause et al. \(2013\)](#). 30
- 4.1 Disk surface density of the gas component at 500 Myr in isolated Milky Way-like galaxy simulations for nine of the mentioned hydrodynamic codes both edge on (top panel) and face on (bottom panel). ART-I, ART-II, ENZO and RAMSES use the Eulerian approach and are therefore mesh bases, while CHANGA, GASOLINE, GADGET-3, GEAR and GIZMO adopt the Lagrangian one, being particle-based. All codes aim at modeling similarly star formation, feedback, radiative cooling, UV background, metal enrichment and the pressure floor. Likewise, the resolution is kept constant in all the simulations, although this might be incorrect due to the differences between AMR and SPH. Nevertheless, clear differences can be seen between the results of the various codes, the most evident of which is between mesh and particle-based codes, in particular in the inter-arm regions. The figure is taken from the Agora code comparison project ([Kim et al., 2016](#)). 42

List of Figures

4.2	The grid hierarchy starts from the coarser grid, level 0, represented by a Cartesian grid, to the subsequent refined levels. As shown on the top left grid, the refinement must be gradual so that neighboring cells can not have refinement levels that differ more than unity. Credits: Fernando Becerra.	44
4.3	Cooling rate as a function of temperature for a primordial gas composed by H and He in collisional ionizing equilibrium. Contributions from some of the channels highlighted in the text are reported. At low temperatures, cooling is dominated by the excitation of H and He, while at high temperatures by bremsstrahlung. Taken from Katz et al. (1996) .	53
4.4	Cooling functions variations with temperature and metallicity in collisional ionizing equilibrium. The bottom line represents the case of gas with primordial composition and, therefore, metal-free. The higher the metal content, the stronger the cooling. Taken from Sutherland & Dopita (1993) .	54
5.1	The rotation amplitude profiles of NGC 6093 for the primordial (FG) and two subgroups of the SG, labeled intermediate and extreme populations depending on their degree of enrichment (from top to bottom). Taken from Kamann et al. (2020) .	63
5.2	Two-dimensional maps of the gas density (left-hand panels), of the temperature (central panels) and the helium mass fraction (right-hand panels) on the x-y plane for the LDanaz simulation. The corresponding evolutionary time of each set of panels is reported at the top. The white arrows in the helium mass fraction maps represent the gas velocity field.	70
5.3	Two-dimensional maps of the stellar component at two evolutionary times for the LDanaz simulation on the x-y plane (top panels) and y-z plane (bottom panels) at 26 Myr (time reported on the left panels). The first column shows the surface density, the second represents the helium mass fraction Y , and the third the line-of-sight velocity of the stars.	72
5.4	Two-dimensional maps of the stellar component for the LDanaz model at 65 Myr. The reported quantities are as in Figure 5.3.	73

List of Figures

5.5 Total SG density profile at the end of the simulation and SG density profiles for three intervals of the helium mass fraction Y , for the low-density model LDanaz. The density profile of FG stars is also shown (see the legend for the details)	74
5.6 Stellar rotation profiles for the model LDanaz at 65 Myr. On the left: Rotation amplitude of the Cartesian velocity components for SG stars as a function of θ , defined as the angle between the direction of each star projected on the xy plane and the x axis, for three bins of the helium mass fraction Y (see the legend for more details). The FG rotation amplitudes are also shown by the black line. On the right: Radial profiles of the cylindrical velocity components (solid lines) and velocity dispersions σ (dashed lines) for SG stars for three bins of the helium mass fraction Y	75
5.7 Two-dimensional slices of the gas density (left-hand panels) and temperature (right-hand panels) on the x-y plane for the HDanaz simulation. The corresponding evolutionary time is reported on the top of each set of panels. The white arrows in the density maps represent the velocity field of the gas.	77
5.8 Two-dimensional surface density maps of the stellar component at two evolutionary times for the HDanaz simulation on the x-y plane, on the left, and y-z plane, on the right.	79
5.9 Stellar rotation profiles of the model HDanaz at 65 Myr. The reported quantities are as in Figure 5.6.	80
5.10 Two-dimensional maps of the gas density (left-hand panels), of the temperature (central panels) and helium mass fraction (right-hand panels) on the x-y plane for the LDanax simulation. The time is reported on the top of each set of panels. The white arrows in the helium mass fraction maps show the gas velocity field.	81
5.11 Two-dimensional maps of the stellar component for the LDanax model at 28 Myr. The reported quantities are as in Figure 5.3.	83
5.12 Two-dimensional maps of the stellar component for the LDanax model at 64 Myr. The reported quantities are as in Figure 5.3.	84

List of Figures

5.13 Stellar rotation profiles of the model LDanax at 65 Myr. The reported quantities are as in Figure 5.6. Note that the x component is the one parallel to the rotational axis that here is along the x axis.	85
5.14 Two-dimensional maps of the stellar component for the LDsbz model at 27 Myr. The reported quantities are as in Figure 5.3.	87
5.15 Two-dimensional maps of the stellar component for the LDsbz model at 63 Myr. The reported quantities are as in Figure 5.3.	88
5.16 Stellar rotation profiles of the model LDsbz at 65 Myr. The reported quantities are as in Figure 5.6.	89
5.17 The mass distributions of Y in SG stars at the end of the simulations (~ 65 Myr) for different models. On the left: low-density models: LDanaz (blue), LDanax (orange), LDsbz (purple) and LD (green). On the right: high-density models: HDanaz (blue), HDanax (orange) and HD (green). Each distribution is normalised to its maximum value. The pristine gas helium mass fraction Y_{pg} is shown by the black dashed line.	90
6.1 Evolution of a massive cluster $10^7 M_{\odot}$ by means of 1D hydrodynamic simulations. Upper panel: star formation rate evolution. Lower panel: evolution of the amount of mass in gas (solid line) and of SG stars (dashed line). In both panels, the thick lines refer to the model without SNe Ia, while the thin lines represent the model where SNe Ia are exploding every 5×10^4 yr starting at 40 Myr. Taken from D'Ercole et al. (2008).	98
6.2 Spatial distribution of Type Ia SNe as a function of the radius. In black, we show the analytical result for the Plummer profile assuming $M_{\text{FG}} = 10^7 M_{\odot}$ and a Plummer radius $a = 23\text{pc}$. The red line indicates the mean of 1000 realizations with the associated regions within 1 and 2σ in green and light green, respectively. The chosen realization is shown in blue, corresponding to the one that deviates less from the mean among the 1000 realizations. All the plotted lines are normalized imposing $\int_0^{r_{\text{max}}} N_r dr = 1$ with maximum radius $r_{\text{max}} = 80\text{pc}$, which corresponds to half the size of the computational box.	100

6.3 Delay time distribution function. In black, we show the theoretical one from Eq.16 of Greggio (2005) assuming $\alpha = 2.35$ and $\gamma = 2$. The red line indicates the mean of 1000 realizations with the associated regions within 1 and 2 σ in green and light green, respectively. The chosen configuration among the 1000 realizations is shown in blue, namely, the one that deviates less from the mean. The plotted lines are all normalized imposing $\int_{\tau_i}^{\tau_x} N_\tau \, d\tau = 1$ where $\tau_i = 40\text{Myr}$ is the lifetime of a $8M_\odot$ star and $\tau_x = 140\text{Myr}$ in order to cover all the timespan we are focusing on, with the normalization factor in units of Gyr^{-1} 101
6.4 The distribution of the gas density in the cells where the SNe are exploding for the low-density simulation. The red shaded area represents the region of densities for which the Kim & Ostriker (2015) criterion is not satisfied. 103
6.5 The distribution of the gas density in the cells where the SNe are exploding for the high-density simulation. The red shaded area represents the region of densities for which the Kim & Ostriker (2015) criterion is not satisfied. 104
6.6 Two-dimensional maps of the gas density (left-hand panels) and of the temperature (right-hand panels) in the x-y plane at different evolutionary times (reported on top of each pair of panels) for the low-density simulation (LD). From the top left to the bottom right: $t = 10, 26, 39, 48$ Myr. The black arrows in the density maps represent the velocity field, while the green shaded areas represent the regions of the plane where the gas is moving toward the cluster centre (see the text for details). The white dots in the temperature maps represent the newborn stars (with a lifetime of $< 0.05\text{Myr}$). The red contour in the temperature maps describes the region enclosing 50% of the SG mass 108

List of Figures

6.7 First and second columns: total density profile of SG stars at $t = 10, 26, 39, 48$ Myr and density profiles of SG stars for several ranges of the helium mass fraction Y and the [Fe/H] ratio, respectively, for the low-density model (LD). The FG density profile is also plotted (see the legend for the details). Third and fourth columns: the mass distribution of Y and [Fe/H] ratio, respectively, in the SG stars at the aforementioned evolutionary times (reported in each panel). The distributions have been obtained by summing, in each bin, the masses of the stars belonging to it, and then normalizing every distribution to its maximum value. The black dashed lines represent the pristine gas composition both for Y and [Fe/H] ratio, while the solid black line represents the normalized cumulative mass as a function of the [Fe/H] ratio.	111
6.7 Continued	112
6.8 Two-dimensional maps of the gas density on the left-hand panels of each plot and of the temperature on the right-hand panels in the x-y plane at different evolutionary times for the low-density simulation with delayed Type Ia SNe (LD_DS). From the top left to the bottom right: $t = 10, 27, 39, 48$ Myr. Other symbols and lines as in Figure 6.6.	115
6.9 First and second columns: total density profile of SG stars at $t = 10, 27, 39, 48$ Myr and density profiles of SG stars for several ranges of the helium mass fraction Y and the [Fe/H] ratio, respectively, for the low-density model with delayed Type Ia SNe (LD_DS). The FG density profile is also plotted (see the legend for the details). Third and fourth columns: the mass distribution of Y and [Fe/H] ratio, respectively, in the SG stars at the aforementioned evolutionary times (reported in each panel). Other symbols and lines as in Figure 6.7.	117
6.9 Continued	118
6.10 Two-dimensional maps of the gas density on the left-hand panels of each plot and of the temperature on the right-hand panels in the x-y plane at different evolutionary times for the high density (HD) simulation. From the top left to the bottom right: $t = 6, 14, 26, 48$ Myr. Other symbols and lines as in Figure 6.6.	121

6.11 First and second columns: total density profile of SG stars at $t = 6, 14, 26, 39$ Myr and density profiles of SG stars for several ranges of the helium mass fraction Y and the [Fe/H] ratio, respectively, for the high-density model (HD). The FG density profile is also plotted (see the legend for the details). Third and fourth columns: the mass distribution of Y and [Fe/H] ratio, respectively, in the SG stars at the aforementioned evolutionary times (reported in each panel). Other symbols and lines as in Figure 6.7.	124
 6.11 Continued	125
 6.12 First and second columns: total density profile of SG stars at $t = 6, 14, 26, 39$ Myr and density profiles of SG stars for several ranges of the helium mass fraction Y and the [Fe/H] ratio, respectively, for the high-density model with delayed cooling (HD_DC). The FG density profile is also plotted (see the legend for the details). Third and fourth columns: the mass distribution of Y and [Fe/H] ratio, respectively, in the SG stars at the aforementioned evolutionary times (reported in each panel). Other symbols and lines as in Figure 6.7.	127
 6.12 Continued	128
 6.13 Upper panel: evolution of the SG stellar mass for all our simulations. Lower panel: evolution of the SFR for all our models. The blue lines represent the standard low-density models while the red lines the high-density ones. The thin lines show the results obtained by Calura et al. (2019) for their high-resolution simulations. The purple line in the upper panel represents the result of the low-density model at high resolution (LD_HR). The orange lines represent the high-density model with delayed cooling while the light-blue lines represent the low-density model with delayed Type Ia SNe. The green dashed lines represent the low-density model where the infall is switched off once the first SN bubble has reached the negative x boundary.	130

List of Figures

- 7.1 Distribution of the A_2^+ parameter as a function of t/t_{rh} . The A_2^+ parameter is calculated as the area enclosed between the cumulative radial distributions of the two populations, and therefore reveals the degree of mixing. The quantity t_{rh} is the half-mass relaxation time, which determines the dynamical age of the system. The grey dots represent the observed clusters, out of which one belongs to the Small Magellanic Cloud, one to the Large Magellanic Cloud, and the rest to the Milky Way. The blue and green lines are the results of N -body simulations for a second population 5 ad 10 times more centrally concentrated than the first population, respectively. Taken from [Dalessandro et al. \(2019\)](#). 138

7.2 Schematic representation of the Galaxy model adopted for the simulations, on the left, includes the presence of both the thick and thin disk plus the halo, while the effects of the bulge are here not considered. On the right, it is shown the GC model, where the simulated cluster is located at 4 kpc from the Galactic centre and is assumed to orbit on the plane of the disk. Credits: Alessandra Mastrobuono-Battisti. 143

7.3 Mass (top) and mass loss (bottom) as a function of time. The models with the FG only and without stellar evolution, listed in Table 7.1, are shown on the left, while the models with only FG but where stellar evolution is taken into account, listed in Table 7.2, are shown on the right. 148

7.4 Evolution of the half mass radius (top left), mass (top right), SG mass fraction (bottom left), mass loss (bottom right) for some of the models in Table 7.2 reported in the legend. The solid lines in the top panels represent the whole cluster, and the dotted the SG. 153

7.5 Two-dimensional maps at 1 ad 12 Gyr for the model 2N7m1K. *Left panel:* Distribution of the FG (cyan) and SG (magenta) *Right panel:* Mass surface density of the whole cluster. At the centre of both panels, we show a zoom-in focused on the centre of mass of the cluster. 155

List of Figures

- 7.6 Density profiles of the FG (grey), SG (cyan) and the whole cluster (orange) for the model 2N7m1K at three different times, indicated on top of each panel. The half-mass radii of the three components are reported in the legend. In black, blue and red are reported the density profiles at 12 Gyr of the FG, SG and the whole cluster, respectively, for comparison, with the corresponding half-mass radius in the right panel. 156
- 7.7 The profile of M_{SG}/M_{tot} in black and the fraction of enriched stars within r , $f_{\text{enriched}}(< r)$, in red for the model 2N7m1K at 12 Gyr. The vertical grey line represents the half-mass radius of the whole cluster, $r_{h,tot}$ 157
- 7.8 Two-dimensional maps at 2 ad 12 Gyr for the model 5Y7M3.7K. *Left panel:* Distribution of the FG (cyan) and SG (magenta) *Right panel:* Mass surface density of the whole cluster. At the centre of both panels, we show a zoom-in focused on the centre of mass of the cluster. 159
- 7.9 Density profiles of the FG (grey), SG (cyan) and the whole cluster (orange) for the model 5Y7M3.7K at three different times, indicated on top of each panel. The half-mass radii of the three components are reported in the legend. In black, blue and red are reported the density profiles at 12 Gyr of the FG, SG and the whole cluster, respectively, for comparison, with the corresponding half-mass radius in the right panel. 160
- 7.10 The profile of M_{SG}/M_{tot} in black and the fraction of enriched stars within r , $f_{\text{enriched}}(< r)$ in red for the model 5Y7M3.7K at 12 Gyr. The vertical grey line represents the half mass radius of the whole cluster, $r_{h,tot}$ 161
- 7.11 The distribution of stars of the Palomar 5 Galactic globular cluster. The white blob represents the stellar cluster, while the two orange tidal tails are its leading (right) and trailing arms (left), which are extending for almost 10 kpc ([Odenkirchen et al., 2003](#)) and are even more massive than the cluster itself. Credits: Sloan Digital Sky Service. 163

LIST OF TABLES

5.1	Simulations parameters.	65
5.2	Models description. <i>Columns</i> : (1) name of the model, (2) axis around which the cluster rotates, (3) type of velocity profile, (4) density of the pristine gas, (5) starting time of the infall (the initial time of the simulations is fixed at $t_{\text{AGB}} = 39 \text{Myr}$), (6) spatial resolution.	66
6.1	Models description. <i>Columns</i> : (1) name of the model, (2) description of the model, (3) pristine gas density, (4) time of pristine gas reaccretion, (5) starting time of Type Ia SN explosions, (6) resolution. Times listed in (4) and (5) are expressed assuming $t_{\text{AGB}} = 39 \text{ Myr}$ as the time zero.	106
7.1	Models with neither stellar evolution nor SG stars run in this work. The initial mass of each simulated cluster is $M_0 = 8.4 \times 10^6 M_\odot$, after the removal of 16% of its mass.	145
7.2	Models with simplified stellar evolution and without SG stars run in this work. The initial mass of each simulated cluster is $M_0 = 8.4 \times 10^6 M_\odot$, after the removal of 16% of its mass.	146
7.3	Models with both simplified stellar evolution and SG stars. The initial FG mass of each simulated cluster is $M_0 = 8.4 \times 10^6 M_\odot$, after the removal of 16% of its mass. Masses are all in terms of 10^5	150

BIBLIOGRAPHY

- Agrawal P., Hurley J., Stevenson S., Szécsi D., Flynn C., 2020, [MNRAS](#), **497**, 4549
- Allen C., Santillan A., 1991, [Rev. Mexicana Astron. Astrofis.](#), **22**, 255
- Alvarez Garay D. A., Mucciarelli A., Lardo C., Bellazzini M., Merle T., 2022, [ApJ](#), **928**, L11
- Ambartsumian V. A., 1938, [TsAGI Uchenye Zapiski](#), **22**, 19
- Armandroff T. E., 1989, [AJ](#), **97**, 375
- Armandroff T. E., Zinn R., 1988, [AJ](#), **96**, 92
- Arunima A., Pfalzner S., Govind A., 2023, arXiv e-prints, p. [arXiv:2301.03311](#)
- Bagla J. S., 2002, [Journal of Astrophysics and Astronomy](#), **23**, 185
- Bailin J., 2019, [ApJS](#), **245**, 5
- Ballone A., Mapelli M., Di Carlo U. N., Torniamenti S., Spera M., Rastello S., 2020, [MNRAS](#), **496**, 49
- Banerjee S., Kroupa P., 2011, [ApJ](#), **741**, L12
- Barnes J., Hut P., 1986, [Nature](#), **324**, 446
- Bastian N., Lardo C., 2015, [MNRAS](#), **453**, 357
- Bastian N., Lardo C., 2018, [ARA&A](#), **56**, 83

Bibliography

- Bastian N., Lamers H. J. G. L. M., de Mink S. E., Longmore S. N., Goodwin S. P., Gieles M., 2013a, [MNRAS](#), **436**, 2398
- Bastian N., Cabrera-Ziri I., Davies B., Larsen S. S., 2013b, [MNRAS](#), **436**, 2852
- Baumgardt H., Hilker M., 2018, [MNRAS](#), **478**, 1520
- Baumgardt H., Kroupa P., 2007, [MNRAS](#), **380**, 1589
- Baumgardt H., Makino J., 2003, [MNRAS](#), **340**, 227
- Baumgardt H., De Marchi G., Kroupa P., 2008, [ApJ](#), **685**, 247
- Bedin L. R., Piotto G., Anderson J., Cassisi S., King I. R., Momany Y., Carraro G., 2004, [ApJ](#), **605**, L125
- Bekki K., 2010, [ApJ](#), **724**, L99
- Bekki K., 2011, [MNRAS](#), **412**, 2241
- Bekki K., 2012, [MNRAS](#), **421**, L44
- Bekki K., 2019, [MNRAS](#), **486**, 2570
- Bekki K., Jeřábková T., Kroupa P., 2017, [MNRAS](#), **471**, 2242
- Bellazzini M., Bragaglia A., Carretta E., Gratton R. G., Lucatello S., Catanzaro G., Leone F., 2012, [A&A](#), **538**, A18
- Bellini A., et al., 2015, [ApJ](#), **810**, L13
- Bellini A., et al., 2018, [ApJ](#), **853**, 86
- Berger M. J., Colella P., 1989, [Journal of Computational Physics](#), **82**, 64
- Berger M. J., Oliger J., 1984, [Journal of Computational Physics](#), **53**, 484
- Bianchini P., van der Marel R. P., del Pino A., Watkins L. L., Bellini A., Fardal M. A., Libralato M., Sills A., 2018, [MNRAS](#), **481**, 2125
- Bica E., Bonatto C., Barbuy B., Ortolani S., 2006, [A&A](#), **450**, 105

Bibliography

- Bica E., Ortolani S., Barbuy B., 2016, [PASA](#), **33**, e028
- Binney J., Tremaine S., 2008, Galactic Dynamics: Second Edition
- Bloecker T., Schoenberner D., 1991, [A&A](#), **244**, L43
- Boberg O. M., Vesperini E., Friel E. D., Tiongco M. A., Varri A. L., 2017, [ApJ](#), **841**, 114
- Bondi H., Hoyle F., 1944, [MNRAS](#), **104**, 273
- Boothroyd A. I., Sackmann I. J., Wasserburg G. J., 1995, [ApJ](#), **442**, L21
- Breen P. G., 2018, [MNRAS](#), **481**, L110
- Bryan G. L., et al., 2014, [ApJS](#), **211**, 19
- Bullock J. S., Johnston K. V., 2005, [ApJ](#), **635**, 931
- Cabrera-Ziri I., Bastian N., Davies B., Magris G., Bruzual G., Schweizer F., 2014, [MNRAS](#), **441**, 2754
- Cabrera-Ziri I., et al., 2015, [MNRAS](#), **448**, 2224
- Cabrera-Ziri I., et al., 2016, [MNRAS](#), **457**, 809
- Calura F., Few C. G., Romano D., D'Ercole A., 2015, [ApJ](#), **814**, L14
- Calura F., D'Ercole A., Vesperini E., Vanzella E., Sollima A., 2019, [MNRAS](#), **489**, 3269
- Calura F., et al., 2021, [MNRAS](#), **500**, 3083
- Calura F., et al., 2022, [MNRAS](#), **516**, 5914
- Cameron A. G. W., Fowler W. A., 1971, [ApJ](#), **164**, 111
- Capuzzo-Dolcetta R., Mastrobuono-Battisti A., Maschietti D., 2011, [New A](#), **16**, 284
- Carretta E., 2015, [ApJ](#), **810**, 148
- Carretta E., et al., 2009a, [A&A](#), **505**, 117
- Carretta E., Bragaglia A., Gratton R., Lucatello S., 2009b, [A&A](#), **505**, 139

Bibliography

- Carretta E., Bragaglia A., Gratton R., D’Orazi V., Lucatello S., 2009c, [A&A, 508, 695](#)
- Carretta E., Bragaglia A., Gratton R. G., Recio-Blanco A., Lucatello S., D’Orazi V., Cassisi S., 2010, [A&A, 516, A55](#)
- Carretta E., Bragaglia A., Lucatello S., Gratton R. G., D’Orazi V., Sollima A., 2018, [A&A, 615, A17](#)
- Chantereau W., Biernacki P., Martig M., Bastian N., Salaris M., Teyssier R., 2020, [MNRAS, 493, 1306](#)
- Charbonnel C., Chantereau W., Krause M., Primas F., Wang Y., 2014, [A&A, 569, L6](#)
- Chen Y., Li H., Vogelsberger M., 2021, [MNRAS, 502, 6157](#)
- Chernoff D. F., Weinberg M. D., 1990, [ApJ, 351, 121](#)
- Ciotti L., D’Ercole A., Pellegrini S., Renzini A., 1991, [ApJ, 376, 380](#)
- Claeyssens A., Adamo A., Richard J., Mahler G., Messa M., Dessauges-Zavadsky M., 2023, [MNRAS,](#)
- Clarke C. J., Bonnell I. A., 2008, [MNRAS, 388, 1171](#)
- Cohen J. G., Kirby E. N., 2012, [ApJ, 760, 86](#)
- Colella P., Glaz H. M., 1985, [Journal of Computational Physics, 59, 264](#)
- Contenta F., Varri A. L., Heggie D. C., 2015, [MNRAS, 449, L100](#)
- Cordero M. J., Pilachowski C. A., Johnson C. I., McDonald I., Zijlstra A. A., Simmerer J., 2014, [ApJ, 780, 94](#)
- Cordero M. J., Hénault-Brunet V., Pilachowski C. A., Balbinot E., Johnson C. I., Varri A. L., 2017, [MNRAS, 465, 3515](#)
- Cordoni G., Milone A. P., Mastrobuono-Battisti A., Marino A. F., Lagioia E. P., Tailo M., Baumgardt H., Hilker M., 2020a, [ApJ, 889, 18](#)
- Cordoni G., et al., 2020b, [ApJ, 898, 147](#)

Bibliography

- Côté P., 1999, [AJ, 118, 406](#)
- Cottrell P. L., Da Costa G. S., 1981, [ApJ, 245, L79](#)
- Couchman H. M. P., 1991, [ApJ, 368, L23](#)
- Creasey P., Theuns T., Bower R. G., 2013, [MNRAS, 429, 1922](#)
- D'Antona F., Caloi V., D'Ercole A., Tailo M., Vesperini E., Ventura P., Di Criscienzo M., 2013, [MNRAS, 434, 1138](#)
- D'Antona F., Vesperini E., D'Ercole A., Ventura P., Milone A. P., Marino A. F., Tailo M., 2016, [MNRAS, 458, 2122](#)
- D'Antona F., Ventura P., Fabiola Marino A., Milone A. P., Tailo M., Di Criscienzo M., Vesperini E., 2019, [ApJ, 871, L19](#)
- D'Ercole A., Vesperini E., D'Antona F., McMillan S. L. W., Recchi S., 2008, [MNRAS, 391, 825](#)
- D'Ercole A., D'Antona F., Ventura P., Vesperini E., McMillan S. L. W., 2010, [MNRAS, 407, 854](#)
- D'Ercole A., D'Antona F., Vesperini E., 2011, [MNRAS, 415, 1304](#)
- D'Ercole A., D'Antona F., Carini R., Vesperini E., Ventura P., 2012, [MNRAS, 423, 1521](#)
- D'Ercole A., D'Antona F., Vesperini E., 2016, [MNRAS, 461, 4088](#)
- D'Orazi V., Gratton R., Lucatello S., Carretta E., Bragaglia A., Marino A. F., 2010, [ApJ, 719, L213](#)
- D'Orazi V., Angelou G. C., Gratton R. G., Lattanzio J. C., Bragaglia A., Carretta E., Lucatello S., Momany Y., 2014, [ApJ, 791, 39](#)
- D'Orazi V., et al., 2015, [MNRAS, 449, 4038](#)
- Dalessandro E., Lapenna E., Mucciarelli A., Origlia L., Ferraro F. R., Lanzoni B., 2016, [ApJ, 829, 77](#)
- Dalessandro E., et al., 2019, [ApJ, 884, L24](#)

Bibliography

- Dalejandro E., Raso S., Kamann S., Bellazzini M., Vesperini E., Bellini A., Beccari G., 2021, [MNRAS](#), **506**, 813
- Decressin T., Charbonnel C., Meynet G., 2007, [A&A](#), **475**, 859
- Dejonghe H., 1987, [MNRAS](#), **224**, 13
- Denissenkov P. A., Hartwick F. D. A., 2014, [MNRAS](#), **437**, L21
- Denissenkov P. A., Herwig F., 2003, [ApJ](#), **590**, L99
- Di Matteo P., 2016, [PASA](#), **33**, e027
- Dondoglio E., Milone A. P., Lagioia E. P., Marino A. F., Tailo M., Cordoni G., Jang S., Carlos M., 2021, [ApJ](#), **906**, 76
- Efstathiou G., Eastwood J. W., 1981, [MNRAS](#), **194**, 503
- Einsel C., Spurzem R., 1999, [MNRAS](#), **302**, 81
- Elmegreen B. G., 2017, [ApJ](#), **836**, 80
- Emerick A., Bryan G. L., Mac Low M.-M., 2019, [MNRAS](#), **482**, 1304
- Ernst A., Glaschke P., Fiestas J., Just A., Spurzem R., 2007, [MNRAS](#), **377**, 465
- Errani R., Penarrubia J., Tormen G., 2015, [MNRAS](#), **449**, L46
- Fabricius M. H., et al., 2014, [ApJ](#), **787**, L26
- Faisst A. L., Chary R. R., Brammer G., Toft S., 2022, [ApJ](#), **941**, L11
- Ferland G. J., Korista K. T., Verner D. A., Ferguson J. W., Kingdon J. B., Verner E. M., 1998, [PASP](#), **110**, 761
- Fernández-Trincado J. G., et al., 2021, [A&A](#), **648**, A70
- Fernández-Trincado J. G., et al., 2022, [A&A](#), **663**, A126
- Ferraro F. R., et al., 2018, [ApJ](#), **860**, 50
- Few C. G., Courtey S., Gibson B. K., Michel-Dansac L., Calura F., 2014, [MNRAS](#), **444**, 3845

Bibliography

- Fiocrentino G., et al., 2017, arXiv e-prints, p. [arXiv:1712.04222](https://arxiv.org/abs/1712.04222)
- Fischer P., Welch D. L., Cote P., Mateo M., Madore B. F., 1992, [AJ, 103, 857](#)
- Fischer P., Welch D. L., Mateo M., 1993, [AJ, 105, 938](#)
- Frenk C. S., Fall S. M., 1982, [MNRAS, 199, 565](#)
- Fryxell B., et al., 2000, [ApJS, 131, 273](#)
- Fujii M. S., Portegies Zwart S., 2011, [Science, 334, 1380](#)
- Gatto M., et al., 2020, [MNRAS, 499, 4114](#)
- Gieles M., et al., 2018, [MNRAS, 478, 2461](#)
- Giersz M., Askar A., Wang L., Hypki A., Leveque A., Spurzem R., 2019, [MNRAS, 487, 2412](#)
- Gingold R. A., Monaghan J. J., 1977, [MNRAS, 181, 375](#)
- Gnedin O. Y., Ostriker J. P., 1997, [ApJ, 474, 223](#)
- Gratton R. G., Carretta E., Bragaglia A., 2012, [A&A Rev., 20, 50](#)
- Gratton R., Bragaglia A., Carretta E., D’Orazi V., Lucatello S., Sollima A., 2019, [A&A Rev., 27, 8](#)
- Greggio L., 2005, [A&A, 441, 1055](#)
- Haffner L. M., et al., 2009, [Reviews of Modern Physics, 81, 969](#)
- Haghi H., Hoseini-Rad S. M., Zonoozi A. H., Küpper A. H. W., 2014, [MNRAS, 444, 3699](#)
- Harris W. E., 2010, arXiv e-prints, p. [arXiv:1012.3224](https://arxiv.org/abs/1012.3224)
- Hénault-Brunet V., et al., 2012, [A&A, 545, L1](#)
- Hénault-Brunet V., Gieles M., Agertz O., Read J. I., 2015, [MNRAS, 450, 1164](#)
- Herschel W., 1789, [Philosophical Transactions of the Royal Society of London](#)
- Herwig F., 2004, [ApJ, 605, 425](#)

Bibliography

- Hockney R. W., Eastwood J. W., 1981, Computer Simulation Using Particles
- Hockney R. W., Goel S. P., Eastwood J. W., 1974, *Journal of Computational Physics*, **14**, 148
- Hong J., Kim E., Lee H. M., Spurzem R., 2013, *MNRAS*, **430**, 2960
- Hopkins P. F., Murray N., Quataert E., Thompson T. A., 2010, *MNRAS*, **401**, L19
- Hopkins P. F., Quataert E., Murray N., 2012, *MNRAS*, **421**, 3522
- Hypki A., Giersz M., Hong J., Leveque A., Askar A., Belloni D., Otulakowska-Hypka M., 2022, arXiv e-prints, p. [arXiv:2205.05397](https://arxiv.org/abs/2205.05397)
- Inoue S., Yoshida N., Hernquist L., 2021, *MNRAS*, **507**, 6140
- Jang S., et al., 2022, *MNRAS*, **517**, 5687
- Jeans J. H., 1902, *Philosophical Transactions of the Royal Society of London Series A*, **199**, 1
- Jessop C., Duncan M., Chau W. Y., 1994, *Journal of Computational Physics*, **115**, 339
- Johnson C. I., Rich R. M., Pilachowski C. A., Caldwell N., Mateo M., Bailey John I. I., Crane J. D., 2015, *AJ*, **150**, 63
- Kacharov N., et al., 2014, *A&A*, **567**, A69
- Kamann S., et al., 2018, *MNRAS*, **473**, 5591
- Kamann S., et al., 2020, *MNRAS*, **492**, 966
- Kapse S., de Grijs R., Kamath D., Zucker D. B., 2022, *ApJ*, **927**, L10
- Karakas A., Lattanzio J. C., 2007, *PASA*, **24**, 103
- Karakas A. I., Lattanzio J. C., 2014, *PASA*, **31**, e030
- Katz N., 1992, *ApJ*, **391**, 502
- Katz N., Weinberg D. H., Hernquist L., 1996, *ApJS*, **105**, 19

Bibliography

- Keller S. C., 2004, [PASA](#), **21**, 310
- Kennicutt Robert C. J., 1998, [ARA&A](#), **36**, 189
- Khalaj P., Baumgardt H., 2015, [MNRAS](#), **452**, 924
- Khokhlov A., 1998, [Journal of Computational Physics](#), **143**, 519
- Kim C.-G., Ostriker E. C., 2015, [ApJ](#), **802**, 99
- Kim E., Einsel C., Lee H. M., Spurzem R., Lee M. G., 2002, [MNRAS](#), **334**, 310
- Kim E., Lee H. M., Spurzem R., 2004, [MNRAS](#), **351**, 220
- Kim E., Yoon I., Lee H. M., Spurzem R., 2008, [MNRAS](#), **383**, 2
- Kim J.-h., et al., 2016, [ApJ](#), **833**, 202
- Kim C.-G., Ostriker E. C., Raileanu R., 2017, [ApJ](#), **834**, 25
- Kimm T., Cen R., Rosdahl J., Yi S. K., 2016, [ApJ](#), **823**, 52
- King I. R., 1966, [AJ](#), **71**, 64
- Klypin A. A., Shandarin S. F., 1983, [MNRAS](#), **204**, 891
- Koch A., Grebel E. K., Martell S. L., 2019, [A&A](#), **625**, A75
- Krause M., Charbonnel C., Decressin T., Meynet G., Prantzos N., 2013, [A&A](#), **552**, A121
- Kravtsov A. V., Gnedin O. Y., 2005, [ApJ](#), **623**, 650
- Kravtsov A. V., Klypin A. A., Khokhlov A. M., 1997, [ApJS](#), **111**, 73
- Kroupa P., 2001, [MNRAS](#), **322**, 231
- Kruijssen J. M. D., 2015, [MNRAS](#), **454**, 1658
- Krumholz M. R., McKee C. F., Bland-Hawthorn J., 2019, [ARA&A](#), **57**, 227
- Küpper A. H. W., Maschberger T., Kroupa P., Baumgardt H., 2011, [MNRAS](#), **417**, 2300
- Lacchin E., Calura F., Vesperini E., 2021, [MNRAS](#), **506**, 5951

Bibliography

- Lacchin E., Calura F., Vesperini E., Mastrobuono-Battisti A., 2022, [MNRAS](#), **517**, 1171
- Lada C. J., Lada E. A., 2003, [ARA&A](#), **41**, 57
- Lada C. J., Margulis M., Dearborn D., 1984, [ApJ](#), **285**, 141
- Lagioia E. P., et al., 2018, [MNRAS](#), **475**, 4088
- Lagioia E. P., Milone A. P., Marino A. F., Dotter A., 2019, [ApJ](#), **871**, 140
- Lançon A., et al., 2021, in Siebert A., et al., eds, SF2A-2021: Proceedings of the Annual meeting of the French Society of Astronomy and Astrophysics. pp 447–450 ([arXiv:2110.13783](#))
- Lanzoni B., et al., 2018a, [ApJ](#), **861**, 16
- Lanzoni B., et al., 2018b, [ApJ](#), **865**, 11
- Lardo C., Bellazzini M., Pancino E., Carretta E., Bragaglia A., Dalessandro E., 2011, [A&A](#), **525**, A114
- Lardo C., et al., 2015, [A&A](#), **573**, A115
- Larsen S. S., Strader J., Brodie J. P., 2012, [A&A](#), **544**, L14
- Larsen S. S., Brodie J. P., Grundahl F., Strader J., 2014, [ApJ](#), **797**, 15
- Larsen S. S., Baumgardt H., Bastian N., Brodie J. P., Grundahl F., Strader J., 2015, [ApJ](#), **804**, 71
- Lattanzio J. C., 1992, [PASA](#), **10**, 120
- Leanza S., et al., 2022, arXiv e-prints, p. [arXiv:2203.07294](#)
- Lee J.-W., 2015, [ApJS](#), **219**, 7
- Lee J.-W., 2017, [ApJ](#), **844**, 77
- Lee J.-W., 2018, [ApJS](#), **238**, 24
- Lee Y. W., Joo J. M., Sohn Y. J., Rey S. C., Lee H. C., Walker A. R., 1999, [Nature](#), **402**, 55

Bibliography

- Lee M. G., Bae J. H., Jang I. S., 2022, [ApJ](#), **940**, L19
- Legnardi M. V., et al., 2022, [MNRAS](#), **513**, 735
- Leigh N. W. C., Mastrobuono-Battisti A., Perets H. B., Böker T., 2014, [MNRAS](#), **441**, 919
- Li H., Gnedin O. Y., 2019, [MNRAS](#), **486**, 4030
- Li C., et al., 2022, [Research in Astronomy and Astrophysics](#), **22**, 095004
- Libralato M., Bellini A., Piotto G., Nardiello D., van der Marel R. P., Anderson J., Bedin L. R., Vesperini E., 2019, [ApJ](#), **873**, 109
- Lim D., Lee Y.-W., Pasquato M., Han S.-I., Roh D.-G., 2016, [ApJ](#), **832**, 99
- Lind K., Primas F., Charbonnel C., Grundahl F., Asplund M., 2009, [A&A](#), **503**, 545
- Livernois A. R., Vesperini E., Varri A. L., Hong J., Tiongco M., 2022, [MNRAS](#), **512**, 2584
- Lucatello S., Sollima A., Gratton R., Vesperini E., D’Orazi V., Carretta E., Bragaglia A., 2015, [A&A](#), **584**, A52
- Lucertini F., Nardiello D., Piotto G., 2020, arXiv e-prints, p. [arXiv:2012.06590](#)
- Lucy L. B., 1977, [AJ](#), **82**, 1013
- Lützgendorf N., et al., 2013, [A&A](#), **552**, A49
- Lynden-Bell D., 1967, [MNRAS](#), **136**, 101
- Ma X., et al., 2020, [MNRAS](#), **493**, 4315
- Mackey A. D., Da Costa G. S., Ferguson A. M. N., Yong D., 2013, [ApJ](#), **762**, 65
- Maio U., Dolag K., Ciardi B., Tornatore L., 2007, [MNRAS](#), **379**, 963
- Maoz D., Mannucci F., Nelemans G., 2014, [ARA&A](#), **52**, 107
- Mapelli M., 2017, [MNRAS](#), **467**, 3255
- Marino A. F., Villanova S., Piotto G., Milone A. P., Momany Y., Bedin L. R., Medling A. M., 2008, [A&A](#), **490**, 625

Bibliography

- Marino A. F., et al., 2014, [MNRAS](#), **437**, 1609
- Marino A. F., et al., 2015, [MNRAS](#), **450**, 815
- Marino A. F., et al., 2018, [ApJ](#), **859**, 81
- Marino A. F., et al., 2019a, [MNRAS](#), **487**, 3815
- Marino A. F., et al., 2019b, [ApJ](#), **887**, 91
- Marino A. F., et al., 2021, Solving the globular clusters multiple population enigma through JWST, JWST Proposal. Cycle 1
- Martell S. L., Grebel E. K., 2010, [A&A](#), **519**, A14
- Martell S. L., Smolinski J. P., Beers T. C., Grebel E. K., 2011, [A&A](#), **534**, A136
- Martell S. L., et al., 2016, [ApJ](#), **825**, 146
- Martens S., et al., 2023, [arXiv e-prints](#), p. arXiv:2301.08675
- Martins F., Chantereau W., Charbonnel C., 2021, [arXiv e-prints](#), p. arXiv:2104.13988
- Martocchia S., et al., 2018, [MNRAS](#), **473**, 2688
- Masseron T., et al., 2019, [A&A](#), **622**, A191
- Mastrobuono-Battisti A., Perets H. B., 2013, [ApJ](#), **779**, 85
- Mastrobuono-Battisti A., Perets H. B., 2016, [ApJ](#), **823**, 61
- Mastrobuono-Battisti A., Perets H. B., 2021, [MNRAS](#), **505**, 2548
- Mastrobuono-Battisti A., Di Matteo P., Montuori M., Haywood M., 2012, [A&A](#), **546**, L7
- Mastrobuono-Battisti A., Khoperskov S., Di Matteo P., Haywood M., 2019, [A&A](#), **622**, A86
- McKenzie M., Bekki K., 2021, [MNRAS](#), **500**, 4578
- McLaughlin D. E., van der Marel R. P., 2005, [ApJS](#), **161**, 304

Bibliography

- Menon H., Wesolowski L., Zheng G., Jetley P., Kale L., Quinn T., Governato F., 2015, [Computational Astrophysics and Cosmology](#), 2, 1
- Mészáros S., et al., 2015, [AJ](#), 149, 153
- Meštrić U., et al., 2022, [MNRAS](#), 516, 3532
- Mignone A., Bodo G., Massaglia S., Matsakos T., Tesileanu O., Zanni C., Ferrari A., 2007, [ApJS](#), 170, 228
- Milone A. P., Marino A. F., 2022, [Universe](#), 8, 359
- Milone A. P., et al., 2012, [ApJ](#), 744, 58
- Milone A. P., et al., 2015, [ApJ](#), 808, 51
- Milone A. P., et al., 2017, [MNRAS](#), 464, 3636
- Milone A. P., Marino A. F., Mastrobuono-Battisti A., Lagioia E. P., 2018a, [MNRAS](#), 479, 5005
- Milone A. P., et al., 2018b, [MNRAS](#), 481, 5098
- Milone A. P., et al., 2019, [MNRAS](#), 484, 4046
- Milone A. P., et al., 2020a, [MNRAS](#), 491, 515
- Milone A. P., et al., 2020b, [MNRAS](#), 492, 5457
- Milone A. P., et al., 2023
- Minniti D., 1995, [AJ](#), 109, 1663
- Moeckel N., Clarke C. J., 2011, [MNRAS](#), 410, 2799
- Moeckel N., Throop H. B., 2009, [ApJ](#), 707, 268
- Mowla L., et al., 2022, [ApJ](#), 937, L35
- Mucciarelli A., Origlia L., Ferraro F. R., Pancino E., 2009, [ApJ](#), 695, L134
- Mucciarelli A., Bellazzini M., Ibata R., Merle T., Chapman S. C., Dalessandro E., Sollima A., 2012, [MNRAS](#), 426, 2889

Bibliography

- Mucciarelli A., Bellazzini M., Merle T., Plez B., Dalessandro E., Ibata R., 2015, [ApJ, 801, 68](#)
- Mucciarelli A., Salaris M., Monaco L., Bonifacio P., Fu X., Villanova S., 2018, [A&A, 618, A134](#)
- Naiman J. P., Ramirez-Ruiz E., Lin D. N. C., 2011, [ApJ, 735, 25](#)
- Nardiello D., et al., 2015, [MNRAS, 451, 312](#)
- Nardiello D., Piotto G., Milone A. P., Rich R. M., Cassisi S., Bedin L. R., Bellini A., Renzini A., 2019, [MNRAS, 485, 3076](#)
- Niederhofer F., et al., 2017, [MNRAS, 465, 4159](#)
- Nipoti C., Cherchi G., Iorio G., Calura F., 2021, [MNRAS, 503, 4221](#)
- Norris J., Freeman K. C., 1979, [ApJ, 230, L179](#)
- Odenkirchen M., et al., 2003, [AJ, 126, 2385](#)
- Osborn W., 1971, *The Observatory*, [91, 223](#)
- Pancino E., Ferraro F. R., Bellazzini M., Piotto G., Zoccali M., 2000, [ApJ, 534, L83](#)
- Pancino E., Galfo A., Ferraro F. R., Bellazzini M., 2007, [ApJ, 661, L155](#)
- Pancino E., et al., 2017, [A&A, 601, A112](#)
- Pasquini L., Bonifacio P., Molinaro P., Francois P., Spite F., Gratton R. G., Carretta E., Wolff B., 2005, [A&A, 441, 549](#)
- Phillips S. G., et al., 2022, [MNRAS, 510, 3727](#)
- Piotto G., 2009, in Mamajek E. E., Soderblom D. R., Wyse R. F. G., eds, Vol. 258, *The Ages of Stars*. pp 233–244, doi:10.1017/S1743921309031883
- Piotto G., et al., 2005, [ApJ, 621, 777](#)
- Piotto G., et al., 2007, [ApJ, 661, L53](#)
- Piotto G., et al., 2015, [AJ, 149, 91](#)

Bibliography

- Plummer H. C., 1911, [MNRAS](#), **71**, 460
- Portegies Zwart S. F., Makino J., McMillan S. L. W., Hut P., 1999, [A&A](#), **348**, 117
- Portegies Zwart S. F., Baumgardt H., Hut P., Makino J., McMillan S. L. W., 2004, [Nature](#), **428**, 724
- Pouliasis E., Di Matteo P., Haywood M., 2017, [A&A](#), **598**, A66
- Prantzos N., Charbonnel C., Iliadis C., 2017, [A&A](#), **608**, A28
- Press W. H., Teukolsky S. A., Vetterling W. T., Flannery B. P., 1992, Numerical recipes in FORTRAN. The art of scientific computing
- Price D. J., et al., 2018, [PASA](#), **35**, e031
- Priestley W., Ruffert M., Salaris M., 2011, [MNRAS](#), **411**, 1935
- Ramírez I., Meléndez J., Chanamé J., 2012, [ApJ](#), **757**, 164
- Rasera Y., Teyssier R., 2006, [A&A](#), **445**, 1
- Reina-Campos M., Kruijssen J. M. D., Pfeffer J., Bastian N., Crain R. A., 2018, [MNRAS](#), **481**, 2851
- Renaud F., Agertz O., Gieles M., 2017, [MNRAS](#), **465**, 3622
- Renzini A., et al., 2015, [MNRAS](#), **454**, 4197
- Renzini A., Marino A. F., Milone A. P., 2022, arXiv e-prints, p. [arXiv:2203.03002](#)
- Revaz Y., Jablonka P., 2012, [A&A](#), **538**, A82
- Richer H. B., Heyl J., Anderson J., Kalirai J. S., Shara M. M., Dotter A., Fahlman G. G., Rich R. M., 2013, [ApJ](#), **771**, L15
- Roe P. L., 1986, [Annual Review of Fluid Mechanics](#), **18**, 337
- Romano D., Calura F., D’Ercole A., Few C. G., 2019, [A&A](#), **630**, A140
- Rosdahl J., Schaye J., Dubois Y., Kimm T., Teyssier R., 2017, [MNRAS](#), **466**, 11

Bibliography

- Rosen A., Bregman J. N., 1995, [ApJ, 440, 634](#)
- Roy A., Sutherland R. S., Krumholz M. R., Heger A., Dopita M. A., 2020, [MNRAS, 494, 3861](#)
- Salaris M., Cassisi S., Weiss A., 2002, [PASP, 114, 375](#)
- Saltzman J., 1994, [Journal of Computational Physics, 115, 153](#)
- Scalzo R. A., Ruiter A. J., Sim S. A., 2014, [MNRAS, 445, 2535](#)
- Schaerer D., Charbonnel C., 2011, [MNRAS, 413, 2297](#)
- Schiavon R. P., et al., 2017, [MNRAS, 465, 501](#)
- Schmidt M., 1959, [ApJ, 129, 243](#)
- Shen Z. X., Bonifacio P., Pasquini L., Zaggia S., 2010, [A&A, 524, L2](#)
- Shima E., Matsuda T., Takeda H., Sawada K., 1985, [MNRAS, 217, 367](#)
- Siess L., 2010, [A&A, 512, A10](#)
- Simioni M., Milone A. P., Bedin L. R., Aparicio A., Piotto G., Vesperini E., Hong J., 2016, [MNRAS, 463, 449](#)
- Smith L. J., Crowther P. A., Calzetti D., Sidoli F., 2016, [ApJ, 823, 38](#)
- Sollima A., 2021, [MNRAS, 502, 1974](#)
- Sollima A., Ferraro F. R., Bellazzini M., Origlia L., Straniero O., Pancino E., 2007, [ApJ, 654, 915](#)
- Sollima A., Nipoti C., Mastrobuono Battisti A., Montuori M., Capuzzo-Dolcetta R., 2012, [ApJ, 744, 196](#)
- Sollima A., Baumgardt H., Hilker M., 2019, [MNRAS, 485, 1460](#)
- Sollima A., Gratton R., Lucatello S., Carretta E., 2022, [MNRAS, 512, 776](#)
- Spitzer Lyman J., 1940, [MNRAS, 100, 396](#)

Bibliography

- Springel V., 2010, [MNRAS](#), **401**, 791
- Springel V., Yoshida N., White S. D. M., 2001, [New A](#), **6**, 79
- Stone J. M., Norman M. L., 1992, [ApJS](#), **80**, 753
- Stone J. M., Gardiner T. A., Teuben P., Hawley J. F., Simon J. B., 2008, [ApJS](#), **178**, 137
- Stone J. M., Tomida K., White C. J., Felker K. G., 2020, [ApJS](#), **249**, 4
- Sutherland R. S., Dopita M. A., 1993, [ApJS](#), **88**, 253
- Szigeti L., Mészáros S., Szabó G. M., Fernández-Trincado J. G., Lane R. R., Cohen R. E., 2021, [MNRAS](#), **504**, 1144
- Tanikawa A., Fukushige T., 2009, [PASJ](#), **61**, 721
- Teuben P., 1995, in Shaw R. A., Payne H. E., Hayes J. J. E., eds, Astronomical Society of the Pacific Conference Series Vol. 77, Astronomical Data Analysis Software and Systems IV. p. 398
- Teyssier R., 2002, [A&A](#), **385**, 337
- Teyssier R., Pontzen A., Dubois Y., Read J. I., 2013, [MNRAS](#), **429**, 3068
- Tiongco M. A., Vesperini E., Varri A. L., 2017, [MNRAS](#), **469**, 683
- Tiongco M. A., Vesperini E., Varri A. L., 2018, [MNRAS](#), **475**, L86
- Tiongco M. A., Vesperini E., Varri A. L., 2019, [MNRAS](#), **487**, 5535
- Tiongco M., Collier A., Varri A. L., 2021, [MNRAS](#), **506**, 4488
- Tiongco M. A., Vesperini E., Varri A. L., 2022, [MNRAS](#), **512**, 1584
- Toro E., 1997, Riemann Solvers and Numerical Methods for Fluid Dynamics, doi:[10.1007/b79761](https://doi.org/10.1007/b79761).
- Truelove J. K., Klein R. I., McKee C. F., Holliman John H. I., Howell L. H., Greenough J. A., 1997, [ApJ](#), **489**, L179
- Van Den Bergh S., 2003, [ApJ](#), **590**, 797

Bibliography

- Vanzella E., et al., 2017, [MNRAS](#), **467**, 4304
- Vanzella E., et al., 2019, [MNRAS](#), **483**, 3618
- Vanzella E., et al., 2021a, Constraining the nature of the first stellar complexes: globular cluster precursors and Population III stellar clusters at z 6-7, JWST Proposal. Cycle 1, ID. #1908
- Vanzella E., et al., 2021b, [A&A](#), **646**, A57
- Vanzella E., et al., 2022, [ApJ](#), **940**, L53
- Vasiliev E., Baumgardt H., 2021, [MNRAS](#), **505**, 5978
- Ventura P., D'Antona F., 2008, [A&A](#), **479**, 805
- Ventura P., D'Antona F., 2011, [MNRAS](#), **410**, 2760
- Ventura P., D'Antona F., Di Criscienzo M., Carini R., D'Ercole A., vesperini E., 2012, [ApJ](#), **761**, L30
- Ventura P., di Criscienzo M., D'Antona F., Vesperini E., Tailo M., Dell'Agli F., D'Ercole A., 2014, [MNRAS](#), **437**, 3274
- Vesperini E., Heggie D. C., 1997, [MNRAS](#), **289**, 898
- Vesperini E., McMillan S. L. W., Portegies Zwart S., 2009, [ApJ](#), **698**, 615
- Vesperini E., McMillan S. L. W., D'Antona F., D'Ercole A., 2010, [ApJ](#), **718**, L112
- Vesperini E., McMillan S. L. W., D'Antona F., D'Ercole A., 2013, [MNRAS](#), **429**, 1913
- Vesperini E., Hong J., Giersz M., Hypki A., 2021, [MNRAS](#), **502**, 4290
- Wadsley J. W., Stadel J., Quinn T., 2004, [New A](#), **9**, 137
- Walch S., et al., 2015, [MNRAS](#), **454**, 238
- Walker A. R., 1999, [AJ](#), **118**, 432
- Wang L., Kroupa P., Takahashi K., Jerabkova T., 2020, [MNRAS](#), **491**, 440

Bibliography

- Wang S., Chen B., Ma J., 2021, [A&A, 645, A115](#)
- Webb J. J., Harris W. E., Sills A., Hurley J. R., 2013, [ApJ, 764, 124](#)
- Wirth H., Jerabkova T., Yan Z., Kroupa P., Haas J., Šubr L., 2021, [MNRAS, 506, 4131](#)
- Yaghoobi A., Calura F., Rosdahl J., Haghi H., 2022, [MNRAS, 510, 4330](#)
- Zennaro M., Milone A. P., Marino A. F., Cordini G., Lagioia E. P., Tailo M., 2019, [MNRAS, 487, 3239](#)
- Ziegler U., 2005, [A&A, 435, 385](#)
- Zinn R., 1985, [ApJ, 293, 424](#)
- de Mink S. E., Pols O. R., Langer N., Izzard R. G., 2009, [A&A, 507, L1](#)
- van Leer B., 1977, [Journal of Computational Physics, 23, 276](#)
- van Leer B., 1979, [Journal of Computational Physics, 32, 101](#)
- van den Hoek L. B., Groenewegen M. A. T., 1997, [A&AS, 123, 305](#)
- von Hoerner S., 1957, [ApJ, 125, 451](#)

ACKNOWLEDGEMENTS

*If not for you,
Winter would have no spring,
Couldn't hear the robin sing,
I just wouldn't have a clue,
Anyway it wouldn't be true,
If not for you.*

If not for you, Bob Dylan

I would like to express my sincere gratitude to my supervisor, Francesco Calura for having introduced me to the topic of hydrodynamic simulations and for his trust in me. I am so thankful for his guidance and for his being always available even in the hard pandemic times, helping me to improve and become a better researcher.

I thank so much all the other collaborators, Enrico Vesperini, Carlo Nipoti and Antonino Milone for the useful discussions we had and for the support they always showed me during these years.

A big thank goes to Alessandra Mastrobuono-Battisti for hosting me in a blooming Paris. I have learned a lot in the months I spent there and I am happy about the work we did together, but, above all, I am thankful for her support, help and patience in this last year of my Ph.D., not only concerning work-related topics.

I wish to thank all my colleagues in Bologna for the friendly working atmosphere which made the ride to the department more pleasant, especially in the foggy November days, but also for all the time spent outside the University. A special thank goes to my

Acknowledgements

officemates for all the breaks spent together, especially the ones on the terrace of the INAF third floor staring at the sunset.

I would like to thank my Parisian mates: Linda for all the dinners spent together, I could not have wished for a better neighbor and Simon, for joining me in the exploration of this amazing city.

I sincerely thank also my long-standing friends for being supportive and so close even if it was much harder to see each other in person in these last few years.

A special thank goes to my mum, for her support and encouragement even in the darkest times. I am so grateful for her help, for her being always by my side and for all the sacrifices she has done for me.

Dulcis in fundo, I want to immensely thank Marco for his distance-invariant love, his limitless patience and his ability to make me smile every time.